Ground Motion Selection for Seismic Response Analysis

a dissertation submitted to the university of Canterbury in partial fulfilment of the requirements for the degree of doctor of philosophy

Karim Tarbali

April 2017

department of civil and natural resources engineering, university of Canterbury

Christchurch, New Zealand

Abstract

This dissertation addresses several fundamental and applied aspects of ground motion selection for seismic response analyses. In particular, the following topics are addressed: the theory and application of ground motion selection for scenario earthquake ruptures; the consideration of causal parameter bounds in ground motion selection; ground motion selection in the near-fault region where directivity effect is significant; and methodologies for epistemic uncertainty consideration and propagation in the context of ground motion selection and seismic performance assessment. The paragraphs below outline each contribution in more detail.

A scenario-based ground motion selection method is presented which considers the joint distribution of multiple intensity measure (IM) types based on the generalised conditional intensity measure (GCIM) methodology (Bradley, 2010b, 2012c). The ground motion selection algorithm is based on generating realisations of the considered IM distributions for a specific rupture scenario and then finding the prospective ground motions which best fit the realisations using an optimal amplitude scaling factor. In addition, using different rupture scenarios and site conditions, two important aspects of the GCIM methodology are scrutinised: (i) different weight vectors for the various IMs considered; and (ii) quantifying the importance of replicate selections for ensembles with different numbers of desired ground motions. As an application of the developed scenario-based ground motion selection method, ground motion ensembles are selected to represent several major earthquake scenarios in New Zealand that pose a significant seismic hazard, namely, Alpine, Hope and Porters Pass ruptures for Christchurch city; and Wellington, Ohariu, and Wairarapa ruptures for Wellington city.

A rigorous basis is developed, and sensitivity analyses performed, for the consideration of bounds on causal parameters (*e.g.,* magnitude, source-to-site distance, and site condition) for ground motion selection. The effect of causal parameter bound selection on both the number of available prospective ground motions from an initial empirical as-recorded database, and the statistical properties of IMs of selected ground motions are examined. It is also demonstrated that using causal parameter bounds is not a reliable approach to implicitly account for

ground motion duration and cumulative effects when selection is based on only spectral acceleration (SA) ordinates. Specific causal parameter bounding criteria are recommended for general use as a 'default' bounding criterion with possible adjustments from the analyst based on problem-specific preferences.

An approach is presented to consider the forward directivity effects in seismic hazard analysis, which does not separate the hazard calculations for pulse-like and non-pulse-like ground motions. Also, the ability of ground motion selection methods to appropriately select records containing forward directivity pulse motions in the near-fault region is examined. Particular attention is given to ground motion selection which is explicitly based on ground motion IMs, including SA, duration, and cumulative measures; rather than a focus on implicit parameters (*i.e.,* distance, and pulse or non-pulse classifications) that are conventionally used to heuristically distinguish between the near-fault and far-field records. No *ad hoc* criteria, in terms of the number of directivity ground motions and their pulse periods, are enforced for selecting pulse-like records. Example applications are presented with different rupture characteristics, source-to-site geometry, and site conditions. It is advocated that the selection of ground motions in the near-fault region based on IM properties alone is preferred to that in which the proportion of pulse-like motions and their pulse periods are specified *a priori* as strict criteria for ground motion selection.

Three methods are presented to propagate the effect of seismic hazard and ground motion selection epistemic uncertainties to seismic performance metrics. These methods differ in their level of rigor considered to propagate the epistemic uncertainty in the conditional distribution of IMs utilised in ground motion selection, selected ground motion ensembles, and the number of nonlinear response history analyses performed to obtain the distribution of engineering demand parameters. These methods are compared for an example site where it is observed that, for seismic demand levels below the collapse limit, epistemic uncertainty in ground motion selection is a smaller uncertainty contributor relative to the uncertainty in the seismic hazard itself. In contrast, uncertainty in ground motion selection process increases the uncertainty in the seismic demand hazard for near-collapse demand levels.

Acknowledgement

Firstly, I would like to thank my main advisor Professor Brendon Bradley for the tremendous opportunity of working under his supervision. While living far away from my family was a challenge, I enjoyed every day of my PhD experience because of his kind spirit, positive mindset, and amazing guidance. I learned so much from his vast technical knowledge, in addition to his extraordinary leadership. Professor Bradley has set the example of excellence as a researcher, teacher, and leader for me. I cannot overstate his significant impact on my personal and professional development. I am deeply indebted to him for his kindness to consider my family's condition, and provide me with means to support them effectively.

It was an honour to have Professor Jack Baker as a co-advisor of my PhD research. I am earnestly grateful to him for devoting his invaluable time to my research. His kind spirit and motivating guidance were always encouraging me to do my very best.

I also would like to thank Professor Misko Cubrinovski for providing insightful comments on my PhD research, and the opportunity of teaching in his Geotechnical Earthquake Engineering class, which was an amazing learning experience for me. Many thanks to Professor Cubrinovski and Professor Bradley for their kind guidance on lecturing.

I would like to express my sincere gratitude to Dr. Peter Powers of the U.S. Geological Survey for hosting me in The National Earthquake Information Center in Golden, Colorado. I enjoyed my time in Colorado because of Dr. Powers's kind hospitality and the opportunity I had to learn from his vast knowledge in seismic hazard analysis and software development.

I have been blessed with an amazing advisor in my BSc at the University of Mohaghegh Ardabili, Professor Kazem Shakeri, who patiently taught me the fundamentals of scientific research. He is a dear friend of mine who supported me through tough times. Professor Shakeri had a significant impact on my personal and professional development and I am indebted to him for many things he has taught me directly and indirectly. Having great technical and non-technical discussions is among the greatest memories I have from his company.

I also would like to thank my MSc advisor, Professor Fariborz Nateghi-Elahi, for his kind support and teaching me to be an independent thinker in research and life. My MSc experience in the International Institute of Earthquake Engineering and Seismology was fruitful because of his kind support.

I have amazing friends from my home town, Ardabil, Iran, who have been sincerely kind to me all my life and their friendship means the world to me. I want

to express my deepest gratitude to several people — Hamed Rasouli for being like a brother to me, who opened doors to many opportunities for me, and his kind company through many happy and sad moments of life; Mehdi Ebrahimi, Ahmad Dehgani, Hasan Sahranavard, Masoud Shoja, and Davood Dadras for creating some of the greatest memories of my life, their company kept me coming back home every year; Mehran Aflakparast and Morteza Ziyadi for their kind support and hosting me in the Nederlands and the U.S. I want to especially thank Sohrab Bouzari and Bahareh Nouri for being such amazing friends, and helping me in many challenging moments of life, like a brother and sister.

I have many great friends in New Zealand, among them Farhad Dashti is a dear friend of mine without whom I could not survive many hard days of my PhD. We had unforgettable sweet memories of getting food from take-away shops, listening to Turkish music, and having conversations about many interesting topics in life.

I would like to exclusively thank Tony Hearn, Annette Hearn (deceased), and Angela Clay for being like a family for me in New Zealand. Tony is a dear friend of mine and I am sincerely indebted to him for all the kind things he has done for me in the past three years.

My fellow PhD and MSc students, Robin Lee, Ethan Thomson, Xavier Bellagamba, Kevin Foster, Chris de la Torre, and Varun Joshi are gratefully thanked for being such amazing friends. We had great times together in and outside the work environment. Special thanks to Xavier and Kevin for their kind support. Also, many thanks to postdoc fellows of our group, Ahsan Nazer, Hoby Razafindrakoto, Seokho Jeong, and Chris McGann.

I am also thankful to my dear friends in Christchurch — Amir Malek, Naeimeh Abi, Samaneh Dashti, Daneil Court-Patience, Morteza Tagihzadeh, Amirhossein Orumiyehei, Anne-Catherine Berrut, and Sara Pienisch for their kindness. I am especially grateful to Amir Malek for helping me find a doctor for my father.

Financial support of the University of Canterbury, New Zealand Earthquake Commission (EQC), and Rutherford Discovery Fellowship are gratefully acknowledged.

Finally, but foremost, I would like to thank my parents and sisters for their life-long love, encouragement, and support. My parents were my greatest teachers in life and their thoughts and prayers were always with me each and every step of the way. I dedicate this dissertation to my parents, because I owe it all to them.

To my parents

Alleruzun gabarin opuram

Yorgun januzi seviram

Duaa eliyan dodaxlaruza madyunam

Gozlaruzun ishigi gunduzumun aydinigi, va sozlaruzun istisi urayimin guvvati dir

Contents

List of Figures

List of Tables

Chapter 1

Introduction

1.1 Motivation

Accurately assessing seismic performance of engineered systems requires ground motion time series to perform time-domain seismic response analysis of the system, and in essence, such ground motions provide the connection between seismic hazard and seismic response analysis steps in the performance assessment process. Hence, selected ground motions should appropriately represent the seismic hazard (at the site of interest) in order to provide a means to obtain an unbiased distribution of the system's seismic response.

Numerous approaches have been proposed for selecting ground motion time series recorded during past earthquakes and/or from ensembles of simulated ground motions (*e.g.,* McGuire, 1995; Shome et al., 1998; Bommer and Acevedo, 2004; Kottke and Rathje, 2008; Baker, 2011; Jayaram et al., 2011; Wang, 2011; Bradley, 2012c; Bradley et al., 2015). A review of these methods reveals that they are principally based on matching the (pseudo) acceleration response spectrum of the prospective ground motions to a target spectrum, which is obtained from either seismic hazard analysis, or a seismic design code (Katsanos et al., 2010). One methodology, in particular, is concerned with selecting ground motions based on multiple intensity measures (IMs) representing amplitude, frequency content,

duration, and cumulative measures (Bradley, 2010b, 2012c). Considering the importance of selecting appropriate ground motion ensembles for seismic response analysis, there are several issues that are not adequately addressed in the existing literature. Some of these issues, which are the focus of this dissertation, are outlined here.

While seismic hazard is frequently defined based on probabilistic seismic hazard analysis, understanding the anticipated seismic performance due to the occurrence of specific 'scenario' earthquake ruptures is also of interest, which requires ground motion ensembles selected based on scenario seismic hazard analysis (FEMA-P58, 2012). Since, previous scenario-based ground motion selection methods (*e.g.,* Kottke and Rathje, 2008; Baker, 2011; Jayaram et al., 2011; Wang, 2011) have considered only spectral amplitudes, there is a need for adequate consideration of the joint consideration of multiple IM types.

Performing ground motion selection based on multiple IM types requires considering the relative importance of them in the selection process using a weight vector (Bradley, 2012c). It is important to identify an appropriate weight distribution on IMs that represent the salient features of ground motion (*i.e.,* amplitude, frequency content, duration, and cumulative effects) to obtain an unbiased response of the system of interest.

Utilising bounds on causal parameters (*e.g.,* magnitude, source-to-site distance, and site condition) of prospective ground motion prior to performing a rigorous selection based on explicit IMs is common practice in ground motion selection (*e.g.,* Stewart et al., 2001; Bommer and Acevedo, 2004; Baker, 2011; Katsanos et al., 2010; Wang et al., 2015). However, the consideration of such bounds impacts the 'remaining' set of prospective ground motions which can be selected based on misfits to target IM values. As a result, there is a need to develop a consistent approach for setting these bounds as a function of the seismic hazard at the site.

Ground motions in the near-fault region often exhibit characteristics such as

forward directivity velocity pulses which are not observed in the far-field ground motions. The occurrence of such characteristics have been long recognised and numerous studies conducted to illustrate the effect of such ground motions on seismic response of engineered systems (*e.g.,* Bertero et al., 1978; Anderson and Bertero, 1987; Hall et al., 1995; Alavi and Krawinkler, 2001; Luco and Cornell, 2007; Champion and Liel, 2012). Considering the occurrence of directivity pulses in seismic hazard analysis and the subsequent ground motion selection is necessary to accurately estimate seismic response of systems susceptible to such ground motions.

Epistemic uncertainty in the characteristics of causative rupture scenarios and resulting ground motions in probabilistic seismic hazard analysis results in a set of alternative hazard curves for the site of interest. While the consideration of seismic hazard epistemic uncertainties is commonplace, a generalised approach for their propagation to ground motion selection and impact on seismic performance metrics has not been developed.

1.2 Objectives

Considering the above-mentioned issues, the objectives of this dissertation are as follows:

(i) Develop a method to select ground motion ensembles based on scenario seismic hazard analysis results

(ii) Examine different weight vectors to identify an appropriate weight distribution on multiple IMs utilised in scenario-based ground motion selection

(iii) Develop a hazard-consistent basis for the consideration of bounds on causal parameters of prospective ground motions based on scenario and probabilistic seismic hazard analysis results

(iv) Develop an approach to consider forward directivity effect in seismic hazard analysis and ground motion selection in the near-fault region

(v) Develop methods with different levels of rigour to propagate seismic hazard and ground motion selection epistemic uncertainties to seismic performance metrics

1.3 Organisation

Chapter Two extends the generalised conditional intensity measure (GCIM) method (Bradley, 2010b, 2012c) to select ground motion ensembles associated with scenario earthquake ruptures. In addition, using different rupture scenarios and site conditions, various aspects of the GCIM methodology are scrutinised, including: (i) implementation of different weight vectors and the composition of the **IM** vector; (ii) quantifying the importance of replicate selections for different number of desired ground motions; (iii) examining the positive effect of conducting replicate selections to select a suite of motions with a precise representation for the distribution of the considered IMs. A minimum number of replicates for different desired number of motions are also presented.

Chapter Three develops representative ground motion ensembles for several major earthquake scenarios in New Zealand, as an application of the scenario-based ground motion selection methodology developed in Chapter Two. Cases considered include representative ground motions for the occurrence of Alpine, Hope, and Porters Pass earthquakes in Christchurch city, and the occurrence of Wellington, Wairarapa, and Ohariu fault ruptures in Wellington city. These scenario-based ground motion sets can be utilised to understand the performance of structures for the question 'what if this fault ruptures?'

Chapter Four investigates the effect of considering bounds on causal parameters of prospective ground motions for the purpose of ground-motion selection based on scenario and probabilistic seismic hazard analysis results. A rigorous

basis is developed, and sensitivity analyses performed, for the consideration of bounds on magnitude, source-to-site distance, and site condition. The implications of utilising 'wide' and 'narrow' causal parameter bounds in terms of the selected ground motion properties are also discussed.

Chapter Five presents an approach to consider the forward directivity effects in seismic hazard analysis and examines the ability of ground motion selection methods to appropriately select records which exhibit pulse-like ground motions in the near-fault region in order to appropriately represent directivity effects considered in scenario and probabilistic seismic hazard analyses. Particular attention is given to ground motion selection which is explicitly based on ground motion IMs, including spectral amplitudes, duration, and cumulative measures; rather than a focus on implicit parameters (*i.e.,* pulse or non-pulse classifications) that are conventionally used to heuristically distinguish between near-fault and far-field records. The implications of the selected records in terms of the conditional demand distribution and the demand hazard are discussed.

Chapter Six investigates various approaches to propagate the effect of epistemic uncertainty in seismic hazard and ground motion selection to seismic performance metrics. Specifically, three methods with different levels of rigour are presented for establishing the conditional distribution of IMs considered for ground motion selection, selecting ground motion ensembles, and performing nonlinear response history analyses to probabilistically characterise seismic response.

Chapter Seven presents the key contributions of this dissertation in the field of ground motion selection, together with recommendations for future work.

Since each chapter of this dissertation is prepared to be a stand-alone publication, there are introductory and concise literature review parts in each chapter.

Chapter 2

Ground motion selection for scenario ruptures using the generalised conditional intensity measure (GCIM) method

Tarbali, K. and Bradley, B. A. (2015). Ground-motion selection for scenario ruptures using the generalised conditional intensity measure (GCIM) method. *Earthquake Engineering & Structural Dynamics*, 44(10):1601-1621.

2.1 Summary

In this chapter, the generalised conditional intensity measure (GCIM) method is extended to ground motion selection for scenario earthquake ruptures. The selection algorithm is based on generating random realisations of the considered intensity measure (IM) distributions for a specific rupture scenario and then finding the prospective ground motions which best fit the realisations using an optimal amplitude scale factor. Using different rupture scenarios and site conditions, two important aspects of the GCIM methodology are scrutinised: (i) different weight

vectors for the various **IM**'s considered; and (ii) quantifying the importance of replicate selections for ensembles with different numbers of desired ground motions. It is demonstrated that considering only spectral acceleration (SA) ordinates in the selection process, as is common in many conventional selection procedures, may result in selected motions with a biased representation for duration and cumulative ground motion effects. In contrast, considering IMs other than SA ordinates (in particular, Significant Duration, cumulative absolute velocity, and Arias Intensity) results in ensembles with an appropriate representation of these IMs, without a practically significant effect on SA ordinates. The benefit of conducting replicate selections to obtain a suite of motions with an improved representation for the distribution of the considered IMs is demonstrated, and a minimum number of replicates is suggested for different ground motion ensemble sizes.

2.2 Introduction

Nonlinear response history analysis requires a ground motion time series as an input. One of the general approaches to acquire the input ground motion time series is to select appropriate as-recorded ground motions from previously recorded seismic events. Selecting a suite of ground motions for the purpose of conducting seismic response analysis can be based on the results from either scenario seismic hazard analysis (scenario SHA) or probabilistic seismic hazard analysis (PSHA) (Bommer, 2002; FEMA-P58, 2012).

Methods have been proposed to select ground motions based on the intensity of motion predicted by scenario SHA or PSHA (*e.g.,* McGuire, 1995; Shome et al., 1998; Bommer and Acevedo, 2004; Kottke and Rathje, 2008; Baker, 2011; Jayaram et al., 2011; Wang, 2011). A review of the existing methods reveals that majority of them are principally based on matching the (pseudo) acceleration response spectrum of the selected ground motions to a target spectrum. This target spectrum is obtained from either scenario SHA, PSHA, or a seismic design

code (see Katsanos et al. (2010) for a more detailed review). In addition to the predicted intensity of motion, in order to select ground motions with an appropriate representation of the dominant scenario ruptures, implicit causal parameters of ground motions (*e.g.,* magnitude, source-to-site distance) as well as the site condition of the recorded motions are also considered in conventional methods (Katsanos et al., 2010). Another important aspect in ground motion selection is to consider variability in the characteristics of ground motions due to uncertain nature of seismic events. A few of the existing methodologies address this issue in terms of variability in spectral acceleration ordinates of ground motions (*e.g.,* Kottke and Rathje, 2008; Jayaram et al., 2011; Wang, 2011).

It is important to note that the severity of ground motions is not dependent solely upon spectral accelerations, but is a general function of the amplitude, frequency content, cumulative effects, and duration of the ground motion. In addition, there are uncertainties associated with the calculated seismic hazard and the predicted severity of ground motions for a given site, which needs to be addressed in ground motions selection process. In order to properly represent the effect of seismic hazard on engineering systems via selected ground motions, a comprehensive ground motion selection methodology is required to consider all of the factors that affect the severity of a ground motion and also take into account the variability in these factors due to ground motion uncertainty.

The generalised conditional intensity measure (GCIM) approach (Bradley, 2010b) provides a holistic framework to select ground motions considering the distribution of various intensity measures (IMs) to evaluate the appropriateness of a selected suite of ground motions. Application of the GCIM method to select ground motions based on the results of PSHA has been demonstrated by Bradley (2012c); however, an extension of this method has not previously been presented for scenario SHA and it is therefore examined here. This chapter first provides an overview of the GCIM methodology for ground motion selection with scenario SHA, followed by several examples to illustrate the salient features of the procedure, including: (i) implementation of different weight vectors and the com-

position of the **IM** vector; (ii) quantifying the importance of replicate selections for different number of desired ground motions.

2.3 GCIM-based ground motion selection for scenario seismic hazard analysis (scenario SHA)

The GCIM method (Bradley, 2010b) provides the distribution of a vector of ground motion IMs, **IM**, consistent with the results of the seismic hazard analysis. It is considered that this general IM vector (which may contain, *e.g.,* spectral acceleration ordinates, peak ground velocity, Arias Intensity, and Significant Duration, among others) can adequately represent ground motion severity for the engineering systems considered. The steps towards conducting GCIM-based ground motion selection for scenario SHA are explained in the following sections.

2.3.1 Constructing the distribution of the IMs

Selection of ground motions for seismic response analysis requires a 'target', based on which the appropriateness of the selected ground motions is measured. In the GCIM approach, the multivariate distribution of the considered IMs is used as the target. Although not essential (Bradley, 2010b), the lognormal multivariate distribution is considered here for the joint distribution of **IM** based on its observed appropriateness in previous applications (*e.g.,* Baker and Jayaram, 2008; Bradley, 2011c,b,a, 2012b,a, 2015). Based on this consideration, the marginal distribution of each IM_i in **IM** can be expressed as:

$$f_{IM_i|Rup} \sim LN(\mu_{lnIM_i|Rup}, \sigma^2_{lnIM_i|Rup}) \tag{2.1}$$

where $f_{IM_i|Rup}$ is the probability density function of IM_i, given the scenario rupture Rup; $X \sim LN(\ )$ is shorthand notation for X having a lognormal distribution; and $\mu_{lnIM_i|Rup}$ and $\sigma^2_{lnIM_i|Rup}$ are the mean and variance of $lnIM_i$, re-

spectively. The necessary parameters to construct the marginal distribution of IM_i with respect to a specific scenario (*i.e.,* $\mu_{lnIM_i|Rup}$ and $\sigma^2_{lnIM_i|Rup}$) can be obtained from empirical ground motion prediction equations (*e.g.,* Boore and Atkinson, 2008). In order to construct the multivariate distribution of the considered IMs, empirical correlation equations (*i.e.,* Baker and Jayaram (2008); Bradley (2011c,b,a, 2012b,a, 2015)) are used to construct the correlation matrix, *i.e.,* $\boldsymbol{\rho}_{\ln \mathbf{IM}|Rup}(i,j) = \rho_{ij}$, where ρ_{ij} is the correlation coefficient between $lnIM_i$ and $lnIM_j$ for the given rupture, *Rup.* The methodology adopted here to select ground motions is similar in concept to the method proposed by Wang (2011); however, the GCIM-based approach considers the multivariate distribution of a general vector of IMs as the target model in contrast to considering only spectral acceleration ordinates as in Wang (2011), and also allows for non-uniform weighting of the different intensity measures (as discussed in the next section).

2.3.2 Ground motion selection

2.3.2.1 Generating random realisations for the IMs

In order to account for the inherent variability of the IM values for a given scenario rupture it is necessary to select ground motions with an explicit representation of this variability. The most computationally efficient means to select ground motions that capture this variability is to generate random realisations of the considered IMs based on the multivariate GCIM distribution, and then select ground motions that most closely match the generated random realisations (Jayaram et al., 2011; Wang, 2011; Bradley, 2012c).

In order to generate random realisations for the considered IMs, a vector of uncorrelated random numbers with standard normal distribution is first generated ($\mathbf{u}^{nsim}$). Using the calculated correlation matrix, $\boldsymbol{\rho}_{\ln \mathbf{IM}|Rup}$, the uncorrelated random numbers ($\mathbf{u}^{nsim}$) are converted to a vector of correlated random numbers,

as illustrated in Equation 2.2:

$$\mathbf{v}^{nsim} = \mathbf{L}.\mathbf{u}^{nsim} \tag{2.2}$$

where $\mathbf{L}$ is from the Cholesky decomposition of the correlation matrix (*i.e.,* $\boldsymbol{\rho}_{\ln \mathbf{IM}|Rup} = \mathbf{L}\mathbf{L}^T$) and $\mathbf{v}^{nsim}$ is the resulting vector of correlated random numbers with a standard normal distribution. Subsequently, random realisations of the considered IMs are calculated using Equation 2.3:

$$lnIM_i^{nsim} = \mu_{lnIM_i|Rup} + \sigma_{lnIM_i|Rup}\ v_i^{nsim} \tag{2.3}$$

where $\sigma_{lnIM_i|Rup}$ is the square root of the variance (*i.e.,* standard deviation) of $lnIM_i$ and v_i^{nsim} is the i^{th} element of v^{nsim}. The various values of IM_i^{nsim} for all i represent the $nsim^{\text{th}}$ realisation of the IM vector, IM^{nsim}.

2.3.2.2 Finding an appropriate ground motion for nsim$^{\text{th}}$ realisation

For each realisation of the IM vector, $\mathbf{IM}^{nsim}$, a specific ground motion can be selected from a set of prospective motions, *e.g.,* from the NGA database (Chiou et al., 2008), based on the specific motion which has the minimum mismatch to the generated random realisation. Following Bradley (2012c), the mismatch of a prospective ground motion before applying any amplitude scale factor is calculated using Equation 2.4:

$$r^{m,nsim} = \sum_{i=1}^{N_{IM_i}} w_i \left[\frac{lnIM_i^{nsim} - lnIM_i^m}{\sigma_{lnIM_i|Rup}} \right]^2 \tag{2.4}$$

where IM_i^{nsim} is the i^{th} IM value of the $nsim^{\text{th}}$ random realisation; IM_i^m is the i^{th} IM value of the m^{th} prospective ground motion; $\sigma_{lnIM_i|Rup}$ is the standard deviation of $lnIM_i$; w_i is the weight-vector component emphasising the importance of IM_i, as discussed further in Bradley (2012c); and r_m^{nsim} is the calculated residual of the m^{th} prospective ground motion with respect to $nsim^{\text{th}}$ random realisation.

It is important to highlight that, unlike the PSHA-based ground motion selection case, there is no uniquely defined amplitude scale factor for each ground motion (Bradley, 2010b). Therefore, in order to rank the appropriateness of a prospective ground motion in the database, and identify the most suitable ground motion for$nsim^{\text{th}}$ realisation, the calculated residual for each prospective ground motion is minimised with respect to the applied amplitude scale factor (SF), as presented in Equation 2.5:

$$r_{min}^{m,nsim} = \underset{SF}{\text{minimize}}\left(\sum_{i=1}^{N_{IM_i}} w_i \left[\frac{lnIM_i^{nsim} - ln(SF^{\alpha} IM_i^m)}{\sigma_{lnIM_i|Rup}}\right]^2\right) \tag{2.5}$$

whereSF is the amplitude scale factor; α is an integer describing how the IM value scales with SF (*e.g.,* $\alpha = 1$ for spectral acceleration; $\alpha = 2$ for Arias Intensity; and $\alpha = 0$ for Significant Duration) (Bradley, 2012c). The $r_{\text{min}}^{m,nsim}$ value for the m^{th} prospective ground motion is used to rank it among all of the prospective ground motions in the database. The ground motion with the smallest $r_{\text{min}}^{m,nsim}$ value among all prospective motions is then selected as the ground motion for the $nsim^{\text{th}}$ realisation. It is also noted that the minimisation problem to be solved in Equation 2.5 is straightforward using standard single variable optimisation routines because $r^{m,nsim}$ is a smooth function of SF.

2.3.2.3 Conducting Replicate Selections

Since ground motions are selected based on the random realisation of the considered IMs using the above procedure, performing the selection process successive times may result in different selected ground motions. By repeating the selection process several times, the 'best' replicate can be obtained by comparing the distribution of the IMs from the selected sets with the predicted GCIM distribution for the scenario rupture (Bradley, 2013c). This comparison is made on basis of calculating an overall residual, R, for a given selected set of ground

motions, presented in Equation 2.6:

$$R = \sum_{i=1}^{N_{IM}} w_i (D_{IM_i})^2 \tag{2.6}$$

where D_{IM_i} is the Kolmogorov-Smirnov (KS) test statistic which is the maximum difference between the empirical distribution of IM_i (*i.e.,* from the selected ground motions) and the corresponding target (theoretical) distribution calculated by the GCIM approach (*i.e.,* Equation 2.1). As indicated by Equation 2.6, the calculated overall residual, R, consists of the mismatch between the empirical and theoretical distributions of all of the IMs (*i.e.,* D_{IM_i}), considering their relative importance dictated by the weight-vector component (*i.e.,* w_i). Therefore, R is used to identify the best set of ground motions among the selected sets from the various replicates. It is expected that when a small number of ground motions is desired, the effect of replicate selection will be important (as one small set of realisations may not well represent the target distribution), with a decreasing importance as the desired number of ground motions increases. The process of conducting replicate selections along with the other steps in a GCIM-based ground-motion selection process is illustrated in Figure 2.1.

2.3.2.4 Summary of the scenario-based GCIM ground motion selection procedure

In order to summarise the required steps to select ground motions based on the GCIM methodology for scenario SHA, and depict the role of ground motion selection in a seismic performance assessment framework, Figure 2.1 presents a flow chart illustrating the ground motion selection steps along with the necessary calculations before and after the selection. As seen in this flow chart, ground motion selection provides the key link between seismic hazard analysis and seismic response analysis. Therefore, it is important to note that any bias introduced at the ground motions selection stage may lead to bias in the obtained responses of the system and consequently decisions regarding the performance of the system.

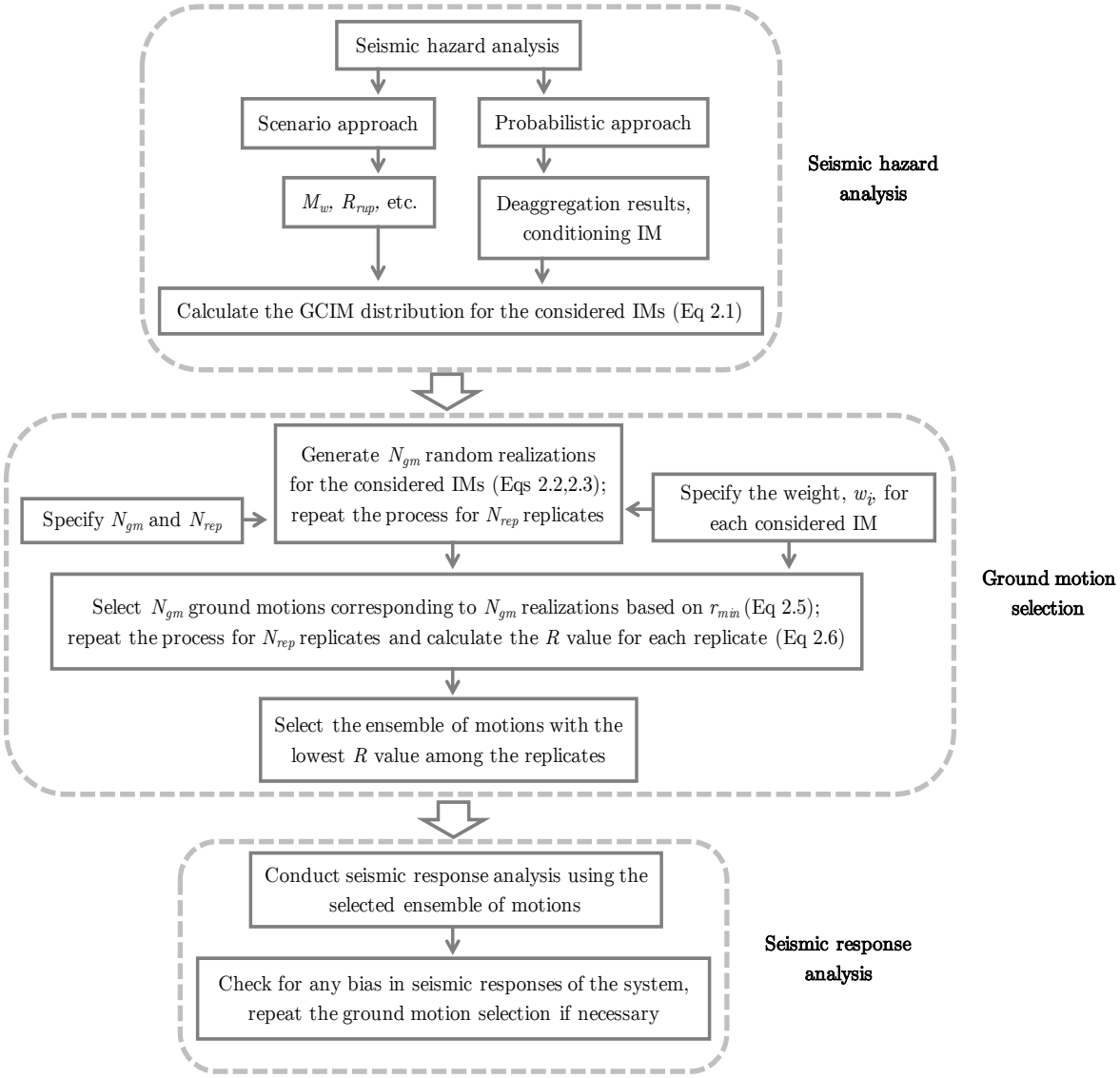

Figure 2.1: Ground motion selection based on the GCIM methodology in a seismic performance assessment framework

2.4 Application of the GCIM methodology for scenario SHA-based ground motion selection

In this section, ground motion selection applications using the GCIM methodology is presented. Different rupture scenarios and site conditions are considered and particular attention is given to the possible external inputs required by the user to facilitate the ground motion selection. The specific issues covered in this section are:

i. Using different weight vectors, w_i, and their corresponding effects on the characteristics of selected ensemble of ground motions.

ii. Quantifying the importance of replicate selection for different numbers of desired ground motions.

The considered rupture scenarios and the site conditions are presented in Table 2.1. As seen in this table, rupture scenarios with moderate and large magnitudes (M_w6.5 and 7.5) are considered, as well as small and moderate source-to-site distances (10 km and 40 km). Since the empirical ground motion prediction equations are not well-constrained for ruptures with extremely large magnitudes (8~9 M_w), these scenarios are not considered here. Soil conditions considered represent soft and stiff soil, and soft rock conditions (V_{s30}= 200, 400, and 600 m/s). A strike-slip mechanism is used as the only focal mechanism for the considered scenario ruptures, because the average effect of focal mechanism are well captured simply through amplitude scaling of ground motions.

A range of IMs are considered in this study in order to adequately represent ground motion amplitude, frequency content, duration, and cumulative effects. Specifically, these IMs include spectral acceleration for 18 vibration periods (T=0.05, 0.075, 0.1, 0.15, 0.2, 0.25, 0.3, 0.4, 0.5, 0.75, 1.0, 1.5, 2.0, 3.0, 4.0, 5.0, 7.5, and 10.0 s); peak ground acceleration (PGA); peak ground velocity (PGV); acceleration spectrum intensity (ASI); spectrum intensity (SI); displacement spec-

Table 2.1: Characteristics of the considered scenario ruptures and site conditions

Scenario	Magnitude, M_w	Source-to-site distance, R_{rup} (km)	Fault type	Site condition, V_{s30} (m/s)
M7.5R10V200	7.5	10	Strike Slip	200
M7.5R10V400	7.5	10	Strike Slip	400
M7.5R10V600	7.5	10	Strike Slip	600
M7.5R40V200	7.5	40	Strike Slip	200
M7.5R40V400	7.5	40	Strike Slip	400
M7.5R40V400	7.5	40	Strike Slip	600
M6.5R10V200	6.5	10	Strike Slip	200
M6.5R10V400	6.5	10	Strike Slip	400
M6.5R10V600	6.5	10	Strike Slip	600
M6.5R40V200	6.5	40	Strike Slip	200
M6.5R40V400	6.5	40	Strike Slip	400
M6.5R40V600	6.5	40	Strike Slip	600

trum intensity (DSI); cumulative absolute velocity (CAV); Arias Intensity (AI); and 5-57% and 5-95% Significant Durations (D_{s575} and D_{s595}, respectively). Empirical ground motion models (GMMs) to obtain the marginal distribution of these IMs are presented in Table 2.2. Also, presented in Table 2.3 are the empirical correlation equations and the corresponding values between the considered IMs based on Baker and Jayaram (2008); Bradley (2011c,b,a, 2012b,a, 2015).

Table 2.2: GMMs to obtain the marginal distribution of the considered IMs

IM	SA, PGA, PGV	ASI	SI	DSI
GMM	Boore and Atkinson (2008)	Bradley (2010)	Bradley et al. (2009)	Bradley (2011)

IM	CAV	AI	D_{s575}	D_{s595}
GMM	Campbell and Bozorgnia (2010)	Campbell and Bozorgnia (2012)	Bommer et al. (2009)	Bommer et al. (2009)

Table 2.3: Empirical correlation equations and values between the considered IMs

IM	SA	PGA	PGV	ASI	SI	DSI	CAV	D_{s575}	D_{s595}	AI
SA	BJ08	B11(b)	B12(b)	B11(b)	B11(b)	B11(c)	B12(a)	B11(a)	B11(a)	B15
PGA	-	1.0	0.73	0.93	0.60	0.40	0.70	-0.41	-0.44	0.83
PGV	-	-	1.0	0.73	0.89	0.80	0.69	-0.21	-0.26	0.73
ASI	-	-	-	1.0	0.64	0.37	0.70	-0.41	-0.37	0.81
SI	-	-	-	-	1.0	0.78	0.68	-0.13	-0.08	0.68
DSI	-	-	-	-	-	1.0	0.57	0.07	0.16	0.51
CAV	-	-	Symmetric	-	-	-	1.0	0.08	0.12	0.89
D_{s575}	-	-	-	-	-	-	-	1.0	0.84	-0.19
D_{s595}	-	-	-	-	-	-	-	-	1.0	-0.20
AI	-	-	-	-	-	-	-	-	-	1.0

Equations are functions of vibration period: BJ08=Baker and Jayaram (2008); B11(b)=Bradley (2011b); B12(b)=Bradley (2012b); B11(c)=Bradley (2011c); B12(a)=Bradley (2012a); B11(a)=Bradley (2011a); B15=Bradley (2015).

2.4.1 Effect of the weight vector on the characteristics of selected ensemble of motions

Different aspects of a ground motion affect the seismic response of different engineering systems, and even different seismic response metrics within the same system (Bradley et al., 2010). Therefore, prior to selecting ground motions, it is important to identify the type of engineering system and seismic response metrics considered for seismic performance assessment, so that the selection process can aim to place emphasis on those intensity measures important to determine the characteristic response of the system. For instance, empirical evidence suggests that the peak inter-story drift of a building structure is strongly affected by spectral acceleration ordinates of the applied motion for periods near the first several vibration modes of the structure (*e.g.,* Shome et al., 1998; Tothong and Cornell, 2007). In contrast, for example, the response of geotechnical structures with liquefaction-susceptible soils and the collapse capacity of building structures can be considerably affected by duration and cumulative effects of ground motions (Bradley, 2010b; Bradley et al., 2013; Villaverde, 2007). This problem-specific is-

sue has been addressed in the GCIM-based ground motion selection methodology by using a weight vector in the selection algorithm (Bradley, 2012c), to weight these different ground motion aspects in record selection. In order to consider different aspects of a ground motion (*i.e.,* intensity, frequency content, duration, and cumulative effect) the selection procedure should be based on representativeness of multiple intensity measures for the considered rupture scenarios.

The effect of the weight vector is illustrated by presenting the results for the selection of 20 motions (*i.e.,* $N_{gm} = 20$) by conducting 10 replicate selections (*i.e.,* $N_{rep} = 10$). $N_{rep} = 10$ is shown subsequently to be more than sufficient to give stable results for $N_{gm} = 20$. Table 2.4 presents the weight vectors examined in this study to scrutinise the corresponding effects on the characteristics of selected ensembles of ground motions. Weight vector case 1 represents the conventional approach to select ground motions based only on SA ordinates. Case 2 represents a selection mainly based on SA ordinates with some consideration allocated to Significant Duration of motion. Case 3, 4, and 5 represent the consideration of CAV and AI (as well as SA ordinates) as metrics to account for cumulative effects of ground motions in lieu of duration. Case 6 represents a selection based on Significant Duration and cumulative effects (*i.e.,* CAV and AI) as well as SA ordinates. Finally, case 7 represents a selection based on ASI, SI, and DSI in lieu of SA ordinates given that ASI, SI, and DSI represents the amplitude of the ground motion in short, moderate, and long vibration periods. Because of the large number of permutations resulting from the consideration of the numerous values of the above variables, a complete presentation of all of the permutation results is not attempted. Rather, illustrative figures and summary statistics are used to convey the key features of the obtained results.

2.4.1.1 Selection based only on spectral acceleration ordinates

Spectral acceleration ordinates have been conventionally used as a metric to represent the amplitude of ground motions via the response of a simplified substi-

Table 2.4: Weight vectors considered for the ground motion selections

Case	SA	D_{s575}	D_{s595}	AI	CAV	ASI	SI	DSI
1	1.0[1]	-	-	-	-	-	-	-
2	0.7[1]	0.15	0.15	-	-	-	-	-
3	0.7[1]	-	-	0.3	-	-	-	-
4	0.7[1]	-	-	-	0.3	-	-	-
5	0.7[1]	-	-	0.15	0.15	-	-	-
6	0.6[1]	0.10	0.10	0.10	0.10	-	-	-
7	-	-	-	-	-	0.33	0.33	0.33

[1] Evenly distributed to 18 *SA* ordinates, *e.g.,* for case 1 each SA ordinates has a weight of $w_i = 1/18$.

tute single-degree-of-freedom system. As a result, acceleration response spectral ordinates are considered in the majority of ground motion selection procedures as the target to select ground motions (*e.g.,* Jayaram et al., 2011; Wang, 2011; ASCE/SEI7-10, 2010; NEHRP, 2011; NZS1170.5, 2004). In order to investigate the characteristics of the motions selected based only on SA ordinates, GCIM-based ground motion selection is conducted for the considered rupture scenarios and site conditions, considering only SA ordinates in the weight vector (*i.e.,* case 1).

Figure 2.2a presents the 16^{th}, 50^{th}, and 84^{th} percentiles of the target (*i.e.,* GCIM) distribution for SA ordinates of the M6.5R10V400 rupture scenario (*i.e.,* $M_w = 6.5$, $R_{rup} = 10\ km$, , $V_{s30} = 400\ m/s$) and the acceleration response spectrum of the individual motions selected using weight vector case 1. The 16^{th}, 50^{th}, and 84^{th} percentiles of SA ordinates of the selected motions are also presented in this figure. It can be seen that the selected motions properly address the variability in SA ordinates of the target (*i.e.,* GCIM) distribution for the whole range of vibration periods, as intended by the adopted weight vector. An appropriate representativeness of the selected motions can be seen by the conformity of the

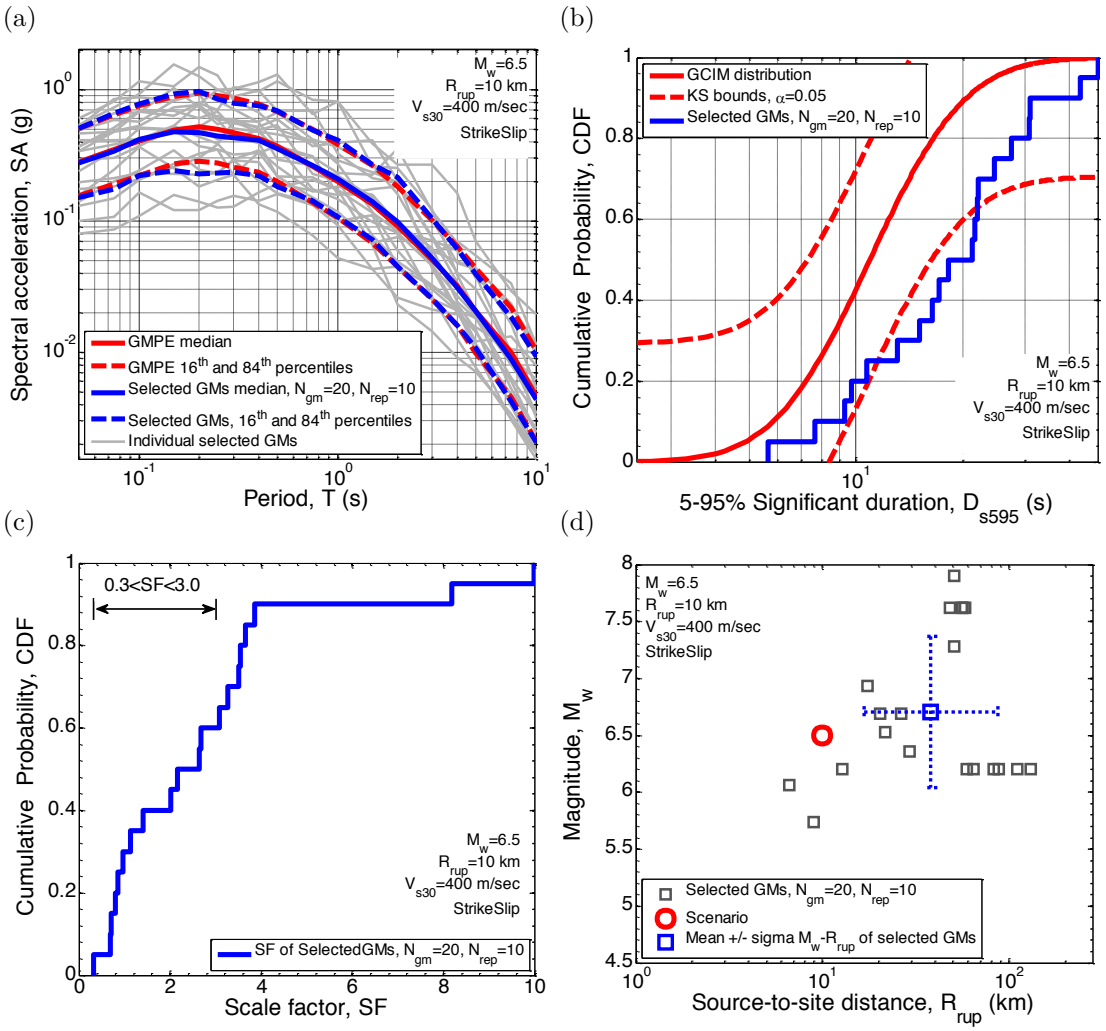

Figure 2.2: Properties of selected motions based only on SA ordinates (*i.e.,* weight vector case 1 for the M6.5R10V400 rupture scenario: (a) SA ordinates; (b) cumulative distribution of D_{s595}; (c) cumulative distribution of the amplitude scale factors; and (d) M_w-R_{rup} distribution.

16th, 50th, and 84th percentiles of the selected motions to the 16th, 50th, and 84th percentiles of the GCIM distribution.

Despite the conformity of the selected motions to the target distribution of SA ordinates, the selected motions may have a biased representation for other important IMs. As depicted in Figure 2.2b, as an example, the 5-95% Significant Duration, D_{s595}, of the selected motions based only on SA ordinates (*i.e.,* weight vector case 1) have a bias in representing the predicted distribution of D_{s595} for the considered rupture scenario, as indicated by the empirical distribution lying

outside the Kolmogorov-Smirnov (KS) test bounds for $\alpha = 5\%$ significance level (Ang and Tang, 1975). It is important to note that having a biased distribution for certain IMs will cause a bias in the obtained seismic responses of the system, if such responses are affected by these biased IMs (Bradley, 2010b, 2012c).

While ground motion selection using the GCIM method does not make explicit use of the amplitude scale factors or other implicit causal parameters such as magnitude, source-to-site distance, and site condition, examining the distributions of these parameters for the selected motions is often a good independent check of the quality of the obtained results (Bradley, 2012c). Figure 2.2c presents the cumulative distribution of the amplitude scale factors of the selected motions for the considered scenario. As seen in this figure, approximately 70% of the selected ground motions have an amplitude scale factor in the range of 0.3-3.0. Similar ranges are often recommended as scaling limits in seismic design standards (ASCE/SEI7-10, 2010; NZS1170.5, 2004)).

Figure 2.2d illustrates the magnitude and source-to-site distance distribution of the motions selected based only on SA ordinates with respect to the target rupture scenario. As seen in this figure, the mean magnitude of the selected motions is fairly close to the magnitude of the target scenario; however, the selected motions have mostly greater R_{rup} values when compared to the small R_{rup} of the rupture scenario. The slightly larger magnitude, and larger source-to-site distance are the likely reason for the biased distribution of D_{s595} shown in Figure 2.2b, given that D_{s595} increases with M_w and R_{rup} (Bommer et al., 2009).

The $M_w - R_{rup}$ distribution of selected motions is also obviously a function of the seismic rupture scenario considered in addition to the weight vector adopted. For example, in contrast to Figure 2.2d (with $M_w = 6.5$, $R_{rup} = 10\ km$, $V_{s30} = 400\ m/s$), Figure 3a illustrates the $M_w - R_{rup}$ distribution of the selected motions for the M7.5R10V400 rupture scenario (*i.e.,* $M_w = 7.5$, $R_{rup} = 10\ km$, $V_{s30} = 400\ m/s$), using weight vector case 1 (*i.e.,* SA only). In this case it can be seen that the average magnitude of the selected motions is less than that for the

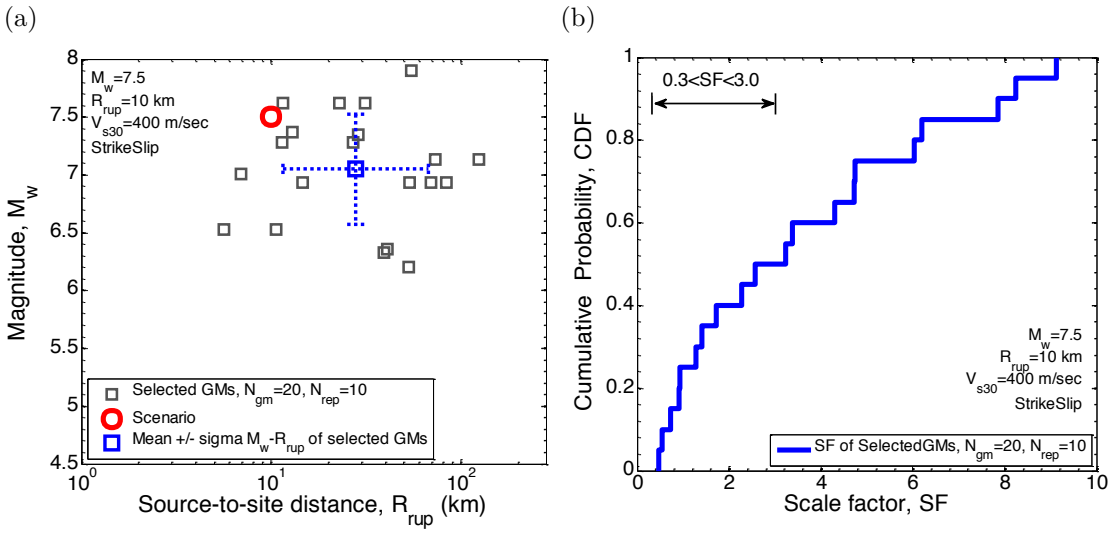

Figure 2.3: (a) M_w-R_{rup} distribution; and (b) amplitude scale factors of selected ground motions for the M7.5R10V400 rupture scenario using weight vector case 1 (*i.e.,* SA only).

rupture scenario, principally as a result of the paucity of the recorded motions during events with large magnitudes (and the use of a weight vector with non-zero values only for SA ordinates). As presented in Figure 2.3b, in contrast to the results presented in Figure 2.2c, amplitude scale factors of the selected motions for the M7.5R10V400 rupture scenario are mostly larger compared to those for the M6.5R10V400 rupture scenario. This is due to the fact that the database of strong ground motions is not well-constrained for motions from large magnitude scenarios, therefore, large amplitude scaling factors are required to scale the available motions to match the intensity of motion predicted for those scenarios.

Figures 2.4b-c present the shear wave velocity versus source-to-site distance (*i.e.,* $V_{s30} - R_{rup}$) distribution of the selected motions for the scenarios with $M_w = 6.5$, $R_{rup} = 10\ km$ and V_{s30} =200, 400, and 600 m/s soil conditions. As seen in this figure, the selected motions do not have an appropriate representation for V_{s30} of a soft soil (*i.e.,* $V_{s30} = 200$) and soft rock (*i.e.,* $V_{s30} = 600$), as much as they have for a stiff soil (*i.e.,* $V_{s30} = 400$). This is again likely a result of the larger portion of ground motions recorded on stiff soils in empirical ground motion databases

than records on soft soils and soft rock. Similar results have been obtained using other weight vectors for the considered rupture scenarios presented in Table 2.1.

Further discussion on the representativeness of the selected motions for these and other implicit causal parameters is elaborated on further when bounds are applied on the implicit causal parameters of prospective ground motions in the chapter four.

2.4.1.2 Selection based on SA ordinates and significant duration

As depicted in Figure 2.2b, selecting ground motions based only on SA ordinates may result in motions with an inadequate representation for Significant Duration, a result of the fact that SA ordinates only explicitly consider the amplitude and frequency content of a ground motion. Although there are many definitions to represent duration of ground motions (Bommer and Martinez-Pereira, 1999), Significant Duration is chosen here as the duration-metric for reasons discussed in Bradley (2011a).

In order to explicitly examine the influence of considering significant duration on the characteristics of the selected ground motions, a second weight vector case was considered (*i.e.,* case 2) which prescribes a total of 70% weight across the SA ordinates and 30% weight to Significant Duration-based metrics (*i.e.,* D_{s575} and D_{s595}). The reason for allocating 30% of the total weight on D_{s575} and D_{s595} is based on the numerous selections conducted in this study, indicating that using a total weight of less than 60% on SA ordinates results in motions with a poor representation for the target distribution of SA ordinates.

Figures 2.5a-c present the cumulative distribution of 5-75% and 5-95% Significant Duration IMs of the ground motions selected for the M6.5R10V400 scenario using weight vector case 2 (*i.e.,* SA, D_{s575}, and D_{s595}). As seen in this figure, the selected motions have an unbiased representation for D_{s575} and D_{s595}, along with an appropriate representation for the median, 16^{th}, and 84^{th} percentiles of the SA ordinates presented in Figure 2.5c. Figure 2.5d illustrates the magnitude

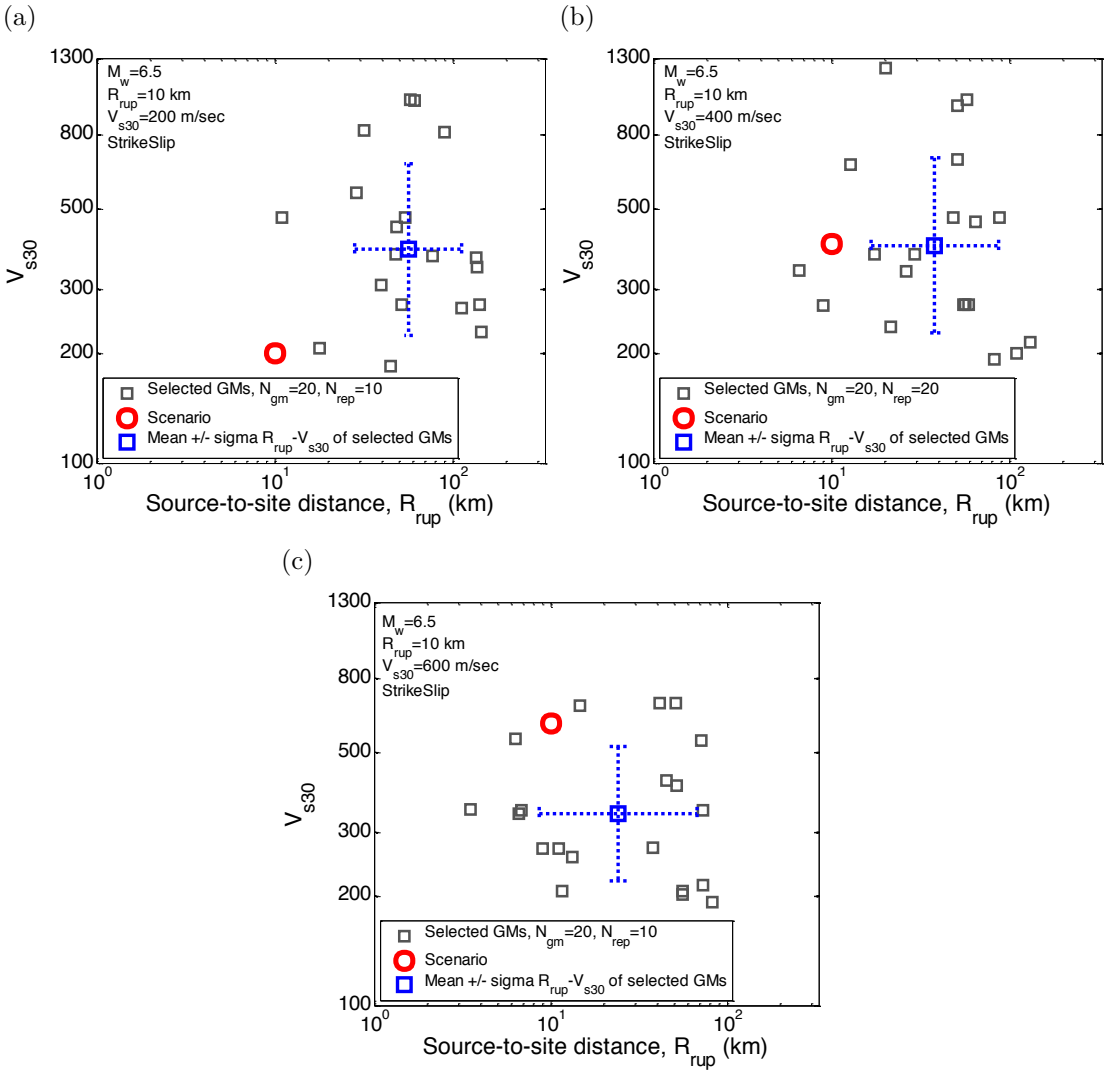

Figure 2.4: M_w-R_{rup} distribution of selected motions using weight vector case 1 (*i.e.*, SA only) for the M6.5R10 rupture scenario with: (a) V_{s30}=200 m/s; (b) V_{s30}=400 m/s; and (c) V_{s30}=600 m/s soil conditions.

and source-to-site distance distribution of the selected motions using weight vector case 2 (*i.e.,* SA, D_{s575}, and D_{s595}). It can be seen that source-to-site distance of the selected motions are closer to the target scenario in comparison with the results presented in Figure 2.2d (*i.e.,* the mean-standard deviation of R_{rup} now encompass the R_{rup} value of the rupture scenario). Since, as mentioned previously, Significant Duration of a ground motion is correlated with magnitude and source-to-site distance of the rupture scenario (Bommer et al., 2009), then enforcing ground motion selection to consider Significant Duration is seen to have a positive effect on the proper representation of the scenario source-to-site distance.

2.4.1.3 Including cumulative effects in ground motion selection

Considering ground motion cumulative effects is an important issue for seismic response analysis of systems susceptible to these effects. Arias intensity (AI) and cumulative absolute velocity (CAV) are commonly used in research and practice to consider the cumulative effects of ground motions (Campbell and Bozorgnia, 2010, 2012). Each of these IMs represents slightly different cumulative aspects of a ground motion. Bradley (2015) illustrates that AI is principally correlated with the high frequency content of a ground motion, whereas CAV is principally correlated with the moderate-to-low frequency content. As a result, depending on the problem considered, ground motion selection based on only one of these IMs may not appropriately represent the important cumulative aspects of the ground motions for the system considered. This issue is elaborated on in this section.

Before considering cumulative effects in ground motion selection, it is worthwhile observing the distribution of AI and CAV in selected ground motions when they are not explicitly considered in the weight vector. Figure 2.6 presents the cumulative distribution of AI and CAV for the M6.5R40V200 scenario using weight vector case 1 (*i.e.,* SA only). As seen in this figure, both distributions of AI and CAV are biased with respect to the target distribution.

Figure 2.7 presents the cumulative distribution of AI and CAV for the M6.5R10V200

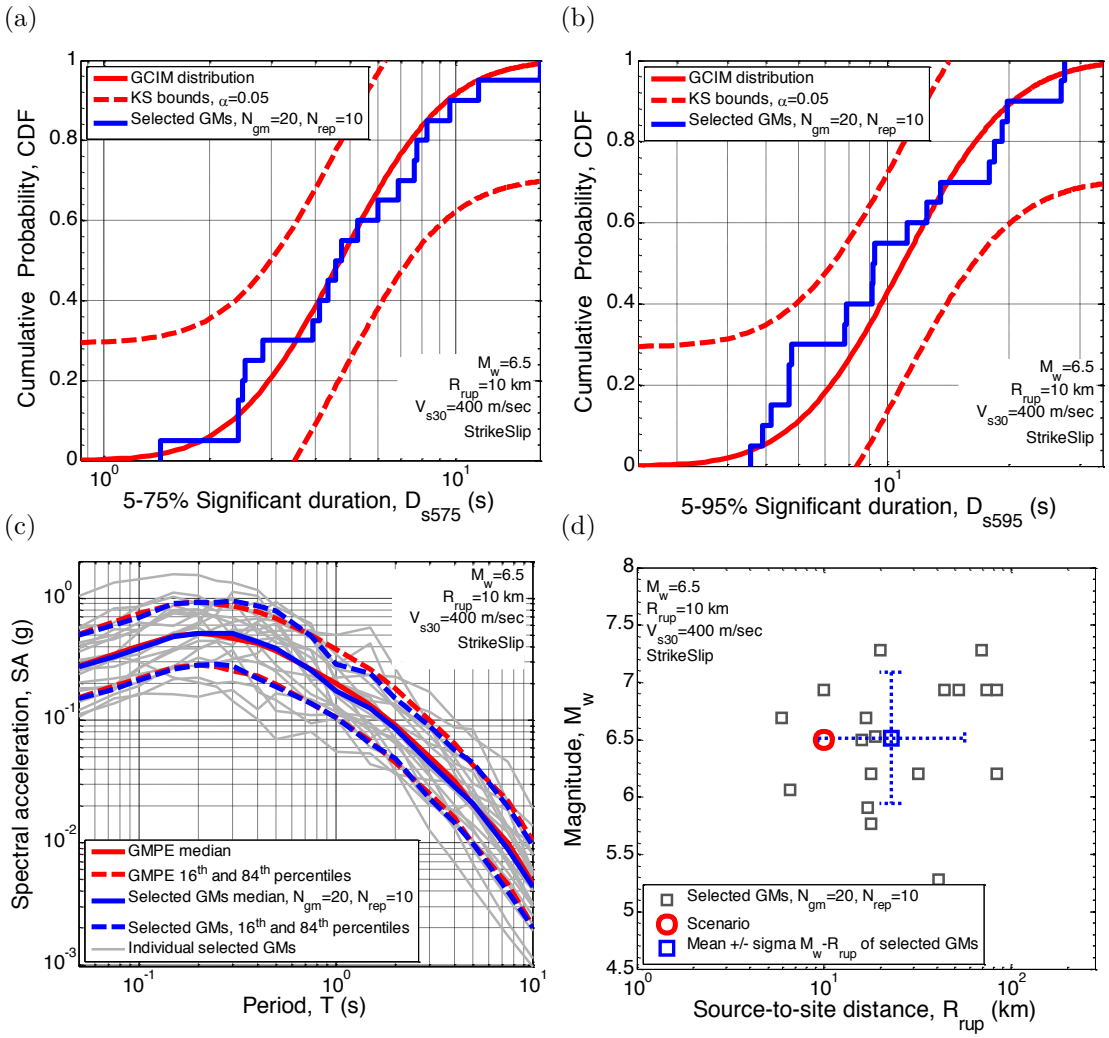

Figure 2.5: Properties of selected motions using weight vector case 2 (*i.e.*, SA, D_{s575}, and D_{s595}) for the M6.5R10V400 rupture scenario: (a) cumulative distribution of D_{s575}; (b) cumulative distribution of D_{s595}; (c) SA ordinates; and (d) M_w-R_{rup} distribution.

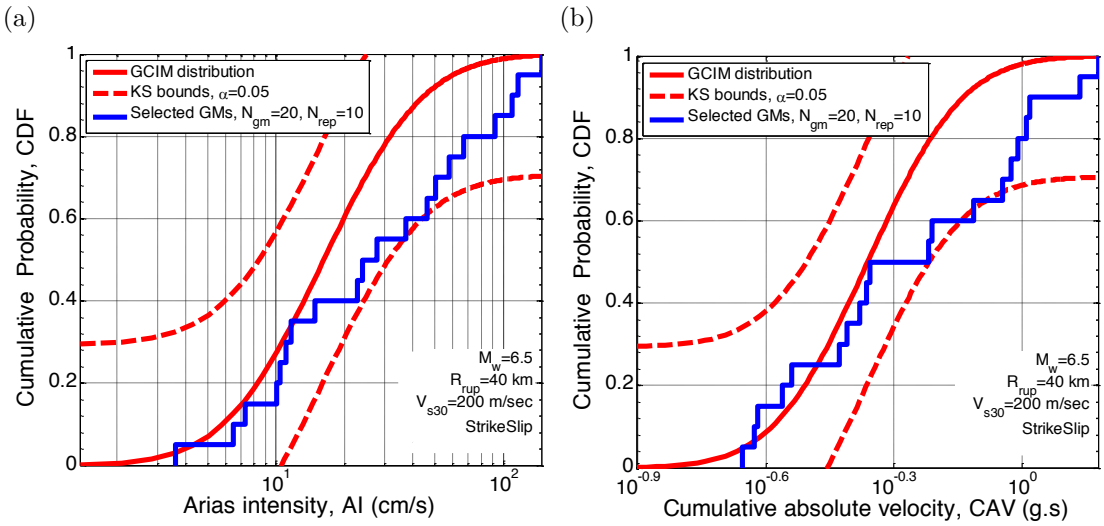

Figure 2.6: Cumulative distribution of: (a) AI; and (b) CAV for the M6.5R40V200 rupture scenario using weight vector case 1 (*i.e.,* SA only).

scenario when weight vector case 2 (*i.e.,* SA, D_{s575}, and D_{s595}) is used for selecting ground motions. As seen in Figure 2.7, considering both significant duration IMs (*i.e.,* D_{s575}, D_{s595}) and SA ordinates does not result in an unbiased representation of AI and CAV for the M6.5R10V200 rupture scenario, as the empirical distribution of AI and CAV for this scenario are intersecting with the KS bounds at 5% significance level. It should be noted that, as presented in Table 2.3, the correlation between Significant Duration IMs and cumulative effects of ground motions (*i.e.,* AI and CAV) is relatively small (having negative correlation with AI). Therefore it is not unexpected that considering the Significant Duration IMs in the weight vector (*i.e.,* case 2) does not assist in achieving a proper representation for AI and CAV.

The results presented in Figures 2.6 and 2.7 indicate the inadequacy of considering only SA, or SA and Significant Duration IMs, to capture the cumulative effects of ground motions. Therefore it is necessary to consider these effects by assigning non-zero weights to them in the weight vector, rather than relying on SA and duration to enforce an appropriate representation for them. In this regard, weight vector cases 3, 4, and 5 (see Table 2.4) are used to investigate incorporating cumulative ground motion effects in the selection process. Specifically, in weight

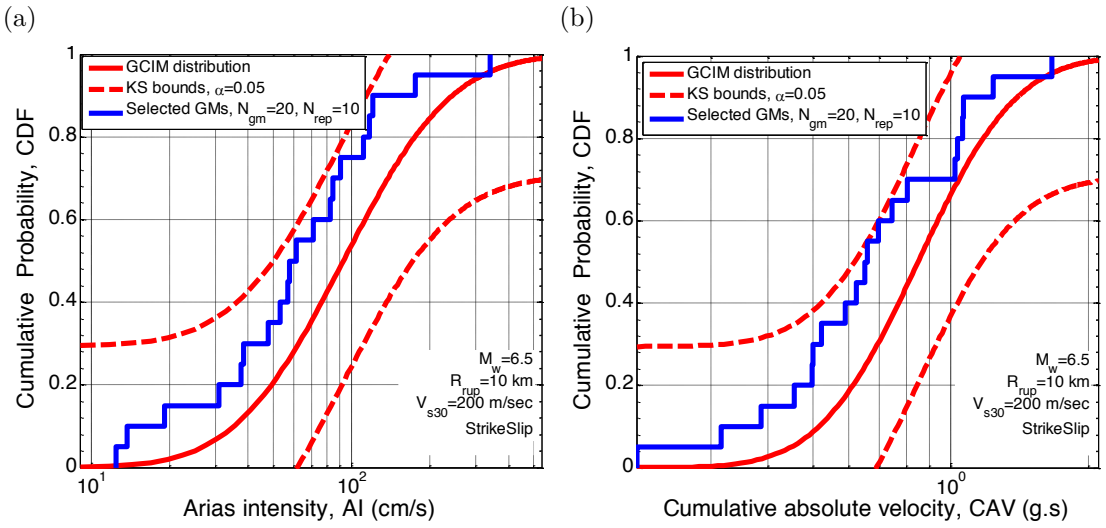

Figure 2.7: Cumulative distribution of: (a) AI; and (b) CAV for the M6.5R10V200 rupture scenario using weight vector case 2 (*i.e.,* SA, D_{s575}, and D_{s595}).

vector cases 3 and 4, only AI or CAV are considered in addition to SA ordinates, while in weight vector case 5 both AI and CAV are considered in addition to SA ordinates. In all three weight vector cases, similar to weight vector case 2 (*i.e.,* SA, D_{s575}, and D_{s595}), a 70% weight is given to SA ordinates and 30% weight to the cumulative intensity measures (as presented in Table 2.4).

Figure 2.8 presents the cumulative distribution of AI and CAV for the M6.5R10V400 scenario when the cumulative effects are considered by placing a weight only on AI and SA ordinates (*i.e.,* weight vector case 3). It can be seen in Figure 2.8 that the AI distribution of the selected motions is consistent with the target distribution; however, the selected motions have a bias in representing CAV for the considered scenario at the 5% significance level. It should be noted, though not shown, that these selected motions have an appropriate representation for the distribution of SA ordinates, but a biased representation for D_{s575}, and D_{s595}.

In contrast to the results presented in Figure 2.8, Figure 2.9 presents the cumulative distribution of AI and CAV when the weight is only placed on CAV and SA ordinates (*i.e.,* weight vector case 4). As seen in this figure, there is a proper representation for CAV (as expected), and also there is an unbiased distribution of AI. The reason for having an unbiased representation of the AI

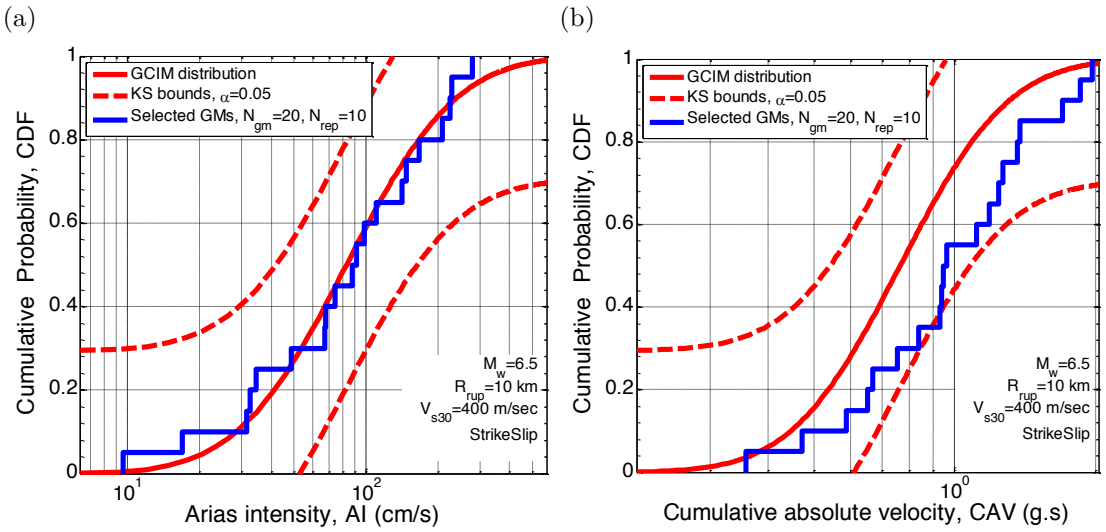

Figure 2.8: Properties of selected motions using weight vector case 3 (*i.e.,* SA and AI) for the M6.5R10V400 rupture scenario: cumulative distribution of (a) AI; and (b) CAV.

distribution for most of the considered scenarios and site conditions in Table 2.1 when CAV and SA ordinates are considered in the weight vector (*i.e.,* weight vector case 4) can be related to the strong correlation of AI with the short-period SA ordinates of the ground motion (Bradley, 2015), which are relatively well covered by the implemented weight vector here (*i.e.,* 18 SA ordinates). Although not shown here, the selected motions provide an appropriate representation for the SA ordinates, but a biased representation for Significant Duration IMs exists, illustrating that the observed bias in AI and CAV when only SA and D_{s575}/ D_{s595} are considered in the weight vector is also reciprocated with bias in D_{s575}/ D_{s595} when only SA and CAV or AI are considered in the weight vector (discussed in the subsequent paragraph).

Given the fact that considering AI or CAV in ground motion selection does not necessarily imply that the distribution of the other intensity measure will be well represented in the selected ground motions, it is beneficial to consider the effect of including both of AI and CAV in the selection process with equal weights (*i.e.,* weight vector case 5 in Table 2.4). Figures 2.10a-b illustrate AI and CAV distributions of the selected motions compared with the corresponding

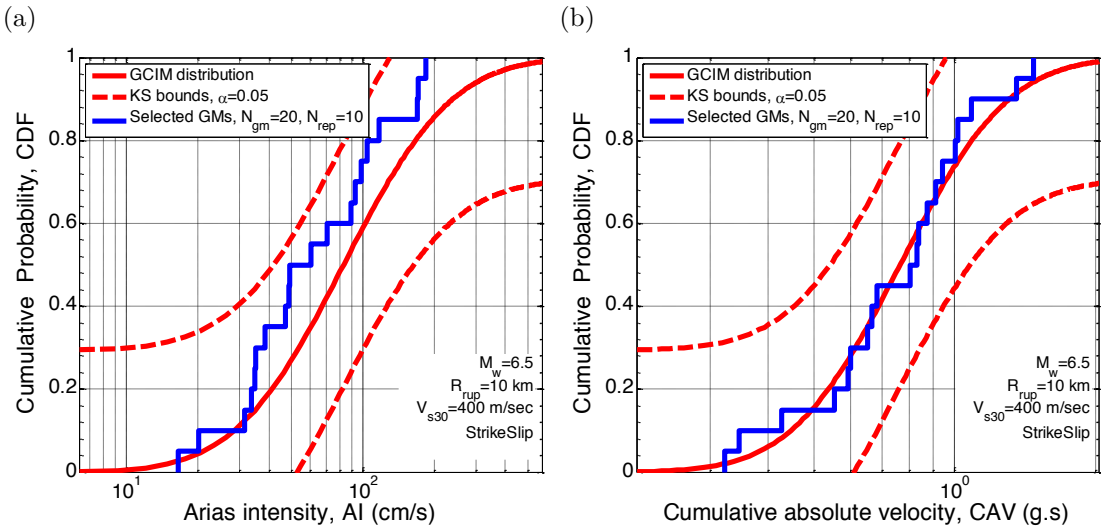

Figure 2.9: Properties of selected motions using weight vector case 4 (*i.e.,* SA and CAV) for the M6.5R10V400 rupture scenario: cumulative distribution of (a) AI; and (b) CAV.

target distributions, for which it can be seen that the selected motions provide a good representation. Figure 2.10c also illustrates the appropriate representation of the selected motions for SA ordinates. However, as shown in Figure 2.10d, the selected motions have a biased representation for the 5-95% Significant Duration of the considered rupture scenario. Although not presented here, distribution of the 5-75% significant duration is also biased.

Based on the obtained results it can be seen that having an appropriate representation for the cumulative effects of ground motions for a scenario rupture does not necessarily guarantee an appropriate representation for Significant Duration IMs of the motions as well. This is consistent with the results of Bradley (2011a, 2015) who found a near-zero correlation between the residual of Significant Duration IMs (*i.e.,* D_{s575} or D_{s595}) and AI and CAV; and the results of Bommer et al. (2006) who found a relatively weak correlation between durations and equivalent number of cycles (*i.e.,* a cumulative IM).

It is worth mentioning that depending on the rupture scenario characteristics and the site condition, having a biased representation for D_{s595} does not necessarily imply a biased representation for D_{s575}. This is due to the fact that the

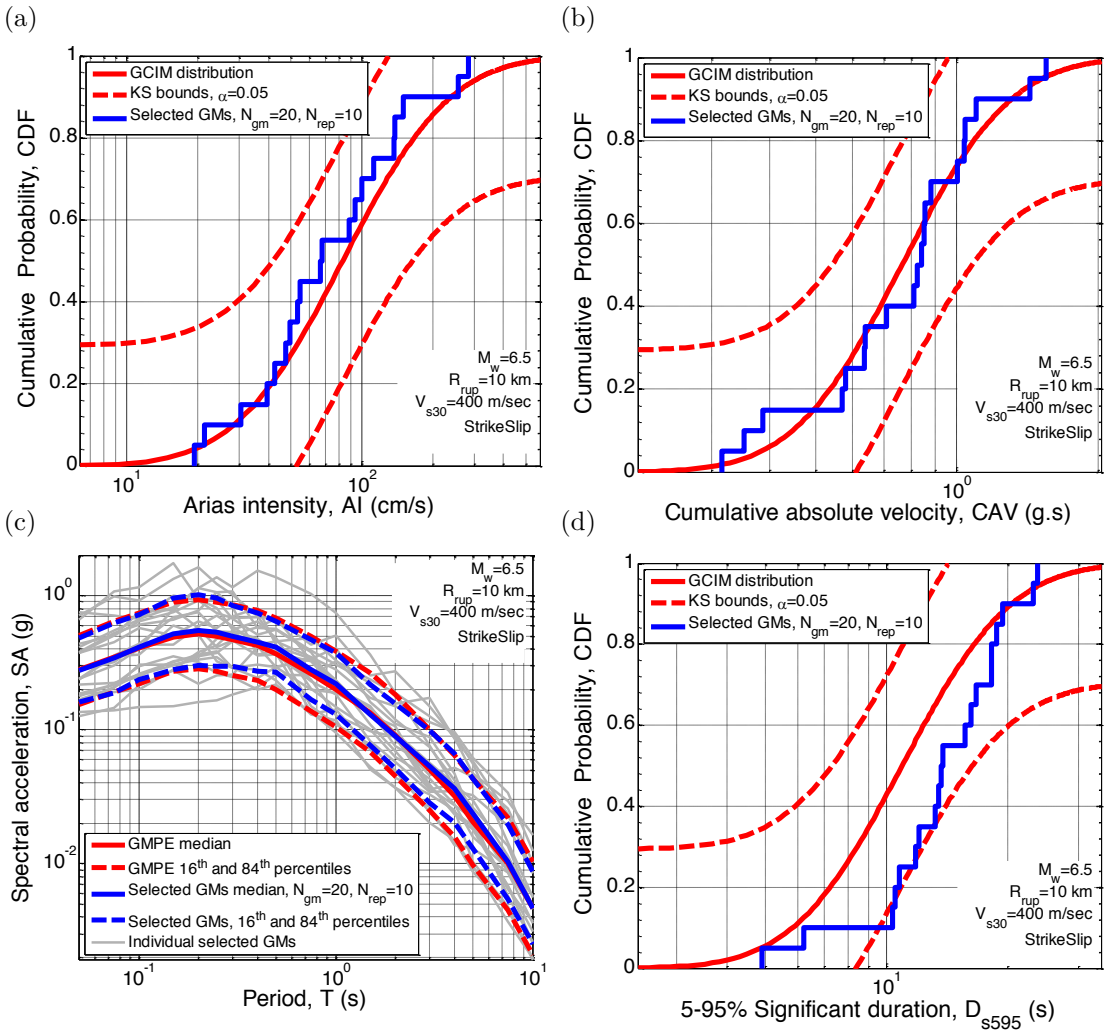

Figure 2.10: Properties of selected motions using weight vector case 5 (*i.e.*, SA, AI, and CAV) for M6.5R10V400 rupture scenario: (a) cumulative distribution of AI; (b) cumulative distribution of CAV; (c) SA ordinates; and (d) cumulative distribution of D_{s595}.

5-75% and 5-95% Significant Duration IMs do not have a perfect correlation (*i.e.,* $\rho\left(D_{s575}, D_{s595}\right)$ =0.843, as presented in Table 2.3.

2.4.1.4 Including both cumulative and duration effects in ground motion selection

Based on the presented results so far, it is evident that neglecting certain aspects of the ground motion for a rupture scenario (*e.g.,* duration or cumulative effects) will most likely result in ground motions with a biased representation for the IMs representing those aspects. For instance, as elaborated, capturing the cumulative effects of the ground motion does not necessarily result in capturing the duration effect of the motion and vice versa. This is due to the fact that the cumulative effects of ground motions (presented in this study by AI and CAV) are proxy representatives for the total energy content of the motion and not the duration of motion, whereas, Significant Duration IMs (*i.e.,* $\mathrm{D_{s595}}$ and $\mathrm{D_{s575}}$) represents the arrival time between certain thresholds of the total energy of the motion and not the amount of the energy itself. Therefore, the distinction between the cumulative effects (*i.e.,* energy content) and the Significant Duration of the motion should be noted in the selection process. In order to conduct response history analysis of systems susceptible to the cumulative and duration effects, such as geotechnical structures with liquefaction-susceptible soils or structural systems (*i.e.,* buildings and bridges) with strength and stiffness degrading behaviour, it is therefore prudent to consider both Significant Duration and cumulative effects (as well as SA ordinates) in the selection process, because the damage in these types of structures is dependent upon amplitude of the applied motion, as well as the total input energy and duration of the strong phase of the motion (Bradley, 2010b; Bradley et al., 2013; Villaverde, 2007; Bommer et al., 2006).

Based on the abovementioned issues, ground motion selection is conducted using weight vector case 6, in which cumulative and duration effects are both considered with SA ordinates in the weight vector. Figure 2.11a illustrates the

conformity of the 16^{th}, 50^{th}, and 84^{th} percentiles of the distribution of SA ordinates to the target distribution for the selected ground motions. Also, Figures 2.11b-d illustrate the appropriate representation of the selected motions to the target distribution of the D_{s595}, AI, and CAV, respectively. Although not presented in this figure, the selected motions have also an appropriate representation for D_{s575}.

It is important to note in the various results presented so far that considering IMs other than SA ordinates does not have an obvious detrimental effect on representativeness of the selected motions for the distribution of SA ordinates themselves. As noted previously, this is observed by the authors to be the results of assigning 60-70% weight to the SA ordinates, and the use of a total weight less than 60% for SA ordinates will result in a degraded representation of the SA ordinate distribution of the selected motions.

2.4.1.5 Representation of the selected motions based on SA ordinates for other spectral intensities (*i.e.,* ASI, SI, DSI)

Acceleration spectrum intensity (ASI), spectrum intensity (SI), and displacement spectrum intensity (DSI) are IMs calculated based on integration of the spectral ordinates over short (*i.e.,* T=0.1-0.5), medium (*i.e.,* T=0.1-2.5), and long (*i.e.,* T=2.0-5.0) vibration periods, respectively (Bradley et al., 2009; Bradley, 2010c, 2011c). Therefore, motions selected based on an appropriate representation for the distribution of SA ordinates (*i.e.,* weight vector case 1) may have a proper representation for ASI, SI, and DSI, without explicitly considering them in the weight vector. Figure 2.12 illustrates the cumulative distribution of ASI, SI, and DSI of the selected motions using weight vector case 1 (*i.e.,* SA only) for the M6.5R10V400 scenario (*i.e.,* the same selection case as considered in Figure 2.2), as an example among the other considered rupture scenarios and site conditions. As seen in this figure, the selected motions have a proper representation for the predicted distribution of ASI, SI, and DSI, which is intuitively consistent with the proper representation of the selected motions for the whole range of the scenario

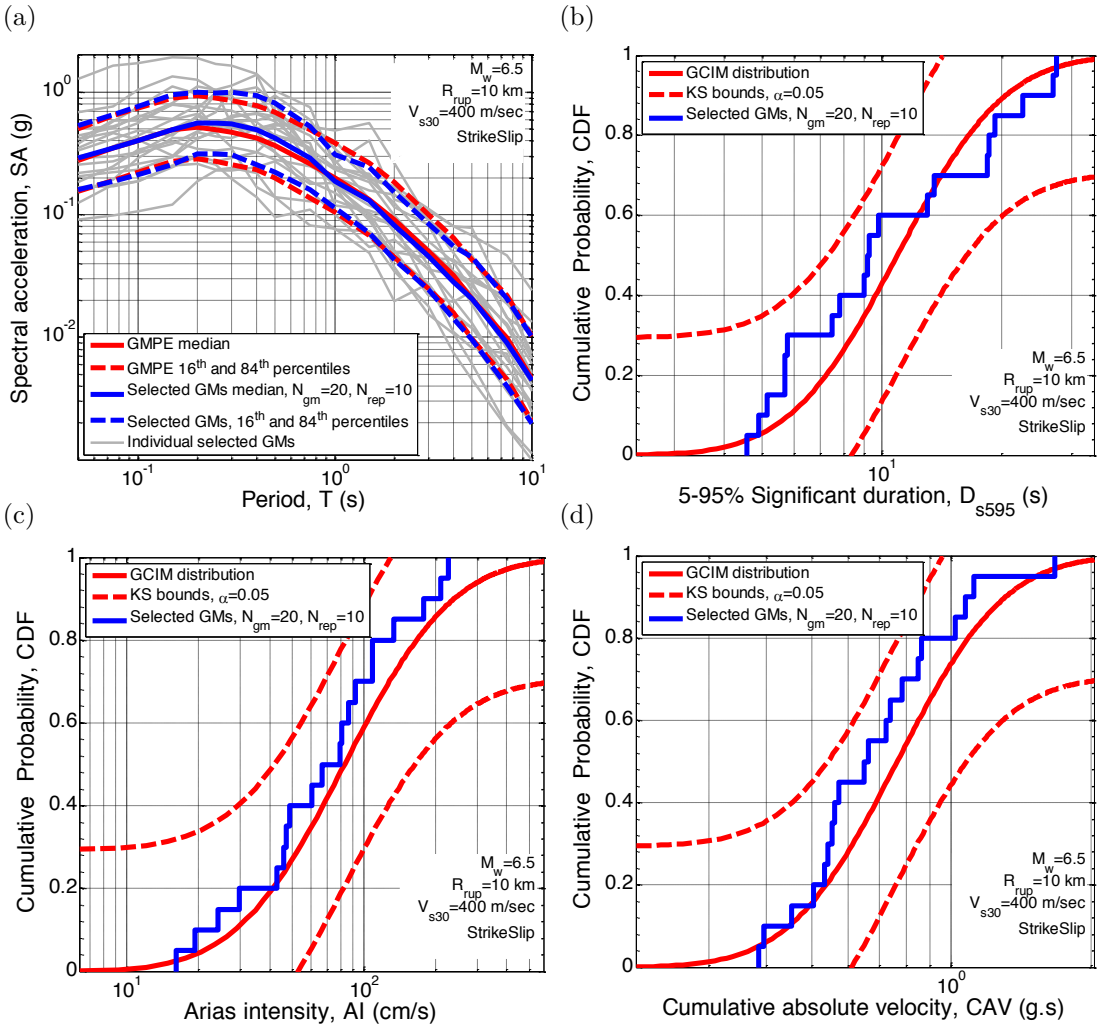

Figure 2.11: Properties of selected motions using weight vector case 6 (*i.e.*, SA, AI, CAV, D_{s595}, and D_{s575}) for the M6.5R10V400 rupture scenario: (a) SA ordinates; cumulative distribution of (b) D_{s595}; (c) AI; and (d) CAV.

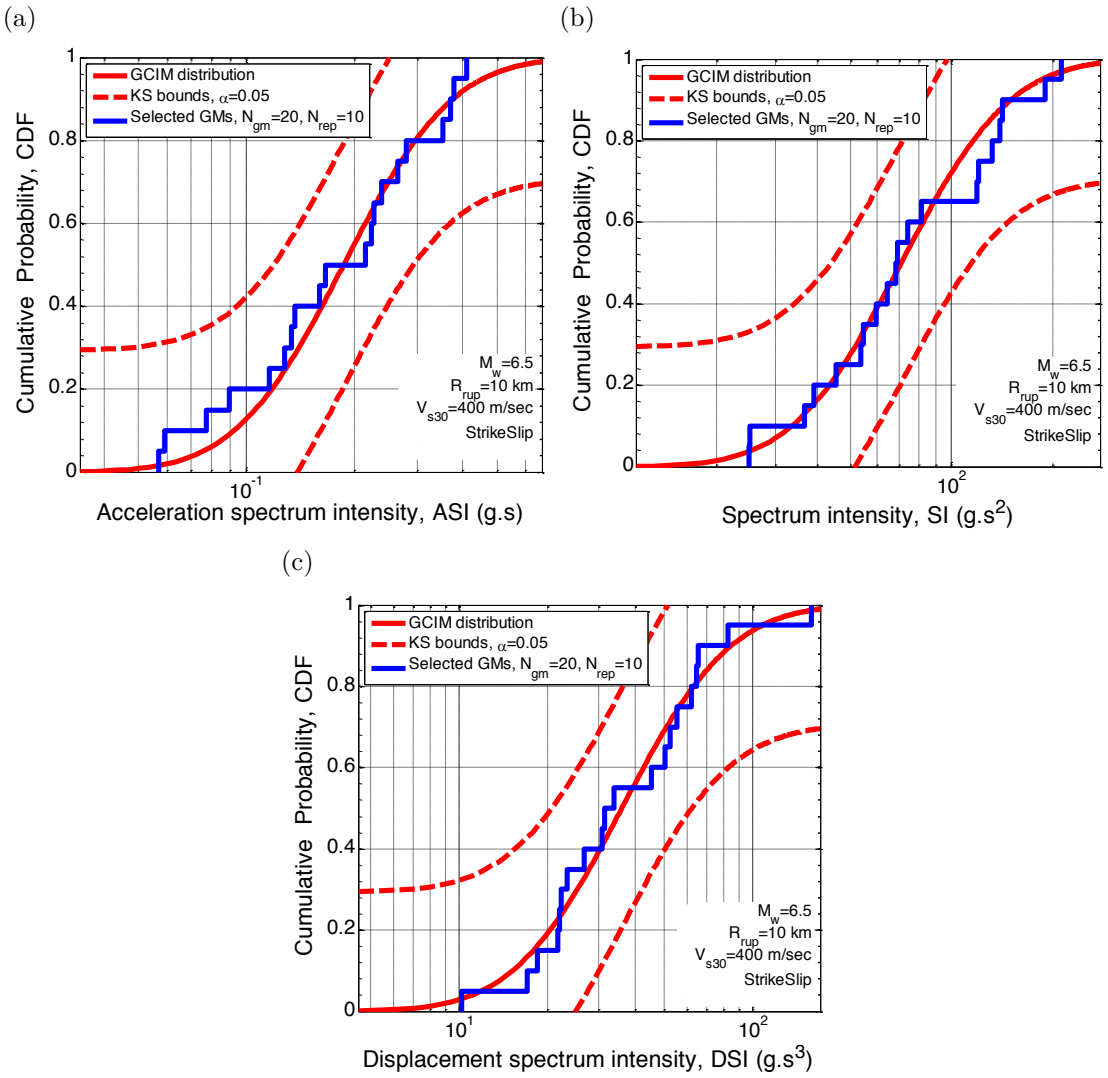

Figure 2.12: Cumulative distribution of ASI, SI, and DSI of selected motions using weight vector case 1 (*i.e.,* SA only) for M6.5R10V400 rupture scenario.

spectrum illustrated in Figure 2.2a. This indicates that placing weights on these IMs in addition to those on SA ordinates would result in duplication.

It is also worthwhile examining the characteristics of the motions selected based only on ASI, SI, and DSI without considering SA ordinates to see if the results of Figure 2.12 hold in the reverse sense. For this purpose, weight vector case 7 is used, in which an equal weight of 0.33 is given to each of ASI, SI, and DSI (see Table 2.4) for the purpose of ground motion selection. Figure 2.13 illustrates the median, 16^{th}, and 84^{th} percentiles of SA ordinates of the selected motions

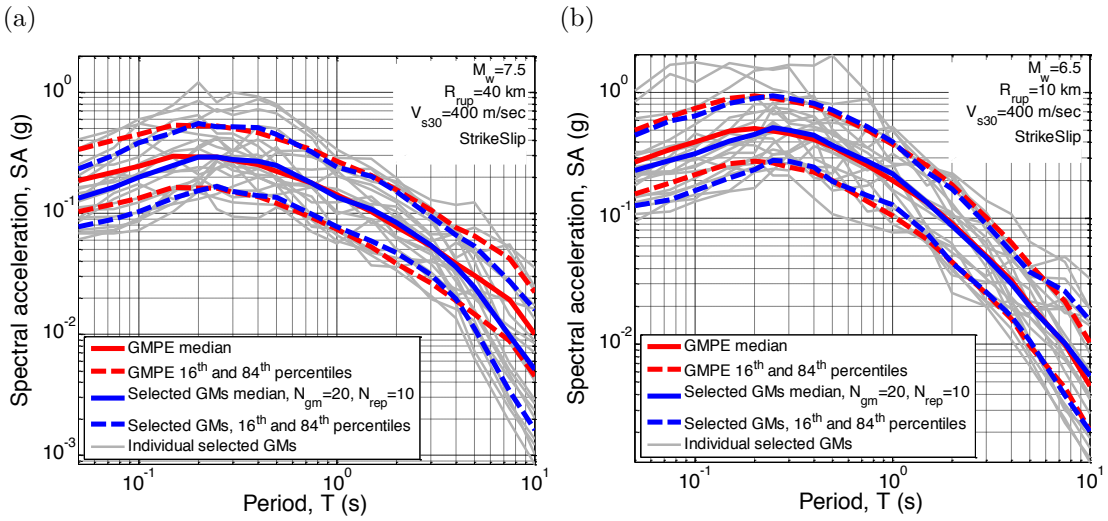

Figure 2.13: Median, 16th, and 84th percentiles of SA ordinates of selected motions using weight vector case 7 (*i.e.,* ASI, SI, and DSI) for: (a) M7.5R40V400; and (b) M6.5R10V400 rupture scenarios.

for the M7.5R40V400 and M6.5R10 V400 scenarios. As seen in this figure, and based on the obtained results for other scenarios and site conditions, the selected motions have an appropriate representation for SA ordinates mostly at 0.2-3.5 period range, because this period range is well represented in the implemented weight vector via ASI, SI, and DSI. For the vibration periods out of this range, the median, 16^{th}, and 84^{th} percentile spectra of the selected motions may exhibit moderate to large deviations from the target GCIM distribution.

2.4.1.6 Discussion: Appropriate weight vectors for generic problems

It is evident that considering only SA ordinates, as it is common in many conventional ground motions selection procedures, will result in misrepresentation of the cumulative and duration effects of ground motions. Since considering these cumulative and duration effects does not impose any burden on the ground motion selection process it is recommended to include them in the selection procedure.

As investigated and discussed by Bradley (2011a, 2012a, 2015), the residuals of duration and cumulative intensity measures have a relatively low correlation with each other, *e.g.*, $\rho\left(D_{s595},\ CAV\right) = 0.122$ and $\rho\left(D_{s595},\ AI\right) = -0.2$, therefore

considering only one of these aspects (*e.g.,* D_{s575}, D_{s595}) in the ground motion selection does not imply a satisfactory representation for the others (*e.g.,* AI, CAV). The low correlation between the duration and cumulative IMs indicates that these IMs provide non-redundant information useful for characterising the severity of ground motions. In contrast, some IMs provide largely redundant information (*e.g.,* ASI, SI, DSI and SA ordinates over certain period ranges) and therefore their joint consideration is largely ineffective.

When using a total weight of 60-70% for all SA ordinates, the consideration of cumulative and duration-related IMs does not result in any appreciable reduction in the conformity of the distribution of SA ordinates of the selected ground motions to the target distribution. Thus, there is no obvious negative to the consideration of the cumulative and duration-related intensity measures. It should be noted here that this is for 60-70% weight given to SA ordinates. If a lower total weight is used, then the consideration of these other IMs is likely to result in a degraded representation of SA ordinates. The reason for having a large portion of the total weight on SA ordinates, compared to other IMs, is due to the fact that SA ordinates represent the amplitude and frequency content of the ground motion and are therefore of primary importance. In order for cumulative- and duration-related responses to become important, a ground motion's amplitude and frequency content must first be large enough to induce nonlinear response.

2.4.2 Effect of conducting replicate selections on ground motions selection

2.4.2.1 Number of replicate selections

In addition to the choice of weight vector discussed in the previous section, another important aspect of the GCIM-based ground motion selection is to conduct replicate selections to obtain an ensemble of motions with the 'best' representation for the considered scenario rupture (*i.e.,* Equation 2.6). The need for replicate

selection is a result of the fact that random realisation of the GCIM distributions are used in the selection process, meaning that each replicate may result in a different ground motion ensemble. The number of the replicate selections (*i.e.,* N_{rep}) to reach to a stable result is dependent upon the number of the selected motions (*i.e.,* N_{gm}), which is investigated here by selecting N_{gm} =10, 20, and 50 motions for 12 considered scenarios and site conditions outlined previously in Table 2.1. Table 2.5 presents the number of replicate selections considered for each corresponding number of selected motions. Because the amount of computation in the GCIM-based ground motion selection procedure is directly proportional to the number of replicates considered, identifying a minimum value of N_{rep} which produces stable results is desirable.

Table 2.5: Number of replicates (N_{rep}) considered corresponding to the number of selected motions (N_{gm})

N_{gm}	Numbers of replicate (N_{rep})					
10	1	3	5	10	20	50
20	1	3	5	10	20	
50	1	3	5			

As mentioned before, for a given number of desired motions, the ensemble with the lowest overall residual (*i.e.,* R value) is chosen as the 'best' ensemble among the selected sets of motions, as illustrated in Figure 2.1. This process is repeated here for the different $N_{gm} - N_{rep}$ combinations in Table 2.5. In order to reach a conclusion about the required number of N_{rep} to obtain a stable result, the R value of the best set of motions from each replicate is compared with values obtained from the other replicates. Figure 2.14 presents the results from this process, as an example, for the motions selected using weight vector case 1 (*i.e.,* SA only) for the stiff soil site condition cases. As seen in this figure, by conducting more than one replicate selection, the overall residual (*i.e.,* R value) of the ensembles with the best representation for N_{gm} =10 and 20 selected motions decreases considerably compared to the R value for one replicate (*i.e.,* $N_{rep} = 1$).

For the replicate selections larger than N_{rep} =3, R tends to gradually decrease with some fluctuations due to the random nature of the sampling, which is more accentuated for N_{gm} =10. For ensembles with N_{gm} =50 motions, as illustrated in Figure 2.14c, the effect of conducting replicate selections is not as significant as it is for N_{gm} =10 or 20 motions, because a large number of selected motions are more likely to properly represent the target distribution of the IMs (*i.e.,* the random simulations are a better representation of the probabilistic distribution). Whereas the representativeness of a smaller number of motions can be relatively weak, which is also implied by the smaller R values of the ensembles with $N_{gm} = 50$ in comparison to R values for the ensembles with $N_{gm} = 10$ and 20. However, due to the fact that the selection process in the GCIM method is based on random realisations for the considered IMs, conducting replicate selections is recommended even if the number of the selected motions is large.

Overall, conducting several replicate selections has generally a positive effect on obtaining a set of motions with a smaller overall residual, compared to using one replicate. As mentioned before, conducting an excessive number of replicate selections can result in unnecessary computational burden, therefore it is useful to identify an acceptable minimum number of replicate selections based on the number of the desired motions (N_{gm}). Based on the obtained results for different considered scenarios, soil conditions, and weight vectors, conducting N_{rep} =10, 5, and 3 replicate selections are recommended to select N_{gm} =10, 20, and 50 motions, respectively.

2.4.2.2 Replicate selections and representativeness of selected motions for the considered IMs

In order to investigate the effect of conducting replicate selections on the representativeness of the selected motions for the target distribution of the considered IMs, Figures 2.15a-c present the median, 16^{th}, and 84^{th} percentiles of SA ordinates of the ensemble of motions with the best and worst representation (*i.e.,*

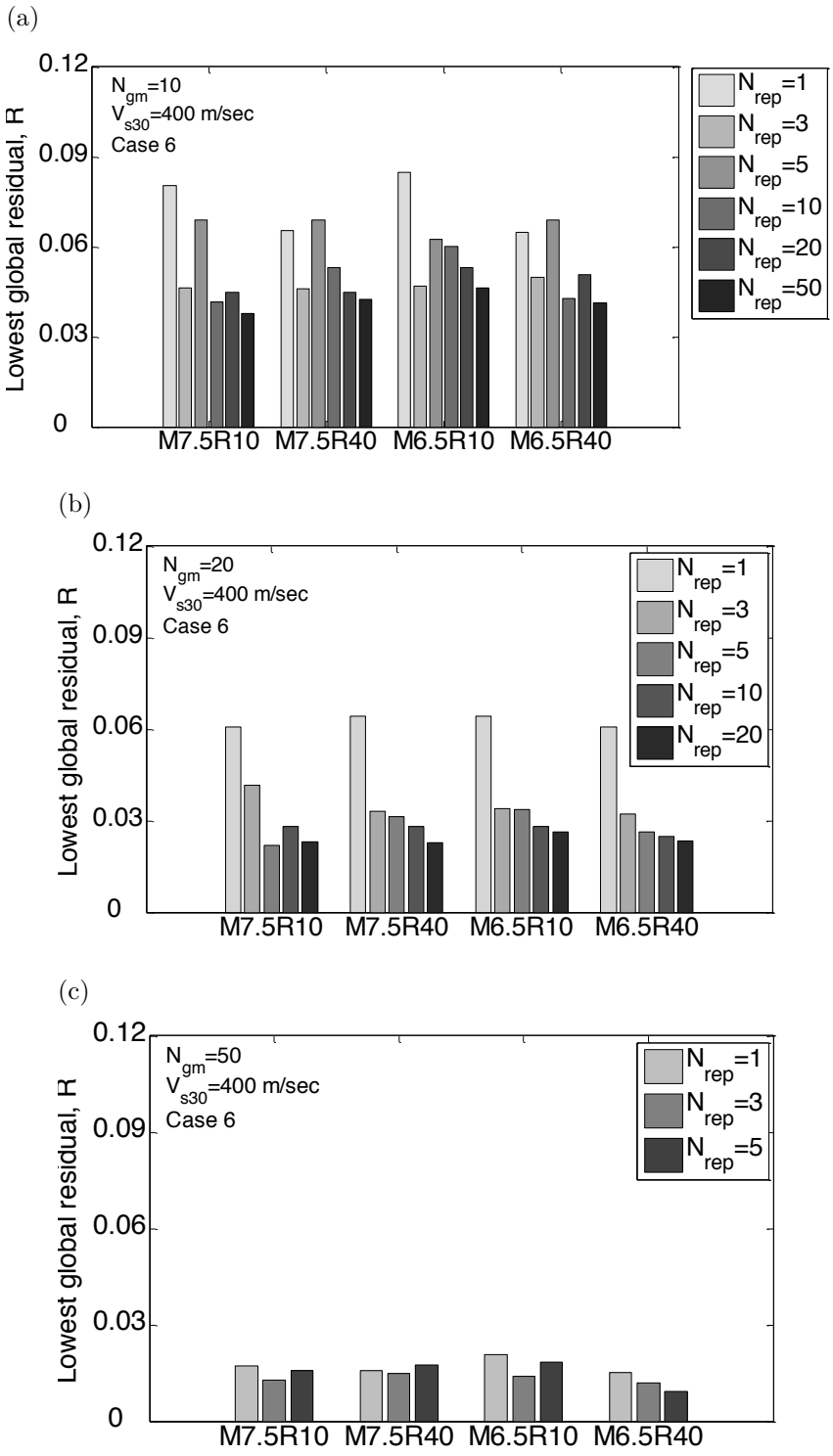

Figure 2.14: The lowest R value for different number of replicate selections, considering the selection based on the weight vector case 1 (*i.e.,* SA only): (a) $N_{gm} = 10$; (b) $N_{gm} = 20$; (c) $N_{gm} = 50$.

the ensembles with lowest and highest R values, respectively) when 10, 20, and 50 motions are selected for the M6.5R10V400 scenario using weight vector case 1 (*i.e.,* SA only). As seen in this figure, by conducting replicate selections, considerable improvement can be achieved (especially when the number of selected motions is small, as seen in Figure 2.15a), in contrast to selecting motions using only one replicate in which the result might be similar to the set of motions with the worst representation (*i.e.,* the set with the highest R value). Although not presented here, the positive effect of conducting replicate selections holds true when other considered weight vectors are used for the selection.

In order to quantify the results in Figure 2.15 in a summative manner, Figure 2.16 presents the KS test statistic, $D_{\max}$, which is the maximum difference between the empirical distribution of the considered IMs and the corresponding target (*i.e.,* GCIM) distribution, for SA ordinates of the selected 10, 20, and 50 motions. $D_{\max}$ values for the ensembles with the best and worst representation are illustrated in this figure along with the scatter of $D_{\max}$ values for all of the replicate selections.

As illustrated in this figure, although the $D_{\max}$ value for all of the IMs of the best ensemble may not be the minimum value for all vibration periods, by conducting replicate selections, the IMs considered in the weight vector (*i.e.,* SA ordinates in this case) tend to collectively have smaller $D_{\max}$ values for the best set of motions (depicted in the blue line in Figure 2.16). It is also important to note that the minimum values and also variability in the $D_{\max}$ values tends to decrease as the number of the selected motions increases. This indicates that for a small number of motions (*e.g.,* $N_{gm} = 10$), conducting replicate selections is more crucial than is for a larger number of motions. This was also depicted in Figure 2.14 using the overall residual (*i.e.,* R) value.

Figure 2.17a presents the $D_{\max}$ values of IMs other than SA ordinates (*i.e.,* PGA, PGV, ASI, SI, DSI, AI, CAV, D_{s595}, and D_{s575}) for the selected motions based on weight vector case 1 (*i.e.,* SA only) for the M6.5R10V400 rupture scenario. As seen in this figure, although none of these IMs are considered explicitly

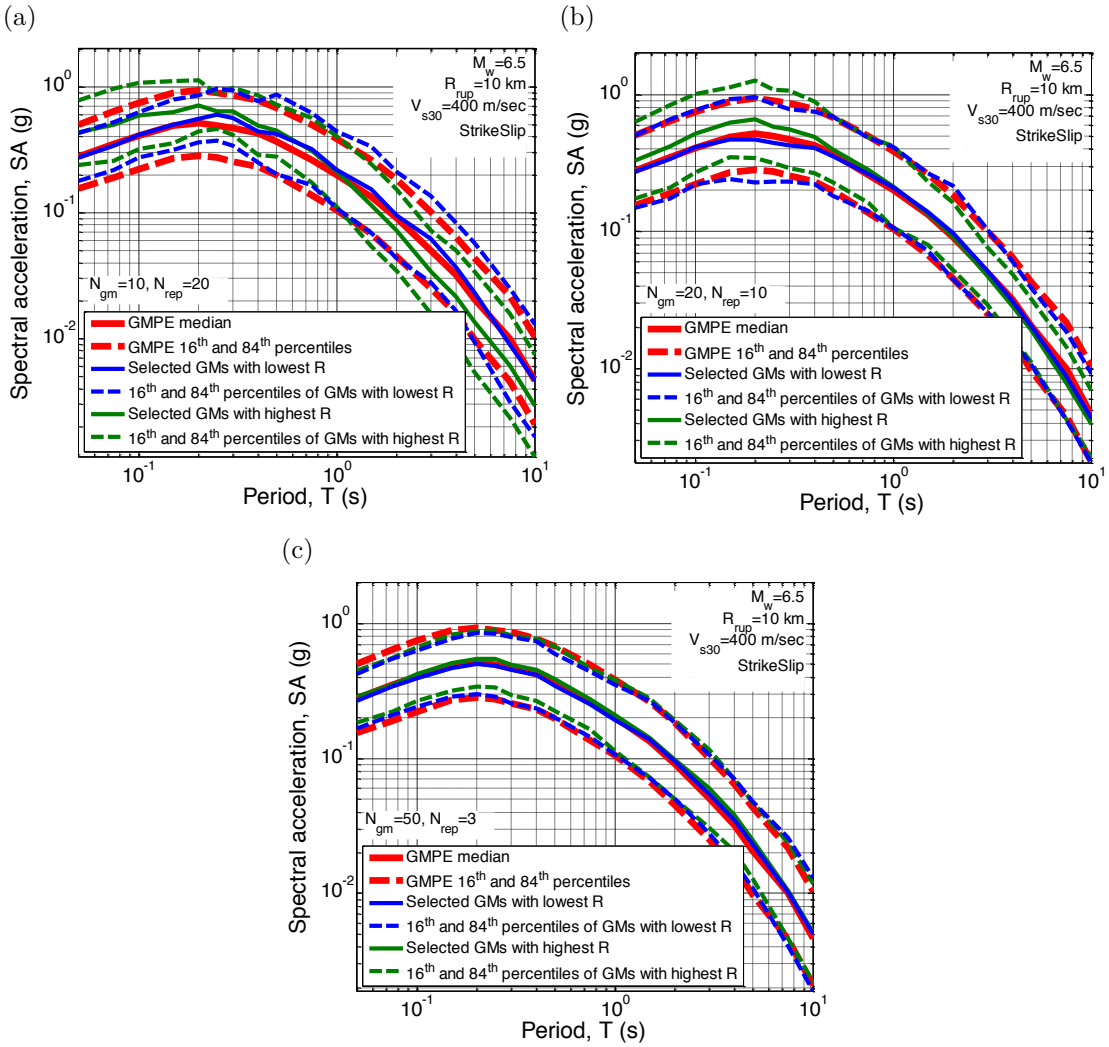

Figure 2.15: Median, 16th, and 84th percentiles of SA ordinates of selected motions using weight vector case 1 (*i.e.*, SA only) for the M6.5R10V400 rupture scenario with: (a) $N_{gm} = 10$; (b) $N_{gm} = 20$; (c) $N_{gm} = 50$.

(a)

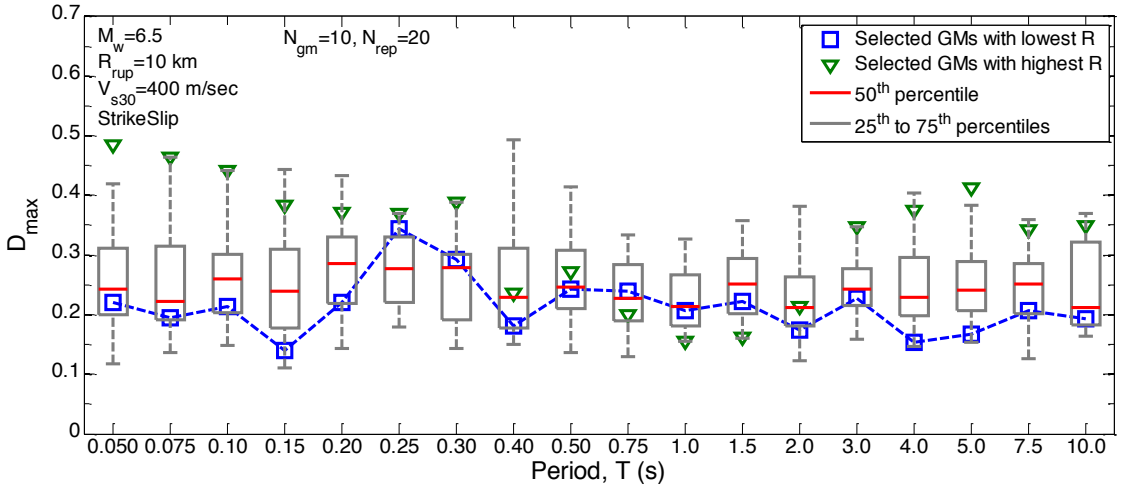

(b)

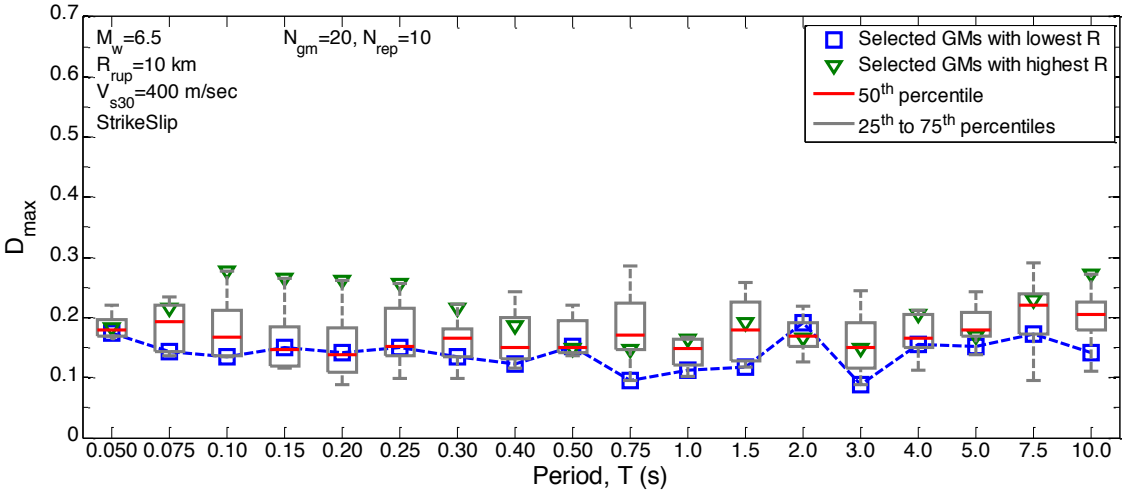

(c)

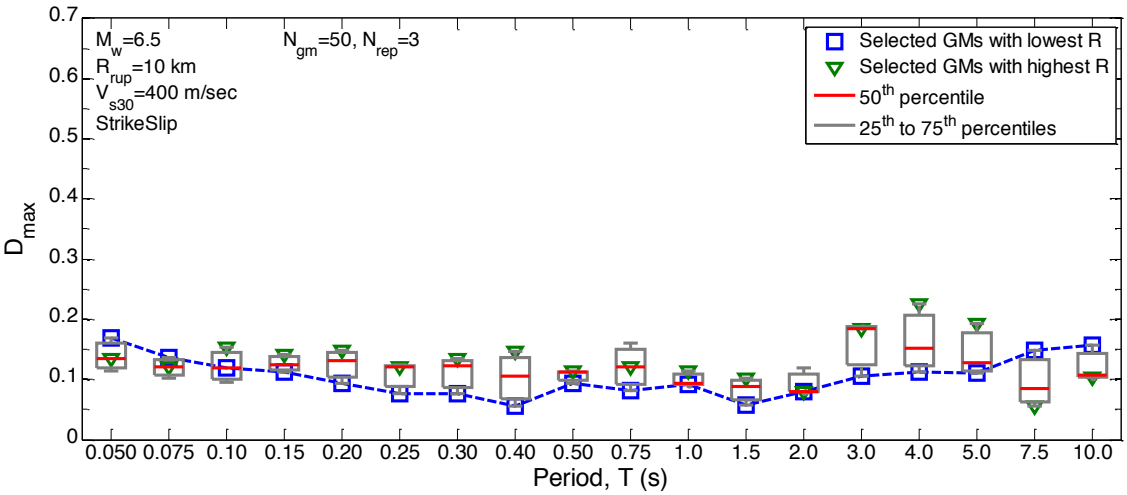

Figure 2.16: D_{max} value of SA ordinates of selected motions using weight vector case 1 (*i.e.*, SA only) for the M6.5R10V400 rupture scenario with: (a) $N_{gm} = 10$; (b) $N_{gm} = 20$; (c) $N_{gm} = 50$.

in the weight vector, the variability in the $D_{\max}$ values for CAV, D_{s575}, and D_{s595} is the greatest of those depicted. The variation can be seen to be related to the extent that these IMs correlate with those IMs contained within the weight vector. Since only SA ordinates are considered in the case 1 weight vector, then those IMs which correlate strongly with some of these SA ordinates (*i.e.,* PGA, PGV, ASI, SI, DSI, and AI) will have relatively low variability and low $D_{\max}$ values. In contrast, those IMs which have little correlation with SA ordinates (*i.e.,* CAV, D_{s775}, and D_{s595}) will have relatively high variability and high $D_{\max}$ values. This indicates the weak representation of motions selected using weight vector case 1 (*i.e.,* SA only) for these IMs, as discussed before. These results also illustrate the reason why the considered weight vector case 3 (*i.e.,* SA ordinates and AI) resulted in a biased distribution of CAV, but that weight vector case 4 (*i.e.,* SA ordinates and CAV) did not result in a biased distribution of AI – because the distribution of AI of selected motions can be relatively well captured via the use of several short period SA ordinates because of the strong correlation (Bradley, 2015).

Figure 2.17b presents the $D_{\max}$ values of PGA, PGV, ASI, SI, DSI, AI, CAV, D_{s595}, and D_{s575} of selected motions for the M6.5R10V400 scenario based on weight vector case 6 (*i.e.,* considering weights on SA, AI, CAV, D_{s595}, and D_{s575}). By comparing the variation of the $D_{\max}$ values for CAV, D_{s575}, and D_{s595} with those presented in Figure 2.17a, it can be seen that the variation in the $D_{\max}$ values is considerably decreased for CAV, D_{s595}, and D_{s575}, indicating that in order to obtain ensemble of motions with a proper representation for duration (characterised by D_{s595}, and D_{s575}) and cumulative effects (characterised partially by CAV), these IMs should be explicitly considered in the weight vector. As seen in this figure, variation in the $D_{\max}$ values for AI of the selected motions is increased due to a negative correlation between duration IMs and the AI (*i.e.,* $\rho(D_{s595},\ AI)$ = -0.2, $\rho(D_{s575},\ AI)$ = -0.19). However, since AI is explicitly considered in the implemented weight vector, the $D_{\max}$ value of AI for the ensemble with the best representation has not been increased compared to the result presented in Figure

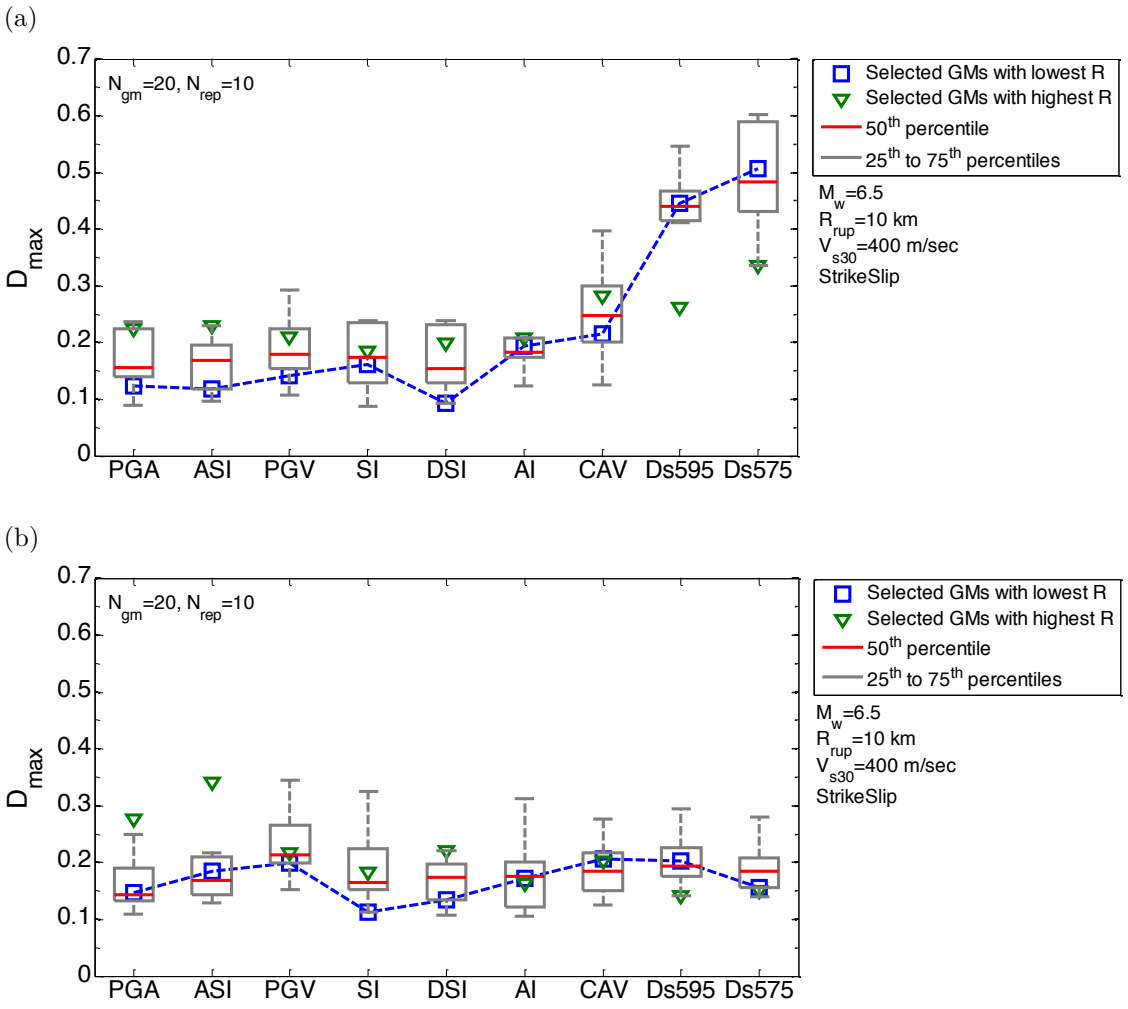

Figure 2.17: D_{max} value of PGA, PGV, ASI, SI, DSI, AI, CAV, D_{s595}, and D_{s575} of selected 20 motions for the M6.5R10V400 rupture scenario using weight vector: (a) case 1 (*i.e.,* SA only); and (b) case 6 (*i.e.,* SA, AI, CAV, D_{s595}, and D_{s575}).

2.17a where only SA ordinates were included in the weight vector. It is important to note that the negative correlation of AI with D_{s595} and D_{s575} implies the necessity of including AI in the weight vector when D_{s595} and D_{s575} are considered in the selection, so that the negative correlation between these IMs is balanced.

It is insightful to investigate the changes in the variation of the $D_{\max}$ values for SA ordinates, when weight vector case 6 (*i.e.,* weights on SA, AI, CAV, D_{s595}, and D_{s575}) is implemented for the selection as compared to those in weight vector case 1 (*i.e.,* weights only on SA ordinates). Figure 2.18 illustrates the $D_{\max}$ values for SA ordinates for weight vector case 6. By comparing Figures 2.18 and 2.16b it

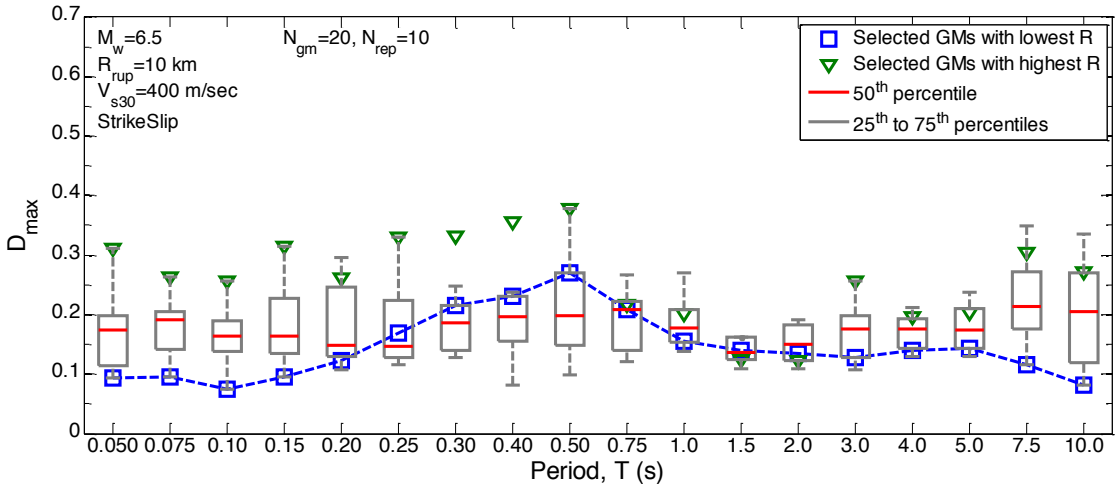

Figure 2.18: D_{max} value of SA ordinates of selected motions for $N_{gm} = 20$ using weight vector case 6 (*i.e.,* SA, AI, CAV, D_{s595}, and D_{s575}) for the M6.5R10V400 scenario rupture.

can be seen that the variation of the $D_{\max}$ values for SA ordinates increases due to the smaller weight on SA ordinates; however, the absolute values of these $D_{\max}$ values is still relatively small (recall that the distribution of the SA ordinates still conforms to the target distribution as shown in Figure 2.11a). The increase in the $D_{\max}$ values of SA ordinates for vibration periods around 0.5 for best ensemble of motions is also depicted in Figure 2.11a as the slight deviation of the 16^{th}, 50^{th}, and 84^{th} percentiles of SA ordinates distributions form the target distribution. This particular observation is due to the fact that compromises have to be made to collectively have a proper representation for all of the considered IMs in the weight vector, especially when the considered IMs reflect different characteristics of the ground motion with a different correlation among them.

In order to investigate the effect of replicate selections on representation of the IMs which are not included in the weight vector, Figure 2.19 presents the cumulative distribution of 5-95% significant duration and CAV of the selected ensemble of motions using weight vector case 1 (*i.e.,* SA weight only) with the best and worst representation for the M6.5R10V400 and M6.5R10V200 rupture scenarios, respectively. These IMs are not considered in the implemented weight vector for the presented results (*i.e.,* weight vector case 1). As seen in this figure,

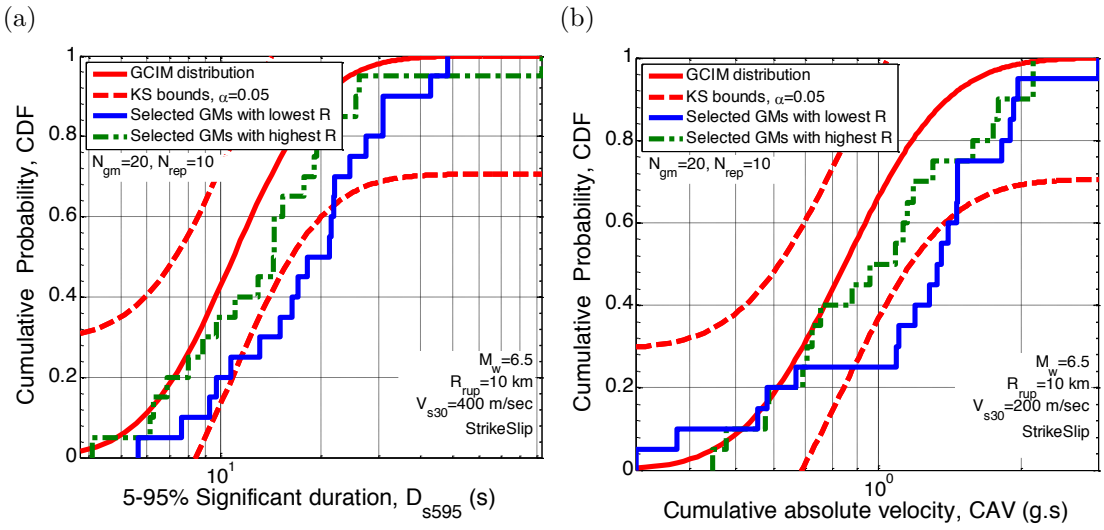

Figure 2.19: Illustration of the effect of replicate selection on the empirical distributions for intensity measures not considered in weight vector: (a) D_{s595} for the M6.5R10V400; and (b) CAV for the M6.5R10V200 rupture scenarios using weight vector case 1 (*i.e.,* SA only).

the ensemble with the worst representation (*i.e.,* highest R value) has an unbiased distribution at the 5% significance level, while, the ensemble with the best representation (*i.e.,* lowest R value) has a biased distribution. This is due to the fact that replicate selections aim to minimise the R value with respect to the IMs considered in the weight vector, hence, the representation of IMs not considered in the weight vector will not directly improved by conducting replicate selections.

2.4.2.3 Replicate selections and representativeness of selected motions for the implicit causal parameters

Figure 2.20 presents the $M_w - R_{rup}$ distribution of the selected motions with the best and worst representation using weight vector case 6 (*i.e.,* SA, AI, CAV, D_{s575}, and D_{s595}). As seen in this figure and based on the general trend of the results, the representativeness of the implicit causal parameters of the selected motions does not notably change by conducting replicate selections. This is due to the fact that the replicate selections relies on the overall residual (*i.e.,* R value) of the selected ensemble of motions, which is governed by the assigned weight values

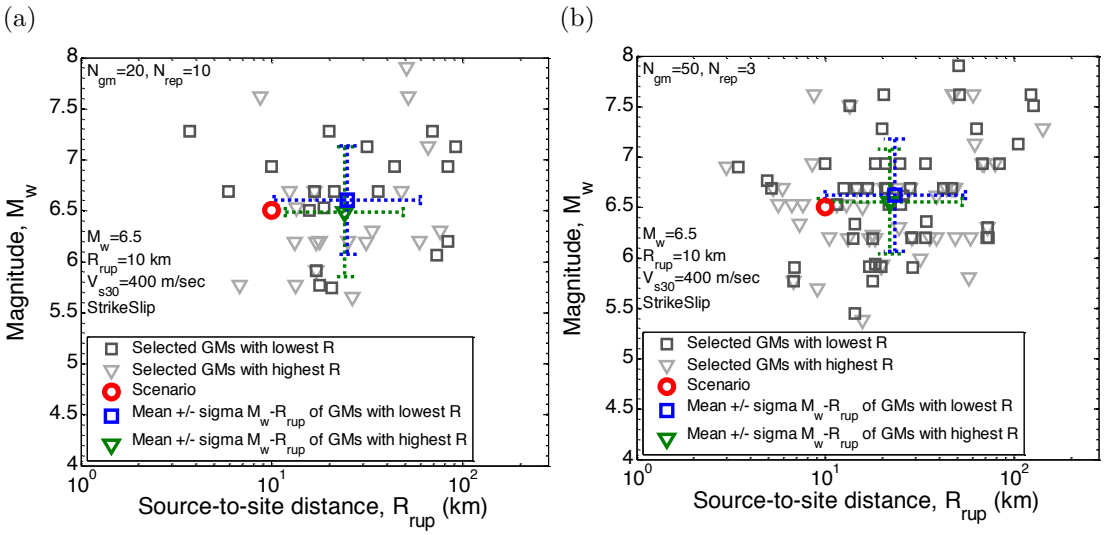

Figure 2.20: $M_w - R_{rup}$ distribution of selected motions for the M6.5R10V400 rupture scenario using weight vector case 6 (*i.e.*, SA, AI, CAV, D_{s575}, D_{s595}): (a) 20; and (b) 50 motions.

on the explicit IMs of ground motion and not the implicit causal parameters.

It is important to note that there is a trade-off when selecting motions with an appropriate representation for the explicitly predicted IMs; implicit causal parameters such as magnitude-distance distribution; and amplitude scale factors. While ideally the selected motions would have the appropriate representation of implicit causal parameters and amplitude scale factors near 1.0, an emphasis in ground motion selection should be placed on the appropriateness of the explicit intensity measures of the ground motion rather than the implicit causal parameters, as elaborated upon by Bradley (2012c).

2.4.2.4 Number of the selected motions and their representativeness for the target distribution of IMs

Since, in the GCIM-based selection, motions are selected to represent the predicted distribution of the considered IMs, it is obvious that a large number of selected motions can have a better representativeness compared to a suite with a relatively smaller number of motions. Figure 2.21 compares the representativeness

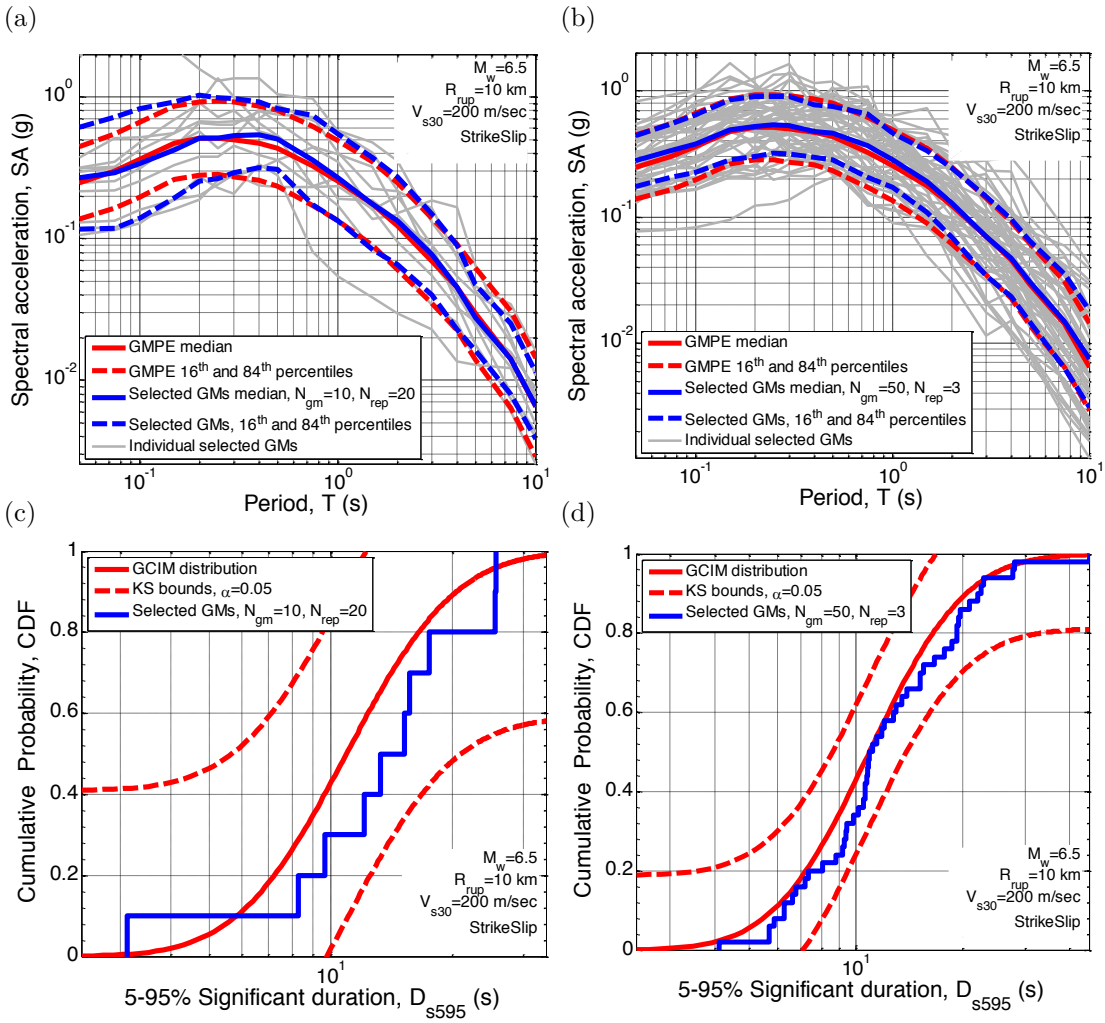

Figure 2.21: Properties of selected ensembles with 20 and 50 ground motions using weight vector case 6 (*i.e.*, SA, AI, CAV, D_{s595}, and D_{s575}) for the M6.5R10V200 rupture scenario: (a)-(b) SA ordinates; (b)-(c) cumulative distribution of D_{s595}.

of SA ordinates and 5-95% Significant Duration of two suites with 10 and 50 motions selected for the M6.5R10V200 scenario using weight vector case 6 (*i.e.*, SA, AI, CAV, D_{s575}, and D_{s595}). By selecting a larger number of motions, deviation in the distribution of the considered IMs with respect to the target distribution tends to decrease. It is important to note that, having a proper representation for an IM is dependent upon the weight of that IM in the implemented weight vector in the first place, rather than the number of the selected motions, however, for a given weight vector, using a large number of motions, on average, results in a better representation.

2.5 Conclusion

In this chapter, the generalised conditional intensity measure (GCIM) approach was extended to scenario-based ground motion selection. The ground motion selection algorithm is based on generating random realisations of the considered intensity measures (IMs) distributions for a specific rupture scenario and then finding the prospective ground motions which best fit the realisations based on an optimal amplitude scale factor. A weight vector is used to define the relative importance of various intensity measures in the selection process. Particular attention was given to illustrating, via examples, the effect of the weight vector and number of replicate selections considered on the properties of the selected ground motions.

It was shown that considering only spectral acceleration (SA) ordinates, as it is common in many conventional selection procedures, likely results in a bias of the cumulative and duration effects of ground motions as compared with that expected for the seismic hazard, which can bias seismic response estimates. Importantly, the results presented illustrate that considering IMs other than SA ordinates does not have any notable detrimental effect on representativeness of the SA ordinate distribution of the selected motions. It has also been demonstrated that conducting several replicate selections has a positive effect on obtaining a set of motions with a smaller global residual (*i.e.,* misfit) and an improved representation for the distribution of the considered IMs. A minimum number of suggested replicate selections was also presented for different number of desired motions.

Chapter 3

Representative ground-motion ensembles for several major earthquake scenarios in New Zealand

Tarbali, K. and Bradley, B. A. (2014). Representative ground-motion ensembles for several major earthquake scenarios in New Zealand. *Bulletin of New Zealand Society of Earthquake Engineering*, 47(4):231-252.

3.1 Summary

In this chapter, representative ground motion ensembles for several major earthquake scenarios in New Zealand are developed. Cases considered include representative ground motions for the occurrence of Alpine, Hope, and Porters Pass earthquakes in Christchurch city, and the occurrence of Wellington, Wairarapa, and Ohariu fault ruptures in Wellington city. For each considered scenario rupture, ensembles of 20 and 7 ground motions are selected using the generalised conditional intensity measure (GCIM) approach, ensuring that the ground motion

ensembles represent both the mean, and distribution of ground motion intensity which such scenarios could impose. These scenario-based ground motion sets can be used to complement ground motions which are often selected in conjunction with probabilistic seismic hazard analysis, in order to understand the performance of structures for the question 'what if this fault ruptures?'

3.2 Introduction

Conducting nonlinear response history analysis of structures for the purpose of seismic performance assessment requires selecting ground-motion time series which provide a hazard-consistent representation of the seismic hazard at the site. Although it is common to conduct seismic performance assessment based on the results from probabilistic seismic hazard analysis (PSHA), scenario-based assessments can also be highly informative and provide complementary insights (Bommer, 2002; FEMA-P58, 2012).

Many methods have been proposed to select ground motions based on matching the (pseudo) acceleration response spectrum of the selected motions to a target spectrum and considering implicit causal parameters of dominant scenario ruptures (*e.g.,* magnitude, source-to-site distance, site conditions) (Baker, 2011; Bommer and Acevedo, 2004; Jayaram et al., 2011; Kottke and Rathje, 2008; Shome et al., 1998; Wang, 2011). Katsanos et al. (2010) present a detailed review of the existing ground motion selection methodologies. Typically such approaches have been considered in the context of a response spectrum obtained from the PSHA results, or a code-based response spectrum (see Oyarzo-Vera et al. (2012) for ensembles based on NZS1170.5 standard (NZS1170.5, 2004) for the North Island of New Zealand). Such approaches generally have several shortcomings (Bradley, 2010b), namely: (1) ground motion severity is a function of the amplitude, frequency content, duration, and cumulative effects of the motion, which is not embodied simply in spectral acceleration ordinates; (2) ground motion ensembles should represent the full distribution of ground motion intensity and not just the

mean; and (3) the ground motion ensemble should be representative of all the seismic sources which contribute to the hazard at the site. These shortcomings have been addressed through the generalised conditional intensity measure (GCIM) approach developed by Bradley (2010b, 2012c), which provides a theoretically consistent approach to obtain ground motions based on PSHA for seismic performance assessment purposes (Bradley, 2012d). The GCIM-based ground motion selection method has also been recently extended to select ground motions based on the results from scenario seismic hazard analysis (scenario SHA) Tarbali and Bradley (2014a, 2015b).

In the present study, the GCIM method is utilised to select representative ground motion ensembles for several major earthquake scenarios in New Zealand. Two sets of ensembles with 7 and 20 ground motions are selected, which can be used for scenario-based seismic performance assessment purposes (7 motions being a common number prescribed in seismic design guidelines, and the larger number necessary to adequately characterise the full distribution of seismic demand). The earthquake rupture forecast (ERF) model developed by Stirling et al. (2012) is used to obtain the characteristics of seismic sources, and the New Zealand-specific ground motion model (GMM) developed by Bradley (2013d) is used to predict spectral accelerations, peak ground acceleration, and peak ground velocity for the purposes of scenario-based seismic hazard analysis and ground-motion selection. Other ground motion intensity measures of importance in seismic hazard analysis and ground-motion selection are obtained using foreign (*i.e.,* non-NZ-specific) GMMs developed for active shallow crustal events. Results are first presented for rupture scenarios impacting Christchurch city then Wellington city, and finally the current challenges with ground motion selection for subduction zone ruptures are discussed.

3.3 Ground motion selection for scenario ruptures in Christchurch

3.3.1 Dominant seismic sources

In order to identify the scenario ruptures with significant contributions to the seismic hazard at a generic location in central Christchurch city (Lat: -43.5300°; Lon: 172.6203°), PSHA was conducted using the open-source seismic-hazard-analysis software, OpenSHA (Field et al., 2003). The soil condition at the site is assumed to be site class D according to (NZS1170.5, 2004), with an inferred time-averaged 30m shear wave velocity of V_{s30}=250 m/s. Figure 3.1 presents the deaggregation of the seismic hazard at this site for both peak ground acceleration (PGA) and T=2s period spectral acceleration, SA(2.0s), for a 10% probability of exceedance in 50 years. As seen in Figure 3.1, the PGA seismic hazard at this generic site is mostly dominated by events with small magnitudes and small source-to-site distances associated with distributed seismicity, with similar results for SA ordinates at small vibration periods. However, as shown for the deaggregation of the SA(2.0s) hazard, events with large magnitudes and moderate-to-large source-to-site distances dominate at long vibration periods (specifically T>1s).

Based on the scenarios with a large contribution to the seismic hazard for different periods of vibration, ground motions in Christchurch city due to ruptures of the Alpine, Hope, and Porters Pass faults are considered in this study for scenario ground-motion selection. The specific characteristics of these scenario ruptures are presented in Table 3.1.

3.3.2 Intensity measures of the considered scenario ruptures

Table 3.2 presents median predicted values of several intensity measures (IMs) for the rupture scenarios considered for Christchurch city. As shown, the spectral

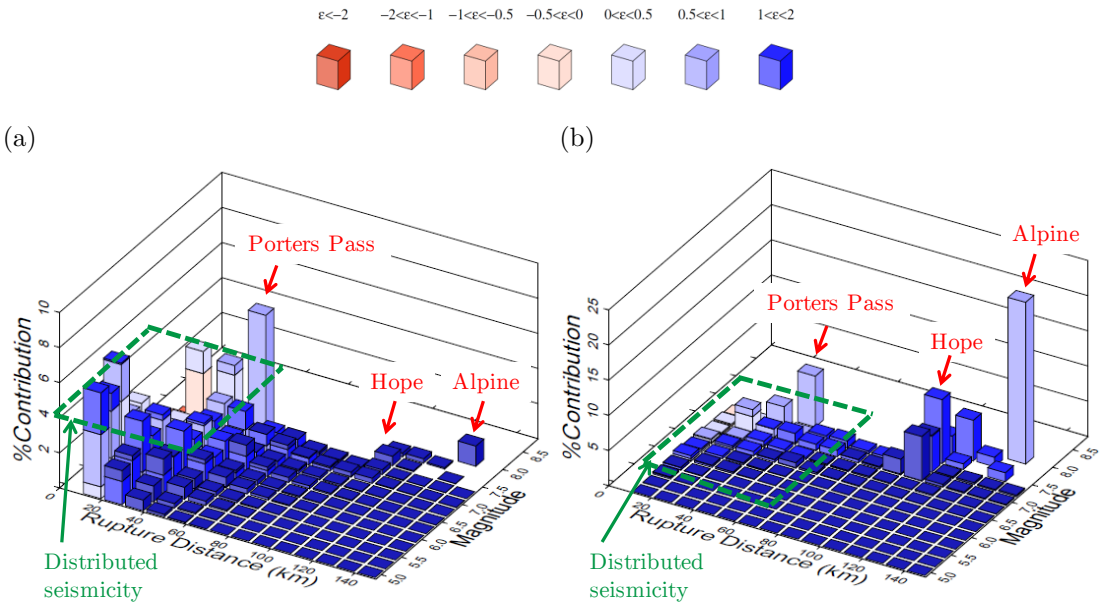

Figure 3.1: Deaggregation of seismic hazard in Christchurch city for a 10% probability of exceedance in 50 years: (a) PGA; and (b) SA(2.0s).

Table 3.1: Characteristics of the considered scenario ruptures for Christchurch city[1]

Fault	Magnitude, M_w	Source-to-site distance, R_{rup}(km)	Rupture mechanism
Alpine (Fiord-Kelly segment)	8.1	133	Strike-slip
Hope (Conway segment)	7.5	106	Strike-slip
Porters Pass	7.5	44	Strike-slip

[1]Based on the ERF of Stirling et al. (2012).

acceleration ordinates (and PGA) of the Porters Pass scenario are greater than those for scenarios with larger source-to-site distances (*i.e.,* Alpine and Hope), especially for periods of vibration smaller than T=2 s. Similarly, the Porter Pass rupture is predicted to produce a greater PGV compared to Alpine and Hope fault ruptures. In contrast, the Alpine fault rupture has a median predicted 5-95% Significant Duration of D_{s595}=56.2 s, which is double the Significant Duration from the Porter Pass rupture (due to a smaller magnitude and source-to-site distance in comparison to the Alpine fault rupture).

Prior to selecting ground motions, it is important to identify the type of engineering system considered for seismic performance assessment, so that the selection process can aim to place emphasis on those IMs that are important to determine the characteristic response of the system. For instance, empirical evidence suggests that the peak inter-story drift of a building structure is strongly affected by spectral acceleration ordinates of the applied motion for periods near the first several vibration modes of the structure (e.g., Shome et al. (1998); Tothong and Cornell (2007). In contrast, for example, the response of geotechnical structures with liquefaction-susceptible soils and the collapse capacity of building structures can be considerably affected by duration and cumulative effects of ground motions (Bradley, 2010b; Bradley et al., 2013; Villaverde, 2007; Chandramohan et al., 2015). This problem-specific issue has been addressed in the GCIM-based ground-motion selection methodology by using a weight vector in the selection algorithm to weight different ground motion IMs in record selection (Bradley, 2012c). In order to consider different aspects of a ground motion, including amplitude, frequency content, duration, and cumulative effects, the selection process is based on distribution of multiple intensity measures for the considered rupture scenarios (Bradley, 2012c; Tarbali and Bradley, 2014a, 2015b).

Based on previous research (Tarbali and Bradley, 2014a, 2015b), the considered intensity measures for the purpose of this study are: spectral acceleration for 18 vibration periods (T=0.05, 0.075, 0.1, 0.15, 0.2, 0.25, 0.3, 0.4, 0.5, 0.75, 1.0, 1.5, 2.0, 3.0, 4.0, 5.0, 7.5, and 10.0 s), cumulative absolute velocity (CAV) (Campbell

Table 3.2: Median intensity measures of the considered scenario ruptures for Christchurch city

Fault	PGA (g)	SA(0.5s) (g)	SA(1.0s) (g)	SA(2.0s) (g)	PGV (cm/s)	CAV[1] (g.s)	D_{s595}[2] (s)
Alpine (Fiord-Kelly segment)	0.07	0.13	0.11	0.07	12.1	0.9	56.2
Hope (Conway segment)	0.05	0.10	0.07	0.04	7.9	0.5	36.6
Porters Pass	0.15	0.23	0.15	0.08	18.0	0.7	27.5

[1]CAV=cumulative absolute velocity (Campbell and Bozorgnia, 2010).

[2]D_{s595}=5-95% Significant Duration (Bommer et al., 2009).

and Bozorgnia, 2010), and Significant Durations (D_{s595} and D_{s575}) (Bommer et al., 2009). The relative importance of these intensity measures is applied by using a weight vector presented in Table 3, in which the total weight of 70% is evenly distributed across the 18 SA ordinates, and 10% weight is allocated to each of CAV, D_{s595}, and D_{s575} intensity measures. Additional intensity measures such as peak ground acceleration (PGA); peak ground velocity (PGV); acceleration spectrum intensity (ASI) (Bradley, 2010c); spectrum intensity (SI) (Bradley et al., 2009); and displacement spectrum intensity (DSI) (Bradley, 2011c) were also considered. Although considering various intensity measures can result in motions with a proper representation for different aspects of ground motions (*i.e.,* amplitude, frequency content, duration, and cumulative effects) for a given scenario rupture, based on the results presented by Tarbali and Bradley (2014a, 2015b), considering SA ordinates, CAV, and Significant Duration intensity measures (*i.e.,* D_{s595} and D_{s575}) can fairly represent these aspects. Therefore, only these intensity measures are given non-zero weights in the implemented weight vector (Table 3.3). Further details on the impact of weight vector selection are discussed at length in Tarbali and Bradley (2014a, 2015b).

Table 3.3: Weight vector considered for ground-motion selection

SA	CAV	D_{s575}	D_{s595}
0.7[1]	0.1	0.1	0.1

[1]Evenly distributed to 18 SA ordinates between T=0-10 s, *i.e.,* each SA ordinate has a weight of 0.7/18.

3.3.3 Selected 20 ground motions for scenario ruptures in Christchurch

For each of the considered scenarios, 20 ground-motion time series are selected from the NGA database of strong ground motions from active shallow crustal earthquakes (Chiou et al., 2008). As discussed by Tarbali and Bradley

(2014a, 2015a), limiting the available database of ground motions to those motions with implicit causal parameters (e.g., magnitude, source-to-site distance, site condition) similar to the characteristics of the considered scenario rupture can result in motions with an appropriate representation for the causal parameters of the scenario, along with the explicit intensity measures of motion. In this regard, for each scenario considered, the NGA database is limited based on the bounds presented in Table 3.4. As seen in this table, the prospective ground motions are limited to those motions one unit of magnitude greater and smaller than the corresponding rupture scenario magnitude, and the source-to-site distances of the motions (R_{rup}) are bounded to 0.5 to 1.5 times the scenario R_{rup}. The site condition of the prospective motions is limited to site class D (deep or soft soils) and E (very soft soils) (NZS1170.5, 2004), using V_{s30} values less than 400 m/s. The implemented bounds on these causal parameters are wide in order to avoid an unreasonably small number of prospective ground motions for the considered scenario ruptures. However, it is re-iterated that the selected ground motions are not based on specific causal parameters once this first screening criteria has been applied.

Table 3.4: Bounds on the implicit causal parameters of the prospective ground motions for the considered scenario ruptures for Christchurch city

Fault	Magnitude, M_w	Source-to-site distance, R_{rup} (km)	Site condition, V_{s30} (m/s)
Alpine (Fiord-Kelly segment)	$7.1 \leq M_w \leq 9.1$	$66 \leq R_{rup} \leq 198$	$V_{s30} \leq 400$
Hope (Conway segment)	$6.5 \leq M_w \leq 8.5$	$53 \leq R_{rup} \leq 159$	$V_{s30} \leq 400$
Porters Pass	$6.5 \leq M_w \leq 8.5$	$22 \leq R_{rup} \leq 66$	$V_{s30} \leq 400$

It should also be noted that the motions in the NGA database have been processed to be directly used in seismic response analyses and are accessible at `http://peer.berkeley.edu/nga/`. The ground motions selected in this study are presented in Appendix A and can also be downloaded from `https://sites.google.com/site/brendonabradley/research/ground-motion-selection`.

In order to illustrate the properties of the selected motions, Figure 3.2 presents

the median, 16^{th} and 84^{th} percentiles, and the individual acceleration response spectra of the selected motions (which have been amplitude scaled), along with the predicted median target spectrum and the target 16^{th} and 84^{th} percentile spectra for the considered rupture scenarios. In addition, Figure 3.2d presents the cumulative distribution of 5-95% Significant Duration, D_{s595}, for the considered rupture scenarios and the corresponding target distribution.

Based on the presented results, it can be seen that the distribution of SA ordinates of the selected motions provides an unbiased representation of the predicted target distribution (*i.e.,* 16^{th}, 50^{th}, and 86^{th} percentiles of the selected motions conform to the predicted target distribution). Also, the distribution of D_{s595} (Figure 3.2d), along with CAV and 5-75% Significant Duration, D_{s575}, (although not presented here for brevity) of the selected motions corresponds well to the target distribution of the scenario ruptures.

As seen in Figure 3.2, the predicted median scenario spectrum, the median spectrum of the selected motions, and the individual acceleration response spectrum of majority of the selected motions for the corresponding scenario ruptures are below the elastic code spectra presented in NZS1170.5 (2004) for Christchurch (Z=0.3; shown here for reference only). In addition, as presented in Figure 3.2d, the M_w8.1 rupture of the Alpine fault and M_w7.5 rupture of the Hope fault (both with large source-to-site distances) will produce motions with long Significant Durations, whereas the M_w7.5 rupture of the Porter Pass fault (with a smaller source-to-site distance) will result in motions with shorter Significant Durations. Large differences in Significant Duration of the considered rupture scenarios and the considerable effect of duration on seismic response of engineering systems (Bradley, 2010b; Bradley et al., 2013; Villaverde, 2007; Chandramohan et al., 2015) illustrates the importance of considering this intensity measure when selecting ground motions for seismic response analysis.

Considering the fact that the implicit causal parameters of ground motions, such as magnitude, source-to-site distance, and site condition are not explicitly

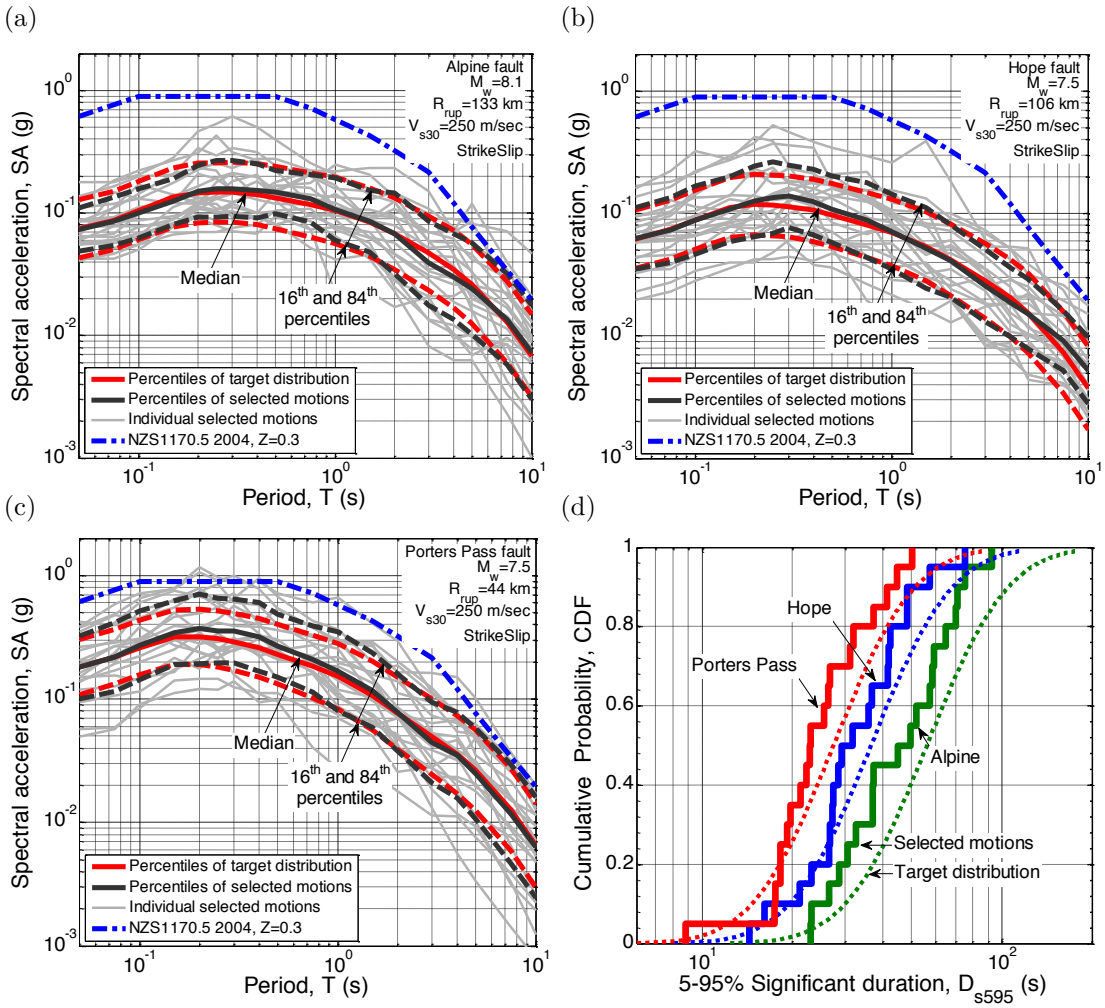

Figure 3.2: SA ordinates of the selected ground motions and the corresponding median, 16th, and 84th percentile spectra representing: (a) Alpine; (b) Hope; (c) Porters Pass scenario ruptures; and (d) cumulative distribution of 5-95% Significant Duration and the corresponding target distribution for the considered scenario ruptures.

considered in the GCIM-based ground-motion selection methodology (Bradley, 2012c; Tarbali and Bradley, 2015b) it is worthwhile examining the distribution of these parameters for the selected motions with respect to each scenario rupture. As illustrated in Figure 3.3, the selected motions for the Hope fault rupture are well distributed with respect to the scenario magnitude (*i.e.,* the 16^{th} to 84^{th} percentile range of M_w encompass the scenario). This is also the case for the Porters Pass fault rupture. In contrast, the selected motions for the Alpine fault rupture have a lower magnitude distribution than the scenario itself. This is caused by the paucity of recorded ground motions with magnitudes larger than M_w7.5-8.0, in contrast to a relative abundance in the recorded motions from events with smaller magnitudes. This is illustrated in Figure 3.3d, which depicts the M_w-R_{rup} distribution of the motions in the NGA database (Chiou et al., 2008) and the motions that are available for the considered rupture scenarios for Christchurch city based on the bounds presented in Table 3.4. As seen in Figure 3.3d, a small portion of the total database of motions is available for the Alpine fault rupture relative to the other two scenarios. Figures 3.3a-c also illustrate that the selected ground motions can properly represent the scenario source-to-site distance for all three of the considered scenario ruptures, with the mean R_{rup} very close to the target scenario R_{rup}.

Figures 3.4a-c present the V_{s30}-R_{rup} distribution of the selected motions representing the considered scenarios for Christchurch city. As shown, the selected motions encompass the scenario within the 16^{th} to 84^{th} percentile bound. Also, the median V_{s30} of the selected motions is similar to the target V_{s30} of the considered site. As discussed by Tarbali and Bradley (2015a, 2016), imposing bounds on magnitude, source-to-site distance, and site condition of prospective ground motions results in motions with a proper representation for these causal parameters, which is illustrated in Figures 3.3a-c and Figures 3.4a-c for the considered scenario ruptures for Christchurch city. In addition to the distributions of the causal parameters (M_w, R_{rup}, *and* V_{s30}), the amplitude scale factor, *SF*, applied on the selected motions can be used to check the quality of the obtained ensemble

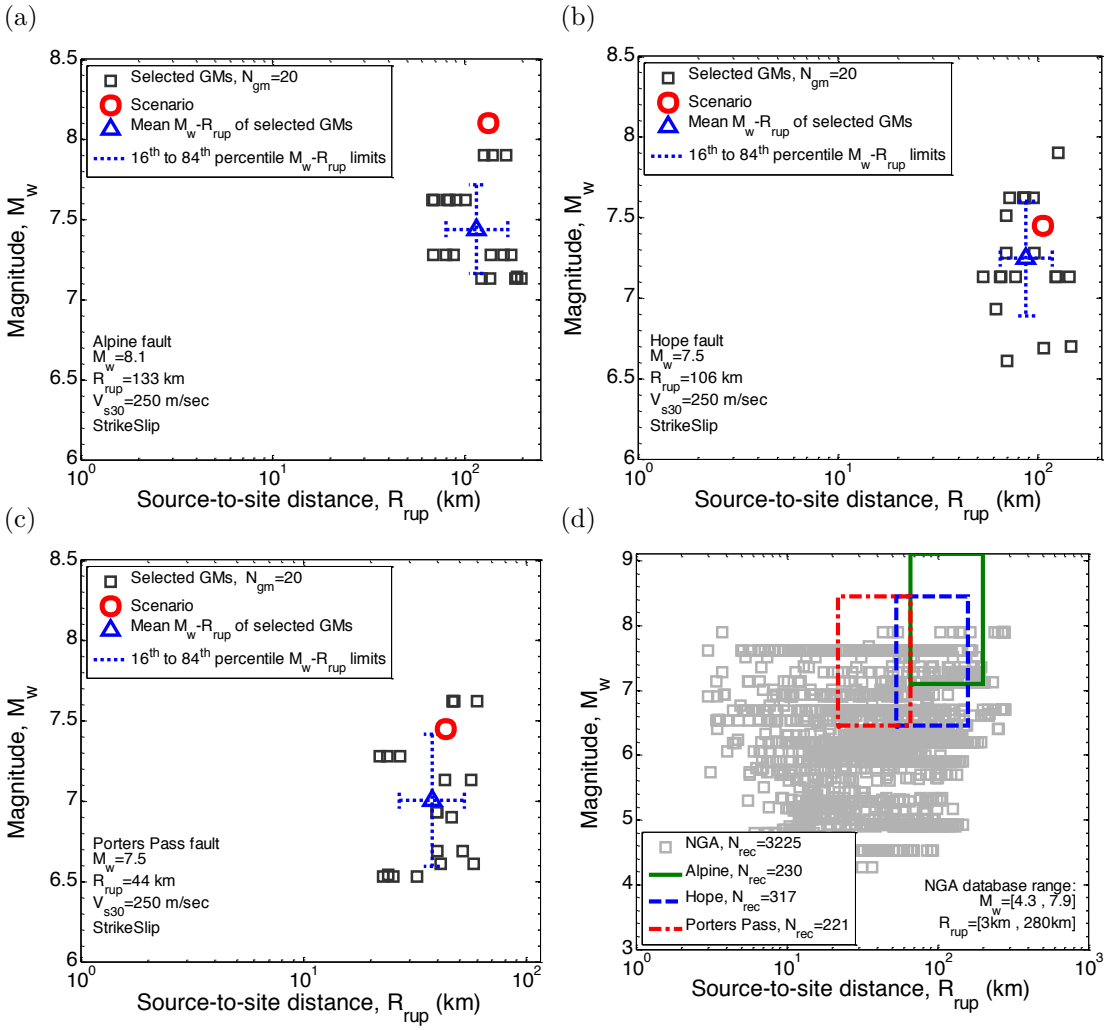

Figure 3.3: Magnitude-distance distribution of the selected ground motions representing: (a) Alpine; (b) Hope; (c) Porters Pass scenario ruptures; (d) available ground motions in the database based on the bounds applied on the causal parameters of prospective ground motions.

of ground motions. Figure 3.4d presents the amplitude scale factor of the selected motions for the considered rupture scenarios for Christchurch city. It is noted that the amplitude scale factors are not constrained by the ground motion selection methodology, but are a by-product of representing the target IMs distribution in an unbiased fashion based on the bounded prospective ground motions. As seen in this figure, all of the amplitude scale factors for the Hope fault rupture and 90% of the amplitude scale factors for the rupture of Alpine and Porter Pass faults are in the range of 0.3 to 3.0. Similar ranges are often recommended as scaling limits in seismic design standards (NZS1170.5, 2004; ASCE/SEI7-10, 2010). It should be noted that, as discussed by Tarbali and Bradley (2015a, 2016), having bounds on the implicit causal parameters of the prospective ground motions results in selecting motions with smaller amplitude scaling factors. This is due to the fact that by limiting the available motions to those with causal parameters similar to the scenario characteristics, small changes in the amplitude of the motions are required to represent the distribution of the explicit intensity measures of motion.

It is important to note that there is a trade-off when selecting motions to achieve an unbiased distribution of the predicted intensity measures (SA, D_{s595} etc.); magnitude-distance distribution (or other implicit causal parameters); and amplitude scale factors. While ideally the selected ground motions would have the appropriate representation of implicit causal parameters and amplitude scale factors near 1.0, an emphasis in ground motion selection should be placed on the distribution of the explicit intensity measures of the ground motion (SA, D_{s595} etc.) rather than the implicit causal parameters, as elaborated on by Bradley (2012c); Tarbali and Bradley (2015a, 2016).

3.3.4 A subset of 7 ground motions from the selected 20 motions

A subset of 7 ground motions from the selected 20 motions are also tabulated in Appendix A, which can be used in code-based analyses to assess the design or

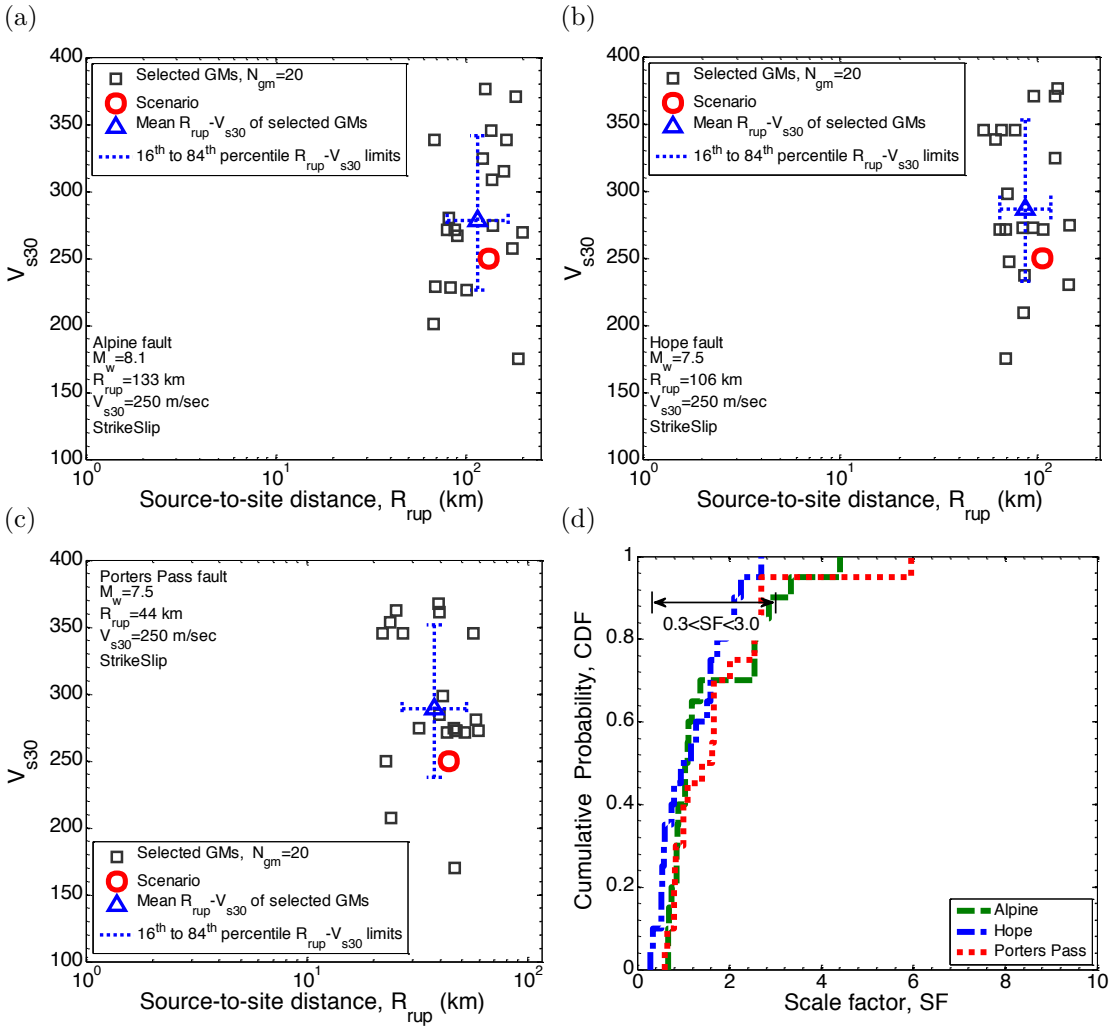

Figure 3.4: V_{s30} -R_{rup} distribution of the selected ground motions, representing: (a) Alpine; (b) Hope; and (c) Porters Pass scenario ruptures, and (d) cumulative distribution of the amplitude scale factors of selected ground motions.

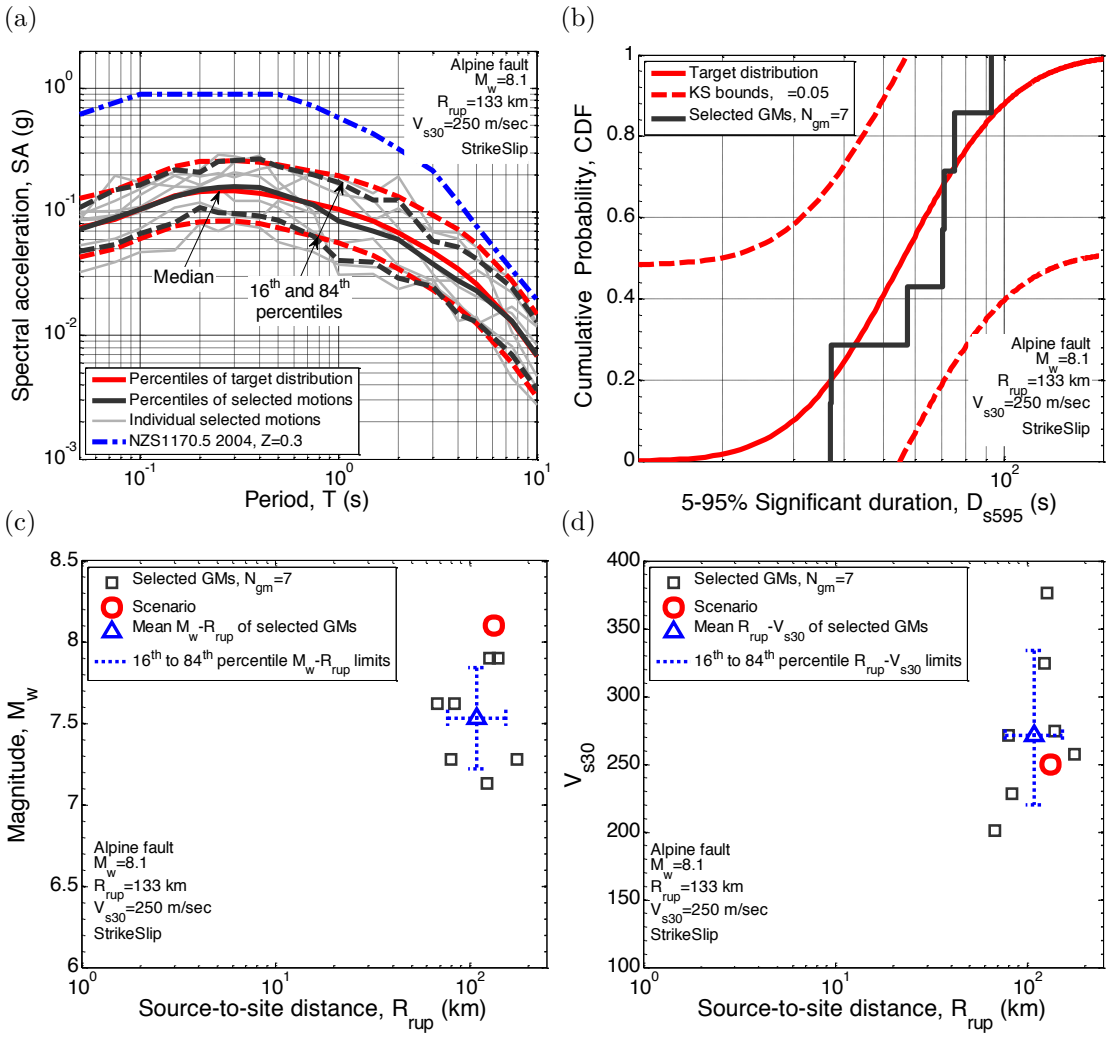

Figure 3.5: Properties of the subset of 7 ground motions representing the Alpine fault scenario rupture: (a) SA ordinates; (b) cumulative distribution of 5-95% Significant Duration; (c) M_w-R_{rup} distribution; and (d) V_{s30}-R_{rup} distribution.

retrofit of engineering systems against the occurrence of the considered rupture scenarios. Figure 3.5, as an example, illustrates the SA ordinates, cumulative distribution of 5-95% Significant Duration, M_w-R_{rup} and V_{s30}-R_{rup} distributions of the subset of 7 motions representing the Alpine fault rupture.

As seen in Figure 3.5, the selected 7 ground motions provide an unbiased representation of the predicted IMs of the motions for the scenario rupture. Considering the distribution of the causal parameters of the 20 motions, the V_{s30} and R_{rup} of the subset of 7 motions have an appropriate representation of the scenario characteristics. It is important to note that the individual amplitude scale fac-

tors applied on these 7 motions, in order to collectively represent the predicted distribution of the considered IMs, are slightly different than those applied on the same motions when they were selected in a set with 20 motions. As presented in Appendix A, all of the amplitude scale factors applied on the subset of 7 motions are within the range of 0.3 to 3.0.

3.4 Ground motion selection for scenario ruptures in Wellington

3.4.1 Dominant seismic sources

PSHA has been conducted for a generic location in central Wellington city (Lat: -41.2889°; Lon: 174.7772°) for a site class D soil (NZS1170.5, 2004) with V_{s30}=250 m/s. Figure 3.6 illustrates the seismic hazard deaggregation for PGA and SA(2.0s) for a 10% probability of exceedance in 50 years. Based on the obtained results for deaggregation of the seismic hazard, it is observed that the seismic hazard at this generic location in Wellington city is mostly dominated by events with large magnitudes and very small source-to-site distances. By identifying the scenarios with large contributions to the seismic hazard, ruptures of the Wellington, Wairarapa, and Ohariu faults are considered in this study for scenario ground-motion selection. Characteristics of these scenario ruptures are presented in Table 3.5.

It is important to note that the presented deaggregation results illustrate the contribution of a M_w8.6 rupture of the Hikurangi subduction zone (Wellington Max segment) approximately 20km from Wellington city. The current issues related to robustly selecting ground motions to represent subduction zone earthquakes are presented later in this chapter, and therefore attention here has been limited to selecting ground motions to represent active shallow-crustal ruptures.

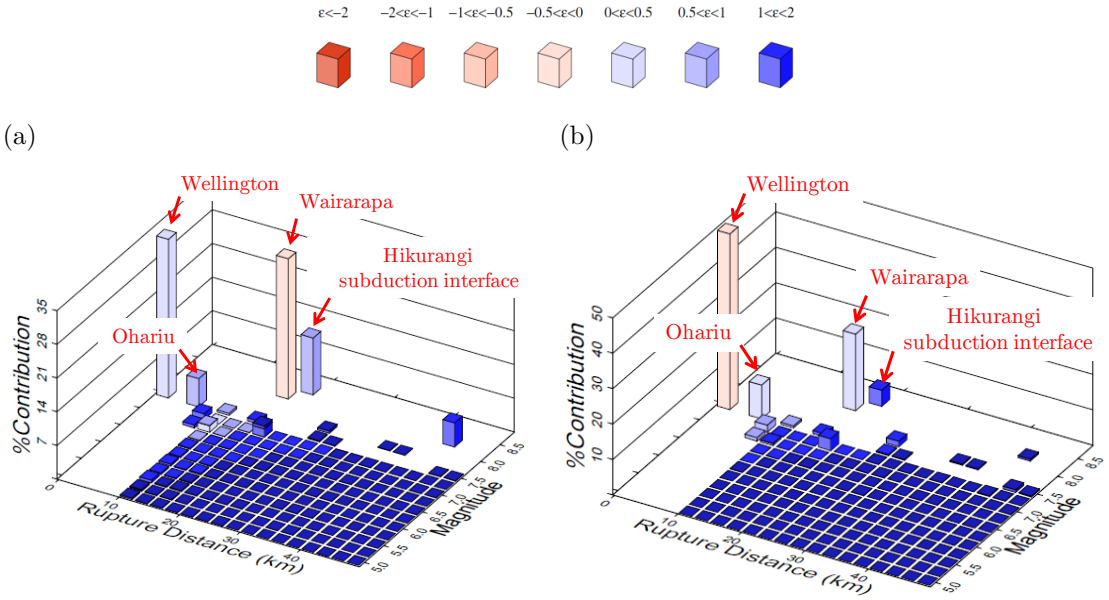

Figure 3.6: Deaggregation of seismic hazard in Wellington city for a 10% probability of exceedance in 50 years: (a) PGA; and (b) SA(2.0s).

Table 3.5: Characteristics of the considered scenario ruptures for Wellington city[1]

Fault	Magnitude, M_w	Source-to-site distance, R_{rup}(km)	Rupture mechanism
Wellington (Well-Hutt Valley segment)	7.5	1.0	Strike-slip
Wairarapa (Nicholson segment)	8.2	17	Strike-slip
Ohariu (South segment)	7.4	6.0	Strike-slip

[1]Based on the ERF of Stirling et al. (2012).

3.4.2 Intensity measures of the considered scenario ruptures

Table 3.6 presents the median intensity measures for the scenario ruptures considered for Wellington city. As presented, the Wellington fault with a large magnitude and very small R_{rup}, and the Wairarapa fault with a very large magnitude and small R_{rup} have close median SA ordinates. In addition, the Wellington rupture results in a greater PGV compared to the Wairarapa and Ohariu ruptures, because of the very small source-to-site distance from this fault to the site. Finally, because of the large magnitude of the rupture in the Wairarapa fault (*i.e.,* M_w 8.2), the median predicted 5-95% Significant Duration (*i.e.,* D_{s595}) is considerably greater than that for the other two ruptures.

3.4.3 Selected 20 ground motions for scenario ruptures in Wellington

Similar to the Christchurch scenarios previously discussed, ensembles of 20 ground motions were selected for each of the three considered ruptures for Wellington city, using the GCIM-based ground-motion selection methodology. Table 3.7 presents the bounds applied on the implicit causal parameters of the prospective ground motions for the considered scenario ruptures. Due to the short source-site distance of the three considered scenarios, R_{rup} of the prospective ground motions are bounded to values less than 30km. The weight vector presented in Table 3.3 is also implemented here for the Wellington city cases.

Figures 3.7a-c present the median, 16^{th}, and 84^{th} percentiles and the individual (amplitude scaled) acceleration response spectrum of the selected motions, along with the predicted median, 16^{th}, and 84^{th} percentile target spectra for the considered scenario ruptures for Wellington city. As shown in Figures 3.7a-b, the predicted median scenario spectrum, and the median spectrum of the selected motions for rupture of the Wellington fault (which has the highest contribution to

Table 3.6: Median intensity measures of the considered scenario ruptures for Wellington city

Fault	PGA (g)	SA(0.5s) (g)	SA(1.0s) (g)	SA(2.0s) (g)	PGV (cm/s)	CAV (g.s)	D_{s595} (s)
Wellington (Well-Hutt Valley segment)	0.6	1.0	0.9	0.6	104.7	2.0	24.0
Wairarapa (Nicholson segment)	0.7	1.1	0.8	0.4	74.7	2.0	41.5
Ohariu (South segment)	0.5	0.7	0.6	0.4	70.0	2.1	21.0

the seismic hazard at the site) and the Wairarapa fault are very close to the Z=0.4 elastic code spectra of NZS1170.5 (2004) at medium to long periods of vibration (provided here for comparison only).

Table 3.7: Bounds on the implicit causal parameters of the prospective ground motions for the considered scenario ruptures for Wellington city

Fault	Magnitude, M_w	Source-to-site distance, R_{rup} (km)	Site condition, V_{s30} (m/s)
Wellington (Well-Hutt Valley segment)	$6.5 \leq M_w \leq 8.5$	$R_{rup} \leq 30$	$V_{s30} \leq 400$
Wairarapa (Nicholson segment)	$7.2 \leq M_w \leq 9.2$	$R_{rup} \leq 30$	$V_{s30} \leq 400$
Ohariu (South segment)	$6.4 \leq M_w \leq 8.4$	$R_{rup} \leq 30$	$V_{s30} \leq 400$

As presented in Figures 3.7a-c, the selected ground motions provide an unbiased representation of the SA ordinates for Wellington and Ohariu fault ruptures, for the whole range of vibration periods (*i.e.,* T=0.05s-10.0s). However for the Wairarapa fault rupture, the selected motions deviate from the target distribution for short (*i.e.,* T<0.2) and long (*i.e.,* T>3.0) vibration period ranges. Also, based on the presented distribution of the 5-95% Significant Duration of the selected ground motions and the corresponding target distribution in Figure 3.7d, it can be seen that the selected motions can properly represent the 5-95% Significant Duration for the Wellington and Ohariu fault ruptures. However, there is a deviation from the target distribution for the Wairarapa fault rupture. When considering the resulting ground motions selected for the Wairarapa rupture scenario (Figure 3.7b and 3.7d), it is important to note that in comparing the selected motions with the 'target' we are implicitly assuming that the target is itself correct. While this is generally a reasonable assumption, in the case of rupture scenarios with very large magnitudes, (*i.e.,* M_w8.2 for Wairarapa), the GMM utilised to calculate the target distribution is weakly constrained for such large events. Therefore, the 'target' may itself be inherently biased, but future research is needed to more appropriately constrain such an assertion.

Figure 3.8 provides a comparison of the magnitude-distance distribution of the selected motions with respect to magnitude-distance pair of the corresponding scenarios for Wellington city. In the case of the Wellington and Ohariu fault

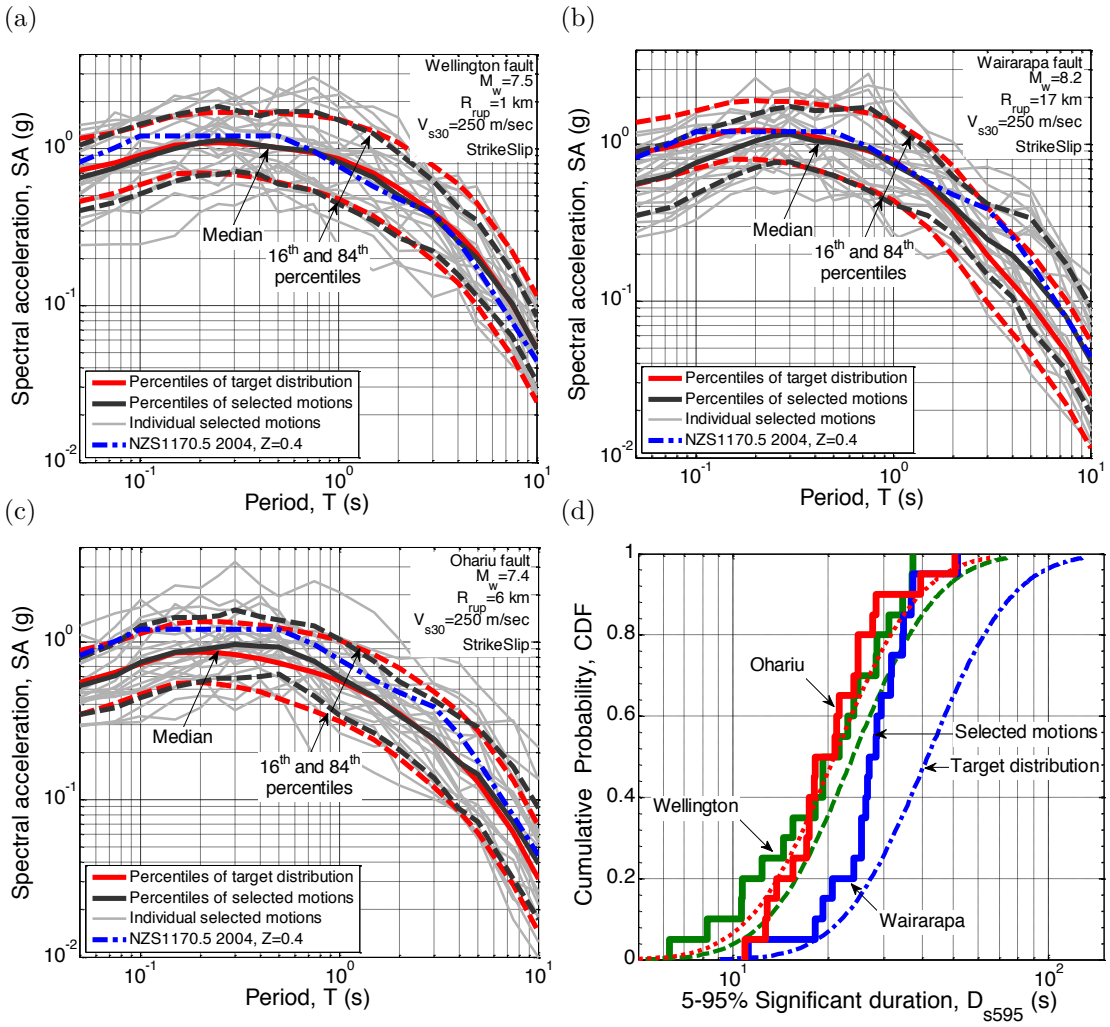

Figure 3.7: SA ordinates of the selected ground motions and the corresponding median, 16th, and 84th percentile spectra representing: (a) Wellington; (b) Wairarapa; (c) Ohariu scenario ruptures; and (d) cumulative distribution of 5-95% Significant Duration and the corresponding target distribution for the considered scenario ruptures.

ruptures, it can be seen that the magnitude distribution of the selected motions fairly corresponds to the rupture magnitude, while the magnitudes of the selected motions for the Wairarapa rupture fall below the scenario magnitude. In terms of source-to-site distances it can be seen that the ground motions selected for the Wairarapa fault rupture corresponds well to the scenario source-to-site distance, with a mean R_{rup} very close to the scenario R_{rup}. However, the source-to-site distances of the selected motions for the Wellington and Ohariu fault ruptures are notably larger than those representative of these scenarios. Clearly, these biases are related to the paucity of the motions recorded from large magnitude events with short source-to-site distances. Figure 3.8d illustrates the M_w-R_{rup} distribution of the motions in the NGA database (Chiou et al., 2008) and the ones that are available for each rupture scenario for Wellington city based on the bounds presented in Table 3.7. As shown, there are few motions with implicit causal parameters close to the characteristics of the Wairarapa fault rupture relative to the other two scenarios.

As already noted, it is important to remember that ground-motion selection requires a trade-off between the intensity measure values of the ground motions themselves, and implicit causal parameters such as M_w, R_{rup}, V_{s30}, etc. Because it is known that there is little variation of ground motion properties in the immediate near-field (*i.e.,* R_{rup}=0-10km) region, then the distance biases shown in Figure 3.8 for the Wellington and Ohariu fault ruptures (with R_{rup} values of 1.0 and 6.0 km, respectively) are not considered significant.

Figures 3.9a-c present V_{s30}-R_{rup} distribution of the selected ground motions representing the considered scenarios for Wellington city. As shown, the V_{s30} values of the selected motions for the Wellington and Ohariu fault ruptures correspond well to the considered site condition. Also, most of the selected motions for the Wairarapa fault rupture have V_{s30} values which are mostly similar to characteristics of a site class D soil (NZS1170.5, 2004).

As presented in Figure 3.9d, the amplitude scale factors of the selected mo-

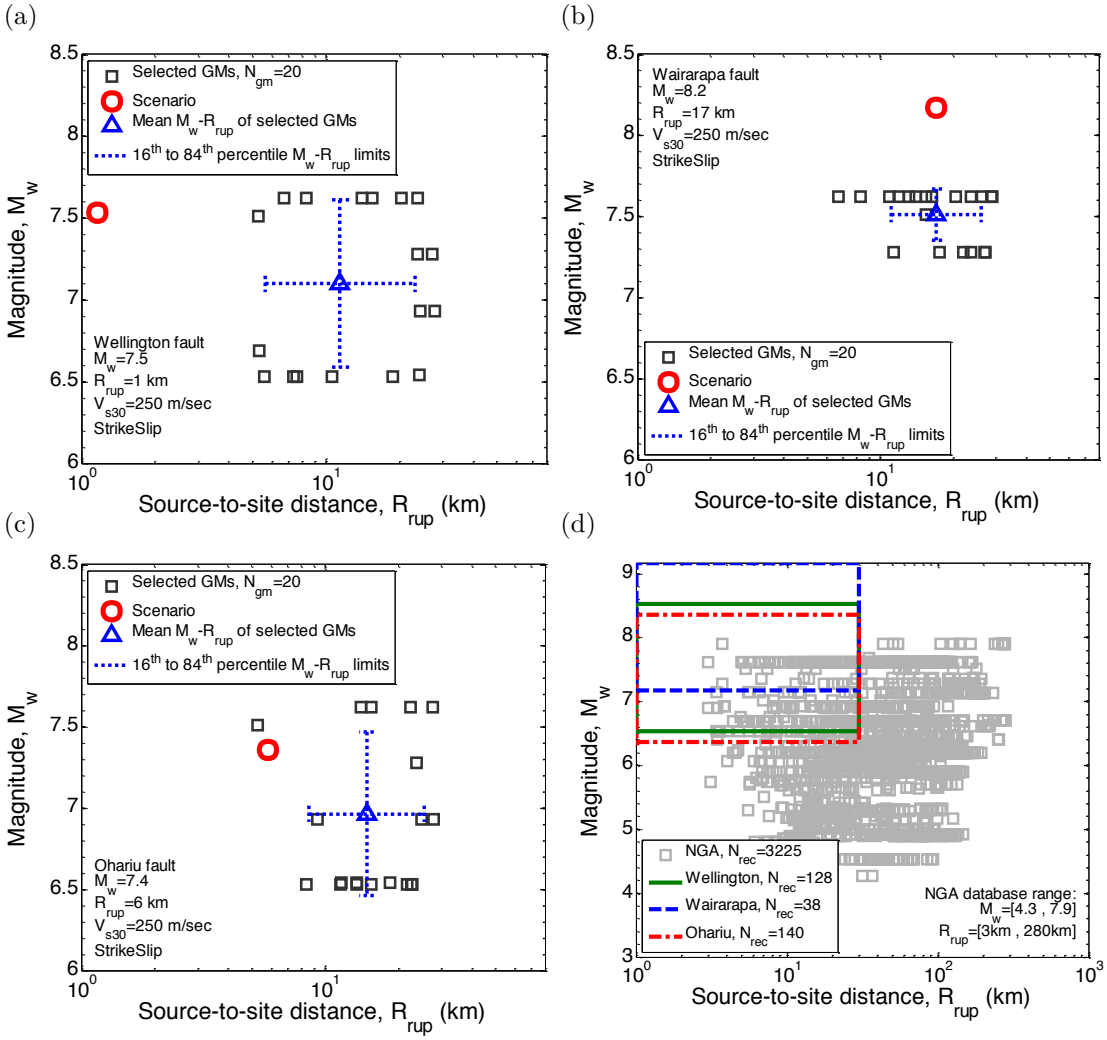

Figure 3.8: Magnitude-distance distribution of the selected ground motions representing: (a) Wellington; (b) Wairarapa; (c) Ohariu scenario ruptures; (d) available ground motions in the database based on the bounds applied on the causal parameters of prospective ground motions.

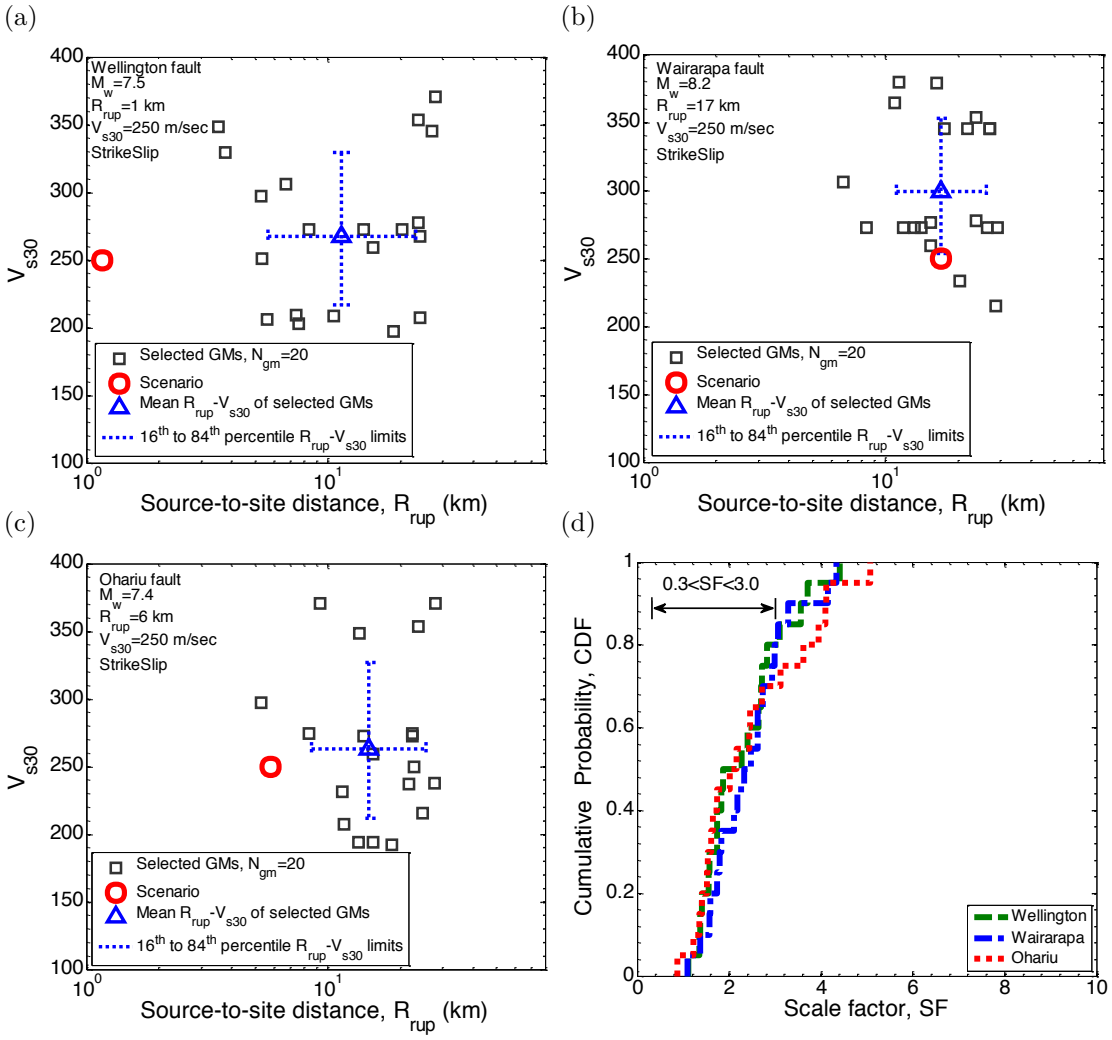

Figure 3.9: V_{s30}-R_{rup} distribution of the selected ground motions, representing: (a) Wellington; (b) Wairarapa; and (c) Ohariu scenario ruptures, and (d) cumulative distribution of the amplitude scale factors of selected ground motions.

tions are mostly large values, compared to the results presented in Figure 3.4d for Christchurch city, with approximately 80% of them for Wellington and Wairarapa fault ruptures and 70% of them for Ohariu fault rupture in the SF=0.3-3.0 range. As discussed by Tarbali and Bradley (2014a), selecting ground motions for scenarios like those encountered in Wellington city (with short source-to-site distances and large magnitudes) often requires scaling the existing motions using larger scale factors, as there is a shortage of motions recorded during such events in the existing strong ground motion database (Chiou et al., 2008) with adequate intensity measure properties and recorded at appropriate site classes.

3.4.4 A subset of 7 ground motions from the selected 20 motions

A subset of 7 ground motions from the selected 20 motions are also tabulated in Appendix A to represent the considered scenario ruptures in Wellington city. Figure 3.10 illustrates the SA ordinates, cumulative distribution of 5-95% Significant Duration, M_w-R_{rup} and V_{s30}-R_{rup} distributions of the subset of 7 motions representing the Wellington fault scenario rupture. As seen in this figure, the selected 7 motions provide an unbiased representation of the predicted distribution of the considered intensity measures. However, the issues associated with representativeness of the causal parameters of the 20 motions elaborated earlier are present in the subset of 7 motions.

3.5 Selecting representative ground motions for subduction zone events

The ground motions selected in this study are aimed to represent major active shallow crustal rupture scenarios in Christchurch and Wellington cities. However, the occurrence of major subduction zone earthquakes (both interface and slab)

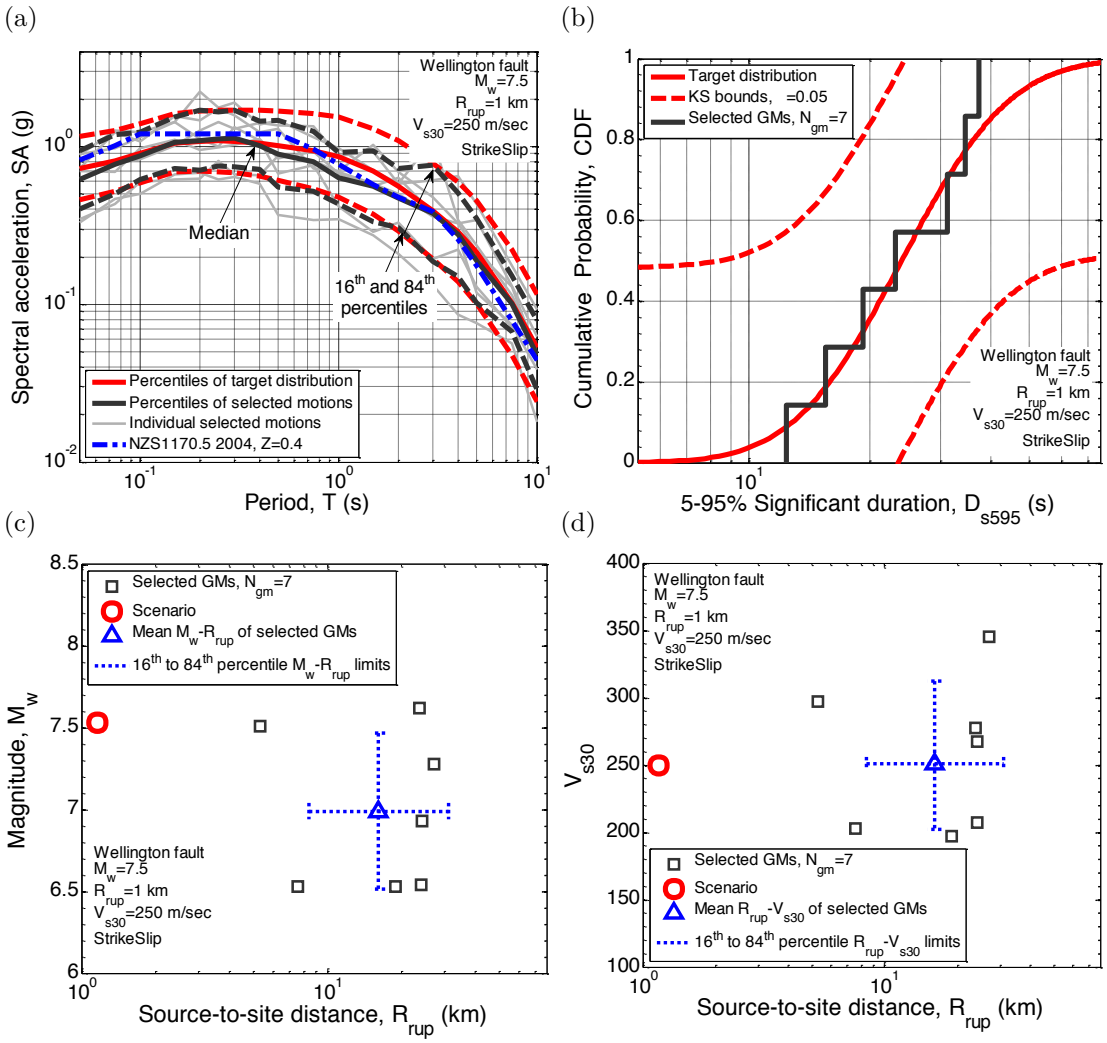

Figure 3.10: Properties of the subset of 7 ground motions representing the Wellington fault scenario rupture: (a) SA ordinates; (b) cumulative distribution of 5-95% Significant Duration; (c) M_w-R_{rup} distribution; and (d) V_{s30}-R_{rup} distribution.

should also be considered in ground-motion selection for regions prone to this type of earthquakes, such as Wellington. As noted, in the presented deaggregation results for Wellington city, the occurrence of a M_w8.6 rupture of the Hikurangi subduction interface (Wellington Max segment) within approximately 20km distance of Wellington city contributes significantly to the seismic hazard. At present, routine ground motion selection for subduction zone events is hindered by a lack of: (1) a comprehensive database of strong ground motions recorded from subduction zone events; and (2) appropriate subduction zone GMMs and correlation equations for various ground-motions intensity measures. Such efforts are topics of on-going research among the authors as well as many others in the research community.

3.6 Conclusion

This chapter demonstrates the selection of ground motions to represent several major earthquake scenarios in New Zealand, using the generalised conditional intensity measure (GCIM) approach. Six different rupture scenarios were considered that pose a significant seismic hazard in Christchurch city (Alpine, Hope and Porters Pass ruptures) and Wellington city (Wellington, Ohariu, and Wairarapa ruptures). For each rupture scenario considered, sets of 20 ground motions were selected to represent the predicted distribution of various intensity measures (spectral accelerations, Significant Duration etc.). Subsets of 7 records from these 20 ground motions were also tabulated and can be utilised for standard code-based seismic response analyses. A paucity of recorded motions from events with large magnitudes and short source-to-site distances in existing strong ground motion databases impedes selecting motions for large magnitude small source-to-site distance rupture scenarios and also consequently requires the use of large amplitude scale factors to scale available motions. However, it should be remembered that implicit causal parameters, such as magnitude and source-to-site distance, are of secondary importance when compared to explicit measures of intensity of ground

motion (spectral accelerations, Significant Duration etc.).

Chapter 4

The effect of causal parameter bounds on scenario- and PSHA-based ground motion selection

Tarbali, K. and Bradley, B. A. (2016). The effect of causal parameter bounds in PSHA-based ground motion selection. *Earthquake Engineering & Structural Dynamics*, 45(9):1515-1535.

4.1 Summary

In this chapter, the effect of considering bounds on causal parameters of prospective ground motions (*e.g.,* magnitude, source-to-site distance, and site condition) for the purpose of ground-motion selection is investigated. Although using bounds on causal parameters is common practice in conventional approaches for ground motion selection, there is presently no consistent approach for setting these bounds as a function of the seismic hazard at the site. A rigorous basis is developed and sensitivity analyses performed for the consideration of bounds on

magnitude, source-to-site distance, and site condition for use in ground motion selection. In order to empirically illustrate the effects of various causal parameter bounds on the characteristics of selected ground motions, 78 and 36 cases of scenario seismic hazard analysis (scenario SHA) and probabilistic seismic hazard analysis (PSHA) are considered, which cover a wide range of causal parameters and site conditions. Ground motions are selected based on the generalised conditional intensity measure (GCIM) approach, which considers multiple ground motion intensity measures (IMs) and their variability in order to appropriately represent characteristics of the seismic hazard at the site. It is demonstrated that the application of relatively 'wide' bounds on causal parameters effectively removes ground motions with drastically different characteristics with respect to the target seismic hazard (improving computational efficiency in the selection process by reducing the subset of prospective records), and results in an improved representation of the target causal parameters. In contrast, the use of excessively 'narrow' bounds can lead to ground motion ensembles with a poor representation of the target IM distributions, especially for ground motions selected to represent PSHA results. As a result, the causal parameter bound criteria advocated in this chapter provide a good 'default' that is expected to be sufficient in the majority of problems encountered in seismic hazard and demand analyses.

4.2 Introduction

Selecting appropriate ground motion ensembles is a key step in assessing the seismic performance of engineered systems through dynamic seismic response analyses. Various methods have been proposed to select ground motions for seismic response analysis (*e.g.,* McGuire, 1995; Shome et al., 1998; Bommer and Acevedo, 2004; Kottke and Rathje, 2008; Baker, 2011; Jayaram et al., 2011; Wang, 2011; Bradley, 2012c). Generally, ground motion selection is conducted based on implicit and explicit measures of ground motion intensity (Bommer and Acevedo, 2004). Implicit measures of ground motion are parameters that do not directly

characterise the severity of ground motions, such as magnitude, source-to-site distance, site condition, and are often referred to as (implicit) causal parameters. On the other hand, explicit intensity measures (IMs) such as spectral acceleration, peak ground velocity, duration, among others are directly related to the ground motion time series itself. It is common in ground motion selection practice to first constrain the database of prospective ground motions based on causal parameters similar to those of earthquakes dominating the seismic hazard for the site (Bommer and Acevedo, 2004; Baker, 2011; Wang, 2011), and then select ground motions based on an explicit IM-based target, most commonly an acceleration spectrum from either site-specific seismic hazard analysis or general design guidelines (see Katsanos et al. (2010) and the references therein).

Despite the prevalent application of causal parameter bounds prior to the ground motion selection process (Katsanos et al., 2010), specifying the limits of the bounds is a subjective choice. For instance, Stewart et al. (2001) recommended that, because of the considerable effect of magnitude on characteristics of ground motions, ± 0.25 magnitude (M_w) units either side of a considered scenario rupture is a desirable bound. Bommer and Acevedo (2004) recommended $\pm 0.2 M_w$ units from the scenario magnitude as the bound on prospective ground motions. In order to include an adequate number of ground motions when this M_w bound is applied, they comment that the source-to-site distance of records can be bounded over a wider range, without specifically mentioning a limit. In terms of site condition, both Stewart et al. (2001) and Bommer and Acevedo (2004) noted the importance of considering records from site conditions compatible with the site of interest. However, in cases where the application of bounds on magnitude and source-to-site distance restricts the number of available ground motions, Bommer and Acevedo (2004) recommended considering ground motions from sites with one site classification (based on NEHRP (2003) or CEN (2005)) either side of the in-situ site condition. Considering the tectonic regime of ground motions (*e.g.,* active shallow crustal or subduction-zone), style of faulting, selecting from multiple events and multiple recording stations within an event are also advo-

cated (*e.g.,* Bommer and Acevedo, 2004; Wang et al., 2015). Literature discussing other common ground motion selection methods (*e.g.,* Kottke and Rathje, 2008; Baker, 2011; Jayaram et al., 2011; Wang, 2011) has also noted the application of causal parameter bounds; however, generally a quantitative approach by which such bounds can be applied is not provided. It is also important to note that the majority of literature commenting on the use of causal parameter bounds is cast in the context of a scenario earthquake of interest, and thus the specific bounds for use in ground motion selection based on PSHA (which is the summation of the hazard from numerous earthquake sources as quantified via deaggregation) is not obvious.

Historically, a primary reason for using causal parameter bounds in ground motion selection stems from the fact that considering spectral acceleration (SA) ordinates as the only explicit IM does not adequately account for an accurate representation of ground motion duration and cumulative effects (Bommer et al., 2004; Wang, 2011; Bradley, 2012c; Tarbali and Bradley, 2014a, 2015b). Ground motion selection should be principally based on explicit ground motion IMs, rather than implicit causal parameters which are not a direct representation of the ground motion at the site (Shome et al., 1998; Baker and Cornell, 2006a; Baker, 2011; Bradley, 2012c).

In contrast to the conventional use of causal parameter bounds to address the shortcomings of selecting ground motions based on only SA ordinates, ground motion selection based on the generalised conditional intensity measure (GCIM) approach (Bradley, 2010b) utilises multiple explicit IMs which can directly represent ground motion amplitude, frequency content, duration, and cumulative effects. As a result, GCIM-based ground motion selection without the need to consider causal parameter bounds has been demonstrated for both probabilistic and scenario seismic hazard analyses (Bradley, 2012c; Tarbali and Bradley, 2015b). However, even with the GCIM method (among others), causal parameter bounds can assist in removing those records that have drastically different characteristics compared to the target seismic hazard at the site. Moreover, the appli-

cation of such bounds will improve the computational efficiency of the selection process by decreasing the size of empirical ground motion databases considered. The latter point is particularly pertinent when comparing the ever-increasing size of empirical databases, for example, comparing the NGA-West1 (Chiou et al., 2008) and NGA-West2 (Ancheta et al., 2013) databases reveals that the number of ground motion records has increased six-fold from 3,551 to 21,336, and the range of the causal parameters of ground motions has also broadened (see Table 4.1). Despite this large increase in empirical database size, approximately half of the NGA-West2 database (*i.e.,* 10,706 records) are from events with magnitude less than 4.5 (Bozorgnia et al., 2014), which are generally not of engineering interest for ground motion selection relating to seismic hazard analysis in regions with moderate-to-high seismicity.

Table 4.1: Comparison between the NGA-West1 and NGA-West2 empirical ground motion databases and causal parameter ranges

	Magnitude, M_w	source-to-site distance (R_{rup},km)	Site condition (V_{s30}, m/sec)	Number of Events	Number of records
NGA-West1*	[4.2 , 7.9]	[0.2 , 300]	[116 , 2016]	173	3,551
NGA-West2**	[3.0 , 7.9]	[0.05 , 1533]	[94 , 2100]	600	21,336

*Chiou et al. (2008) **Ancheta et al. (2013)

From the above discussion it can be seen that it is advantageous to utilise causal parameter bounds for preliminary 'screening' of empirical ground motion databases prior to the primary ground motion selection process based on explicit IMs. In this chapter, the consideration of bounds on magnitude, source-to-site distance, and site condition of prospective ground motions as a function of the seismic hazard at the site is rigorously examined. 78 scenario SHA and 36 PSHA cases are considered which encompass a broad range of rupture scenarios (including varying deaggregation distributions) and site conditions for ground motion selection. Ground motions are selected based on the GCIM methodology (Bradley, 2010b), which has been developed for both PSHA- and scenario-based ground motion selection (Bradley, 2012c; Tarbali and Bradley, 2015b), and is a generalisation of

the conditional mean spectrum method (Baker and Cornell, 2006a; Baker, 2011). The effect of causal parameter bound selection on both the number of available prospective ground motions from an initial empirical as-recorded database, and the statistical properties of IMs of selected ground motions using the GCIM-based approach are examined.

4.3 Ground-motion selection for scenario seismic hazard analysis (scenario SHA)

Scenario-based seismic performance assessment involves obtaining the seismic response of the system given the occurrence of a scenario earthquake with specified rupture characteristics (FEMA-P58, 2012). For system-specific dynamic analyses, such performance assessment requires the selection of ground motion ensembles to represent characteristics of the predicted ground shaking at the site. Since there is a variability in the predicted ground motion intensity for a given scenario earthquake, selected ground motions should aim to explicitly represent this variability (Kottke and Rathje, 2008; Jayaram et al., 2011; Wang, 2011). In addition, since the severity of ground motions cannot be completely presented based on only spectral acceleration ordinates, multiple IMs accounting for amplitude, frequency content, duration, and cumulative effects should be considered to select ground motions with an appropriate representation for these different aspects (Bradley, 2010b, 2012c).

The aforementioned issues to be considered in scenario-based ground motion selection are directly addressed in the GCIM-based ground motion selection methodology for scenario earthquakes presented by Tarbali and Bradley (2015b). In summary, the GCIM method uses the conditional multivariate distribution of a considered vector of IMs, **IM**, as the target to assess the appropriateness of the ensemble of selected ground motions. A so-called weight vector is used to prescribe the relative importance of the considered IMs in the selection process and

calculate the misfit of each prospective ground motion with respect to the target distribution (Bradley, 2012c; Tarbali and Bradley, 2015b). A global misfit is also used to quantify the difference between the selected ground motion ensemble and the target distribution (Bradley, 2013c), as defined by Equation 4.1:

$$R = \sum_{i=1}^{N_{IM}} w_i (D_{IM_i})^2 \tag{4.1}$$

where w_i is the weight vector value for the i^{th} intensity measure (*i.e.,* IM_i); and D_{IM_i} is the Kolmogorov-Smirnov (KS) test statistic (Ang and Tang, 1975), which is the maximum difference between the empirical distribution (of the selected ground motions) and the corresponding target IM_i distribution. Thus, the global misfit, R, consists of the mismatch between the empirical and target distributions of all of the IMs in **IM**, based on the relative importance defined by the weight vector. Herein, both the distribution of selected ground motions in comparison to the target distribution, and the global misfit, R, are used to compare the appropriateness of the ensembles selected with and without causal parameter bounds.

4.3.1 Rupture scenarios and site conditions considered

In order to empirically investigate the effects of causal parameter bounds on the characteristics of selected ground motions, 78 scenario ruptures are considered which encompass a wide range of implicit causal parameters for scenario earthquakes of interest in moderate-to-high seismicity regions. Table 4.2 summarises the characteristics of the considered rupture scenarios and site conditions. As presented in Table 4.2, the considered rupture scenarios range from magnitude M_w=5.5-8.0 and source-to-site distance R_{rup}=5-120 km. Importantly, the maximum R_{rup} for each M_w is selected to ensure that only ground motion amplitudes of engineering importance are considered (*e.g.,* only R_{rup}=5, 15 km is considered for M_w=5.5 scenarios). This is further illustrated in Figure 4.1, in which the median peak ground acceleration (PGA) of the considered rupture scenarios is presented.

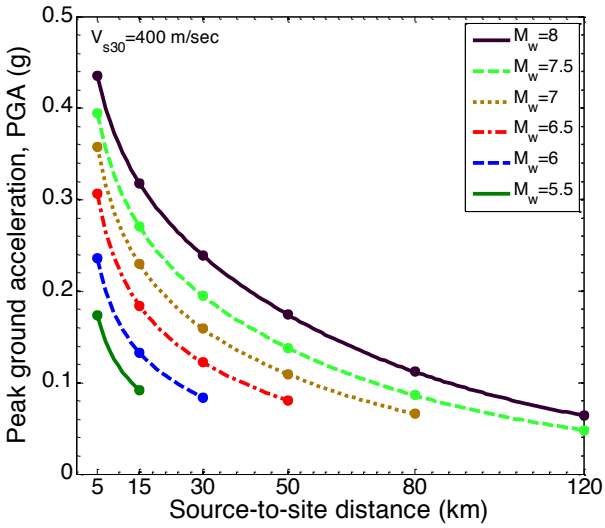

Figure 4.1: Median peak ground acceleration (PGA) for the considered scenario ruptures for V_{s30}=400 m/s site condition (points indicate the considered scenarios in Table 2) illustrating the magnitude-dependent R_{rup} limits in order to consider only significant ground motion amplitudes.

As shown, all the considered scenarios result in median PGAs above 0.05g for the example site condition.

Table 4.2: Characteristics of the 78 considered scenario ruptures and site conditions for scenario-based ground motion selection

Magnitude, M_w	source-to-site distance, R_{rup} (km)	Site condition, V_{s30} (m/sec)	Fault type
5.5	5, 15	200, 400, 800	Strike-slip
6.0	5, 15, 30	200, 400, 800	Strike-slip
6.5	5, 15, 30, 50	200, 400, 800	Strike-slip
7.0	5, 15, 30, 50, 80	200, 400, 800	Strike-slip
7.5	5, 15, 30, 50, 80, 120	200, 400, 800	Strike-slip
8.0	5, 15, 30, 50, 80, 120	200, 400, 800	Strike-slip

Three different site conditions, with a 30 m time-averaged shear wave velocity (*i.e.,* V_{s30}) of 200, 400, and 800 m/s, are considered for each $M_w - R_{rup}$ combination. These V_{s30} values were chosen to represent typical soft soil, stiff soil, and soft rock conditions, approximately corresponding to NEHRP site classes D, C, and A/B, respectively (NEHRP, 2003). Strike-slip faulting is chosen as the only rupture mechanism for the scenarios considered, as evidence suggests that

focal mechanism tends to result in a relatively systematic variation in ground motion intensity, with little effect on frequency content or duration, and thus is adequately captured through simple amplitude scaling (Bommer et al., 2003). For this reason others have also advised that, relative to other variables, focal mechanism can be neglected as a causal parameter of importance when selecting ground motions (*e.g.,* ASCE/SEI7-10, 2010).

4.3.2 Bounds considered on implicit causal parameters

As previously mentioned, the aim of considering causal parameter bounds is to remove ground motions in empirical as-recorded databases that have drastically different characteristics with respect to the target rupture scenario. However, the remaining database should still be large enough to select the desired number of ground motions which can appropriately represent the multiple IM distributions of interest. It is important to reiterate that the process of obtaining a ground motion ensemble which represents the target multivariate distribution of **IM** is based solely on the explicit ground motion IMs. Thus, causal parameter bounds are only a screening criteria applied prior to the ground motion selection process based on explicit IMs. In this regard, the bounds considered in this study are 'wide' in order to avoid excessive removal of potentially reasonable ground motions. Various sensitivity analyses are conducted to determine the bounds. As presented by Tarbali and Bradley (2014a), the application of bounds wider than those considered in this study leads to results consistent with those presented in this chapter. Also, the drawbacks of using narrower bounds, similar to those proposed by Stewart et al. (2001) and Bommer and Acevedo (2004) are discussed subsequently based on the number of available ground motions (presented in Table 4.5).

Table 4.3 presents the considered bounds for magnitude, source-to-site distance, and site condition of prospective ground motions for scenario-based ground motion selection. As shown, ground motions are bounded to half of a magni-

tude greater and smaller than the scenario magnitude. This is twice as large as the magnitude bound recommended by Stewart et al. (2001) and Bommer and Acevedo (2004). Also, the R_{rup} of prospective ground motions are bounded to 0.5 to 1.5 times the scenario R_{rup} (except 'near-fault' scenarios for which R_{rup} $\leq$15 km, where the R_{rup} bound is set to values less than 30 km). The site condition of prospective ground motions are also limited to 0.5 to 1.5 times the V_{s30} of the site, ensuring that ground motions within similar soil classes are included for each site condition. It is noted that the R_{rup} and V_{s30} bounds considered in this study are similar to those implicitly recommended by Stewart et al. (2001) and Bommer and Acevedo (2004) .

Table 4.3: Bounds on the implicit causal parameters of prospective ground motions for scenario-based ground motion selection

Causal parameters	Lower limit	Upper limit
Magnitude, M_w=5.5, 6.0, 6.5, 7.0, 7.5, 8.0	$M_w - 0.5$	$M_w + 0.5$
Site condition, V_{s30}(m/s) =200, 400, 800	$0.5V_{s30}$	$1.5V_{s30}$
Source-to-site distance, R_{rup}(km)=5, 15	0 km	30 km
Source-to-site distance, R_{rup}(km)=30, 50, 80, 120	$0.5R_{rup}$ km	$1.5R_{rup}$ km

For each of the 78 scenarios in Table 4.2, it is beneficial to understand the number of ground motions that will be available for ground motion selection before and after the abovementioned bounds are applied. Table 4.4 presents the number of available records, N_{rec}, from the NGA-West1 database (Chiou et al., 2008) for the considered scenarios after application of the bounds presented in Table 4.3. It is noted that since the ground motion time series in the NGA-West2 database (Ancheta et al., 2013) were not available at the time of this study, the NGA-West1 was adopted as the prospective database unless otherwise noted. Based on the available information on various characteristics of the recorded ground motions, a total of 3222 ground motions from the NGA-West1 database are utilised here for each of the considered scenarios (before the application of causal parameter bounds). As shown in Table 4.4, the number of ground motions after the appli-

cation of causal parameter bounds for the V_{s30}=400 m/s site condition (*i.e.,* V_{s30} range from 200 to 600 m/s) is greater than that for the V_{s30}=200 and 600 m/s site conditions (*i.e.,* V_{s30} range from 100 to 300 and 400 to 1200 m/s, respectively).

Table 4.4: Number of available ground motion records (N_{rec}) from the NGA-West1 database based on the applied bounds for scenario-based ground motion selection cases

Site condition V_{s30}=200 m/s						
scenario	R_{rup}=5	R_{rup}=15	R_{rup}=30	R_{rup}=50	R_{rup}=80	R_{rup}=120
M_w=5.5	86	86	-	-	-	-
M_w=6.0	66	66	108	-	-	-
M_w=6.5	93	93	104	201	-	-
M_w=7.0	68	68	48	54	55	-
M_w=7.5	22	22	30	47	119	119
M_w=8.0	20	20	30	39	105	93
Site condition V_{s30}=400 m/s						
scenario	R_{rup}=5	R_{rup}=15	R_{rup}=30	R_{rup}=50	R_{rup}=80	R_{rup}=120
M_w=5.5	292	292	-	-	-	-
M_w=6.0	268	268	409	-	-	-
M_w=6.5	234	234	349	667	-	-
M_w=7.0	145	145	143	195	210	0
M_w=7.5	97	97	77	173	285	280
M_w=8.0	76	76	59	126	211	152
Site condition V_{s30}=800 m/s						
scenario	R_{rup}=5	R_{rup}=15	R_{rup}=30	R_{rup}=50	R_{rup}=80	R_{rup}=120
M_w=5.5	128	128	-	-	-	-
M_w=6.0	134	134	210	-	-	-
M_w=6.5	124	124	204	445	-	-
M_w=7.0	68	68	68	83	89	-
M_w=7.5	76	76	47	124	171	127
M_w=8.0	61	61	40	109	147	95

In order to compare the effect of using narrower causal parameter bounds on the number of available ground motions, the magnitude bound recommended in Bommer and Acevedo (2004), *i.e.,* $\pm 0.2 M_w$ units from the scenario magnitude, is used to obtain the number of available ground motions for the considered scenarios (while the R_{rup} and V_{s30} bounds are the same as used earlier). Table 4.5 presents the result of applying this narrow bound for all of the considered scenarios, which illustrates that the number of available ground motions is restrictively small for most of the considered rupture scenarios, with the average number of available motions being only 43% of those using the $\pm 0.5 M_w$ bound. As illustrated later in Figure 4.4, ground motions selected based on such a small number of prospective motions may have a poor representation of the target IM distributions, because the narrow causal parameter bounds remove ground motions that can still appropriately represent the target scenario hazard.

In contrast to the results presented in Table 4.5, Table 4.4 illustrated that utilising 'wide' bounds on the causal parameters avoids an unreasonably small number of prospective ground motions for most of the considered scenario ruptures, with the exception of large magnitude ruptures (*i.e.,* $M_w 7.5$ and $M_w 8$) with very short source-to-site distances (*e.g.,* R_{rup}=5 and 15km) on soft soil (*i.e.,* V_{s30}=200 m/s), where few observations exist. Based on Table 4.4 and 4.5 as well as the results presented by Tarbali and Bradley (2014a) the specific bounds presented in Table 4.3 are used in this study to select ground motion ensembles for scenario SHA. In regard to the above, it is important to note that the GCIM-based ground motion selection methodology uses multiple explicit IMs in order to account for various aspects of ground motions (*i.e.,* amplitude, frequency content, duration, and cumulative effects), therefore, bounds on the causal parameters do not need to be overly restrictive.

Table 4.5: Number of available ground motion records (N_{rec}) from the NGA-West1 database based on the R_{rup} and V_{s30} bounds presented in Table 3 with a narrower M_w bound based on Bommer and Acevedo (2004) (*i.e.,* $[M_w - 0.2, M_w + 0.2]$

Site condition V_{s30}=200 m/s						
scenario	R_{rup}=5	R_{rup}=15	R_{rup}=30	R_{rup}=50	R_{rup}=80	R_{rup}=120
M_w=5.5	12	12	-	-	-	-
M_w=6.0	41	41	73	-	-	-
M_w=6.5	54	54	50	88	-	-
M_w=7.0	23	23	21	17	19	-
M_w=7.5	20	20	30	46	113	95
M_w=8.0	0	0	0	0	0	0
Site condition V_{s30}=400 m/s						
scenario	R_{rup}=5	R_{rup}=15	R_{rup}=30	R_{rup}=50	R_{rup}=80	R_{rup}=120
M_w=5.5	55	55	-	-	-	-
M_w=6.0	187	187	294	-	-	-
M_w=6.5	109	109	175	296	-	-
M_w=7.0	52	52	45	57	79	-
M_w=7.5	77	77	60	141	228	158
M_w=8.0	1	1	1	3	4	5
Site condition V_{s30}=800 m/s						
scenario	R_{rup}=5	R_{rup}=15	R_{rup}=30	R_{rup}=50	R_{rup}=80	R_{rup}=120
M_w=5.5	26	26	-	-	-	-
M_w=6.0	98	98	150	-	-	-
M_w=6.5	43	43	91	151	-	-
M_w=7.0	32	32	26	38	50	-
M_w=7.5	64	64	40	110	148	96
M_w=8.0	0	0	0	0	0	0

4.3.3 Explicit intensity measures and the weight vectors considered

Within the framework of the GCIM methodology for ground motion selection, the following explicit IMs are considered: spectral acceleration for 18 vibration periods (T=0.05, 0.075, 0.1, 0.15, 0.2, 0.25, 0.3, 0.4, 0.5, 0.75, 1.0, 1.5, 2.0, 3.0, 4.0, 5.0, 7.5, and 10.0 s); peak ground acceleration (PGA); peak ground velocity (PGV); acceleration spectrum intensity (ASI); spectrum intensity (SI); displacement spectrum intensity (DSI); cumulative absolute velocity (CAV); and 5-75% and 5-95% Significant Durations (D_{s575} and D_{s595}, respectively). These IMs represent various aspects of ground motion severity: amplitude, frequency content, duration, and cumulative effects. The marginal distributions of these IMs for the considered rupture scenarios are obtained based on empirical ground motion models (GMMs), namely: Boore and Atkinson (2008) for SA, PGA, and PGV; Bradley (2010c) for ASI; Bradley et al. (2009) for SI; Bradley (2011c) for DSI; Campbell and Bozorgnia (2010) for CAV; and Bommer et al. (2009) for D_{s575} and D_{s595}. Correlations between these IMs are considered based on existing empirical models (Baker and Jayaram, 2008; Bradley, 2011b,c; Bradley et al., 2009; Bradley, 2012b, 2011a, 2012a).

As mentioned previously, causal parameters bounds are generally considered in ground motion selection in order to implicitly account for the different aspects of ground motions that are not represented by using only SA ordinates in the selection process. In order to illustrate the shortcomings of this approach, ground motion ensembles are first selected with and without causal parameter bounds based on considering only SA ordinates in the weight vector of the GCIM method. This weight vector is denoted as 'SA only' in Table 4.6. The effect of the GCIM weight vector on the characteristics of selected ground motions are discussed thoroughly by Bradley (2012c) and Tarbali and Bradley (2014a, 2015b), based on which the recommended weight vector implemented in this study contains IMs that represent amplitude, frequency content, duration, and cumulative

effects of grounds motion, denoted as the 'generic' weight vector in Table 4.6.

Table 4.6: Weight vectors considered for ground motion selection

Weight vector	Amplitude and frequency content	Duration		Cumulative effects
	Spectral ordinates	D_{s575}	D_{s595}	CAV
SA only	1.0[1]	0.0	0.0	0.0
Generic	0.7[1]	0.1	0.1	0.1

[1]Evenly distributed over 18 *SA* ordinates, *e.g.,* each SA ordinates has a weight of w_i =0.7/18 in the generic weight vector.

4.3.4 Characteristics of the selected ground motion ensembles

In this section, the explicit IM distributions of the selected ground motions with and without the application of causal parameter bounds are compared with the target GCIM distribution for the corresponding rupture scenarios. In addition, the distribution of implicit causal parameters of the selected ground motions (specifically, M_w, R_{rup}, and V_{s30}) are compared with those of the target scenario. A total of 20 ground motions are selected by conducting 10 replicate selections. More details regarding the number of replicate selections corresponding to the size of the ground motion ensemble are presented by Tarbali and Bradley (2014a, 2015b).

4.3.4.1 Explicit intensity measures of selected ground motions—selection based on only SA ordinates

In order to illustrate the inadequacy of using causal parameter bounds to account for the shortcomings of selecting ground motions based on only SA ordinates, ground motion selection for the considered scenarios (see Table 4.2) is conducted with and without bounds based on only SA ordinates in the weight

vector (see Table 4.6 for 'SA only' weight vector). Because ground motions are selected specifically to match the target SA ordinates then the selected ground motions have an appropriate representation of the target SA distribution for the whole range of vibration period considered (*i.e.,* 0.05-10 s), and thus omitted for brevity. Figure 4.2 presents example results for the CAV and D_{s595} distribution of selected ground motions for several scenarios.

Across the six example distributions shown Figure 4.2 it can be seen that in some cases the use of bounds makes no appreciable difference (e.g. Figure 4.2a, e, f); leads to mild improvement (*e.g.,* Figure 4.2c); or results in a poorer empirical distribution (*e.g.,* Figures 4.2b, d) relative to the target distribution. In summary, comparing the selected motions based on the use of causal parameter bounds with the target CAV and D_{s595} distributions, it is clear that using causal parameter bounds cannot resolve the bias in distribution of these IMs of the selected ground motions. Although not presented here for brevity, bias is also evident in distribution of the other IMs such as D_{s575} for various scenarios.

The results presented in Figure 4.2 for sample rupture scenarios and site conditions illustrate that considering causal parameter bounds cannot strictly resolve the bias in distribution of IMs other than SA ordinates when ground motion selection is based solely on SA ordinates. As discussed thoroughly by Bradley (2012c) and Tarbali and Bradley (2014a, 2015b), in order to avoid bias in the distribution of IMs that represent different aspects of ground motions, they need to be explicitly considered in the selection process by using an appropriate weight vector such as the 'generic' weight vector implemented in this study, as discussed in the next section.

4.3.4.2 Explicit intensity measures of selected ground motions—selection based on SA, duration, and cumulative effects

This section examines the effect of causal parameter bounds for ground motions selected based on the generic weight vector (see Table 4.6), which considers

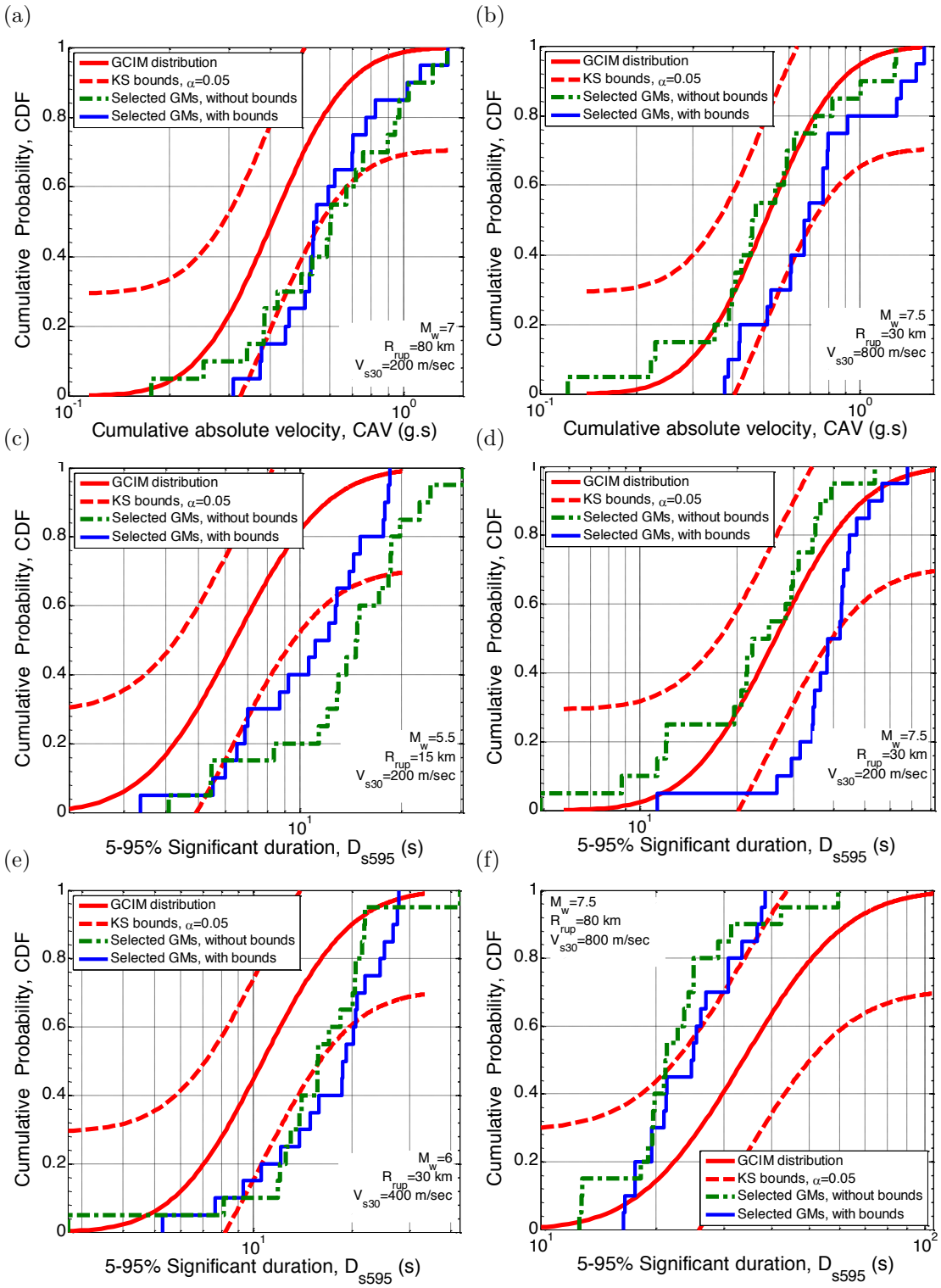

Figure 4.2: Bias in distribution of CAV and D_{s595} for different sample scenarios when ground motions are selected based on only SA ordinates and bounds are applied on the implicit causal parameters of prospective ground motions. Bias (at the $\alpha = 0.05$ significance level) is indicated when the empirical distribution of the selected motions lies outside the KS bounds of the target GCIM distribution.

IMs for duration and cumulative effects along with the SA ordinates in the selection process. Figure 3 presents the characteristics of the ground motions selected for a sample scenario with M_w =6.5, R_{rup} =30 km, and V_{s30} =200 m/s. A total of N_{rec} =104 records are available for this specific scenario (as shown in Table 4.4) after the application of bounds, compared to 3222 available records when no bounds is applied, hence this scenario is an example where a relatively large number of prospective ground motions are available after the application of causal parameter bounds. Figures a-b present the acceleration response spectra of the individual ground motions selected without and with the application of causal parameter bounds along with the corresponding median, 16^{th}, and 84^{th} percentiles spectra representing the target SA distribution of the scenario. As illustrated in Figures 4.3a-b, using bounds on the causal parameters does not degrade the conformity of the selected ground motions to the target SA distribution. In addition, Figure 4.3c illustrates that the consideration of causal parameter bounds does not have a negative effect on the D_{s595} distribution of the selected ground motions (nor the distributions of other non-SA IMs). Figure 4.3d presents the amplitude scaling factors of the selected ground motions with and without the application of causal parameter bounds. As shown, ground motions with smaller amplitude scaling factors are selected when causal parameter bounds are utilized in comparison to those obtained without the use of bounds. This is due to the fact that by restricting the prospective ground motions to motions with causal parameters similar to characteristics of the considered scenario, only a small change in amplitude of the as-recorded motions is required in order to represent the IM distributions for the considered scenario. As shown, most of the selected ground motions when using causal parameter bounds have a scaling factor within 0.3 to 3.0 range, which is similar to the desirable scaling range in seismic design guidelines (NZS1170.5, 2004; ASCE/SEI7-10, 2010).

Since the number of available ground motions for the M_w=6.5, R_{rup}=30 km, and V_{s30}=200 m/s scenario discussed in the previous paragraph was reasonably large (*i.e.,* N_{rec}=104), the selected ground motion based on causal parameter

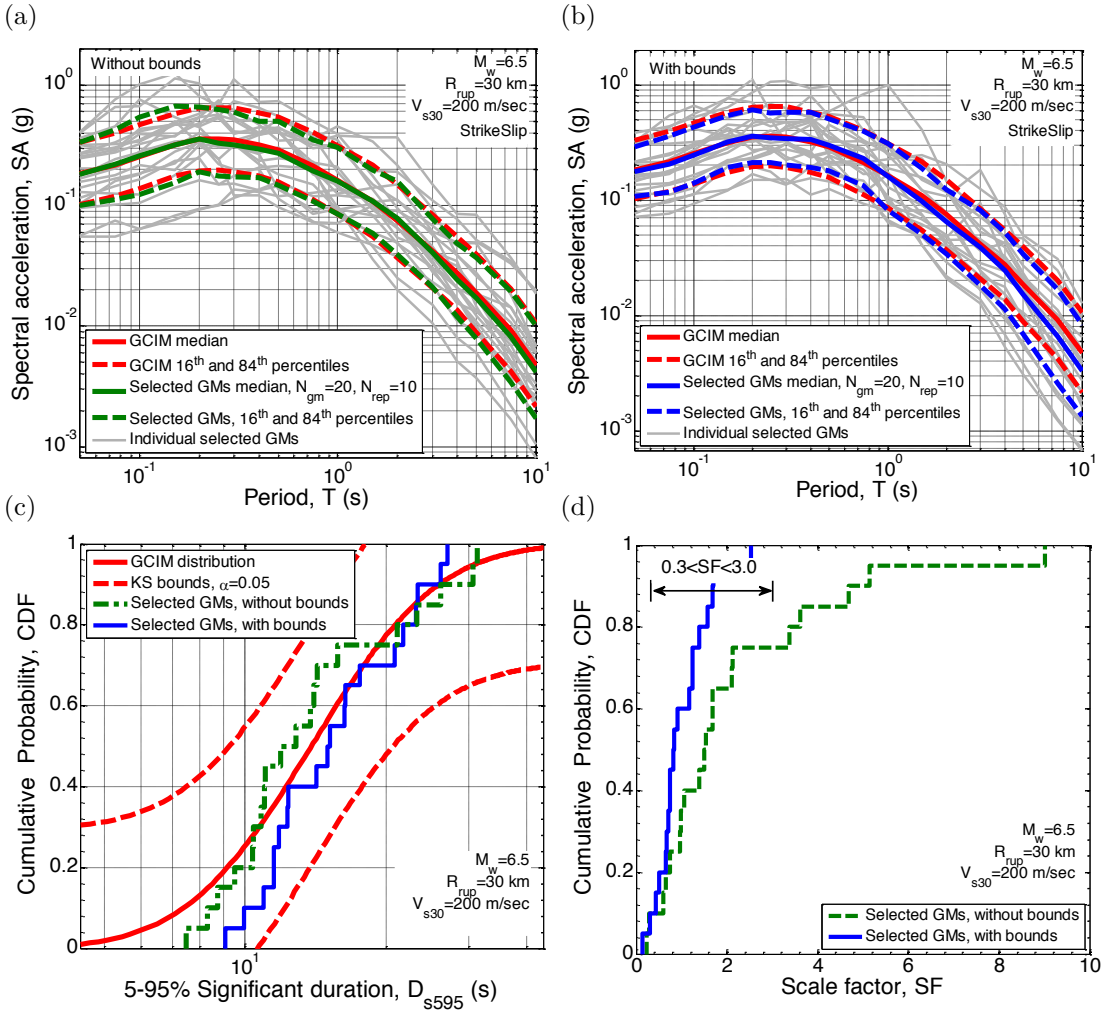

Figure 4.3: Properties of selected ground motions representing the M_w=6.5, R_{rup}=30 km, and V_{s30}=200 m/s scenario without and with the application of causal parameter bounds: (a) SA ordinates without bounds; (b) SA ordinates with bounds; (c) cumulative distribution of D_{s595}; (d) cumulative distribution of amplitude scaling factors.

bounds appropriately represent the target distribution of the considered IMs (Figure 4.3) and provide improved amplitude scale factors (*i.e.,* closer to 1.0) than the selected motions without the use of causal parameter bounds. In contrast to the results presented in Figure 4.3, Figure 4.4 illustrates the characteristics of the selected ground motions to represent another scenario with M_w =7.5, R_{rup} =30 km, and V_{s30} =200 m/s, as an example among the scenarios for which there are relatively smaller number of ground motions available after applying bounds on the causal parameters (*i.e.,* N_{rec} =30 for this specific scenario as presented in Table 4.4).

As shown in Figure 4.4a, the selected ground motions obtained without the use of causal parameter bounds do not have a biased representation of the SA or D_{s595} target distributions. However, the selected ground motions based on the use of causal parameter bounds are seen to exhibit bias in representing the target SA distribution across a wide range of vibration periods as well as the D_{s595} and the other IMs considered in the weight vector (i.e. D_{s575} and CAV). The poor representation of the target IM distributions for these selected ground motions can be attributed to the small number of prospective ground motions available after applying bounds on the causal parameters relative to the number of ground motions desired for selection (*i.e.,* N_{rec}=30, of which 20 ground motions are desired), which is elaborated upon subsequently.

4.3.4.3 Overall representation of selected ground motion ensembles for all scenarios considered

The results presented in Figure 4.3 and 4.4 illustrate the general trends relating to the characteristics of selected ground motions representing scenarios with large and small number of ground motions available after applying bounds on the causal parameters. In order to have an overall view on the obtained results for all of the considered scenario ruptures and site conditions, the global misfit of selected ground motion ensembles with and without bounds are compared in

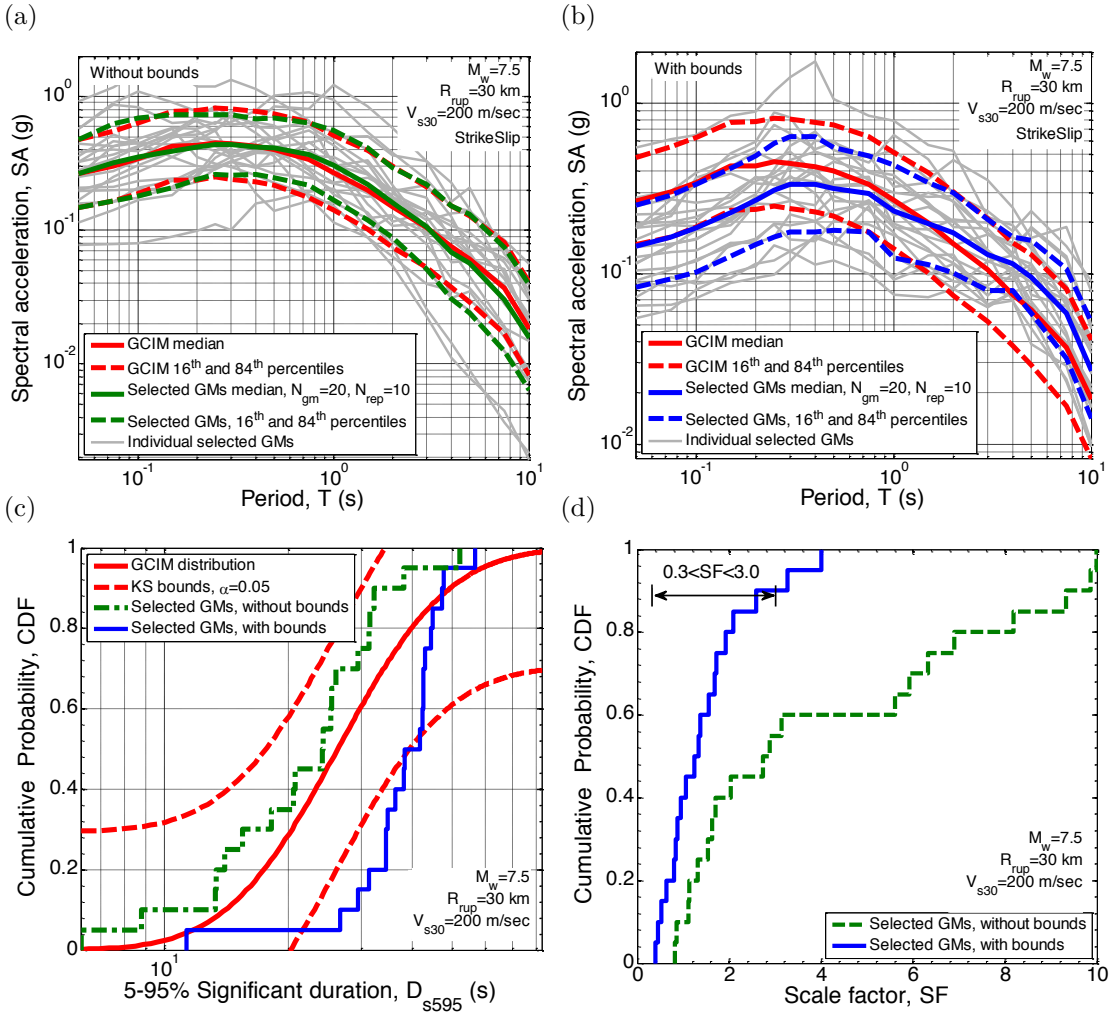

Figure 4.4: Properties of selected ground motions representing the M_w=7.5, R_{rup}=30 km, and V_{s30}=200 m/s scenario without and with the application of causal parameter bounds: (a) SA ordinates without bounds; (b) SA ordinates with bounds; (c) cumulative distribution of D_{s595}; (d) cumulative distribution of amplitude scaling factors.

Figure 4.5 for each of the three different site conditions considered. As mentioned previously, the global misfit, R, indicates the consistency between the IM distributions of the selected ground motions and the target distribution based on the assigned weight on the IMs considered in the selection process.

It can be seen that for all three site conditions, for $M_w \leq 7.0$ there is practically no difference between the global misfit with or without bounds (*i.e.,* the use of bounds does not lead to a degradation in the obtained ground motions with respect to the target IM distributions). In contrast, it can be seen that for the M_w7.5 and 8.0 scenarios the misfit for the selected motions when considering causal parameter bounds increases. This is most pronounced for the V_{s30}=200 m/s site condition, which has the smallest number of prospective ground motions (*i.e.,* Table 4.4), and least pronounced for the V_{s30}=400 m/s site condition, which has the most prospective motions.

By comparing the global misfit values for the M_w8.0 and 7.5 rupture scenarios with V_{s30} =200 m/s site condition (*i.e.,* Figure 4.5a), it can be seen that the global misfits of selected motions for the M_w7.5 rupture scenarios are higher than those for M_w8.0 scenarios, which may be initially counter-intuitive. This is caused by a large bias in the D_{s575} and D_{s595} distributions of selected ground motions compared to the target distribution. This principally occurs because the available ground motions after applying bounds for the M_w7.5 events (*i.e.,* bounds of M_w=7.0-8.0 are predominantly from events with M_w>7.5 (so their D_{s575} and D_{s595} values are greater than the predicted distribution for M_w7.5 rupture scenarios). This is shown in Figure 4.4c, for example, where the median D_{s595} value of the selected ground motions is considerably larger than the median value of the target GCIM distribution. In contrast, ground motions from larger events in the M_w=7.5-8.5 are more suitable for the M_w8.0 rupture scenario, hence a smaller global misfit value for ground motion ensembles selected for M_w8.0 scenarios in Figure 4.5a.

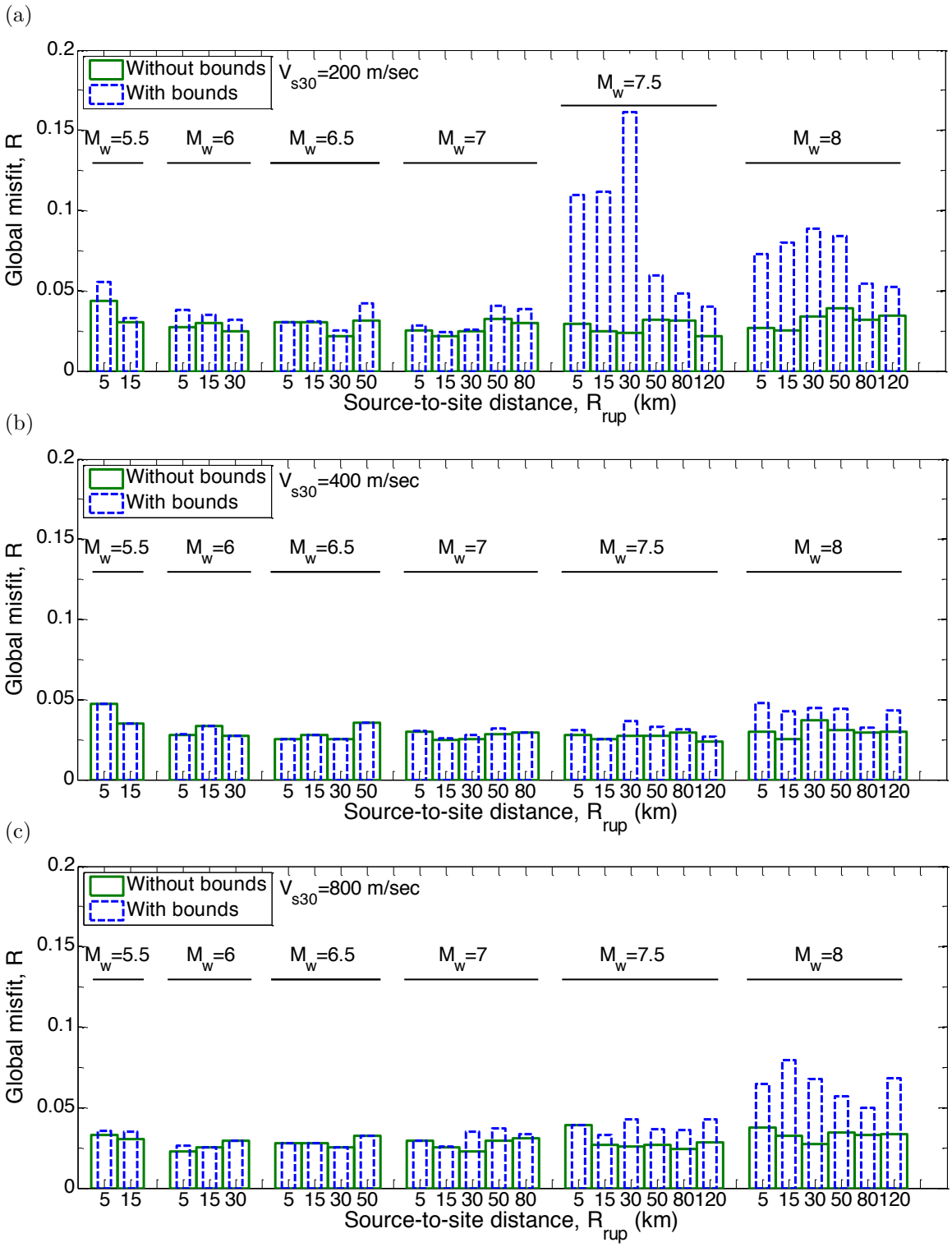

Figure 4.5: Global misfit of selected ground motion ensembles representing all of the considered rupture scenarios for three site conditions: (a) V_{s30}=200; (b) V_{s30}=400; and (c) V_{s30}=800 m/s.

4.3.4.4 Supplementing the NGA-West1 database with large magnitude recordings

In order to further examine the bias in the distribution of selected ground motions for M_w7.5 rupture scenarios when causal parameter bounds are applied, a few available ground motions from the NGA-West2 database (Ancheta et al., 2013) that are within the causal parameters bounds for M_w=7.5 rupture scenarios are added to the database of prospective ground motions. Table 4.7 compares the number of ground motions before and after adding ground motions to the NGA-West1 database (*i.e.,* extended database) for M_w7.5 rupture scenarios. Using the extended database, ground motions are once again selected for M_w7.5 rupture scenarios with V_{s30} =200, 400, and 800 m/s site conditions.

Table 4.7: Number of available ground motion records (N_{rec}) for M_w7.5 scenario ruptures from the NGA-West1 and the extended databases after the application of the causal parameter bounds

Site condition V_{s30}=200 m/s							
	scenario	R_{rup}=5	R_{rup}=15	R_{rup}=30	R_{rup}=50	R_{rup}=80	R_{rup}=120
NGA-West1	M_w=7.5	22	22	30	47	119	119
Extended database	M_w=7.5	60	60	66	135	234	249
Site condition V_{s30}=400 m/s							
scenario	R_{rup}=5	R_{rup}=15	R_{rup}=30	R_{rup}=50	R_{rup}=80	R_{rup}=120	
NGA-West1	M_w=7.5	97	97	77	173	285	280
Extended database	M_w=7.5	143	143	122	239	367	429
Site condition V_{s30}=800 m/s							
scenario	R_{rup}=5	R_{rup}=15	R_{rup}=30	R_{rup}=50	R_{rup}=80	R_{rup}=120	
NGA-West1	M_w=7.5	76	76	47	124	171	127
Extended database	M_w=7.5	84	84	58	143	213	210

Figure 4.6 illustrates the characteristics of selected ground motions based on the extended database representing the M_w=7.5, R_{rup}=30 km, V_{s30}=200 m/s scenario, as an example among others. As presented in Table 4.7, the number of available ground motions for this specific scenario has been increased from 30 to

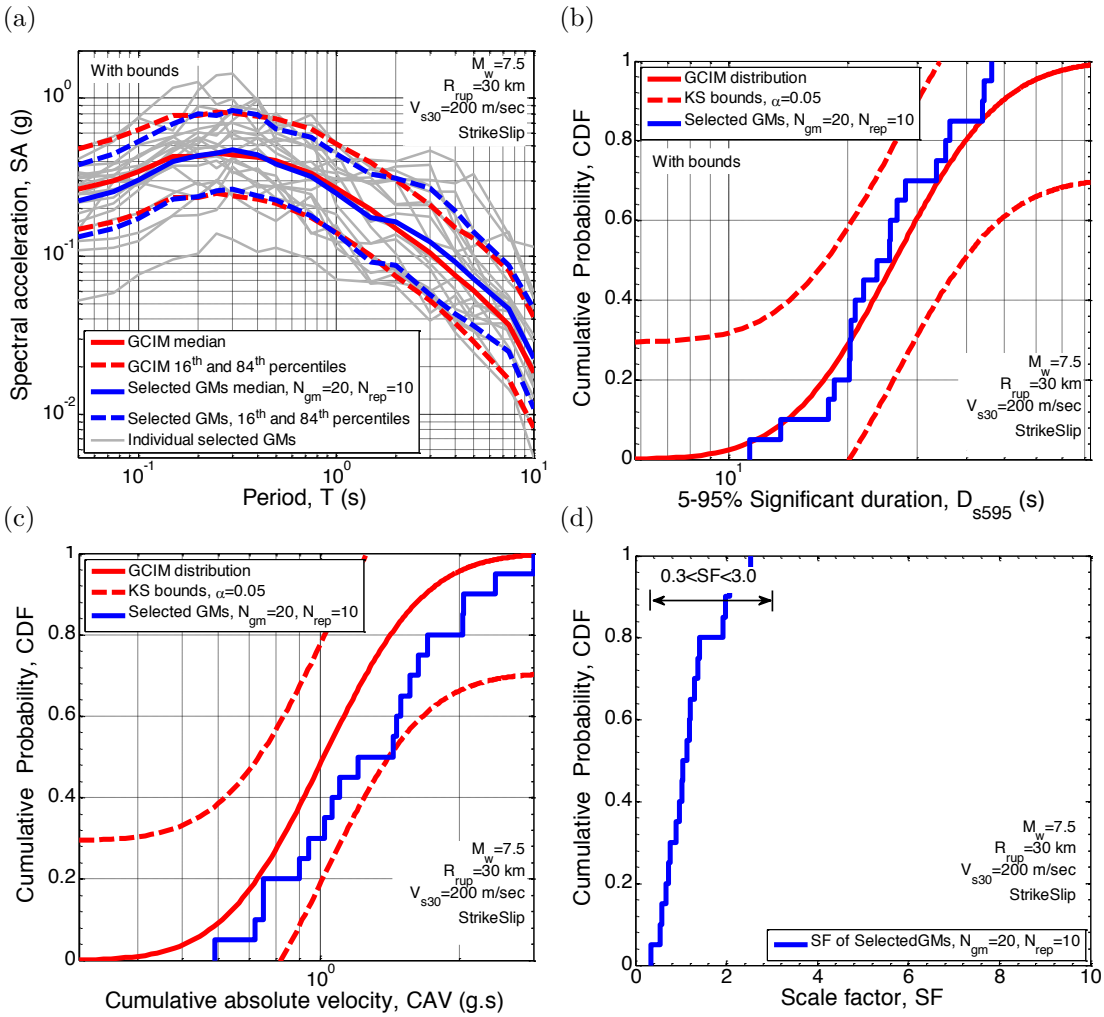

Figure 4.6: Properties of selected ground motions for M7.5R30V200 scenario with causal parameters bounds on the after adding extra ground motions from the NGA-West2 database: (a) SA ordinates; (b) D_{s595}; (c) CAV; (d) amplitude scaling factors.

66. By comparing the results in Figure 4.6 with those presented in Figure 4.4 for the same scenario with the original NGA-West1 database, it can be seen that the additional prospective ground motions now lead to a subset of 20 selected ground motions without the bias in the distribution of SA ordinates and other considered IMs (*i.e.*, CAV, D_{s595}, and D_{s575}). Also, the amplitude scaling factors of all of the selected ground motions are within 0.3 to 3.0 range.

In order to obtain an overall view on the effect of adding extra ground motions within the considered bounds for the M_w7.5 scenarios, Figure 4.7 compares the

global misfits of the ground motions selected before and after extending the NGA-West1 database for M_w7.5 rupture scenarios (at 6 R_{rup} values) with V_{s30} =200, 400, and 800 m/s site conditions. As shown in Figure 4.7, the global misfit of selected ground motions based on causal parameter bounds have decreased, most significantly for the V_{s30} = 200 m/s site condition. These reductions are consistent with the increase in the size of the prospective ground motions after the application of causal parameter bounds (*i.e.,* Table 4.7), and clearly illustrate that the ability to obtain a set of selected ground motions with appropriate IM distributions (as reflected in the global misfit, R) is directly related to the number of prospective motions after the application of the causal parameter bounds relative to the number of desired ground motions. Based on the results presented here (*i.e.,* for 20 desired ground motions) it is recommended that the number of prospective motions after the application of causal parameter bounds should be at least three times the desired number of ground motions (*e.g.,* a minimum of 60 prospective motions if 20 selected motions are desired). If the use of a causal parameter bounds results in a small number of prospective ground motions relative to this factor of 3, then it is advised that the bound criteria are relaxed in order to avoid the selection of mis-representative ground motions (*e.g.,* Figure 4.4).

Table 4.8 presents the available ground motions for the considered scenarios in this study from both the NGA-West1 and NGA-West2 databases. As illustrated in Table 4.8, the number of available ground motions for scenarios with $M_w \leq$7.5 for the three site conditions considered has significantly increased. However, for M_w8.0 scenarios with V_{s30}=200 and 800 m/s site conditions, the NGA-West2 database is still not well-constrained.

4.3.4.5 Implicit causal parameters of selected ground motions

In addition to the distribution of explicit IMs discussed above, considering bounds on the causal parameters affects the causal parameter distribution of the selected ground motions, which is worthy of investigation. Figure 4.8 presents the

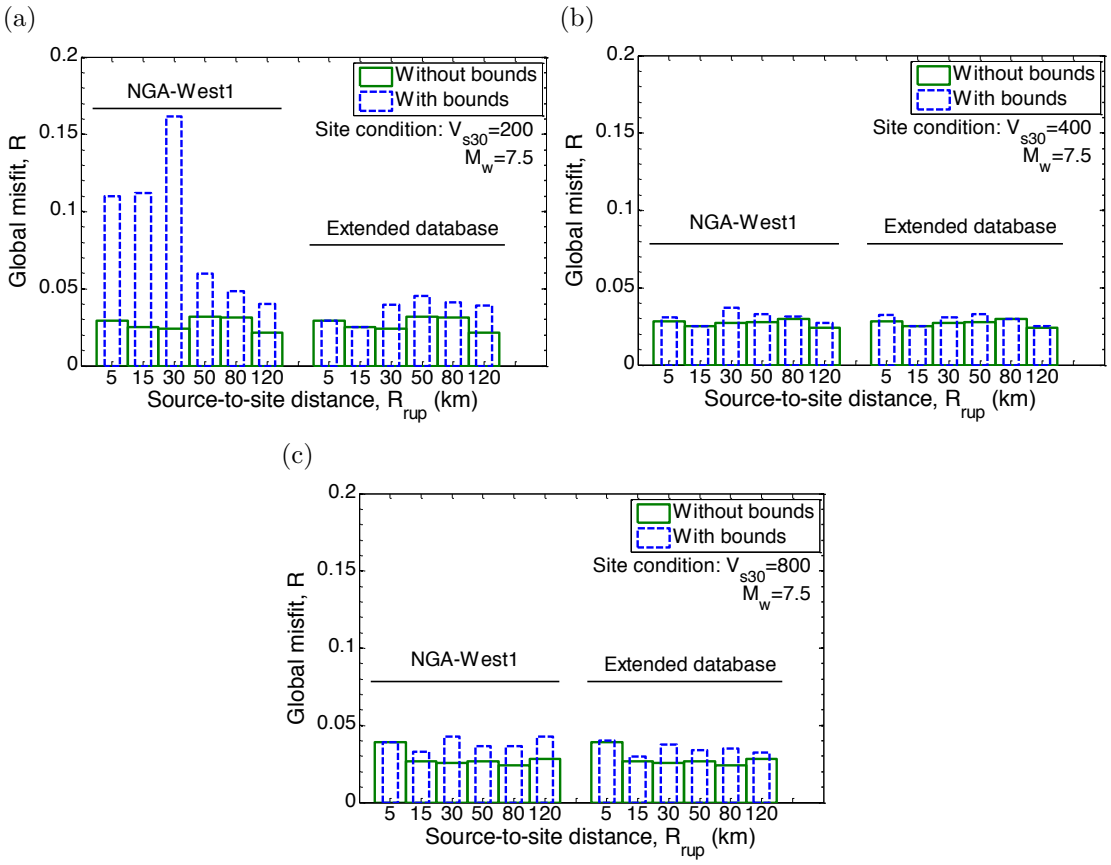

Figure 4.7: Global misfit of selected ground motions for M_w7.5 scenario ruptures based on the NGA-West1 and extended databases for the three considered site conditions: (a) V_{s30}=200 m/s; (b) V_{s30}=400 m/s; (c) V_{s30}=800 m/s.

Table 4.8: Comparison between the number of available ground motion records (N_{rec}) from the NGA-West1 and NGA-West2 databases based on the applied bounds for scenario-based ground motion selection cases considered

Site condition V_{s30}=200 m/s							
Scenario	NGA-West #	R_{rup}=5	R_{rup}=15	R_{rup}=30	R_{rup}=50	R_{rup}=80	R_{rup}=120
M_w=5.5	1	86	86	-	-	-	-
	2	146	146	-	-	-	-
M_w=6.0	1	66	66	108	-	-	-
	2	116	116	142	-	-	-
M_w=6.5	1	93	93	104	201	-	-
	2	187	187	173	305	-	-
M_w=7.0	1	68	68	48	54	55	-
	2	137	137	121	149	184	-
M_w=7.5	1	22	22	30	47	119	119
	2	60	60	67	79	144	142
M_w=8.0	1	20	20	30	39	105	93
	2	21	21	30	42	113	99
Site condition V_{s30}=400 m/s							
scenario	R_{rup}=5	R_{rup}=15	R_{rup}=30	R_{rup}=50	R_{rup}=80	R_{rup}=120	
M_w=5.5	1	292	292	-	-	-	-
	2	575	575	-	-	-	-
M_w=6.0	1	268	268	409	-	-	-
	2	446	446	573	-	-	-
M_w=6.5	1	234	234	349	667	-	-
	2	458	458	544	1001	-	-
M_w=7.0	1	145	145	143	195	210	-
	2	284	284	305	470	659	-
M_w=7.5	1	97	97	77	173	285	280
	2	164	164	135	264	408	475
M_w=8.0	1	76	76	59	126	211	152
	2	92	92	71	150	250	196
Site condition V_{s30}=800 m/s							
scenario	R_{rup}=5	R_{rup}=15	R_{rup}=30	R_{rup}=50	R_{rup}=80	R_{rup}=120	
M_w=5.5	1	128	128	-	-	-	-
	2	271	271	-	-	-	-
M_w=6.0	1	134	134	210	-	-	-
	2	231	231	282	-	-	-
M_w=6.5	1	124	124	204	445	-	-
	2	243	243	331	630	-	-
M_w=7.0	1	68	68	68	83	89	-
	2	145	145	172	243	347	-
M_w=7.5	1	76	76	47	124	171	127
	2	101	101	68	153	239	246
M_w=8.0	1	61	61	40	109	147	95
	2	73	73	50	119	171	129

$M_w - R_{rup}$ distribution of the selected ground motions representing four sample scenarios as noted in the figure insets. Due to the large number of considered rupture scenarios, the presented results depicted here were chosen to illustrate the trend in all of the considered cases. Figure 4.8a provides an example for scenarios with very small source-to-site distances (*i.e.,* 5 and 15 km), in which it can be seen that the R_{rup} values of the selected ground motions without bounds are distributed over a wide range and are mostly larger than that of the target scenario, whereas it can be seen that the application of causal parameter bounds leads to an improved representation of the target R_{rup} values (and also a minor improvement in the M_w distribution). In general, having a small number of prospective ground motions in the near-fault region prevents from selecting ground motions that closely encompass the target scenario R_{rup}.

Figure 4.8b compares the M_w-R_{rup} distribution of the selected ground motions without and with bounds for the M_w=6.5, R_{rup}=50 km, V_{s30}=400 m/s scenario, as an example for scenarios with large number of ground motions after the application of causal parameter bounds (*i.e.,* N_{rec}=667 for this specific scenario as presented in Table 4.4). As shown in Figure 4.8b, the causal parameters of the selected ground motions can appropriately represent the target scenario causal parameters, with mean R_{rup} and M_w values close to the target scenario characteristics. It is noted that for ground motions selected without bounds, the R_{rup} and M_w values of the selected motions are distributed over a very wide range as shown in Figure 4.8b (*i.e.,* M_w =[5.5, 7.6]; and R_{rup}=[0.2, 200]), whereas the ground motions selected based on the bounds are distributed in a narrower range around the scenario parameters.

As an example for scenarios with large magnitudes (*i.e.,* $M_w \leq 7.5$) and large source-to-site distances (*i.e.,* $R_{rup} \geq$80), Figure 4.8c shows the M_w-R_{rup} distribution of the selected ground motions for the M_w=7.5, R_{rup}=120 km, V_{s30}=400 m/s scenario. As illustrated, ground motions selected after applying bounds have a significantly improved representation of the M_w and R_{rup} value of the target scenario. As illustrated in Figures 4.8a-c, ground motions selected based on bounds

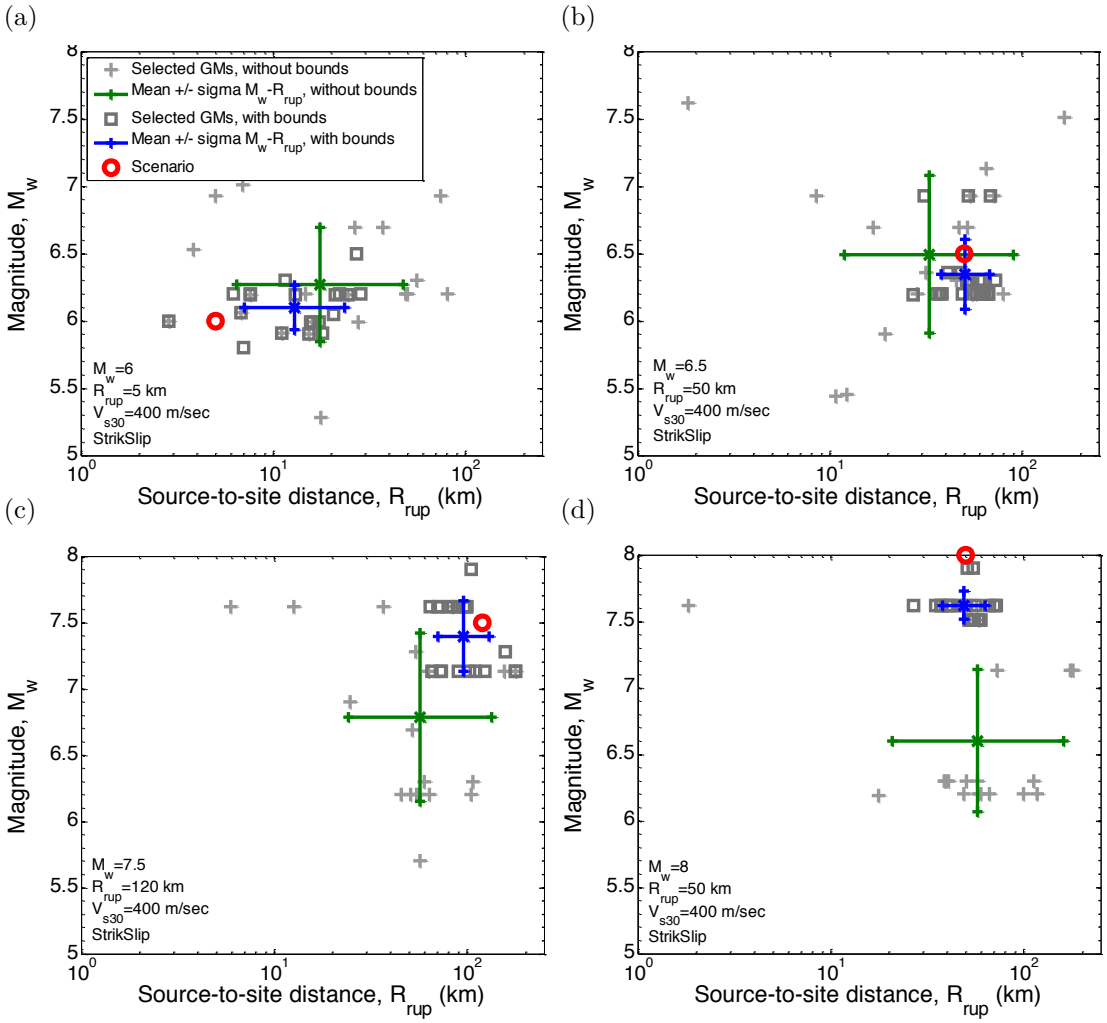

Figure 4.8: Comparison between M_w-R_{rup} distribution of selected ground motions with and without bounds for sample scenarios (scenario details shown in figure insets).

for scenarios with $M_w \leq 7.5$ have an appropriate representation of the target scenario magnitude. In contrast, as shown in Figure 4.8d for scenarios with very large rupture magnitude (*e.g.,* M_w=8.0), the causal magnitudes of the selected ground motions are mostly below the target scenario magnitude due to a paucity of recorded ground motions from events with such large magnitudes.

In order to compare the site condition of selected ground motions with and without the application of bounds on the causal parameters, Figure 4.9 presents the V_{s30}-R_{rup} distribution of the selected ground motions for M_w=7.0, R_{rup}=50 km scenario ruptures, as an example among others, with V_{s30}=200, 400, and 800 m/s site conditions. As shown in Figure 4.9a for soft soil conditions (*i.e.,* V_{s30}=200 m/s), the selected ground motions without bounds have V_{s30} values distributed over a wide range, with ground motions recorded on rock (*i.e.,* V_{s30} ≥800 m/s) being selected. In contrast, when bounds are applied on the causal parameters, the V_{s30} values of the selected ground motions are consistent with the considered site condition (see Figure 4.9a). This also holds true for stiff soil deposit (*i.e.,* V_{s30}=400 m/s) as shown in Figure 4.9b, although the selected ground motions without the consideration of bounds have a more reasonable V_{s30} distribution compared to that for the V_{s30}=200 m/s site condition because of the larger number of prospective ground motions recorded on stiff soil deposits. Figure 9c illustrates that the ground motions selected for the soft rock site have V_{s30} values below that of the target site (V_{s30}=800 m/s). While the use of causal parameter bounds on V_{s30} improves the distribution of V_{s30} values of the selected ground motions, they are still, on average, below 800 m/s simply because of the paucity of as-recorded ground motions on rock conditions.

4.3.4.6 Magnitude-distance-site class distributions of the NGA-West1 and NGA-West2 databases

In order to compare the site class distribution in empirical ground motion databases for different site conditions, Table 4.9 presents the number of available

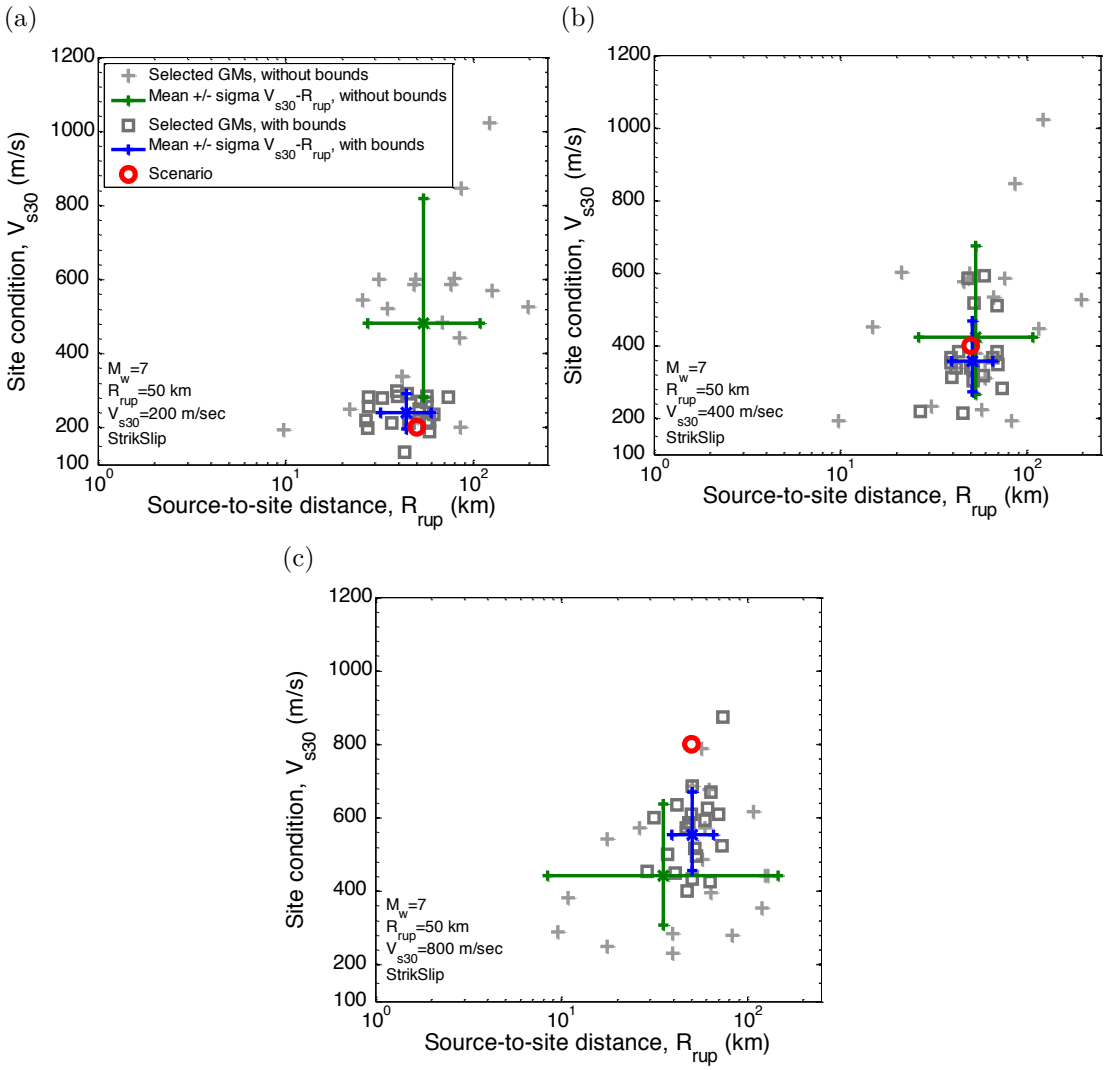

Figure 4.9: Comparison between V_{s30}-R_{rup} distribution of selected ground motions with and without bounds representing a M_w=7-R_{rup}=50 km sample scenario with three site conditions: (a) V_{s30}=200 m/s; (b) V_{s30}=400 m/s; (c) V_{s30}=800 m/s.

ground motions in the NGA-West1 and NGA-West2 databases for four site classes (*i.e.,* A/B, C, D, and E) based on the NEHRP (2003) guidelines. As presented in Table 4.9, ground motions recorded on site class A/B (*i.e.,* V_{s30} ≥760 m/s) and site class E (*i.e.,* V_{s30} ≤180 m/s) represent very small portions of these empirical ground motion databases. On the other hand, it can be seen that a significant improvement in the number of as-recorded ground motions for site class A/B and also site classes C and D has taken place in the NGA-West2 database compared to the NGA-West1 database.

Table 4.9: Number of available ground motions in the NGA-West1 and NGA-West2 databases within the NEHRP (2003) site classes for the whole range of M_w and R_{rup}

	Site class E V_{s30}=(0,180]	Site class D V_{s30}=(180,360]	Site class C V_{s30}=(360,760]	Site class A/B V_{s30}=[760, inf)
NGA-West1*	54 (<2%)	1665 (52%)	1427 (44%)	79 (<2%)
NGA-West2**	196 (<1%)	6827 (32%)	13234 (62%)	1199(6%)

*Based on the flat-file available at `http://peer.berkeley.edu/ngawest/activity_findings.html`

**Based on the flat-file available at `http://ngawest2.berkeley.edu/site/documentation`

Figure 4.10 illustrates the $M_w - R_{rup}$ distribution of the recordings from the NGA-West1 and NGA-West2 databases for three NEHRP (2003) site classes, namely site classes A/B, C, and D (but not E since the number of recordings is small as shown in Table 4.9). As shown in Figure 4.10b, despite the significant growth in the number of recordings, most of the ground motions in the NGA-West2 database with site class A/B have M_w<5.0, which are often not of engineering interest for ground motion selection. Figures 4.10a-b illustrate that ground motions with M_w ≥5.0 from site class A/B are relatively sparse over the whole M_w and R_{rup} range in both databases. In contrast, as shown in Figures 4.10c-f, ground motions recorded on site class C and D cover a large range of M_w and R_{rup} in both databases. Figure 4.10 also illustrates that neither of the NGA databases are well-constrained for ground motions with M_w ≥7.0 in the

near-fault region ($R_{rup} \leq 30$ km). Selecting records from simulated ground motion ensembles (Bradley et al., 2015) can potentially resolve these shortcomings in the empirical databases for ground motion selection once predictive confidence in simulated ground motions is developed through validations (Galasso et al., 2012, 2013).

Comparison between the NGA-West1 and NGA-West2 databases for ground motions with $M_w \geq 5.0$, as presented in Table 4.10, reveals that the number of ground motions for site class A/B has increased from 78 to 297, which provides a notably improved database for conducting ground motion selection for rock sites. Also the number of ground motions with $M_w \geq 5.0$ has increased significantly in the NGA-West2 databases for site class C and D, except in the near-fault region ($R_{rup} \leq 30$ km) for recordings with $M_w \geq 7.0$. As presented in Table 4.8 despite the significant improvement in number of the ground motions in the NGA-West2 database, the number of the available records based on the applied bounds for ground motion selection representing scenario ruptures with $M_w \geq 7.5$ at short-to-moderate source-to-site distances (*i.e.,* $R_{rup} \leq 50$ km) is still small, especially for soft soil and soft rock site conditions (*i.e.,* V_{s30}=200 and 800 m/s).

Table 4.10: Comparison between the number of available ground motions with $M_w \geq 5$ in the NGA-West1 and NGA-West2 databases based on the NEHRP (2003) site classes

	Site class E V_{s30}=(0,180]	Site class D V_{s30}=(180,360]	Site class C V_{s30}=(360,760]	Site class A/B V_{s30}=[760, inf)
NGA-West1*	53 (<2%)	1526 (47%)	1333 (41%)	78 (<2%)
NGA-West2**	191 (<1%)	3422 (<16%)	4540 (21%)	297 (<1%)

*Based on the flat-file available at `http://peer.berkeley.edu/ngawest/activity_findings.html`

**Based on the flat-file available at `http://ngawest2.berkeley.edu/site/documentation`

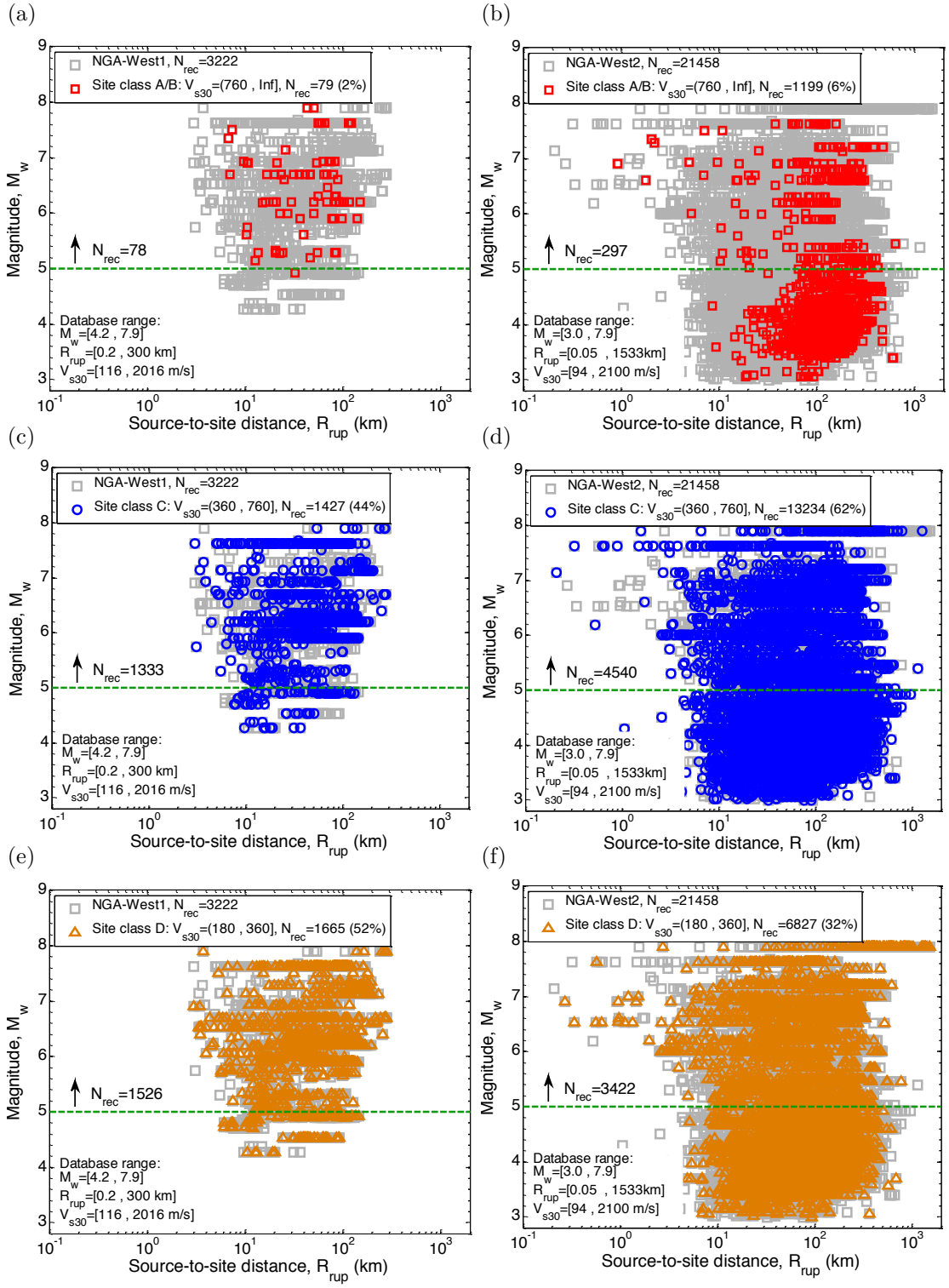

Figure 4.10: M_w-R_{rup} distribution of ground motions from the NGA-West1 and NGA-West2 databases for three different site classes based on the NEHRP (2003) guidelines: (a)-(b) site class A/B; (c)-(d) site class C; (e)-(f) site class D.

4.3.5 Effect of causal parameter bounds on the computational efficiency of scenario-based ground motion selection

The computational cost of ground motion selection is an important issue when selecting ground motion ensembles representing scenario SHA. As elaborated by Tarbali and Bradley (2014a, 2015b), selecting ground motions to represent target distribution of IMs for a scenario SHA requires calculating optimum amplitude scaling factors for all prospective ground motions included in the database. Therefore, reducing the number of prospective ground motions by considering causal parameter bounds increases the computational efficiency of the selection process. As an illustration, Figure 4.11 compares the computational cost of conducting ground motion selections with and without causal parameter bounds for all of the considered scenario ruptures and site conditions in this study. The computational cost is measured based on the time spent to select an ensemble of 20 ground motions by conducting 10 replicate selections using a typical desktop computer (*i.e.,* a Pentium 4 processor with a 2.93 GHz CPU and 4GB).

As shown in Figure 4.11, selecting ground motions from the NGA-West1 database with 3222 available ground motions when no causal parameter bounds are applied takes over 25 minutes of computation time, whereas, by using bounds on the causal parameters, the number of the prospective ground motions reduces to a reasonable number and the selection process requires less than 5 minutes for most of the considered scenarios. It can also be seen that ground motion selection based on causal parameter bounds for V_{s30}=400 m/s scenarios requires longer computational times than that for V_{s30}=200 and 800 m/s scenarios, due to a larger number of records available for V_{s30}=400 m/s scenarios (see Table 4.4). It is obvious that in case of using a larger number of replicate selections to select an ensemble of ground motions (Tarbali and Bradley, 2014a, 2015b) or utilising a database with a large number of prospective ground motions outside of the considered causal parameter bounds, the difference between the computational

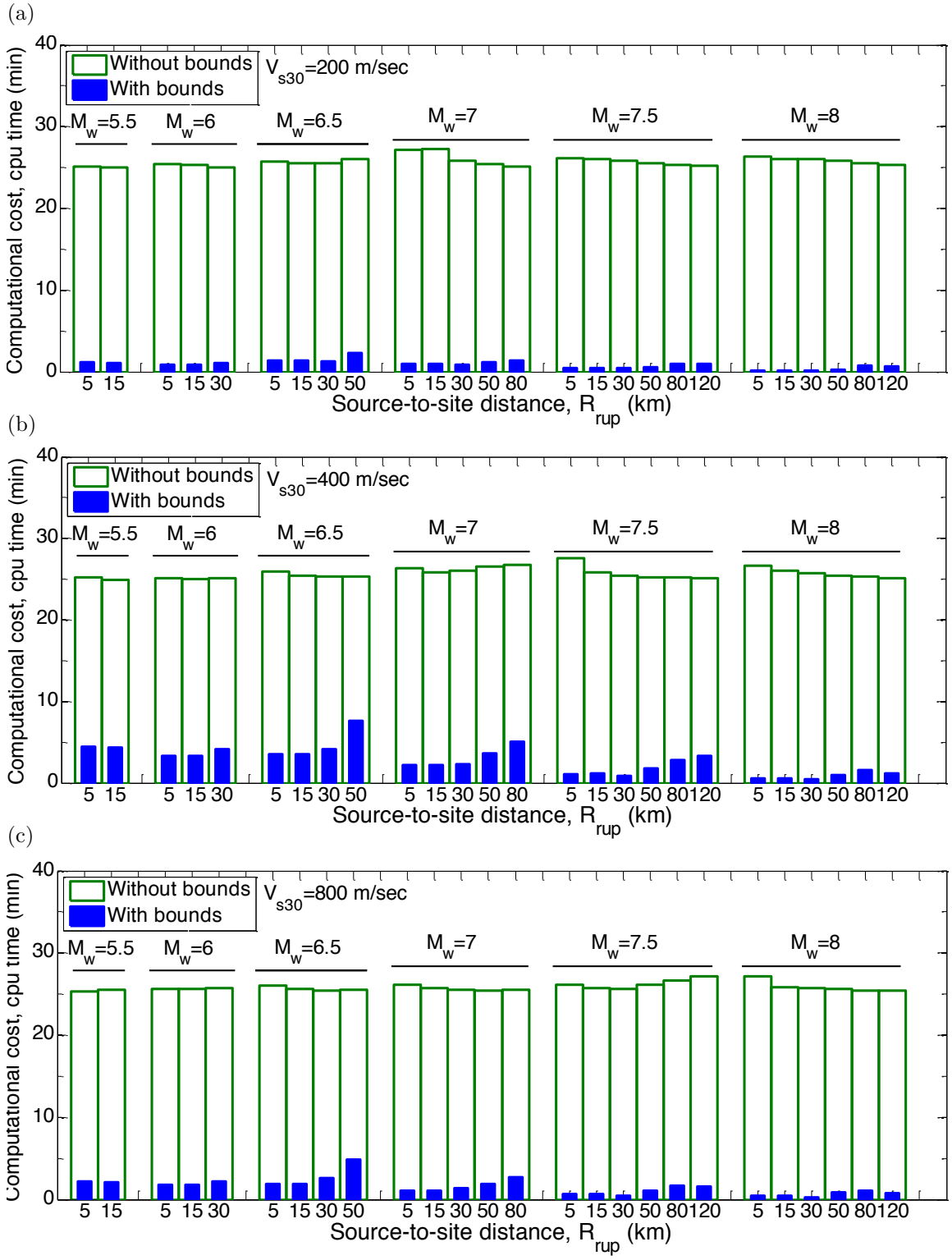

Figure 4.11: Comparison between the computational cost of scenario-based ground motion selection with and without causal parameters bounds for the considered scenario ruptures on three site conditions: (a) V_{s30}=200 m/s; (b) V_{s30}=400 m/s; (c) V_{s30}=800 m/s.

time of ground motion selection with and without the application of bounds will be even more accentuated.

4.4 Ground-motion selection for probabilistic seismic hazard analysis (PSHA)

Probabilistic seismic hazard analysis (PSHA) represents the integrated hazard from all possible scenario ruptures in the vicinity of the site by considering the likelihood of the occurrence of each scenario. Assessing the performance of engineered systems against a probabilistic seismic hazard via dynamic response analysis requires selecting ground motions ensembles representing the desired probabilistic hazard level. Bradley (2012c) developed the GCIM ground motion selection methodology to holistically select ground motions based on PSHA results. In this methodology, the target for ground motion selection is based on the distribution of multiple IMs (which accounts for various aspects of ground motion severity), and incorporates the contribution of all scenario ruptures affecting the seismic hazard based on deaggregation results. Similar to the scenario-based ground motion selection in the previous sections, a weight vector is implemented to allocate the relative importance of the considered IMs (Bradley, 2012c), and the global misfit, *i.e.,* Equation 4.1, is used to assess the overall representation of the selected ground motions to the target IM distributions (Bradley, 2013c).

In the following section, various PSHA cases with noticeably different deaggregation distributions are used to determine appropriate causal parameter bounds on magnitude and source-to-site distance. Subsequently, the impact of alternative proposals for causal parameter bounds on the characteristics of the selected ground motions are investigated and the pertinent implications presented.

4.4.1 Seismic hazard cases and site conditions considered

In order to investigate the effect of various causal parameter bounds on the characteristics of ground motions selected for PSHA cases with different deaggregation distributions, PSHA was conducted for numerous SA vibration periods and sites in California, U.S., using the open-source seismic-hazard analysis software OpenSHA Field et al. (2003). The earthquake rupture forecast of Petersen et al. (2007) and empirical ground motion IM and correlation models presented in section 4.3.3 were used to conduct PSHA and obtained the GCIM distributions of the considered IMs. 12 PSHA cases are considered here which are intentionally chosen to span a wide range of deaggregation conditions in order to examine in detail the subsequently presented proposals for causal parameter bounds. It is noted that each PSHA was conducted for three site conditions with V_{s30}=200, 400 and 800 m/s, *i.e.,* a total of 36 PSHA-based ground motion selection cases. Table 4.11 presents details regarding the considered PSHA cases, including the location, site condition, conditioning IM, and hazard level. Also, Figure 12 illustrates the deaggregation results for the 12 PSHA cases corresponding to the V_{s30}=200 m/s site condition, with PSHAs for the V_{s30}=400 and 800 m/s site conditions result in similar deaggregation distributions, and are therefore omitted for brevity. It can be seen in Figure 12 that these 12 cases span a wide range of causal parameter distributions, including: (i) large M_w scenarios and small R_{rup} values in the near-fault region (*i.e.,* cases 1-5); (ii) large variability in M_w and R_{rup} of the contributing scenarios (*i.e.,* cases 6-8); (iii) dominant scenarios with small, moderate, or large R_{rup} values (*i.e.,* cases 9-12).

4.4.2 Bounds considered on the implicit causal parameters

In this section, various bounding criteria for the magnitude and source-to-site distance of prospective ground motions are defined and applied to the considered deaggregation cases (presented in Table 4.11. These bounding criteria are compared in terms of their inclusiveness to encompass the M_w and R_{rup} distributions

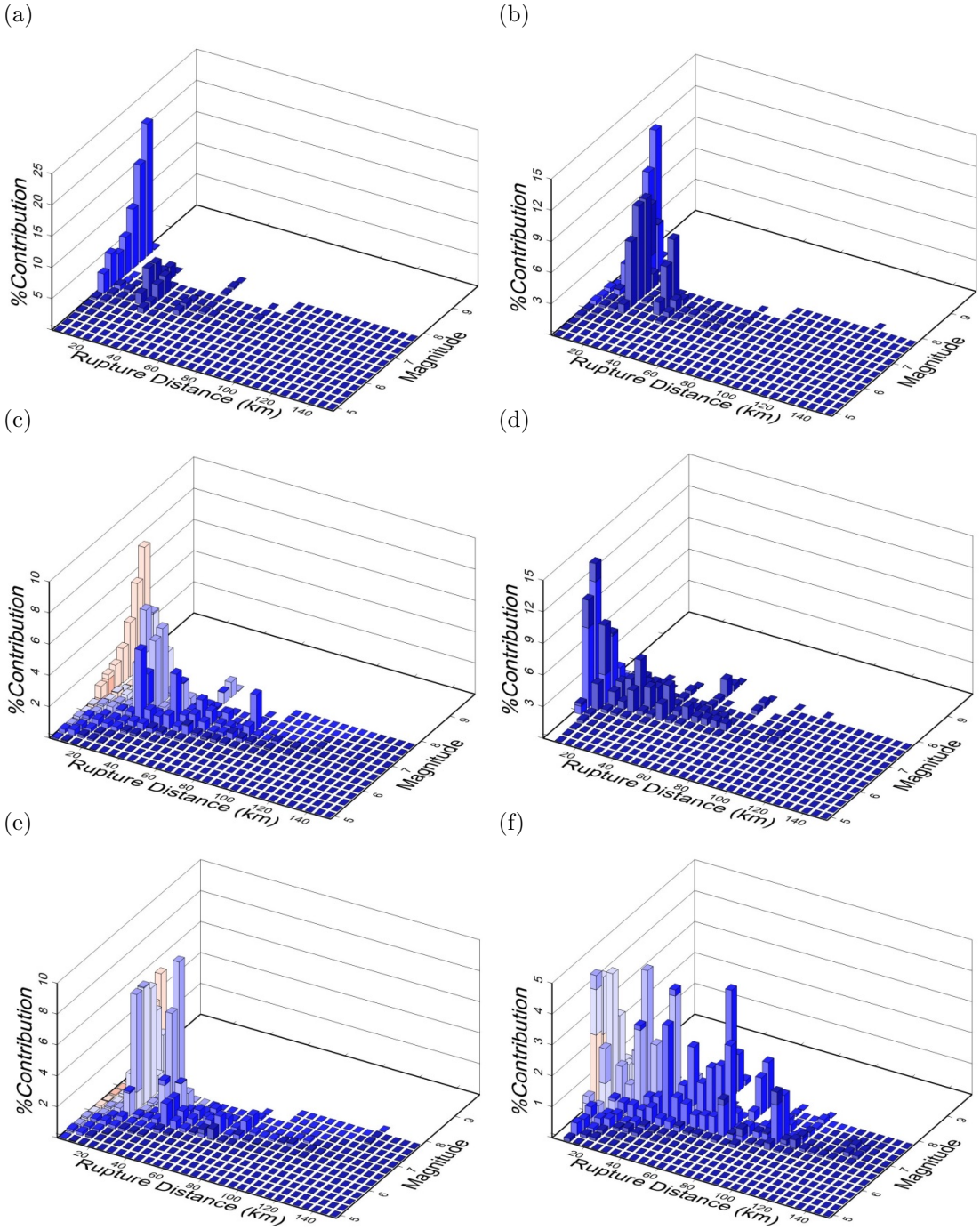

Figure 4.12: Deaggregation distribution of the 12 PSHA cases with the Vs30=200 m/s site condition: (a) Stanford, SA(0.5s) hazard for a 2% probability in 50 years; (b) San Francisco, SA (0.5s) hazard for a 2% in 50 years; (c) Stanford, SA (0.5s) hazard for a 50% in 50 years; (d) Los Angeles, SA (0.5s) hazard for a 2% in 50 years; (e) San Francisco, SA (0.5s) hazard for a 50% in 50 years; (f) Los Angeles, SA(0.5s) hazard for a 50% in 50 years.

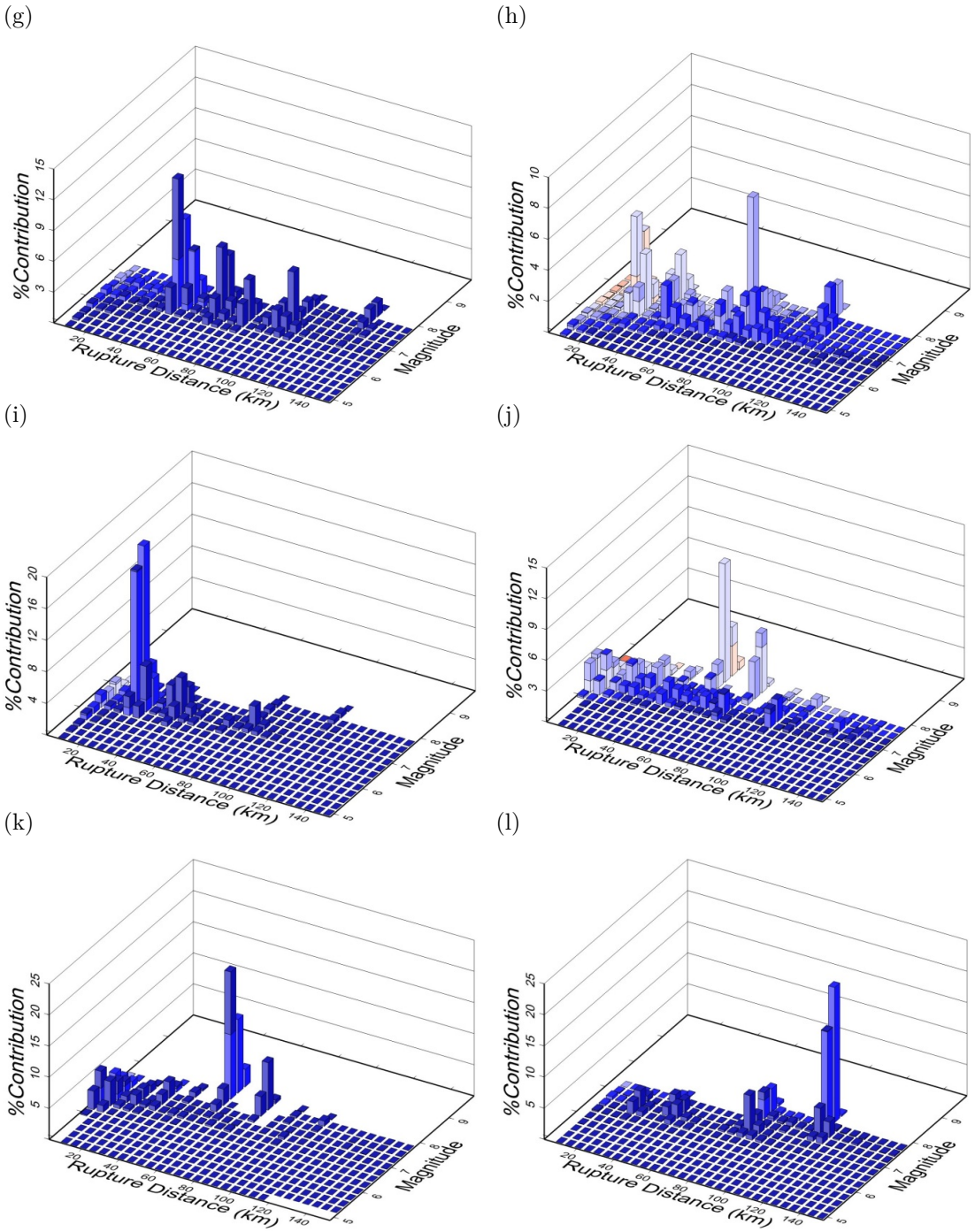

Figure 4.12: *(continued)* Deaggregation distribution of the 12 PSHA cases with the Vs30=200 m/s site condition: (g) Sacramento, SA (0.5s) hazard for a 2% in 50 years; (h) Davis, SA (0.5s) hazard for a 50% in 50 years; (i) Davis, SA (0.5s) hazard for a 2% in 50 years; (j) Los Angeles, SA (3.0s) hazard for a 50% in 50 years; (k) Los Angeles, SA(3.0s) hazard for a 2% in 50 years; (l) Davis, SA (3.0s) hazard for a 2% in 50 years.

Table 4.11: Characteristics of the considered 12 PSHA cases for each site condition in order to examine different causal parameters bounds on M_w and R_{rup}

PSHA case	Site	Latitude, Longitude	Site condition V_{s30}(m/s)	Conditioning IM	Hazard level in 50 years
1	Stanford	37.4225, -122.1653	200, 400, 800	SA(0.5s)	2%
2	San Francisco	37.7833, -122.4167	200, 400, 800	SA(0.5s)	2%
3	Stanford	37.4225, -122.1653	200, 400, 800	SA(0.5s)	50%
4	Los Angeles	34.05, -118.25	200, 400, 800	SA(0.5s)	2%
5	San Francisco	37.7833, -122.4167	200, 400, 800	SA(0.5s)	50%
6	Los Angeles	34.05, -118.25	200, 400, 800	SA(0.5s)	50%
7	Sacramento	38.5556, -121.4689	200, 400, 800	SA(0.5s)	2%
8	Davis	38.5539, -121.7381	200, 400, 800	SA(0.5s)	50%
9	Davis	38.5539, -121.7381	200, 400, 800	SA(0.5s)	2%
10	Los Angeles	34.05, -118.25	200, 400, 800	SA(3.0s)	50%
11	Los Angeles	34.05, -118.25	200, 400, 800	SA(3.0s)	2%
12	Davis	38.5539, -121.7381	200, 400, 800	SA(3.0s)	2%

of the contributing scenarios and the so-called 'discounted' deaggregation contribution. The number of available ground motions based on the defined bounding criteria is also compared for the considered PSHA cases.

4.4.2.1 Definition of various bounding criteria

Since the seismic hazard from PSHA is contributed by several rupture scenarios, bounds on magnitude and source-to-site distance of prospective ground motions should be based on the distribution of these causal parameters obtained from deaggregation results. As a result, the determination of causal parameter bounds for M_w and R_{rup} in PSHA is significantly more complex than for scenario SHA (where there is a single target $M_w - R_{rup}$ combination). With the distributions of M_w and R_{rup} available from deaggregation, an obvious choice is to select bounds for each of these parameters based on certain percentiles. Also, similar to the scenario-based case (which is analogous to a deaggregarion case with a single contributing rupture scenario), it is also appropriate to allow for a certain range

of causal parameters either side of the causal parameters for dominant contributing sources. Based on these two premises, bounding criteria presented in Table 4.12, denoted as criterion A, B, C, D, E, AC, and BD, are defined and examined for the considered deaggregation cases. These different criteria represent various perspectives on the trade-off between wider bounds with more inclusiveness of the deaggregation distribution, yet diminishing returns for the application of causal parameter bounds.

In order to clarify the definition of these criteria, Figure 4.13 schematically illustrates the definition of criteria A and C on the magnitude distribution of a sample deaggregation case. As illustrated in Table 12, for criterion A, the upper and lower bound limits of M_w and R_{rup} are set to values corresponding to 1^{st} and 99^{th} percentiles of their marginal distributions (from deaggregation results). For criterion B and E, these limits are set to values corresponding to 5^{th} and 95^{th} percentiles and 20^{th} and 80^{th} percentiles, respectively. For criterion C, the upper and lower limits are first set to values corresponding to 10^{th} and 90^{th} percentiles, and then further extended by a specified amount (as elaborated upon in the following paragraph). For magnitude and source-to-site distance, the specified amounts are $0.5M_w$ and $0.5R_{rup}$, consistent with those proposed for the scenario-based ground motion selection in the earlier section of this chapter. Criterion D has a similar definition to criterion C, except the initial bound limits correspond to 20^{th} and 80^{th} percentiles.

As shown in Figure 4.13, by using criterion A (or B and E), the scenarios within the bounds encompass most of the total contribution from the deaggregation results. However, for some deaggregation cases, scenarios with a large contribution can exist at tails of the distribution. For such cases, as-recorded ground motions with causal parameters in the vicinity of these scenarios, but beyond the limits, can still be relevant for ground motion selection. For instance, as shown in Figures 4.13a-b, the magnitude limits at 99% and 90% percentiles are equal to $M_w8.1$ and $M_w7.8$, respectively. It may be reasonable to assume that ground motions from ruptures up to $M_w8.5$ can still be relevant to represent

Table 4.12: Bounding criteria examined on M_w and R_{rup} of prospective ground motions for PSHA-based ground motion selection

	Magnitude, M_w		Source-to-site distance, R_{rup}	
Criterion	Lower limit	Upper limit	Lower limit	Upper limit
A	$M_w^{1\%}$	$M_w^{99\%}$	$R_{rup}^{1\%}$	$R_{rup}^{99\%}$
B	$M_w^{5\%}$	$M_w^{95\%}$	$R_{rup}^{5\%}$	$R_{rup}^{95\%}$
C	$M_w^{10\%} - 0.5$	$M_w^{90\%} + 0.5$	$0.5R_{rup}^{10\%}$	$1.5R_{rup}^{90\%}$
D	$M_w^{20\%} - 0.5$	$M_w^{80\%} + 0.5$	$0.5R_{rup}^{20\%}$	$1.5R_{rup}^{80\%}$
E	$M_w^{20\%}$	$M_w^{80\%}$	$R_{rup}^{20\%}$	$R_{rup}^{80\%}$
AC	$min(M_w^{1\%},\ M_w^{10\%} - 0.5)$	$max(M_w^{99\%},\ M_w^{90\%} + 0.5)$	$min(R_{rup}^{1\%},\ 0.5R_{rup}^{10\%})$	$max(R_{rup}^{99\%},\ 1.5R_{rup}^{90\%})$
BD	$min(M_w^{5\%},\ M_w^{20\%} - 0.5)$	$max(M_w^{95\%},\ M_w^{80\%} + 0.5)$	$min(R_{rup}^{5\%},\ 0.5R_{rup}^{20\%})$	$max(R_{rup}^{95\%},\ 1.5R_{rup}^{80\%}$

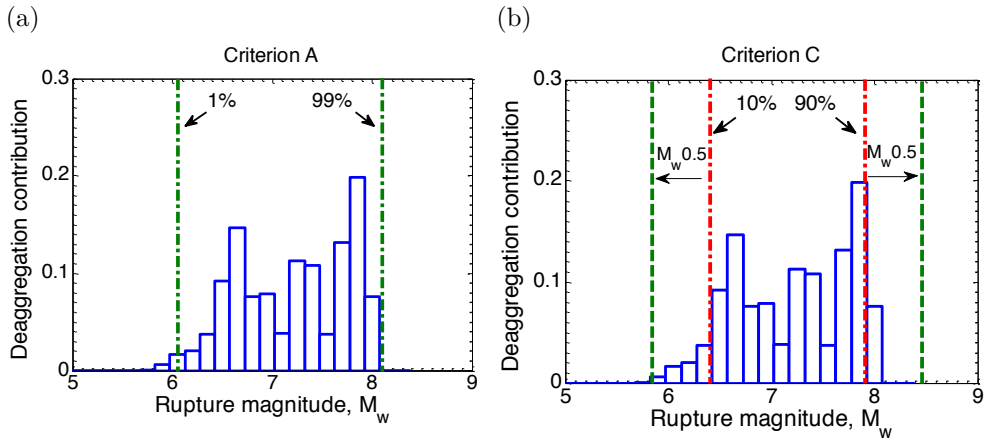

Figure 4.13: Schematic illustration of causal parameter bound criteria for M_w: (a) criterion A; (b) criterion C.

intensity measures of such scenarios. Therefore, setting bounds firmly to limits corresponding to certain percentiles might not result in reasonably wide bounds for ground motion selection. In this regard, similar to the approach taken for scenario-based ground motion selection where bounds are specified either side of the target scenario, bounds for PSHA-based ground motion selection can also be set in a similar manner to include ground motions with similar characteristics in the prospective ground motion subset. Criteria C and D are defined based on this approach, as presented in Table 4.12. Along this line, criteria A and C are combined in order to reach to wider causal parameter bounds. This criterion is denoted as AC, as presented in Table 4.12. Also, in order to obtain a moderately wide bound based on criteria B and D, these criteria were combined to a single criteria, denoted as BD (see Table 4.12). Finally, in order to investigate the effect of using narrow bounds on characteristics of selected ground motions, criterion E is defined based on limits corresponding to 20^{th} and 80^{th} percentiles of the M_w and R_{rup} distributions. Criterion E is aimed to only encompass scenarios with the largest contribution to the hazard for all types of deaggregation distributions considered.

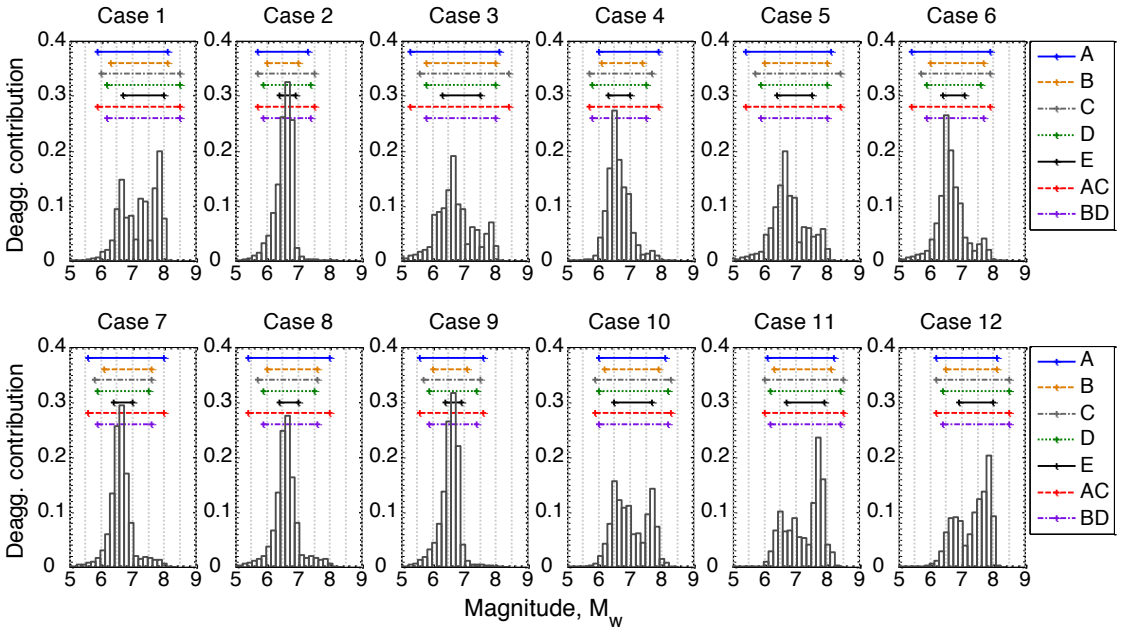

Figure 4.14: Application of causal parameter bounding criteria A, B, C, D, E, AC, and BD on magnitude distribution of deaggregation cases for V_{s30}=200 m/s site condition.

4.4.2.2 Comparison of results from the different bounding criteria

Figure 4.14 presents the rupture magnitude distribution of the 12 deaggregation cases for the V_{s30}=200 m/s site condition, along with the magnitude bound limits determined based on the defined seven bounding criteria in Table 4.12. It can be seen that, for deaggregation cases with dominant scenarios at the tails of the distribution (*i.e.,* cases 1 and 10-12); criteria A, B, and E result in relatively narrow bounds for which the limits are close to the scenarios with large contribution at the tail of the distribution. In contrast, criteria C and AC result in relatively wide bounds. The remaining criteria (*i.e.,* D and BD) result in ranges similar to, but less than C and AC.

For deaggregation cases where the dominant scenarios occur near the centre of the magnitude distribution (*i.e.,* cases 2-9), bound criteria B, D, E, and BD result in neglecting scenarios with small contributions at the tails of the distribution, which summed together can contribute significantly to the total hazard. In contrast, criterion A results in wider bounds that encompass the whole range of causal rupture scenarios. By using criteria AC, in comparison to criterion A, the

defined bounds for these deaggregation cases become wider at one end (*i.e.,* cases 2-5) or do not change (*i.e.,* cases 6-9). From these considerations, criterion AC emerges as the widest criterion to apply bounds on magnitud, while criterion E results in the narrowest bound among the considered criteria. By using criterion E, in particular, only ground motions with similar characteristics to the dominant scenario will be considered for ground motion selection, which can excessively restrict the number of available ground motions, and lead to poor ground motion selection results.

Figure 4.15 presents the source-to-site distance distribution of the 12 deaggregation cases for the V_{s30}=200 m/s site condition, along with the R_{rup} bound limits determined based on the considered seven criteria presented in Table 4.12. It can be seen in Figure 4.15 that criteria B, D, E, and BD result in the most exclusion of scenarios at the tails of the R_{rup} distribution, whereas criteria A, C, and AC result in a relatively wide bounds that encompass the major contributing scenarios. Similar to rupture magnitude distributions, criterion E sets the bound limits close to the dominant scenarios, which results in neglecting other scenarios that in summation may contribute significantly to the hazard. Although not shown directly for brevity, the trends in Figures 4.14 and 4.15 hold true for the V_{s30}=400 and 800 m/s site conditions as well.

In addition to the marginal distributions discussed in relation to Figures 4.14 and 4.15, the considered bounding criteria are compared based on two other important factors, namely: (i) the deaggregation contribution that is 'discounted' (*i.e.,* neglected) by applying bounds on magnitude and source-to-site distance of contributing scenarios; and (ii) the number of available ground motions in the database after applying bounds on the causal parameters. As an example among the three considered site conditions, Figure 16 presents the discounted deaggregation contribution versus the number of available ground motions in the NGA-West1 database (Chiou et al., 2008) for PSHA cases with the V_{s30}=200 m/s site condition. Figure 4.16 illustrates that wide bounds, such as criteria A and AC, result in the lowest discounted deaggregation contribution among the considered

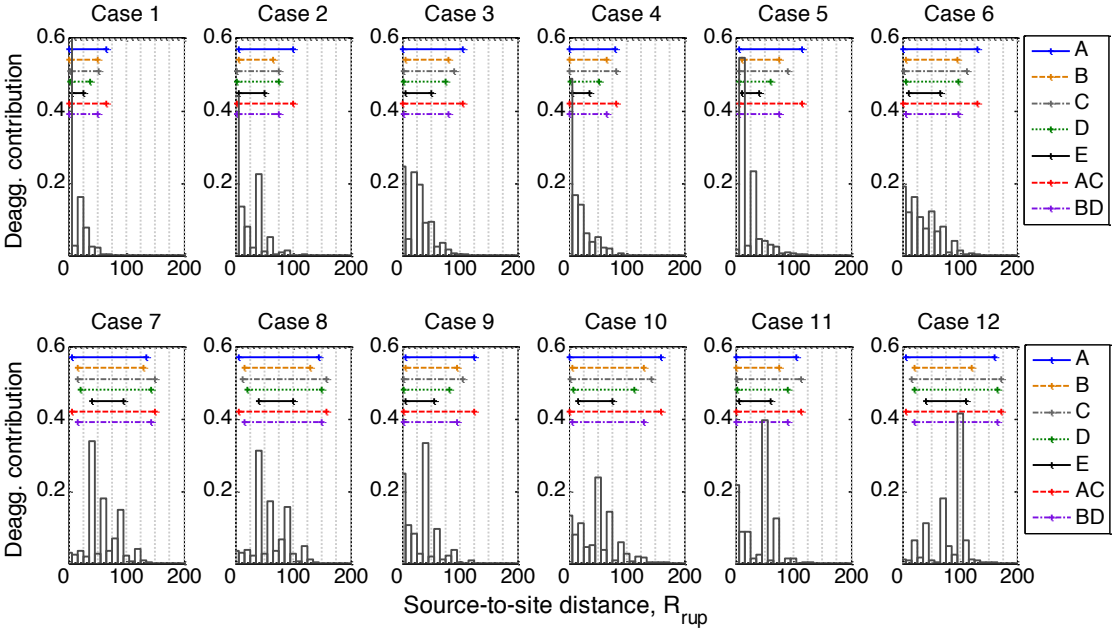

Figure 4.15: Application of causal parameter bounding criteria A, B, C, D, E, AC, and BD on source-to-site distance distribution of deaggregation cases for V_{s30}=200 m/s site condition.

criteria for all of the deaggregation cases. This statement also holds true for the other site conditions considered in this study. In contrast, bounds such as B, D, and BD result in the largest discounted deaggregation contribution for all of the cases considered. It is noted that criterion E results in the lowest number of available ground motions and the largest discounted contribution in order of 0.5, which is out of the range for the presented results in Figure 4.16.

In order to investigate the effect of applying bounds on site condition of the prospective ground motions (*i.e.,* V_{s30} bounds), the number of the available ground motions for each PSHA case is calculated twice; first based on M_w and R_{rup} bounds only, and then based on bounds on the site condition (*i.e.,* V_{s30} bound) in addition to the M_w and R_{rup} bounds. The considered bounds on V_{s30} values of prospective ground motions are the same as those considered for the scenario-based ground motion selection as noted in Table 4.3. As shown in Figure 4.16, the number of available ground motions based on the A and AC criteria are the largest among the considered criteria. This is obviously because of the wide M_w and R_{rup} bounds considered by these criteria. As shown, the number of the

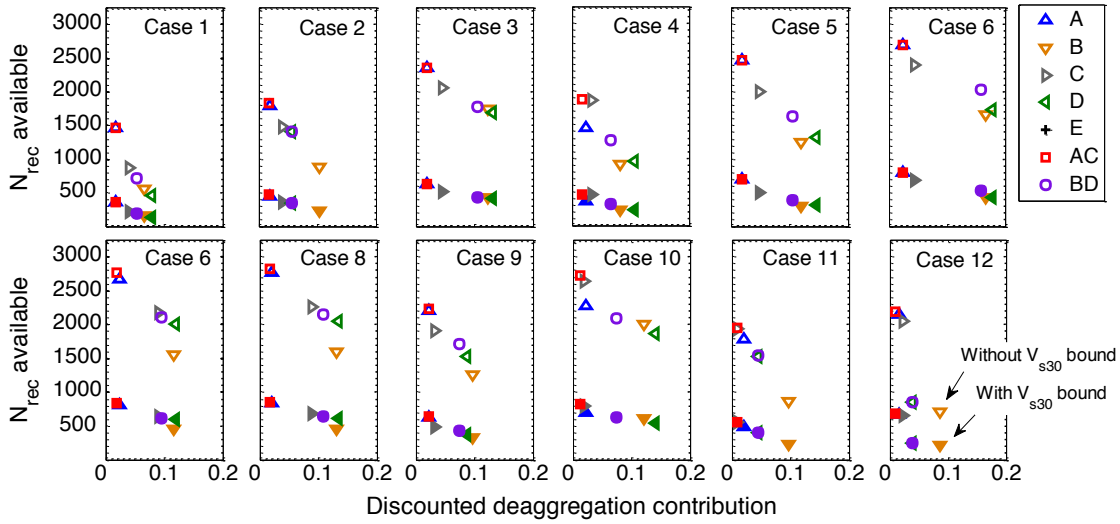

Figure 4.16: 'Discounted' deaggregation contribution versus the number of available ground motions for the 12 deaggregation cases with V_{s30}=200 m/s site condition. Open symbols illustrate the results based on only M_w and R_{rup} bounding criteria and the closed symbols illustrate the results based on the V_{s30} bound in addition to the M_w and R_{rup} bounds.

available ground motions after applying the V_{s30} bound decreases significantly for the V_{s30}=200 m/s site condition.

The number of available ground motions for the considered 36 PSHA cases are presented in Table 4.13 based on the AC criterion as the widest bound among the considered criteria in this study. As illustrated in Table 4.13, by applying bounds on the site condition, the number of the available ground motions decreases significantly for the V_{s30}= 200 and 800 m/s site conditions, in contrast, the reduction for the V_{s30}=400 m/s site condition is not large. This is due to a relative abundance in the number of ground motions in the NGA-West1 database (Chiou et al., 2008) recorded on stiff soil deposits in comparison to those recorded on soft soil or soft rock deposits. Considering the large reduction in the number of available ground motions after application of the V_{s30} bounds, using a wide bounding criteria such as AC on M_w and R_{rup} ensures that the prospective ground motions databases is not overly restricted to a small number of available ground motions.

In order to compare the widest and narrowest bounding criteria considered

Table 4.13: Number of available ground motion records N_{rec} for the considered PSHA cases based on bound criterion AC on M_w and R_{rup}, and the V_{s30} bound

	Bounds only on M_w and R_{rup}			Bounds on M_w, R_{rup}, and V_{s30}		
Deagg. case	V_{s30}=200	V_{s30}=400	V_{s30}=800	V_{s30}=200	V_{s30}=400	V_{s30}=800
1	1463	1565	1821	355	1282	938
2	1835	1866	2662	467	1522	1303
3	2356	2356	2356	633	1901	1187
4	1868	1695	1850	459	1386	946
5	2467	2768	2467	703	2233	1219
6	2692	2692	2692	802	2163	1311
7	2765	2772	2815	838	2231	1354
8	2815	2913	2805	854	2349	1340
9	2227	2750	2772	639	2212	1338
10	2728	2728	2728	830	2181	1334
11	1944	2563	2652	557	2049	1307
12	2181	2669	2752	681	2138	1338

in this study (*i.e.,* criterion AC and E, respectively) in terms of the number of prospective ground motions, Table 14 presents the number of available ground motions based on criterion E and the V_{s30} bound for the 36 PSHA cases considered. By comparing these values with those presented in Table 4.13 based on criterion AC, it is evident that using bounds that only encompass the scenarios with largest contribution to the hazard (*i.e.,* criterion E) will significantly reduce the number of available ground motions. It is important to note that a balance should exist between using excessively wide bounds which provide no meaningful benefit (*i.e.,* no different in comparison to having no bounds at all) and using excessively narrow bounds which result in too few prospective ground motions. As previously mentioned, implicit causal parameters are considered of secondary importance relative to explicit IMs to characterize the intensity of ground motions for the purpose of ground motion selection. Therefore, using excessively narrow causal parameter bounds seems unnecessary, and as shown in the subsequent section, it can be detrimental from a view point that the remaining ground motions might not be able to appropriately represent the distribution of explicit IMs for

the target hazard.

Table 4.14: Number of available ground motion records N_{rec} for the considered PSHA cases based on bound criterion E on M_w and R_{rup}, and the V_{s30} bound

	Bounds only on M_w and R_{rup}			Bounds on M_w, R_{rup}, and V_{s30}		
Deagg. case	V_{s30}=200	V_{s30}=400	V_{s30}=800	V_{s30}=200	V_{s30}=400	V_{s30}=800
1	126	126	248	31	103	125
2	178	178	195	53	145	69
3	394	394	394	115	327	165
4	221	126	283	73	103	127
5	191	366	191	56	306	71
6	271	271	271	78	225	103
7	171	157	182	38	132	72
8	182	160	398	42	134	184
9	193	229	165	55	197	68
10	499	499	499	129	396	233
11	346	462	474	83	372	230
12	393	474	311	123	376	112

Based on the presented results in this section, criteria AC is advocated as a suitable causal parameter bounding criterion to account for the full distribution of causal rupture scenarios and consider an extension beyond the dominant scenarios at the tails of the deaggregation distribution, and is adopted in the presented results to follow. While this criterion is recommended to be used as an initial bounding criterion for general PSHA cases, it is important to note that the user judgement should be utilized in defining the bounding criterion for a specific problem in order to incorporate the characteristics of the problem at hand.

4.4.3 Characteristics of the selected ground motion ensembles

In order to understand the overall impact of using causal parameter bounds, this section compares the IM distributions of selected ground motions with respect

to the corresponding target GCIM distributions for the considered PSHA cases. A total of 20 ground motions are selected, using 10 replicate selections (Bradley, 2012c; Tarbali and Bradley, 2014a, 2015b), for each of the 36 PSHA-based cases considered. Three types of causal parameter bounds are considered: no bounds, narrow bounds (*i.e.,* criterion E and the V_{s30} bound), and wide bounds (*i.e.,* criterion AC and the V_{s30} bound). In order to first illustrate shortcomings in common ground motion selection approaches in which the selection is based only on SA ordinates, ensembles of ground motions are firstly selected by considering only SA ordinates in the weight vector (*i.e.,* the 'SA only' weight vector in Table 4.6). It is noted that for PSHA-based ground motion selection based on no causal parameter bounds, Bradley (2012c) has previously demonstrated bias in distribution of IMs other than SA ordinates when the selection process is based on only SA ordinates. Thus, the aim here is to investigate whether or not considering bounds on the causal parameters can strictly account for the effect of neglecting important IMs that characterize different aspects of ground motions. Subsequently, the effect of considering bounds on the causal parameters is examined when multiple IM types (*i.e.,* SA ordinates, duration, and cumulative effects) are considered via the 'generic' weight vector presented in Table 4.6.

4.4.3.1 Explicit intensity measures of selected ground motions—selection based on only SA ordinates

Figure 4.17 presents the acceleration spectra of ground motions selected based only on SA ordinates (*i.e.,* weight vector 'SA only' in Table 6) and their corresponding median, 16^{th}, and 84^{th} percentiles representing the target SA distribution for a sample PSHA case (*i.e.,* case 7) with the V_{s30}=200 m/s site condition. As illustrated in Figures 4.17a-b, ground motions selected 'without bounds' and with 'wide bounds' (i.e. criterion AC) on the causal parameters have an appropriate representation of the target SA distribution by having the median, 16^{th}, and 84^{th} percentiles of the selected ground motions close to the target GCIM distribution. Figure 4.17c illustrates, in contrast, that considering 'narrow bounds' (i.e. crite-

rion E) on the causal parameters results in selected ground motions with a poor representation of the target SA distribution due to removing an excessive number of ground motions from the database that can appropriately represent the target hazard. Bias in the distribution of SA ordinates when narrow bounds are applied is present for most of the 36 PSHA cases and site conditions considered. As presented in Tables 4.13 and 4.14, the number of available ground motions based on the narrow bounds for the PSHA case considered in Figure 4.17 (*i.e.,* case 7) is 38, whereas, by using wide bounds the number of available motions is 838. Based on the obtained results for the other cases considered, it is noted that the large difference between the number of available ground motions based on narrow and wide bounds is an indicative of a possible degradation in representation of the ground motions selected based on narrow bounds.

In order to investigate the distribution of IMs other than SA ordinates when ground motions are selected based on only SA ordinates, Figure 4.18 presents the CAV and D_{s575} distributions of the selected ground motions for various PSHA cases with the V_{s30}=200 m/s site condition. While the use of no bounds or wide bounds enabled a good representation of the SA distributions, as shown in Figure 4.18, neither option explicitly addresses the bias in the distribution of these IMs representing cumulative and duration-related aspects of ground motions. This issue was also observed in the previous section for scenario-based ground motion selection (*i.e.,* Figure 4.2).

Similar to the results presented in Figure 4.18, Figure 4.19 presents the CAV and D_{s575} distributions of the selected ground motions based on only SA ordinates for sample PSHA cases with V_{s30}=400 and 800 m/s site conditions. As shown in Figure 4.19, considering (narrow or wide) bounds on the causal parameters does not result in remediating the bias in distribution of IMs that are not considered in the weight vector as was the case for the V_{s30}=200 m/s cases in Figure 4.18. Although not presented here for brevity, selection based on narrow bounds also results in a biased distribution of SA ordinates for most of the PSHA cases with V_{s30}=400 and 800 m/s site conditions considered.

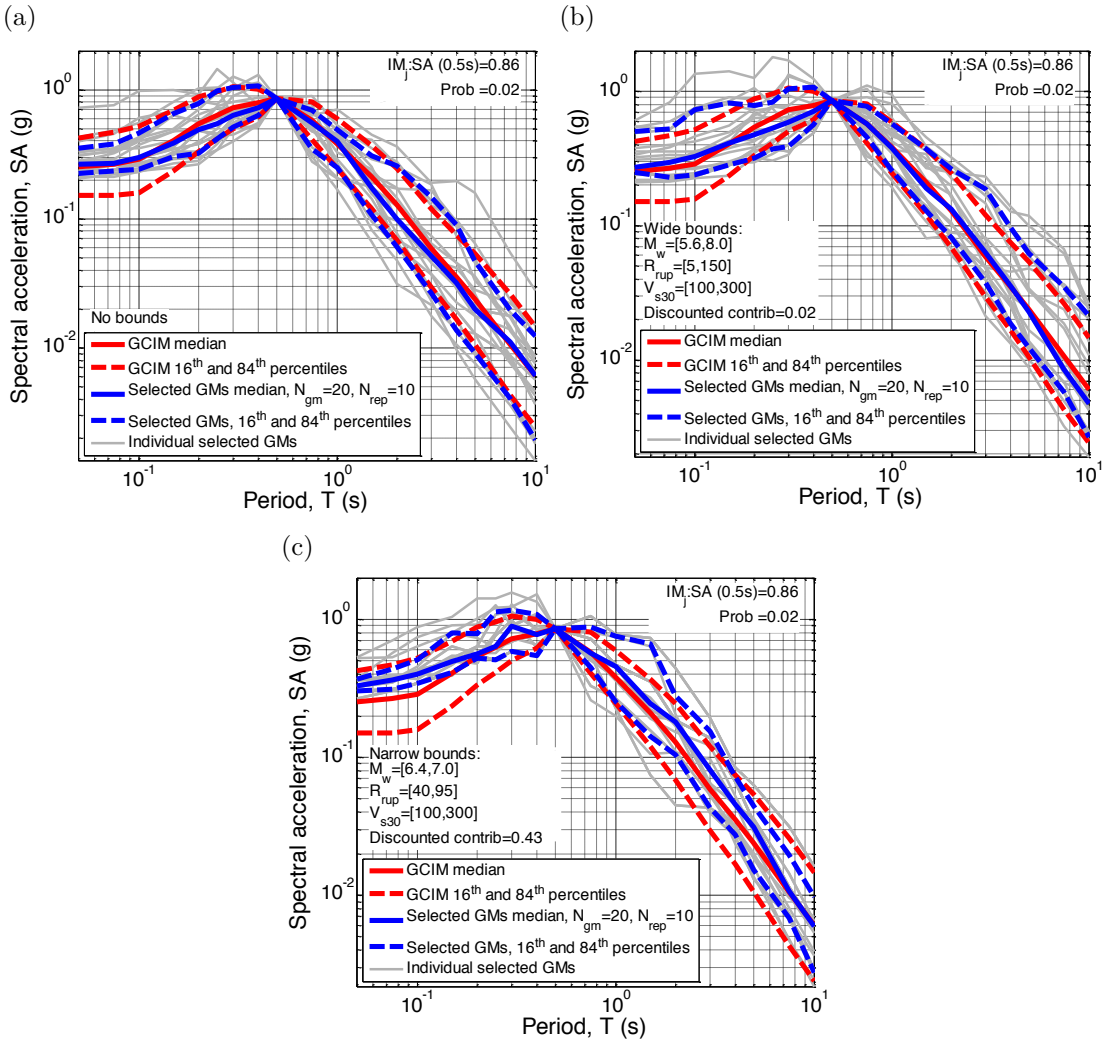

Figure 4.17: Acceleration spectra of selected ground motions by considering only SA ordinates in the weight vector for a sample PSHA case (*i.e.,* case 7 with V_{s30}=200 m/s site condition) and the corresponding median, 16$^{\text{th}}$, and 84$^{\text{th}}$ percentiles for ensembles selected: (a) without bounds; (b) with wide bounds (criterion AC); (c) with narrow bounds (criterion E).

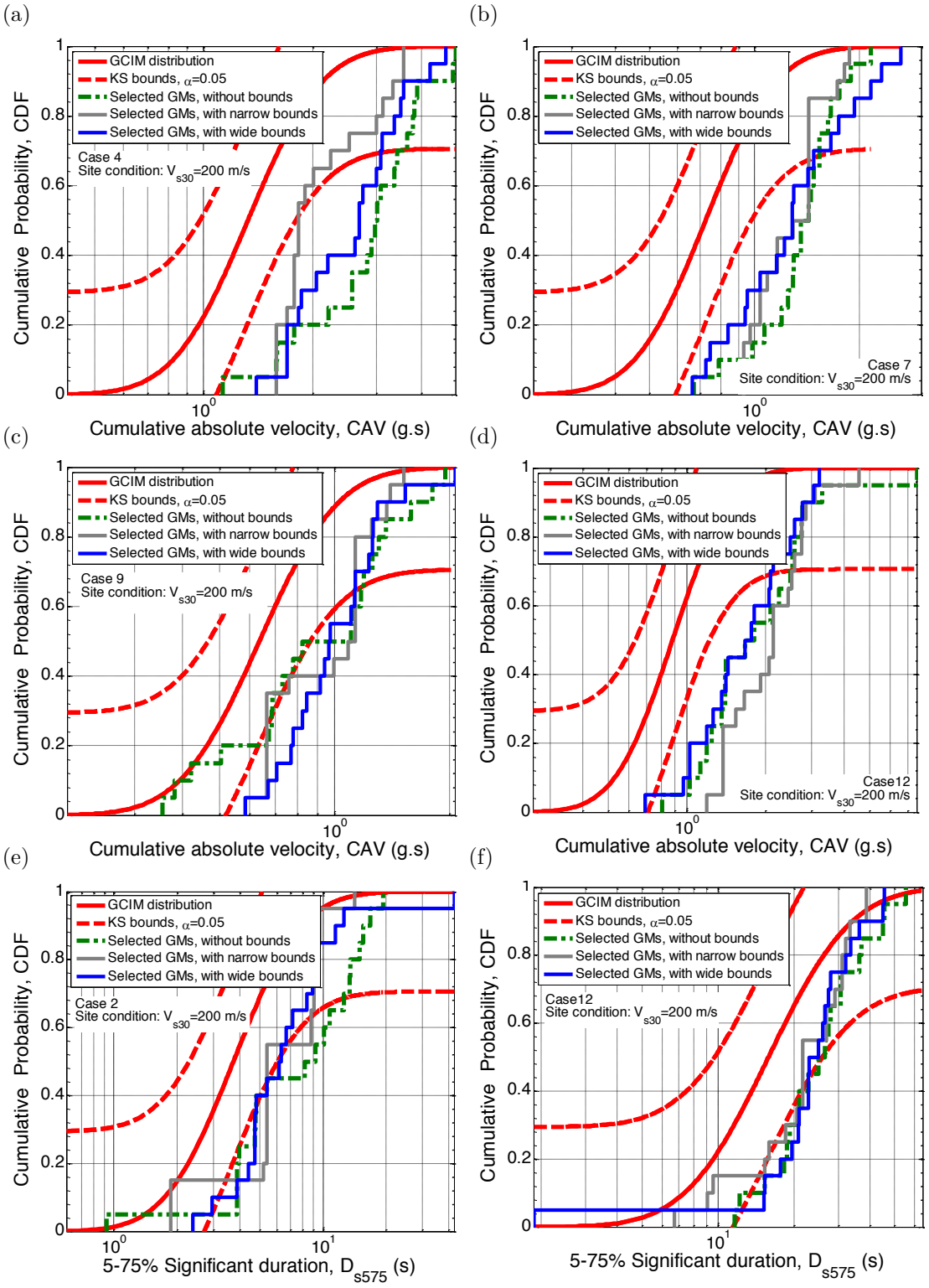

Figure 4.18: Properties of selected ground motions by considering only SA ordinates in the weight vector for sample PSHA cases with V_{s30}=200 m/s site condition based on wide (criterion AC) and narrow (criterion E) causal parameter bounds and also without bounds: (a)-(d) distribution of CAV; (e)-(f) distribution of D_{s575}.

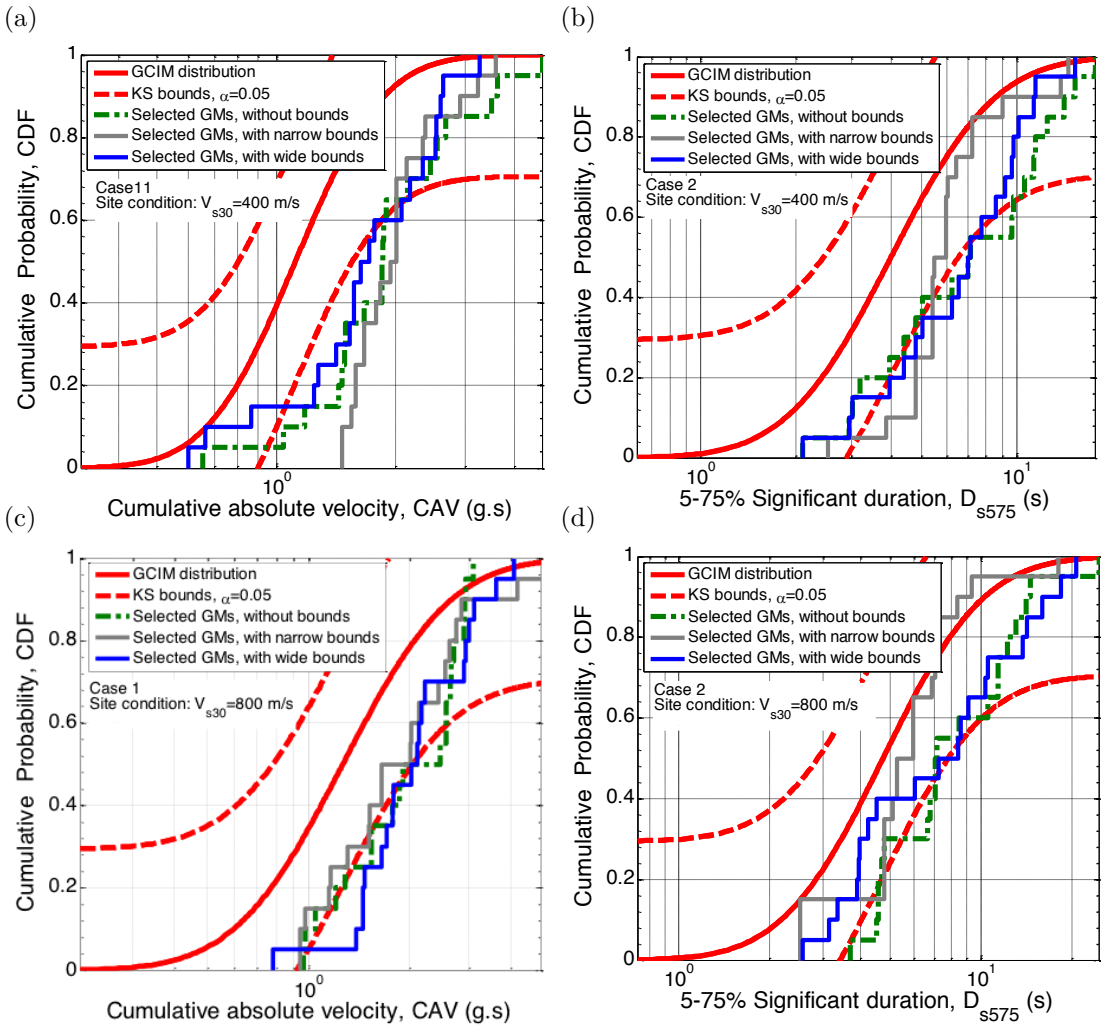

Figure 4.19: Properties of selected ground motions by considering only SA ordinates in the weight vector for sample PSHA cases with V_{s30}=400 and 800 m/s site conditions based on wide (criterion AC) and narrow (criterion E) causal parameter bounds and also without bounds: (a)-(d) distribution of CAV; (e)-(f) distribution of D_{s575}.

It should be noted that the conventional purpose of applying bounds on the causal parameters when the selection is based on only SA ordinates is to attain an appropriate representation for IMs other than SA ordinates that are not considered in the weight vector. This is based on an assumption that the causal parameter bound does not degrade the quality of selected ground motions in representing the target SA distribution. However, as shown in Figure 4.17 for a sample PSHA case among others, using narrow bounds can violate this assumption, resulting in a poor representation for the SA ordinates themselves. In addition, it is demonstrated in Figures 4.18 and 4.19 that using causal parameter bounds (either narrow or wide) is not a reliable approach to strictly account for duration and cumulative effects of ground motions when ground motion selection is based on only SA ordinates.

4.4.3.2 Explicit intensity measures of selected ground motions—selection based on SA, duration, and cumulative effects

As discussed by Bradley (2012c) and Tarbali and Bradley (2015b), bias in the distribution of IMs other than SA ordinates when selecting ground motions can be resolved by explicitly considering them in the weight vector. In order to address this issue, ground motions are selected based on the generic weight vector presented in Table 4.6, which incorporates ground motion amplitude, frequency content, duration, and cumulative effects. Figure presents the acceleration spectra of ground motions selected based on the generic weight vector and their corresponding median, 16^{th}, and 84^{th} percentiles representing the target SA distribution for PSHA case 7 with V_{s30}=200 m/s. Ground motions selected for this PSHA case based on only SA ordinates were previously illustrated in Figure 4.17. Figures 4.20a-c compare the representation of the selected ground motions using the generic weight vector based on no bounds (Figure 4.20a), wide bounds (Figure 4.20b), and narrow bounds (Figure 4.20c). It can be seen that considering narrow bounds has a detrimental effect on representativeness of the selected ground motions to the target SA distribution, while, considering wide bounds or no bounds

does not have such negative effects. Although not presented here for brevity, this holds true for all of the PSHA cases and site conditions considered in this study. This is due to the fact that, as mentioned previously for ground motions selected based on only SA ordinates (*i.e.,* Figure 4.17), using narrow causal parameter bounds removes an excessive number of ground motions which can appropriately represent the target distribution of IMs, whereas, the wide bounds does not have such detrimental effects.

In order to examine characteristics of the IMs other than SA ordinates when ground motions are selected based on the generic weight vector, the CAV and D_{s575} distributions of the selected ground motions for the same PHSA cases presented in Figure 4.18 (that were selected based on only SA ordinates) are shown in Figure 4.21. It can be seen that by using an appropriate weight vector (*i.e.,* considering amplitude, frequency content, duration, and cumulative effects), bias in distribution of ground motions selected without bounds is completely removed, or for some cases significantly improved (*e.g.,* Figure 4.21b and 4.21d). In addition, Figure 4.21 illustrates that ground motions selected based on wide bounds have an appropriate representation of the target distribution, whereas using narrow bounds can result in a biased distribution for some PSHA cases.

The reason for still having bias (for selected ground motions without bounds and with wide bounds) for the cases presented in Figures 4.21b and 4.21d can be considered as a combination of the limited number of available ground motions for soft soil sites, and that ground motions recorded on soft soil sites are more complex to be simply characterized by limited number of IMs using only the V_{s30} parameter to characterize the site condition.

In order to investigate the distribution of IMs other than SA ordinates for PSHA cases with V_{s30}=400 and 800 m/s site conditions when the generic weight vector is implemented for selection, Figure 4.22 presents the CAV and D_{s575} distributions of the selected ground motions for the same sample PSHA cases presented in Figure 4.19 (for which the selection was based on only the SA ordinates). As

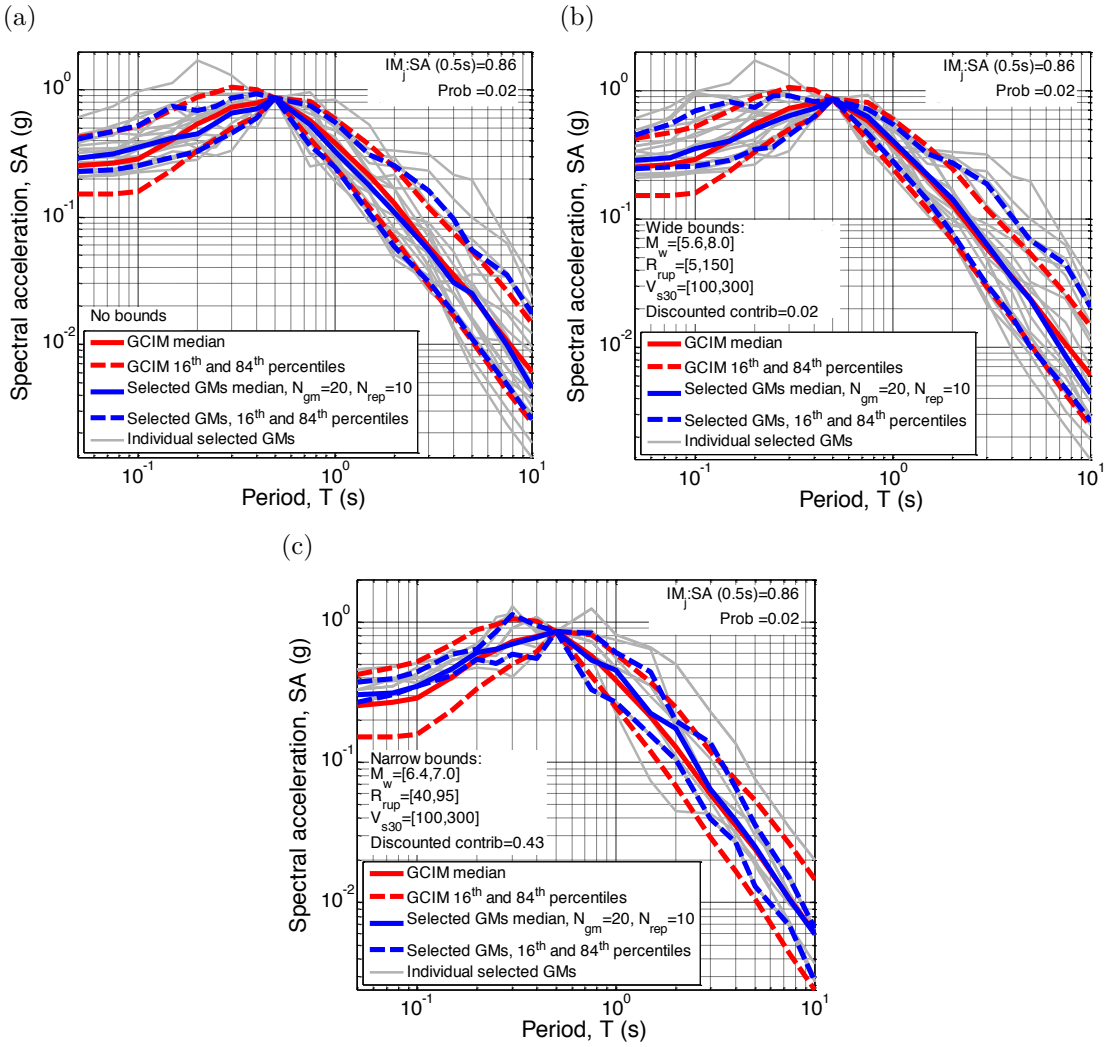

Figure 4.20: Acceleration spectra of selected ground motions based on the generic weight vector (*i.e.,* including SA, duration, and cumulative IMs) for a sample PSHA case (*i.e.,* case 7 with V_{s30}=200 m/s site condition) and their median, 16$^{\text{th}}$, and 84$^{\text{th}}$ percentiles for ensembles selected: (a) without bounds; (b) with wide bounds (criterion AC); (c) with narrow bounds (criterion E).

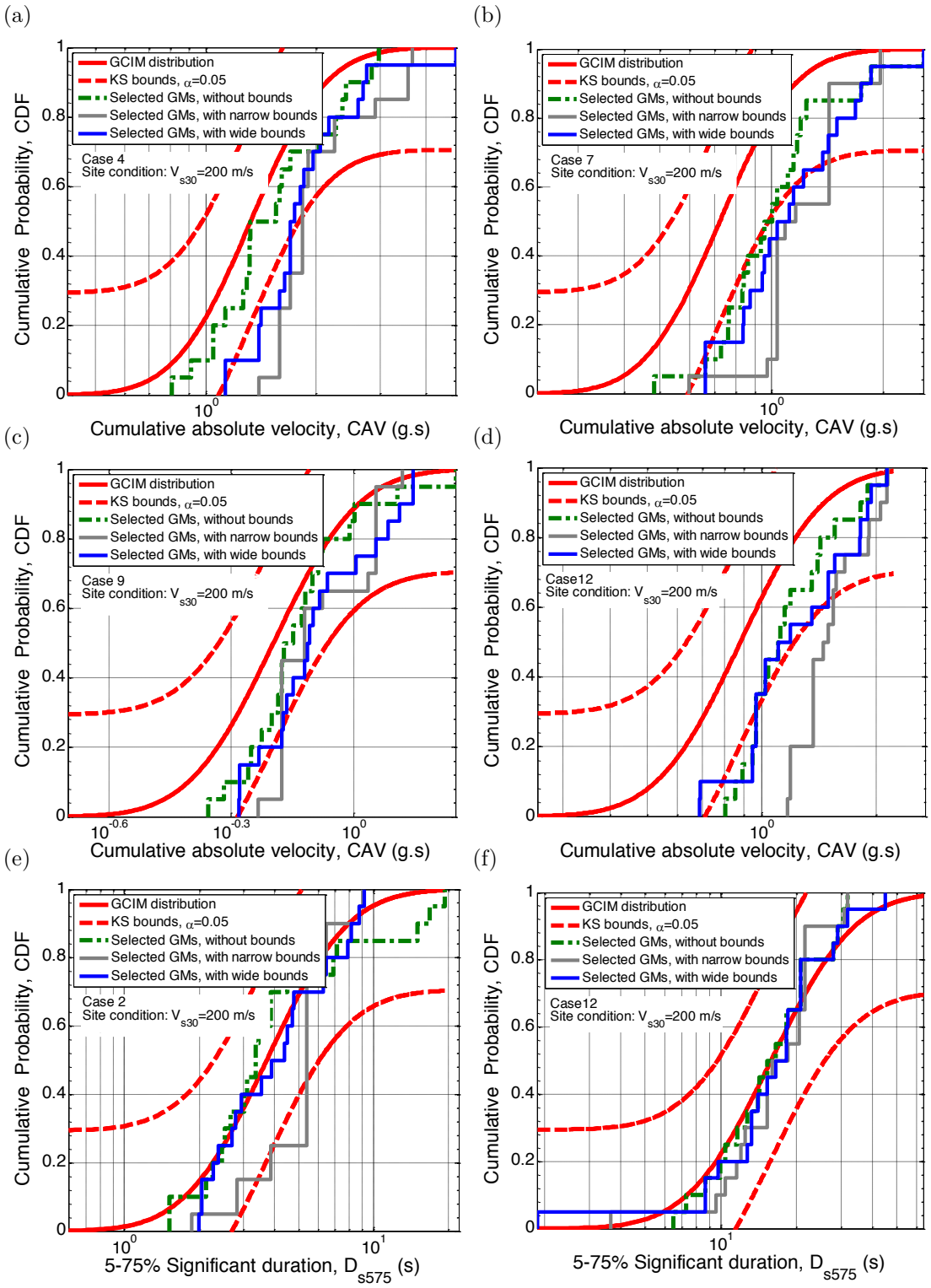

Figure 4.21: Properties of selected ground motions for the same sample PSHA cases presented in Figure 4.18 with V_{s30}=200 m/s site condition, by considering amplitude, frequency content, duration, and cumulative effect in the weight vector (*i.e.,* generic weight vector in Table 6) using wide (criterion AC) and narrow (criterion E) causal parameter bounds and also without bounds: (a)-(d) distribution of CAV; (e)-(f) distribution of D_{s575}.

presented in Figure 4.22, and by comparing with the results presented in Figure 4.19, it can be seen that the bias in distribution of IMs representing the duration and cumulative effects of ground motions selected for the V_{s30}=400 and 800 m/s site conditions is resolved for ground motions selected based on the generic weight vector. Also, ground motions selected based on wide bounds have an appropriate representation of the target distribution. However, ground motions selected based on narrow bounds might still have bias or a poor representation to the target distribution of IMs, as shown in Figures 4.22a and 4.22c for sample PSHA cases.

4.4.3.3 Overall representation of selected ground motion ensembles for all PSHA cases considered

In order to obtain an overall view on the suitability of selected ground motion ensembles in comparison to the target IM distributions, Figure 4.23 presents the global misfit of the selected ground motion ensembles for all of the considered PSHA cases and site conditions. It is noted that the selected ground motions are based on the generic weight vector presented in Table 4.6, which includes weights on SA, duration, and cumulative effects. Figure 4.23a compares the global misfits for ensembles selected based on no bounds with those selected based on the narrow bounds (*i.e.,* criterion E and V_{s30} bound), in which it can be seen that the selected ensembles have larger global misfits for most of the PSHA cases if narrow bounds are utilized, which is most accentuated for V_{s30}=200 m/s site condition due to the small number of available ground motions after the narrow bounds are applied (see Table 4.14). The large bias in distribution of SA ordinates and other IMs presented in Figures 4.20 and 4.21 illustrate the reasons for the large global misfits of ensembles selected based on narrow bounds. In contrast, ground motions selected based on wide bounds (*i.e.,* criterion AC and V_{s30} bound), as presented in Figure 4.23b, result in global misfits that are almost equal to those selected based on no bounds.

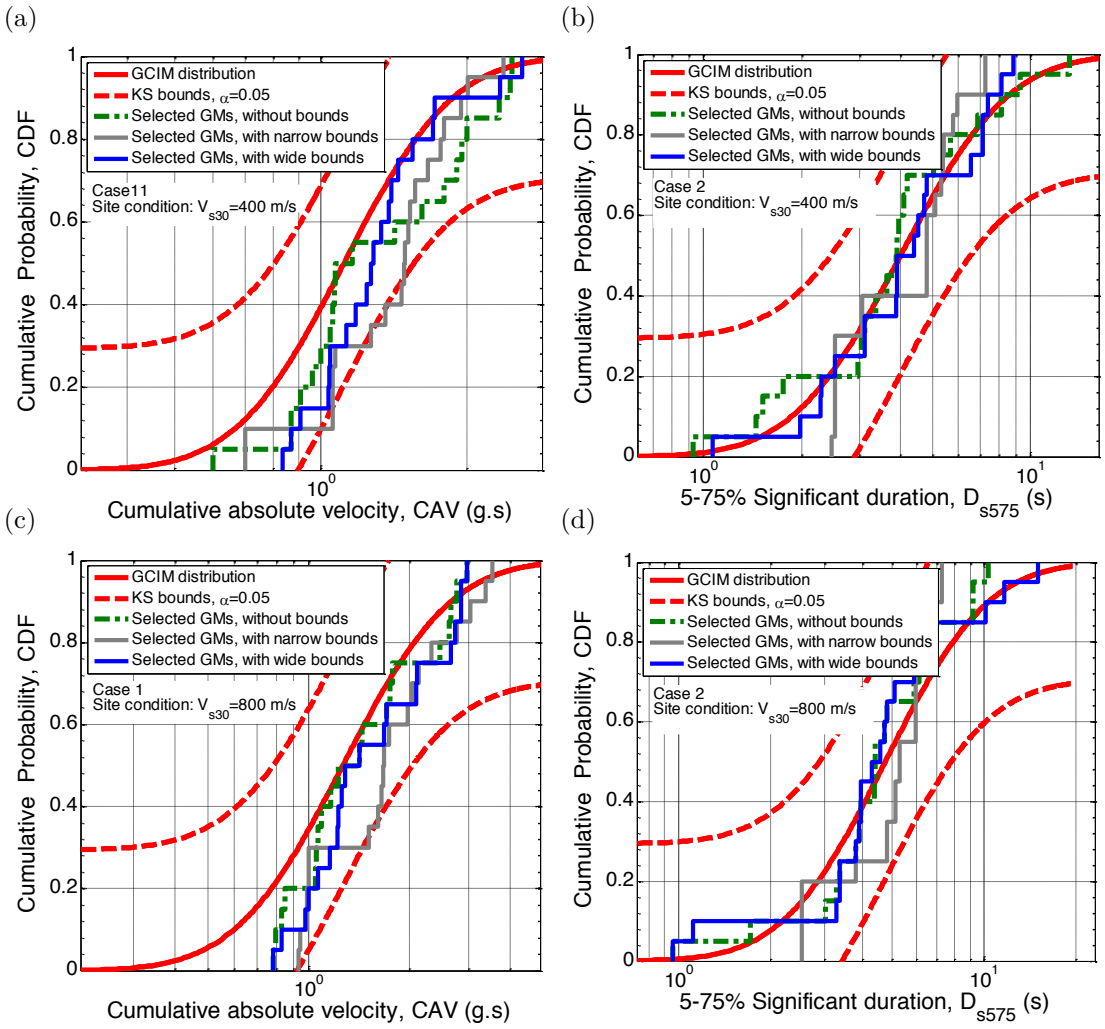

Figure 4.22: Properties of selected ground motions for the same sample PSHA cases presented in Figure 4.19 with V_{s30}=400 and 800 m/s site conditions, by considering amplitude, frequency content, duration, and cumulative effects in the weight vector (*i.e.,* generic weight vector in Table 6) using wide (criterion AC) and narrow (criterion E) causal parameter bounds and also without bounds: (a) and (d) distribution of CAV; (c) and (d) distribution of D_{s575}.

(a)

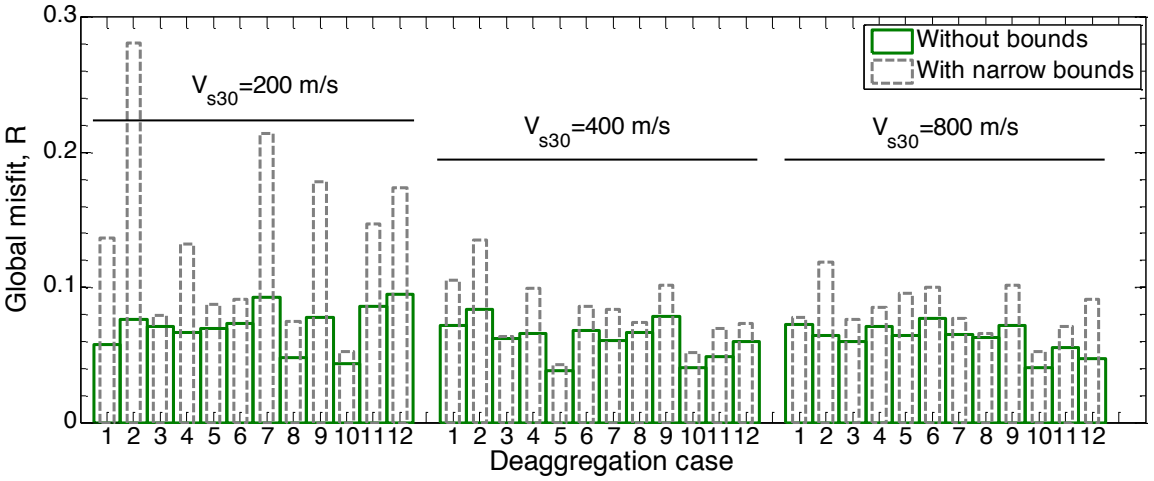

(b)

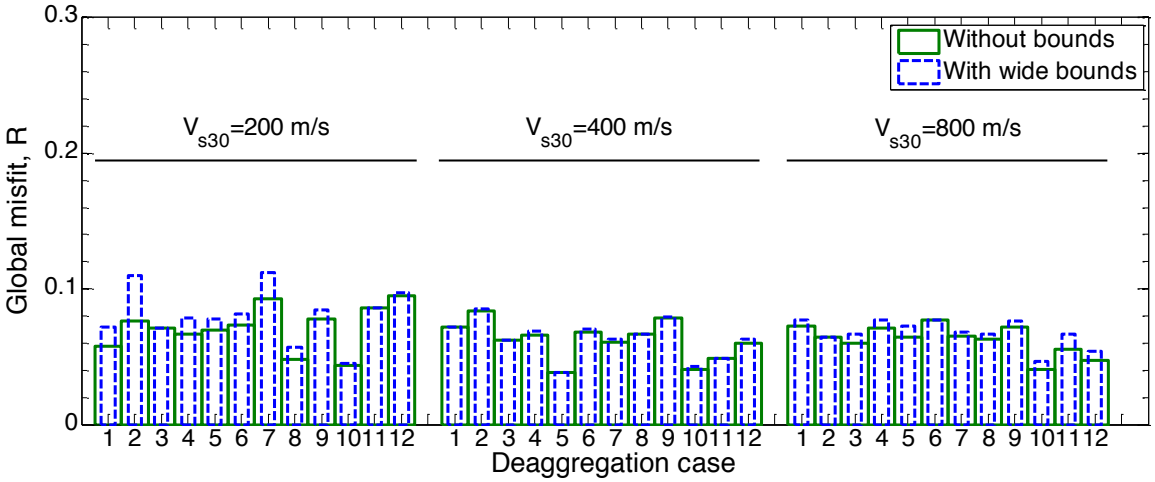

Figure 4.23: Global misfit of selected ground motion ensembles for all of the considered PSHA cases and site conditions: (a) comparison between ensembles selected based on no bounds with those selected based on narrow bounds; (b) comparison between ensembles selected based on no bounds with those selected based on wide bounds.

Based on the presented results for different PSHA cases and site conditions, it is demonstrated that using narrow bounds can unreasonably remove appropriate ground motions from the database and result in a biased distribution of IMs for some PSHA cases. Therefore, it is recommended to use 'wide' M_w and R_{rup} bounds on prospective ground motions such as criterion AC implemented in this study. It is noted that this criterion sets the bounds in a way that most of the contributing scenarios from the deaggregation result are included in addition to extending the bound limits to accommodate ground motions with similar characteristics to any dominant scenario near the tail of the deaggregation distribution (see Figure 4.14 and 4.15). In addition to considering wide bounds on M_w and R_{rup}, it is recommended to constrain the prospective ground motions to those recorded on sites with similar sub-surface soil condition. This can be achieved by constraining the V_{s30} of prospective ground motions as recommended in Table 4.3.

4.4.3.4 Implicit causal parameters of selected ground motions

In addition to the effect of causal parameter bounds on explicit IMs of ground motions, bounds consideration affects the causal parameter distribution of selected ground motions, as discussed in this section. Figure 4.24 and 4.25 present the M_w and R_{rup} distributions, respectively, of the selected ground motions and the corresponding deaggregation distribution for 3 PSHA cases (*i.e.,* cases 4, 6, 10) for the V_{s30}=400 m/s site condition. In all three depicted cases it can be seen that the use of narrow bounds results in ground motions with causal M_w and R_{rup} values closest to the deaggregation distributions, followed by the use of wide bounds, and then no bounds. However, it is noted that this close fit with the use of narrow causal parameter bounds comes with the aforementioned problem of ground motions having a poor fit to the target IM distributions. In contrast, it can be seen that the use of 'wide' bounds leads to a consistent improvement in the empirical distributions of the selected ground motions as compared to the marginal M_w and R_{rup} hazard deaggregation distributions, and ground motion ensembles which provide a good fit to the target IM distributions.

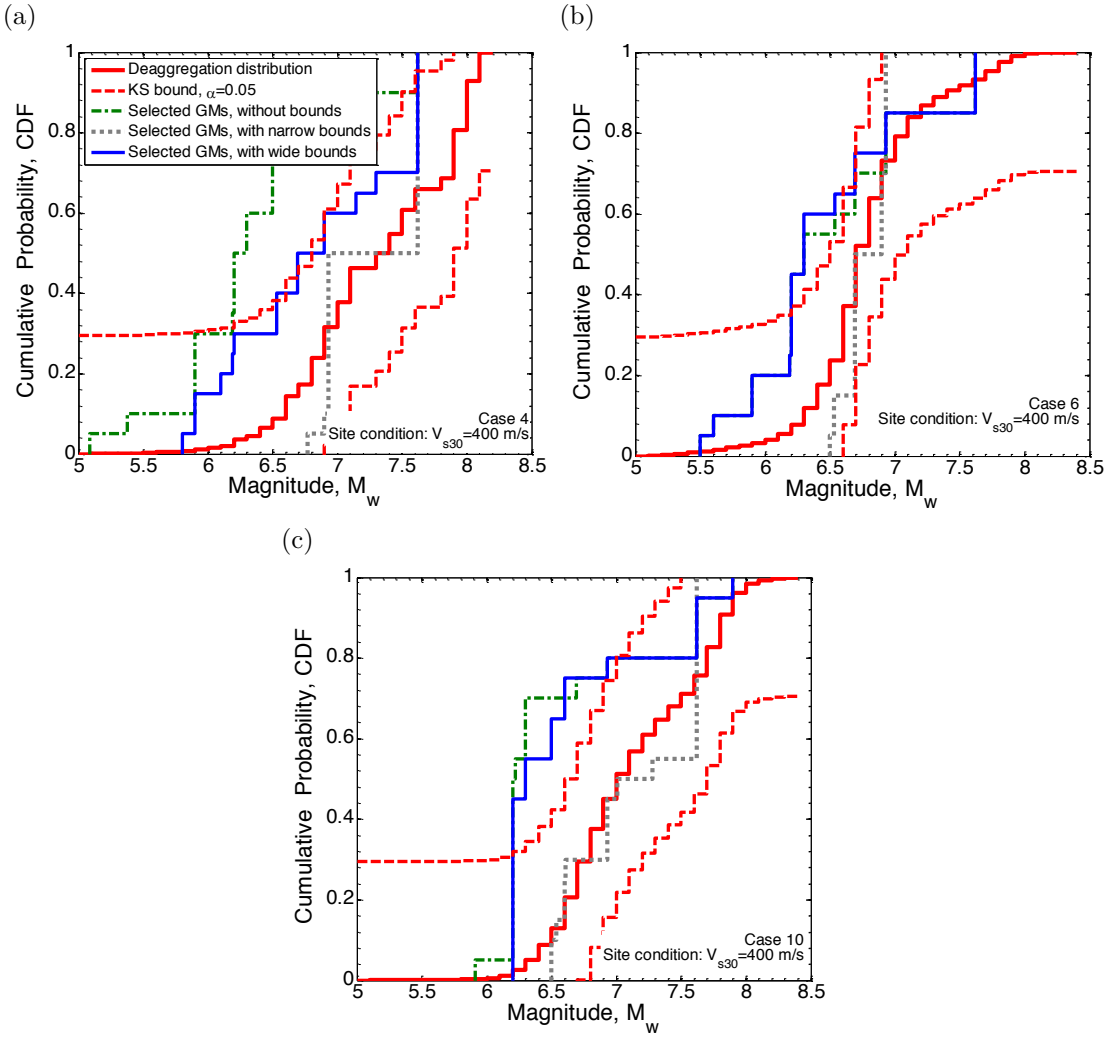

Figure 4.24: Comparison between magnitude distribution of selected ground motions and the deaggregation results for sample PSHA cases with V_{s30}=400 m/s site condition: (a) case 4; (b) case 6; (c) case 10.

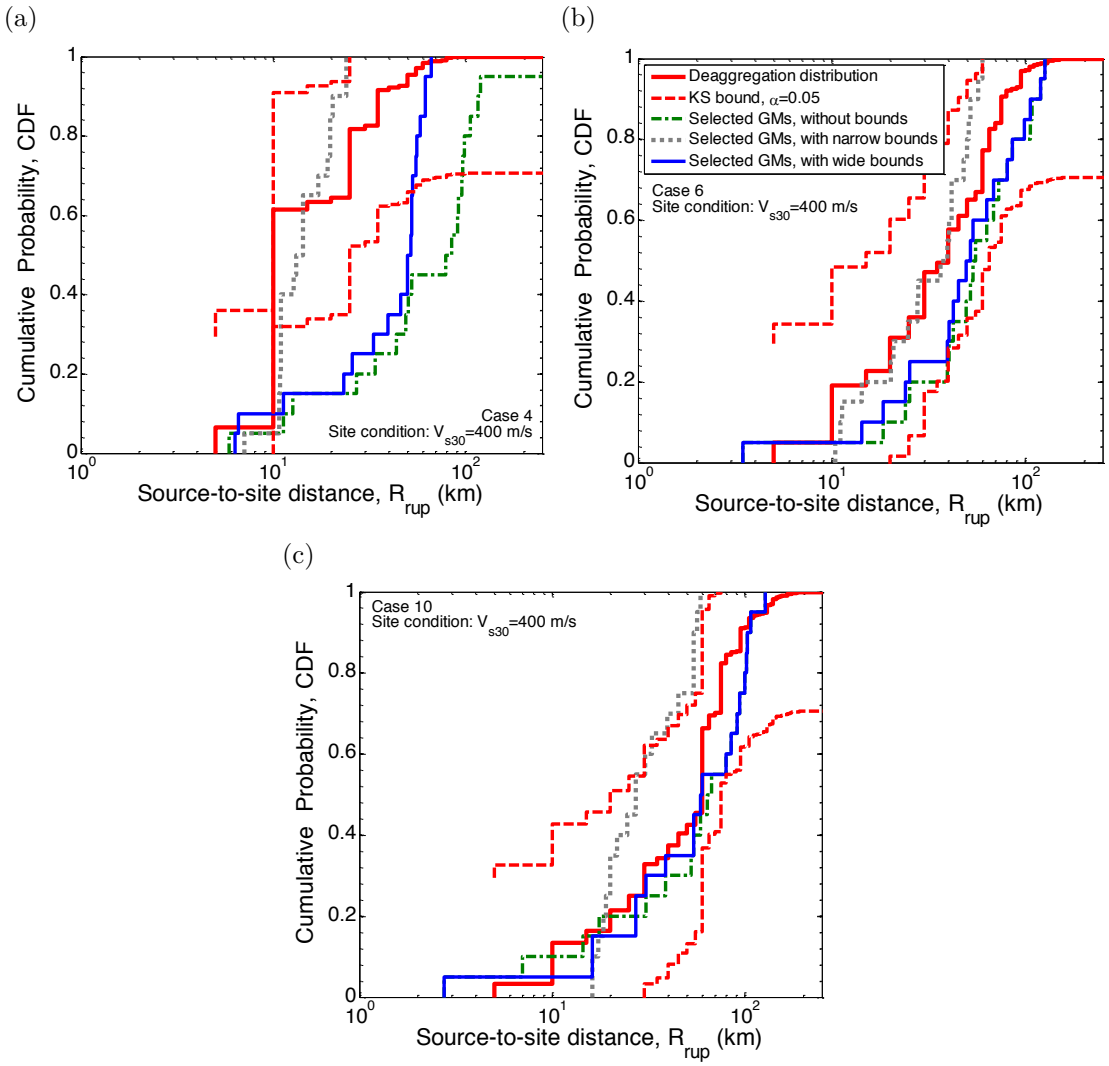

Figure 4.25: Comparison between source-to-site distance distribution of selected ground motions and the deaggregation results for sample PSHA cases with V_{s30}=400 m/s site condition: (a) case 4; (b) case 6; (c) case 10.

In particular, as shown in Figure 4.24a as an example for deaggregation cases with large magnitude causal scenarios in the near-fault region (*i.e.,* cases 1-5), the causal magnitude of ground motions selected based on wide bounds has a close distribution to the deaggregation results which is almost within the KS test bound of the deaggregation distribution. In contrast, the magnitude distribution of ground motions selected based on no bounds does not have an appropriate representation of the target deaggregation distribution. Also, ground motions selected with narrow bounds do not represent the large variance in magnitude distribution of the causal scenarios, appropriately.

For deaggregation cases with a large variability in the M_w and R_{rup} of contributing causal scenarios (*i.e.,* cases 6-8), Figure 4.24b illustrates that the selected ground motions based on narrow bounds have an appropriate representation of the median value of the deaggregation magnitude; however, with a poor representation of the variance of the distribution. Selected ground motions based on no bounds and wide bounds both result in similar distributions, with an appropriate representation of the deaggregation variance but larger median values. As shown in Figure 4.24c for deaggregation cases with dominant scenarios (*i.e.,* cases 9-12), ground motions selected based on narrow bounds have a closer distribution to the target magnitude distribution, which is within the KS test bound.

Figure 4.25 compares the source-to-site distance distribution of selected ground motions and the corresponding deaggregation distributions for 3 PSHA cases (*i.e.,* cases 4, 6, 10) for the V_{s30}=400 m/s site condition. As shown in Figure 4.25a, for deaggregation cases with causal scenarios in the near-fault region, ground motions selected based on narrow bounds have R_{rup} values closer to the deaggregation results than the ensembles selected based on no bounds or wide bounds. In contrast, for deaggregation cases with R_{rup} values distributed in a large range (*i.e.,* cases 6-8), or cases with dominant scenarios (*i.e.,* cases 9-12), ground motions selected based on no bounds and wide bounds result in R_{rup} distributions similar to the deaggregation results, which are within the KS test bound (see Figures 4.25b-c). The R_{rup} distributions of the ensembles selected based on narrow bounds can

slightly deviate from the KS test bounds for these cases.

In order to compare the site condition distribution of selected ground motions with the corresponding target site condition, Figure 4.26 presents the V_{s30} distribution of selected ground motions for a sample PSHA case with V_{s30}=200, 400, and 800 m/s site conditions. It is noted that using wide or narrow bounds only affects the number of available ground motions through the applied bounds on M_w and R_{rup}, as the V_{s30} bound is the same for both narrow and wide bounds. Also, since the PSHA case used in Figure 4.26 is the same across the presented results, the M_w and R_{rup} bounds applied on the prospective ground motions are constant. Thus, only the V_{s30} bound has the main effect on the V_{s30} distribution of selected ground motions presented in Figure 4.26.

As shown in Figure 4.26a, the V_{s30} values of selected ground motions with or without bounds for soft soil condition (*i.e.,* V_{s30}=200 m/s) are generally greater than the target V_{s30} value. This is caused by a paucity of available ground motions in the database recorded on soft soil sites, as previously illustrated in Table 4.13. As presented in Figure 4.26a, selecting ground motions without bounds results in motions with V_{s30} values up to 800 m/s to represent the target V_{s30}=200 m/s site condition, whereas, ground motions selected based on bounds (narrow or wide) results in motions within the specified bounds (*i.e.,* $100 \leq V_{s30} \leq 300$ m/s), representing the soft soil condition.

As shown in Figure 4.26b for the stiff soil condition (*i.e.,* V_{s30}=400 m/s), selected ground motions without bounds and with wide bounds have an appropriate representation of the target site condition with the median V_{s30} close to the target value. In some PSHA cases with stiff soil condition such as case 5 presented in Figure 4.26b, ground motions selected based on narrow bounds have a weaker representation (either large or smaller median value) in comparison to the ground motions selected based on wide bounds and without bounds. This is caused by removing an excessive number of ground motion through the narrow M_w and R_{rup} bounds.

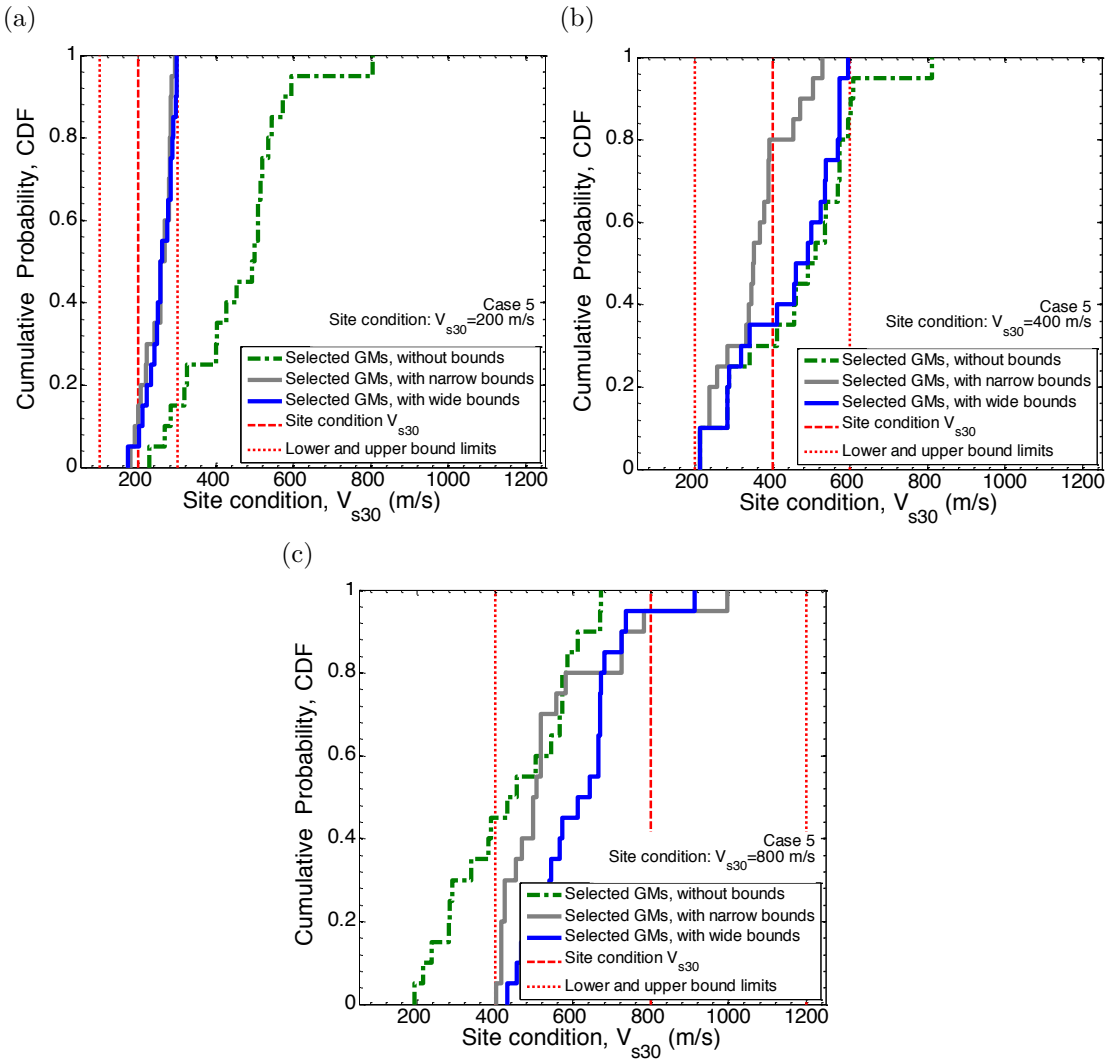

Figure 4.26: Comparison between V_{s30} distribution of selected ground motions and the target V_{s30} for a sample PSHA case representing three site conditions considered: (a) V_{s30}=200 m/s; (b) V_{s30}=400 m/s; (c) V_{s30}=800 m/s.

As shown in Figure 4.26c for soft rock condition (*i.e.,* V_{s30}=800 m/s), half of the ground motions selected without bounds have V_{s30} values smaller than 400 m/s for the considered PSHA case, whereas, half of the ground motions selected based on wide bounds have V_{s30} values greater than 600 m/s, indicating an improved representation of the target site condition for ground motions selected based on wide bounds in comparison to those selected based on no bounds. The V_{s30} distribution of ground motions selected based on narrow bounds is similar to those selected based on wide bounds.

In order to investigate the effect of causal parameter bounds on amplitude scaling factors of selected ground motions, Figure 4.27 presents the distribution of scaling factors of ground motions selected for the same sample PSHA case presented in Figure 4.26 with V_{s30}=200, 400, and 800 m/s site conditions. As shown in Figures 4.27a-c, ground motions selected based on the narrow bounds have lower scaling factors compared to those selected based on no bounds or wide bounds for all three site conditions considered. As already mentioned for scenario-based ground motion selection (section 4.3.4.2), this is due to the fact that by restricting the prospective ground motions to those motions with causal parameters close to characteristics of the causal ruptures affecting the seismic hazard, only a small change in amplitude of as-recorded motions is required to represent the target distribution of IMs. It is important to note that having small amplitude scaling factors does not imply a higher quality in terms of representing the target distribution (both mean and variability) of the considered explicit IMs. This issue is illustrated in Figure 4.18-4.23, as ground motions selected based on narrow bounds have a poor representation of the target IM distributions.

As shown in Figure 4.27a as an example for PSHA cases with V_{s30}=200 m/s site condition, ground motions selected based on wide bounds have mostly lower scaling factors compared to those selected based on no bounds. As presented in Figure 4.27b as an example for PSHA cases with V_{s30}=400 m/s site condition, the applied scaling factors on ground motions selected based on wide bounds are similar to those selected based on no bounds. This holds true for PSHA cases with

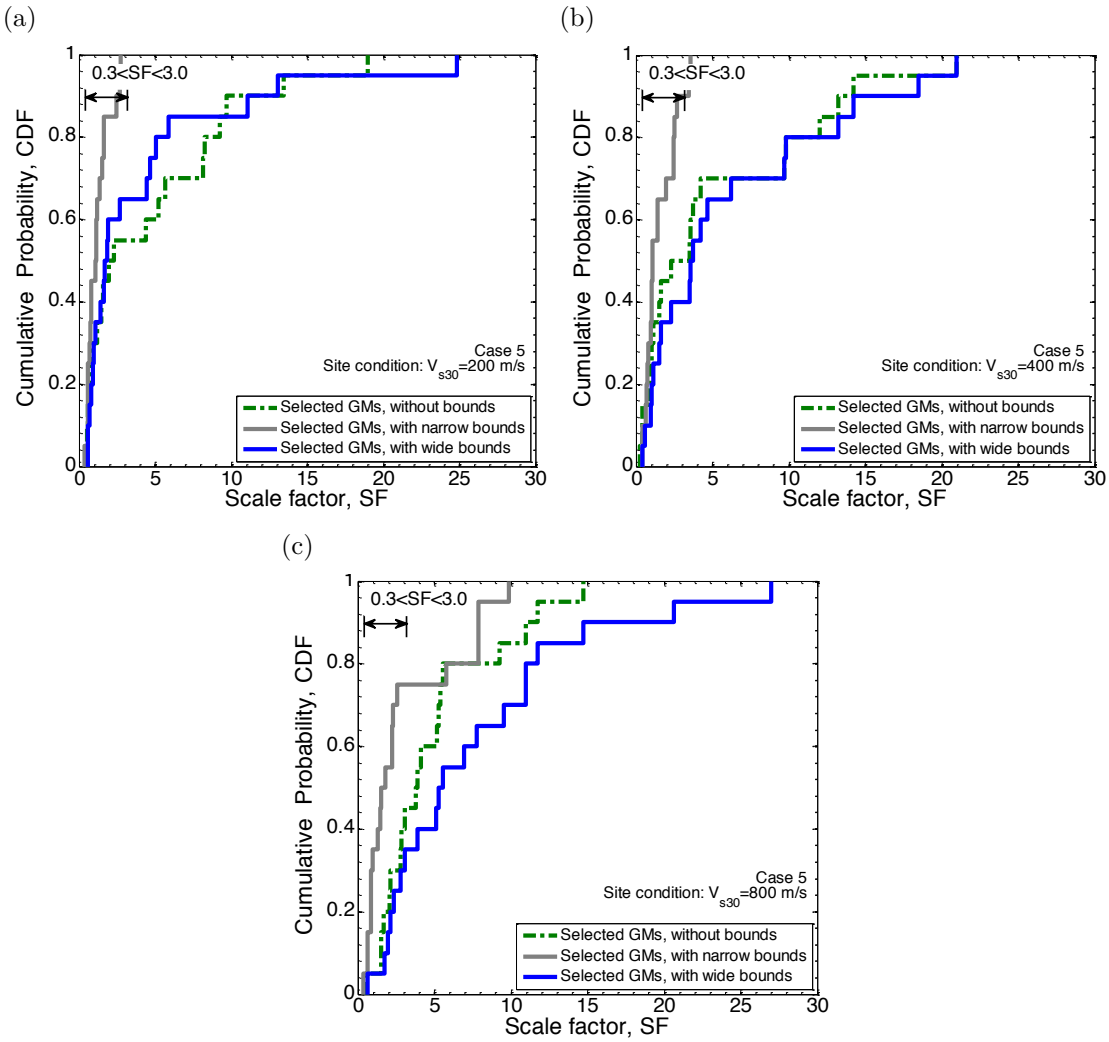

Figure 4.27: Amplitude scaling factor distribution of selected ground motions for a sample PSHA case representing the three site conditions: (a) V_{s30}=200 m/s; (b) V_{s30}=400 m/s; (c) V_{s30}=800 m/s.

V_{s30}=800 m/s site condition as well, except for some cases such as that presented in Figure 4.27c, in which ground motion selected based on wide bounds have larger scaling factors compared to those selected based on no bounds.

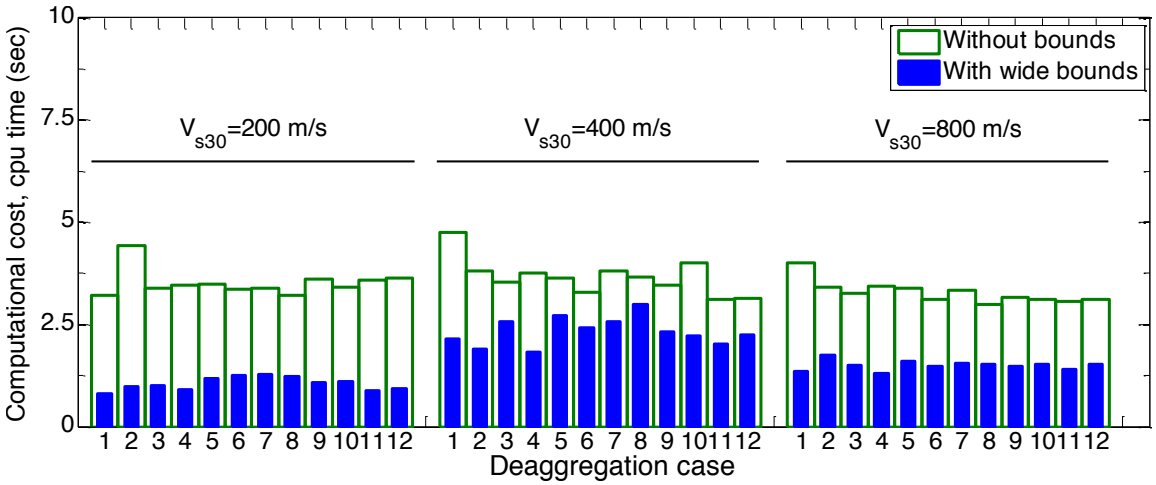

Figure 4.28: Comparison between the computational cost of ground motion selection without bounds and with wide bounds for the considered PSHA cases with V_{s30}=200, 400, and 800 m/s site conditions.

4.4.4 The effect of causal parameter bounds on the computational efficiency of PSHA-based ground motion selection

Similar to the scenario-based ground motion selection, considering bounds on the causal parameters reduces the size of prospective ground motion database and consequently this can reduce the computational time for PSHA-based ground motion selection. Figure 4.28 compares the computational cost of conducting ground motion selections without bounds and with wide bounds for all of the considered PSHA cases with V_{s30}=200, 400, and 800 m/s site conditions. Similar to the scenario cases, the computational cost is measured based on the time spent to select an ensemble of 20 ground motions by conducting 10 replicate selections using a typical desktop computer (*i.e.,* a Pentium 4 processor with 2.93 GHz CPU and 4GB RAM).

As shown in Figure 4.28, bound consideration lowers the computational time of ground motion selection for all of the PSHA cases considered. However, it is noted that the computational time for PSHA-based ground motion selection is significantly lower in comparison to the scenario-based ground motion selection

(*i.e.,* in the order of few seconds as compared to tens of minutes). This is due to the fact that the amplitude scaling factors of prospective ground motions in the PSHA-based ground motion selection is easily obtained from an algebraic equation (Bradley (2012c).Equation 13), whereas for scenario-based ground motion selection optimization is required to obtained the scaling factors (Tarbali and Bradley (2015b), Equation 5). Based on the obtained results in Figure 4.28, it can be seen that the computational cost of PSHA-based ground motion selection can be negligible whether causal parameter bounds are considered or not. Nevertheless, application of the causal parameter bounds can assist in reducing the size of the prospective ground motion database, especially if the number of ground motions outside of the considered bounds is large.

4.5 Conclusion

Using bounds on the causal parameters of prospective ground motions (*e.g.,* magnitude, source-to-site distance, and site condition) is common practice in conventional approaches for ground motion selection. The primary reason for using causal parameter bounds stems from the fact that considering spectral acceleration (SA) ordinates as the only explicit intensity measure does not account for an accurate representation of ground motion duration and cumulative effects which are not explicitly considered. Despite the prevalent application of causal parameter bounds, there is no consistent approach for setting bounds as a function of the seismic hazard at the site. In this chapter, the effect of using bounds on causal parameters of prospective ground motions for the purpose of ground-motion selection for scenario and probabilistic seismic hazard analysis (PSHA) is investigated. 78 scenario and 36 PSHA cases were considered for ground motion selection with and without the application of causal parameter bounds, which cover a wide range of seismic scenarios and site conditions. Ground motions were selected based on the generalized conditional intensity measure (GCIM) approach, which considers multiple ground motion intensity measures (IMs) and their variability in order to

appropriately represent characteristics of the seismic hazard at the site.

The inadequacy of using bounds to account for shortcomings of selecting ground motions based on only SA ordinates was firstly illustrated by performing ground motion selection for the considered scenario and PSHA cases with and without the consideration of causal parameter bounds, in which the distributions of non-SA IMs were seen to be inconsistent between the selected ground motions and the target distributions for the seismic hazard considered.

By considering different aspects of ground motion severity, including amplitude, frequency content, duration, and cumulative effects through the GCIM-based ground motion selection, the effects of causal parameter bounds on characteristics of the selected ground motions were investigated. It was demonstrated that the application of relatively 'wide' bounds on causal parameters can effectively remove ground motions with drastically different characteristics than the target seismic hazard, leading to an improvement in the computational efficiency of the selection process by reducing the subset of prospective records, especially for scenario-based ground motion selections relative to PSHA-based selections. In addition to an improvement in computational efficiency of the ground motion selection process, application of wide bounds improves the representation of causal parameters of the selected ground motions to the target seismic hazard characteristics, and does not degrade the quality of the selected ground motions to represent the target distribution of explicit IMs (which is the primary aim in the ground motion selection process). In contrast, the use of excessively narrow bounds can lead to ground motion ensembles with a poor representation of the target IM distributions, as a result of the narrow bounds resulting in a small database of prospective ground motions relative to the size of the ground motion ensemble desired. It was heuristically evaluated that the subset of prospective ground motions after the application of causal parameter bounds should be a factor of three or more greater than the ground motion ensemble size desired.

The specific causal parameter bound criteria advocated in this chapter (*i.e.,*

criterion AC) is recommended for general use in ground motion selection from PSHA results as a 'default' bounding criterion. However, if such a criterion results in an excessively small subset of prospective ground motions then variations form this default should be considered.

Chapter 5

Seismic hazard analysis and ground motion selection in the near-fault region considering directivity effects

Tarbali, K., Bradley, B. A., and Baker, J. W. (2017). Seismic hazard analysis and ground motion selection in the near-fault region considering directivity effects. *(Under-preparation)*.

5.1 Summary

While the occurrence of forward directivity pulses and their effect on seismic response of engineered systems has been long recognised, and their consideration is advocated in seismic design codes, no commonly accepted procedure exists for ensuring that such records are considered in ground motion selection. An approach is presented to consider the forward directivity velocity pulse effect in seismic hazard analysis without separating the hazard calculations for pulse-like and non-pulse-like ground motions, resulting in a single target hazard at the site

of interest for ground motion selection. In addition, the ability of ground motion selection methods to appropriately select records which exhibit pulse-like ground motions in the near-fault region is examined. Particular attention is given to ground motion selection which is explicitly based on ground motion intensity measures (IMs), including pseudo-acceleration response spectrum, duration, and cumulative measures; rather than a focus on implicit parameters (*i.e.,* pulse or non-pulse classifications) that are conventionally used to heuristically distinguish between the near-fault and far-field records. Example applications are presented for scenario and probabilistic seismic hazard analysis cases with different rupture characteristics, source-to-site geometry, and site conditions. The implications of the selected records, in terms of the conditional demand distribution and the demand hazard, are discussed. It is shown that ground motion selection based on an appropriate set of IMs will lead to a ground motion ensemble with an appropriate representation of the directivity-included target hazard in terms of explicit IMs which are themselves affected by any forward directivity effects. Therefore, implicit directivity measures such as the number of the directivity ground motion in the selected ensemble of records and their pulse period do not need to be specified *a priori* in the ground motion selection process.

5.2 Introduction

Ground motions in the near-fault region may exhibit characteristics such as velocity pulses and permanent static displacement which are not observed in the far-field ground motions. The occurrence of such characteristics have been long recognised and numerous studies conducted to illustrate the effect of such ground motions on seismic response of engineered systems (*e.g.,* Bertero et al., 1978; Anderson and Bertero, 1987; Hall et al., 1995; Alavi and Krawinkler, 2001; Menun and Fu, 2002; Makris and Black, 2004; Mavroeidis et al., 2004; Akkar et al., 2005; Luco and Cornell, 2007; Chioccarelli and Iervolino, 2010; Champion and Liel, 2012). Proximity to the seismic source, source-to-site geometry, and specific rup-

ture characteristics can create favourable conditions for the occurrence of ground motions with large velocity pulses (Archuleta and Hartzell, 1981; Somerville et al., 1997; Pitarka et al., 2000; Mavroeidis and Papageorgiou, 2002; Somerville, 2003; Aagaard et al., 2004; Bray and Rodriguez-Marek, 2004; Mavroeidis and Papageorgiou, 2010). These ground motions, as opposed to pulse-like motions generated by the nonlinear site response or basin generated waves, are referred to as forward directivity pulse-like ground motions and are the focus of this study.

Assessing the seismic performance of engineered systems requires an appropriate representation of the seismic hazard at the site. This can be achieved by selecting ground motion time series recorded during past earthquakes that appropriately represent the seismic hazard at the site. Since near-fault ground motions with velocity pulses can result in ground motion intensity measure (IM) values that are notably different than far-field records, neglecting the occurrence of directivity pulses may result in a biased estimation of the seismic response of systems susceptible to such motions. While various methods have been proposed to select ground motions for seismic response analysis (*e.g.,* McGuire, 1995; Shome et al., 1998; Bommer and Acevedo, 2004; Kottke and Rathje, 2008; Baker, 2011; Jayaram et al., 2011; Wang, 2011; Bradley, 2012c), only few recent studies have been concerned with the explicit selection of near-fault ground motions (*e.g.,* Almufti et al., 2013; Hayden et al., 2014), despite the fact that considering near-fault ground motions is advocated in seismic codes — albeit without providing an explicit process to do so (*e.g.,* NZS1170.5, 2004; ASCE/SEI7-10, 2010).

One of the important issues in the selection of near-fault ground motions is to establish an appropriate 'target' for time series selection (NEHRP, 2011). Almufti et al. (2013) recommend using the conditional mean spectrum (CMS) (Baker, 2011) including a narrow band modification to account for the directivity pulse effect (Shahi and Baker, 2011), while Hayden et al. (2014) also support the CMS as a target with no explicit consideration for the directivity pulse effect. In both methods, the CMS is computed from the governing (or mean) rupture scenario. The use of response spectral ordinates, and not other additional IMs, in

the above two suggested procedures ignores the fact that ground motion severity is a function of amplitude, frequency content, and duration (Kramer, 1996). For example, ground motions with forward directivity pulses frequently have lower Significant Duration in comparison to the far-field records (Somerville et al., 1997; Hayden et al., 2014).

The two aforementioned recent approaches for selecting near-fault ground motions also require the separation of the selection process for ground motions with and without directivity pulses (Almufti et al., 2013; Hayden et al., 2014). While forward directivity is clearly an important phenomenon in the seismic response for some engineering systems, this separation implies that forward directivity is always more important than other factors (which are largely considered in a secondary implicit fashion). Given the fact that a binary categorisation of ground motions as: (i) pulse-like, or (ii) non-pulse-like, is to some extent a generic classification of what is a continuous phenomenon (Bray and Rodriguez-Marek, 2004; Baker, 2007; Hayden et al., 2014; Shahi and Baker, 2014a), ground motions selected based on this binary categorisation may contain directivity pulses that may or may not necessarily have a severe effect on a given engineered system (compared to records without pulses). Given the abovementioned points, a more rigorous approach to select ground motions (for both near-fault and far-field sites) is to perform the ground motion selection based on IMs that explicitly characterise the severity of ground motions (*i.e.,* such IMs are themselves affected by any forward directivity effects).

In this chapter, a ground motion selection methodology is illustrated which is able to select ensembles of ground motions for near-fault ruptures without separating the selection process for pulse-like and non-pulse-like records. The selection procedure uses explicit ground motion IMs, including pseudo spectral acceleration (SA) ordinates over a wide range of vibration periods, duration, and cumulative IMs, and is based on the generalised conditional intensity measure (GCIM) methodology (Bradley, 2010b, 2012c), as an extension of the CMS (Baker and Cornell, 2006a; Baker, 2011). It is demonstrated that by considering an appropriate

range of IMs, the selected ground motion ensembles contain both an appropriate number of records with forward directivity pulses, and also appropriate pulse period distributions, despite neither of these two aspects being explicitly considered in the selection process itself. The reason for this result is the fact that the occurrence and predominant period of velocity pulses do affect the ground motion IMs, and hence are implicitly considered. In the next section, the different components of the ground motion selection methodology are presented. Subsequently, example applications for scenario and probabilistic seismic hazard analysis (SHA) cases are demonstrated; and the pertinent implications are discussed.

5.3 Considering forward directivity effects in seismic hazard analysis

Conventional ground motion models (GMMs) do not explicitly account for the characteristics of near-fault ground motions such as velocity pulses (*e.g.,* Somerville et al., 1997; Ambraseys and Douglas, 2003; Kurzon et al., 2014); however, having such records in the databases utilised for developing GMMs implicitly influences the resulting predictions (Shahi and Baker, 2011; Spudich et al., 2014). Attempts have been made to modify the prediction of conventional GMMs in order to explicitly account for the characteristics of ground motions containing forward directivity pulses by using *post hoc* modifications (*e.g.,* Somerville et al., 1997; Abrahamson, 2000; Somerville, 2003; Tothong et al., 2007; Spudich and Chiou, 2008; Shahi and Baker, 2011; Spudich et al., 2014). A more rigorous approach to address this problem is the direct consideration of the near-fault characteristics in the development of GMMs (*e.g.,* Shahi, 2013; Chiou and Youngs, 2014), which requires improvements in the existing directivity models (Spudich et al., 2014).

The method used in this study to account for directivity in the hazard is based on Shahi and Baker (2011); however, instead of separating the hazard calculations for pulse-like and non-pulse-like ground motions, the 'total' SA distribution is

assumed to be lognormal with the mean and standard deviation accounting for pulse-like and non-pulse-like ground motions. This approach results in a single target hazard at the site for ground motion selection and is a surrogate for future GMMs that will explicitly address the effect of directivity pulses in a rigorous manner instead of using *post hoc* correction models. The following subsections present the existing Shahi and Baker (2011) approach and this modification.

5.3.1 Shahi and Baker (2011) approach

In the framework proposed by Shahi and Baker (2011), the seismic hazard curves for pulse-like and non-pulse-like ground motions are separately calculated based on the corresponding modified median and standard deviation of SA distribution. The 'total' hazard is then obtained by combining the pulse-like and non-pulse-like contributions. Modification to the SA distribution for pulse-like ground motion hazard involves an amplification of the median prediction using Equations 5.1 and 5.2, and a reduction in the standard deviation based on Equations 5.3 and 5.4:

$$\mu_{lnSA,pulse} = \mu_{lnAF} + \mu_{lnSA,GMM} \tag{5.1}$$

$$\mu_{lnAF} = \begin{cases} 1.131 \, \exp\left(-3.11 \, (ln(T/T_p) + 0.127)^2\right) + 0.058 & \text{if } T \leq 0.88 \, T_p \\ 0.924 \, \exp\left(-2.11 \, (ln(T/T_p) + 0.127)^2\right) + 0.255 & \text{if } T > 0.88 \, T_p \end{cases} \tag{5.2}$$

$$\sigma_{lnSA,pulse} = RF \, \sigma_{lnSA,GMM} \tag{5.3}$$

$$RF = \begin{cases} 1 - 0.20 \, \exp\left(-0.96 \, (ln(T/T_p) + 1.56)^2\right) & \text{if } T \leq 0.21 \, T_p \\ 1 - 0.21 \, \exp\left(-0.24 \, (ln(T/T_p) + 1.56)^2\right) & \text{if } T > 0.21 \, T_p \end{cases} \tag{5.4}$$

where $\mu_{lnSA,pulse}$ and $\sigma_{lnSA,pulse}$ are the median and standard deviation of pulse-like ground motions, μ_{lnAF} and RF are the modification factors applied to the median $\mu_{lnSA,GMM}$ and $\sigma_{lnSA,GMM}$ from a conventional GMM (without directivity parameters), respectively; and T and T_p are SA and pulse periods, respectively. These modifications are applied when the observed pulse period is larger than 0.6 s (Shahi and Baker, 2011).

In addition to the above modifications, bias in the median prediction of conventional GMMs for non-pulse-like ground motions should also be accounted for, which is achieved by de-amplifying the median prediction using the diminution factor, μ_{lnDF}, presented in Equations 5.5 and 5.6. It is assumed that the standard deviation of the conventional GMM is sufficiently accurate for the non-pulse-like ground motions (*i.e.,* $\sigma_{lnSA,no\,pulse} = \sigma_{lnSA,GMM}$).

$$\mu_{lnSA,no\,pulse} = \mu_{lnDF} + \mu_{lnSA,GMM} \tag{5.5}$$

$$\mu_{lnDF} = \begin{cases} \max(-0.0905\, lnT\; g_{M_w}\; g_R\; , -0.0905\, ln2\; M_w\; g_R) & \text{for strike-slip} \\ -0.029\, lnT\; g_{M_w}\; g_R & \text{for dip-slip} \end{cases} \tag{5.6}$$

where g_{M_w} and g_R are the magnitude and distance parameters presented in Equations 5.7 and 5.8:

$$g_{M_w} = \begin{cases} 0 & \text{if } M_w < 6 \\ (M_w - 6)/0.5 & \text{if } 6 \leq M_w \leq 6.5 \\ 1 & \text{if } M_w > 6.5 \end{cases} \tag{5.7}$$

$$g_R = \begin{cases} 10 - R_{jb} & \text{if } R_{jb} \leq 10\ km \\ 0 & \text{if } R_{jb} > 10\ km \end{cases} \tag{5.8}$$

where M_w is the rupture magnitude and R_{jb} is the Joyner and Boore distance parameter.

Pulse-like and non-pulse-like hazards are combined using the occurrence probability of directivity pulse-like ground motions, which is obtained based on the source-to-site geometry and the rupture characteristics, as presented in Equation 5.9 (Shahi and Baker, 2014a):

$$P_{Dir} = \begin{cases} \frac{1}{1+e^{(0.7897+0.1378R_{rup}-0.3533\sqrt{s}+0.02\theta)}} & \text{for strike-slip} \\ \frac{1}{1+e^{(1.483+0.124R_{rup}-0.688\sqrt{d}+0.022\phi)}} & \text{for dip-slip} \end{cases} \tag{5.9}$$

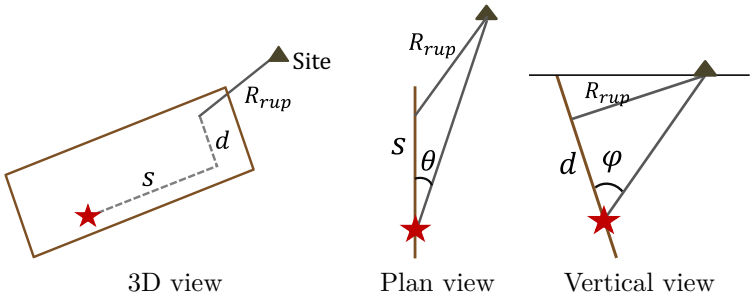

Figure 5.1: Source-to-site parameters for calculating the occurrence probability of directivity pulses (modified from Spudich and Chiou (2008) and Somerville et al. (1997)

where R_{rup} is the closest distance from the site to the rupture surface (denoted as the source-to-site distance in this study), s is the horizontal rupture length and d is the up-dip rupture width from the hypocentre towards the closet point on the rupture surface to the site (as shown in Figure 5.1), and θ and ϕ are are the azimuth and zenith angles respectively, calculated from the hypocentre towards the site (Figure 5.1).

The distribution of pulse period (T_p) for a given rupture can be obtianed based on the empirical model presented in Equation 5.10 and 5.11 (Shahi and Baker, 2014a):

$$lnT_p = -6.256 + 1.084\, M_w \tag{5.10}$$

$$\sigma_{lnT_p} = 0.61 \tag{5.11}$$

Using Equations 5.1-5.11, Shahi and Baker (2011) calculate the hazard for pulse-like ($P_{pulse}(IM > im)$) and non-pulse-like ($P_{nopulse}(IM > im)$) ground motions and combine them to obtain the 'total' hazard, as presented in Equation 5.12:

$$\lambda_{total}(IM > im) = \lambda_{pulse}(IM > im)\, P_{Dir} + \lambda_{no\,pulse}(IM > im)\,(1 - P_{Dir}) \tag{5.12}$$

5.3.2 Approach adopted in this study

In this study, the 'total' SA distribution is assumed to be lognormal with the mean and standard deviation accounting for pulse-like and non-pulse-like ground motions, presented 5.13 and 5.14[1]:

$$\mu_{lnSA,total} = \mu_{lnSA,pulse}\, P_{Dir} + \mu_{lnSA,no\,pulse}\,(1 - P_{Dir}) \tag{5.13}$$

$$\sigma_{lnSA,total} = \{(\mu_{lnSA,pulse} - \mu_{lnSA,no\,pulse})^2\, P_{Dir}.(1 - P_{Dir}) + \sigma^2_{lnSA,pulse}\, P_{Dir} + \sigma^2_{lnSA,GMM}\,(1 - P_{Dir})\}^{0.5} \tag{5.14}$$

Since P_{Dir} depends on the hypocentre location (which affects the source-site-geometrical parameters), there is uncertainty in the calculated P_{Dir} due to the uncertainty in the hypocentre location for future earthquakes. Variation in P_{Dir} is accounted for by assuming the hypocentre location as an aleatory parameter in the scenario and probabilistic SHA, using the rupture dependent probability distribution of Mai et al. (2005). The number of hypocentres along the strike and dip directions are determined based on the dimensions of the rupture surface, specifically at 20 km and 5 km intervals long the strike and dip directions, respectively. Three hypocentres with an equal distance from each other along the strike at a constant down-dip depth (0.6 times the down dip width) are considered for ruptures with lengths and widths smaller than 20 and 5 km, respectively.

In addition to P_{Dir}, the pulse period considered in calculating the median and standard deviation for pulse-like ground motion is also an uncertain variable that affects the hazard analysis results. Instead of assuming a fixed T_p value for a given rupture (*e.g.,* median value from Equation 5.10), the full T_p distribution is used in order to account for the inherent variability in the predicted T_p value.

[1]Law of total variance:
$Var_{lnSA,total} = Var_{lnSA,pulse}\, P_{Dir} + Var_{lnSA,no\,pulse}\,(1 - P_{Dir}) + \mu^2_{lnSA,pulse}\,(1 - P_{Dir})\, P_{Dir} + \mu^2_{lnSA,no\,pulse}\, P_{Dir}\,(1 - P_{Dir}) - 2\,\mu_{lnSA,pulse}\, P_{Dir}\, \mu_{lnSA,no\,pulse}\,(1 - P_{Dir})$

An algorithm is presented in Table 5.1 to illustrate the steps for implementing the adopted approach in this study to consider directivity pulse effects on the SA distribution for scenario and probabilistic SHAs.

Table 5.1: Algorithm to incorporate directivity pulse effects in seismic hazard analysis

For all vibration periods considered:
For all possible rupture scenarios surrounding the site, including multiple realisations for each rupture considering different hypocenter locations:
Determine the rupture characteristics (*e.g.,* M_w, hypocenter location, etc.)
Calculate the pulse period (T_p) distribution for the current rupture scenario using Eq 5.10 and 5.11
$\mu_{lnAF}^{total} = 0$, and $RF^{total} = 0$
For all the pulse period values (t_p) from the T_p distribution:
Calculate the probability of $T_P = t_p$, *i.e.,* $P(t_p - \delta t_p/2 < T_P < t_p + \delta t_p/2)$
Calculate the SA median amplification factor for $T_P = t_p$, *i.e.,* $\mu_{lnAF}(t_p)$ using Eq 5.2
Calculate the standard deviation reduction factor for $T_P = t_p$, *i.e.,* $RF(t_p)$ using Eq 5.4
Calculate the total median amplification factor $\mu_{lnAF}^{total} = \mu_{lnAF}^{total} + \mu_{lnAF}(t_p)\, P(t_p)$
Calculate the total standard deviation factor $RF^{total} = RF^{total} + RF(t_p)\, P(t_p)$
end of the loop for all T_p values considered
Calculate the amplified SA median for pulse-like ground motions, *i.e.,* $\mu_{lnSA,\,pulse} = \mu_{lnAF}^{total} + \mu_{lnSA,\,GMM}$
Calculate the reduced SA standard deviation for pulse-like ground motions, *i.e.,* $\sigma_{lnSA,\,pulse} = RF^{total}\, \sigma_{lnSA,\,GMM}$
Calculate the de-amplified SA median prediction for non-pulse-like ground motions, *i.e.,* $\mu_{lnSA,\,no\,pulse}$, using Eqs 5.5-5.8
Calculate the probability of observing directivity pulse-like ground motions for the current source-to-site geometry using Eq 5.9
Calculate the total median and standard deviation for the current rupture using Eqs 5.13 and 5.14
Establish the SA lognormal distribution for vibration period T conditioned on the current rupture
End of the loop for all rupture scenarios and hypocenter realisations
End of the loop for all vibration periods considered

5.3.3 Comparisons between the two approaches

In order to compare hazard analysis results from the Shahi and Baker (2011) methodology described in the previous subsection with the approach adopted in this study, Figure 5.2 present the distribution of SA at T=3.0 s from the two methods, along with the pulse and no-pulse calculations from Shahi and Baker (2011) for sample M_w= 6.5, 7.0, 7.5 strike-slip scenario ruptures with R_{rup}=5 and 10 km, spanning a wide range of P_{Dir}=[0.16-0.80]. Note that the considered sites were located at the specified R_{rup} from the rupture plane, and multiple realisations of the hypocentre along the strike were used to calculated the SA distribution, as outlined in Table 5.1. Also, the full T_p distribution is utilised for the considered ruptures to modify the corresponding SA distribution. Figure 5.2 shows that both Shahi and Baker (2011) and the approach adopted here result in similar SA distributions, with some negligible differences in the lower or upper tails of the distribution. Such differences are practically not significant when compared to the difference in ground motion estimations from different GMMs (Abrahamson et al., 2008; Bozorgnia et al., 2014).

Figure 5.3 also presents the 16^{th}, 50^{th}, and 84^{th} percentile spectra for a wide range of periods from the same scenarios presented in Figure 5.2. As shown, both methods results in an increased SA values for long periods ($T \geq 1.0$ s), especially for the 50^{th} and 84^{th} percentile SA. As shown in Figures 5.2 and 5.3, for scenarios with smaller P_{Dir} (*e.g.,* M_w= 6.5, R_{rup}=10), both methods result in SA values close to the conventional GMM estimates with no explicit directivity considerations (*i.e.,* Boore and Atkinson (2008) in this case).

In order to investigate the ground motion attenuation with respect to R_{rup} from both methods, Figure 5.4 shows the 50^{th} and 84th SA percentiles at T=3.0 s and 5.0 s for strike-slip ruptures with M_w=6.0-7.5 at R_{rup}=0-50 km. As shown, ground motion estimates from both methods attenuate similarly with distance for a given rupture . Ground motions from both methods converge to the conventional GMM estimates at a certain distance at which directivity effects tends towards

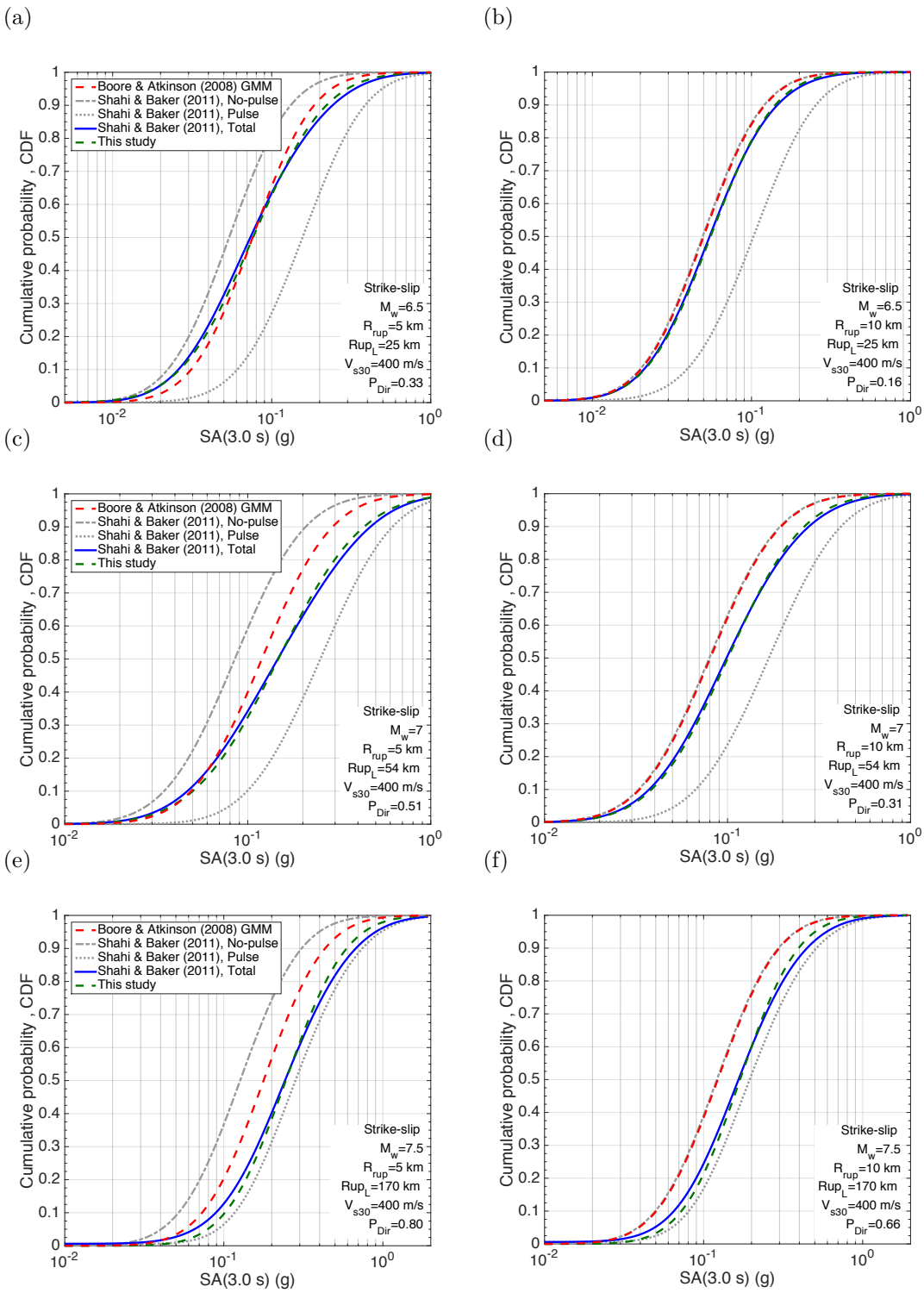

Figure 5.2: Comparison between SA distributions for T=3.0s from the Shahi and Baker (2011) methodology and the approach adopted in this study. Sample strike-slip scenario ruptures with R_{rup}= 5 and 10 km: (a)-(b) M_w=6.5; (c)-(d) M_w=7.0; (e)-(f) M_w=7.5.

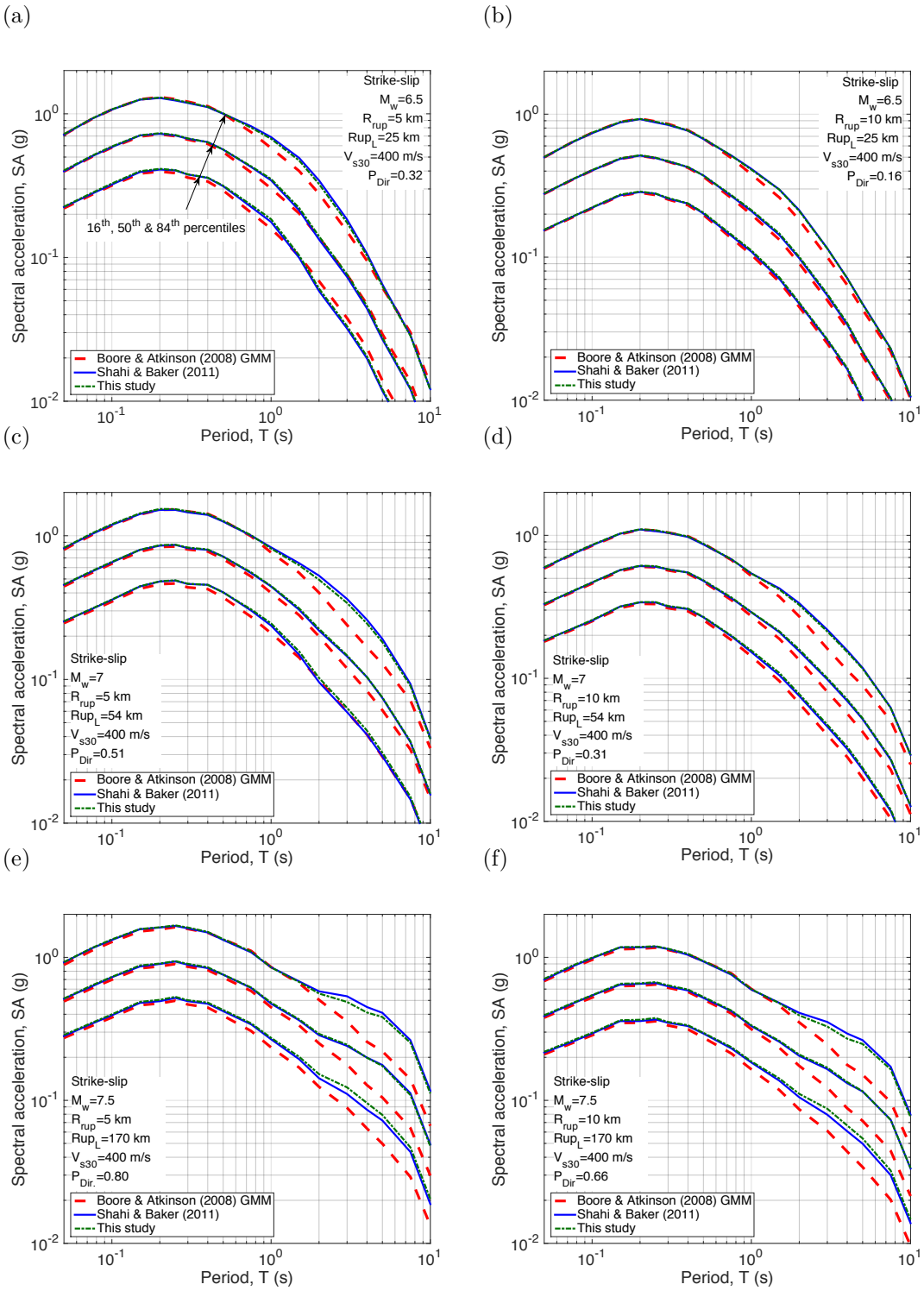

Figure 5.3: Comparison between response spectra from the Shahi and Baker (2011) methodology and the approach adopted in this study. Sample strike-slip scenario ruptures with R_{rup} =5 and 10 km: (a)-(b) M_w=6.5; (c)-(d) M_w=7.0; (e)-(f) M_w=7.5.

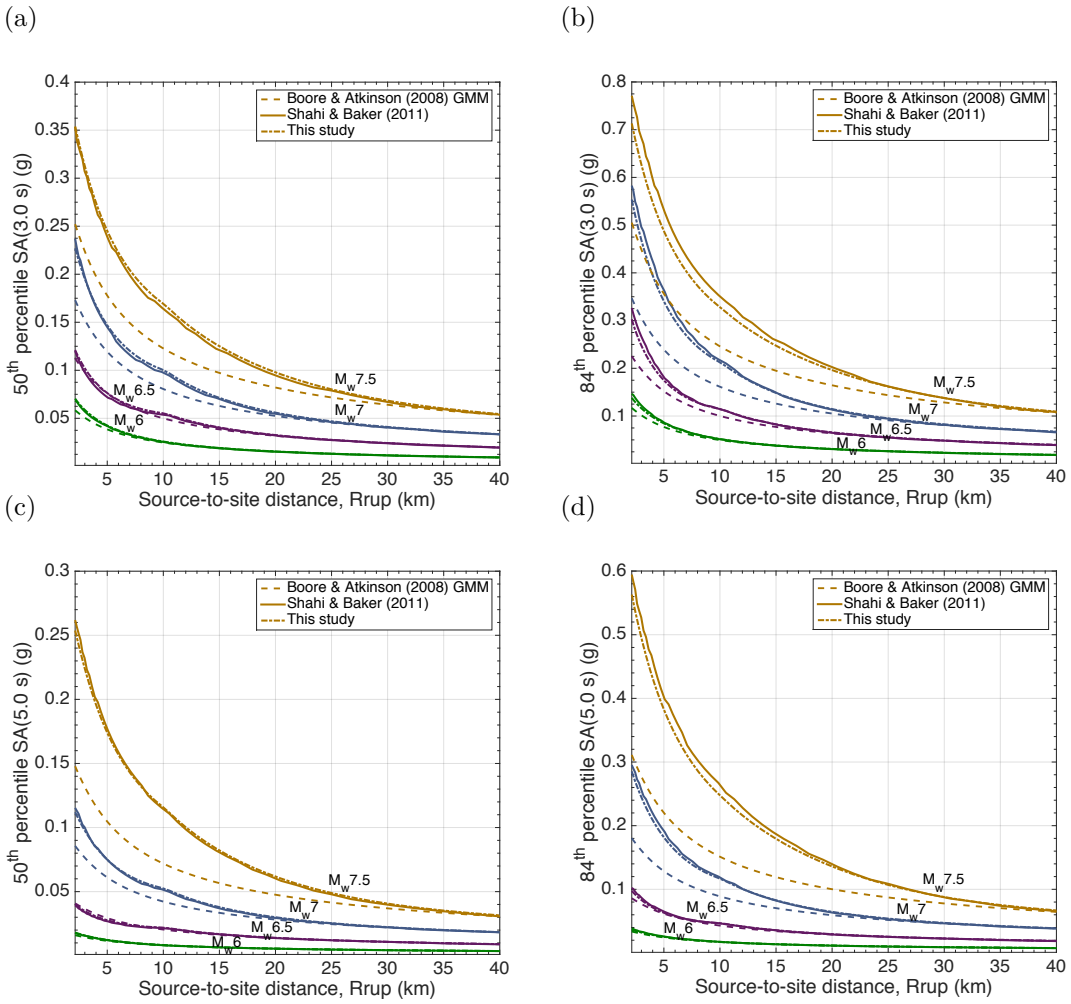

Figure 5.4: Attenuation of the 50$^{\text{th}}$ and 84$^{\text{th}}$ percentile SA with respect to R_{rup} for strike-slip scenario ruptures with M_w=6.0-7.5 and R_{rup}=0-50 km: (a)-(b) SA(3.0s); (c)-(d) SA(5.0s).

zero. It is noted that, although not presented here for brevity, the presented trends in the results hold true for dip-slip scenario ruptures as well.

In addition to the comparison made here, Joshi (2013) demonstrates the appropriateness of the adopted approach in capturing the pulse-like characteristics of the near-fault ground motions recoded during the Canterbury earthquake sequences.

5.4 Ground motion selection methodology

The ground motion selection approach implemented in this study is based on the GCIM methodology of Bradley (2010b, 2012c) and aims to address the aforementioned shortcomings in existing approaches for selecting pulse-like ground motions in the near-fault region. The GCIM methodology considers the contribution of all rupture scenarios affecting the seismic hazard at the site in order to establish the target for ground motion selection. The target is a conditional multivariate distribution of a considered vector of IMs, $\boldsymbol{IM}$, which accounts for various aspects of ground motion severity (*i.e.,* amplitude, frequency content, and duration). A so-called weight vector, w_i, is used to prescribe the relative importance of the considered IMs and calculate the misfit of each prospective ground motion with respect to the target distribution (Bradley, 2012c; Tarbali and Bradley, 2015b). A global misfit is also used to quantify the difference between the selected ground motion ensemble and the target multivariate distribution (Bradley, 2013c), as defined by Equation 5.15:

$$R = \sum_{i=1}^{N_{IM}} w_i (D_{IM_i})^2 \tag{5.15}$$

where w_i is the weight vector value for the i^{th} intensity measure (*i.e.,* IM_i); and D_{IM_i} is the Kolmogorov-Smirnov (KS) test statistic, which is the maximum difference between the empirical IM_i distribution of the selected ground motions and the corresponding target IM_i distribution (Ang and Tang, 1975). Thus, the global misfit, R, consists of the mismatch between the empirical and target distributions of all IMs considered, based on the relative importance defined by the weight vector.

Forward directivity effects are considered in the target for ground motion selection using a directivity-included hazard calculation outlined in Table 5.1, which results in explicit IM distributions containing the directivity effects. No *ad hoc* criterion is enforced in terms of selecting a specific proportion of pulse-like records and their pulse period characteristics in the ground motion selection process.

5.4.1 Causal parameter bounds considered

It is common in ground motion selection practice to first constrain the database of prospective ground motions based on causal parameters similar to those of earthquakes dominating the seismic hazard for the site (*e.g.,* Bommer and Acevedo, 2004; Baker, 2011; Wang, 2011), and then select ground motions based on an explicit IM-based target from either site-specific seismic hazard analysis or general design guidelines (Katsanos et al., 2010). The GCIM methodology has been successfully applied without the need for explicit consideration of causal parameter bounds for ground motion selection based on both probabilistic and scenario seismic hazard analyses (Bradley, 2012c; Tarbali and Bradley, 2015a, 2016). Despite this, causal parameter bounds can assist in removing those records that have drastically different characteristics compared to the target hazard at the site and implicitly constrain ground motion characteristics which are not well represented in the explicit IMs considered (Tarbali and Bradley, 2015a, 2016). The application of causal parameter bounds is also recognised as an important issue in selecting near-fault ground motions by NEHRP (2011). Tarbali and Bradley (2015a, 2016) recommend a criterion for applying causal parameter bounds based on the characteristics of rupture scenarios affecting the seismic hazard at the site. This criterion, which was adopted in this study, is presented in Table 5.2, where $M_w^{k\%}$ and $R_{rup}^{k\%}$ correspond to k^{th} percentiles of M_w and R_{rup} marginal distributions, respectively, from deaggregation results. For a single scenario rupture, M_w and R_{rup} bounds will be simplified to $[M_w - 0.5,\ M_w + 0.5]$ and $[0.5R_{rup},\ 1.5R_{rup}]$. Constrains on the site condition of prospective ground motions is applied based on the 30-m time-averaged shear wave velocity, V_{s30}, for the site, using $[0.5V_{s30},\ 1.5V_{s30}]$ bound (Table 5.2).

As elaborated upon by Tarbali and Bradley (2015a, 2016), these causal parameter bounds are meant to be 'wide' in order to include a large subset of prospective ground motions records for selection based on explicit IMs. Tarbali and Bradley (2015a, 2016) demonstrate the appropriateness of using such bounds

Table 5.2: Bounding criteria on M_w, R_{rup}, and V_{s30} of prospective ground motions for scenario- and PSHA-based ground motion selection

Causal parameter	Lower limit	Upper limit
Magnitude, M_w	$min(M_w^{1\%},\ M_w^{10\%} - 0.5)$	$max(M_w^{99\%},\ M_w^{90\%} + 0.5)$
Source-to-site distance, $R_{rup} \leq 15$	0	30
Source-to-site distance, $R_{rup} > 15$	$min(R_{rup}^{1\%},\ 0.5R_{rup}^{10\%})$	$max(R_{rup}^{99\%},\ 1.5R_{rup}^{90\%})$
Site condition (*i.e.,* V_{s30} value)	$0.5V_{s30}$	$1.5V_{s30}$

for scenario- and PSHA-based ground motion selections. While no explicit bounding criterion is applied specifically for the selection of pulse-like ground motions, it is noted that constraining the M_w of prospective records places a wide (implicit) bound on the T_p of near-fault ground motions (Equation 5.10 demonstrates the dependency of T_p on M_w). Also, the considered R_{rup} bounds assist in selecting records that have close proximity to the rupture scenarios affecting the hazard at the site. The effectiveness of using these causal parameter bounds in selecting ground motion ensembles containing pulse-like and non-pulse-like records is further examined subsequently.

5.4.2 Explicit IMs considered

Within the framework of the GCIM methodology, the following explicit IMs are considered to establish the target for ground motion selection: SA for 18 vibration periods (T= 0.05, 0.075, 0.1, 0.15, 0.2, 0.25, 0.3, 0.4, 0.5, 0.75, 1.0, 1.5, 2.0, 3.0, 4.0, 5.0, 7.5, and 10.0 s); cumulative absolute velocity (CAV); Arias Intensity (AI); and 5-75% and 5-95% Significant Durations (Ds575 and Ds595, respectively). These IMs collectively represent amplitude, frequency content, duration, and cumulative ground motion characteristics. The marginal distributions of these IMs are obtained based on the following GMMs: Boore and Atkinson (2008) for SA; Campbell and Bozorgnia (2010) for CAV; Campbell and Bozorgnia (2012) for AI; and Kempton and Stewart (2006) for Ds575 and Ds595. The geometric mean of the two horizontal ground motion components is used as the

IM definition in this study. Various studies have demonstrated that, depending on the rupture mechanism and the distance from the source, the strike-normal component of the near-fault ground motions may not necessarily represent the strongest direction of the ground motion (Howard et al., 2005; Watson-Lamprey and Boore, 2007; Huang et al., 2009; Shahi and Baker, 2014b).

Correlations between the considered IMs in this study are based on the existing empirical models (Baker and Jayaram, 2008; Bradley, 2011a, 2012a, 2015). It is noted that the database used for calculating these correlation coefficients contains ground motions with forward directivity pulses in addition to non-pulse records. A comparison has been carried out in Appendix B between the correlation coefficients derived solely for the ground motions with directivity pulses and those obtained for a mixed database of records. As shown in Appendix B, for the practical purposes of ground motion selection, the difference between these correlation coefficients can be neglected. It is noted that, as presented by Baker and Bradley (2017), epistemic uncertainty from implementing alternative GMMs to establish the target IM distribution for ground motion selection is significantly greater than the epistemic uncertainty from implementing alternative IM correlation models.

5.4.3 Target IM distributions considered

In order to investigate the effect of explicitly considering directivity modification to the SA distribution discussed in the previous sections, ground motion ensembles were selected representing the target hazard as computed with and without the directivity modification (*i.e.,* with and without the application of Equations 5.1-5.14). For these cases, SA ordinates are the only IMs considered in the GCIM weight vector (*i.e.,* cases 1 and 2 presented in Table 5.3). In order to illustrate the benefits of considering cumulative and duration-related IMs (*e.g.,* CAV, D_{s575}, and D_{s595}) in selecting ground motion ensembles in the near-fault region, two further weight vectors (*i.e.,* cases 3 and 4) are also considered. While

AI is given a zero weight, because as shown by Tarbali and Bradley (2015b), considering CAV yields an appropriate representation of the target AI distribution via the selected records, comparison between the target and empirical AI distributions are provided in any case. The effect of the GCIM weight vector on the characteristics of selected ground motions and the choice of these IMs and the associated weight are discussed thoroughly by Bradley (2012c) and Tarbali and Bradley (2015a,b, 2016).

Table 5.3: Weight vectors and target hazards considered for ground motion selection

Case	Directivity effects	Amplitude and frequency content	Duration		Cumulative effects
		SA	D_{s575}	D_{s595}	CAV
1	Neglected	1.0[1]	0.0	0.0	0.0
2	Considered	1.0[1]	0.0	0.0	0.0
3	Considered	0.8[1]	0.1	0.1	0.0
4	Considered	0.7[1]	0.1	0.1	0.1

[1] Evenly distributed over 18 SA ordinates, *e.g.,* each SA ordinates has a weight of w_i =0.7/18 for case 3.

5.4.4 Empirical database of ground motions considered

The database of recorded ground motions considered in this study contains 6545 non-pulse-like records from the NGA-West2 database (Ancheta et al., 2013) with $M_w \geq 5.0$ and R_{rup}=[0.1, 600] km (the complete NGA-West2 database was not openly accessible at the time of this study), and 143 records identified as containing directivity pulses by Shahi and Baker (2014a). Figure 5.5a illustrates the $M_w - R_{rup}$ distribution of the considered ground motions records, along with the NEHRP (2003) site classification for ground motions containing directivity pulses. It can be seen that the majority of ground motions with directivity pulses belong to site class C ($360 \leq V_{s30} \leq 760$ m/s) and D ($180 \leq V_{s30} \leq 360$ m/s) and have R_{rup} values less than 40 km. Figure 5.5(b) also depicts the T_p distribution

of the directivity ground motion present in the database, which shows that the majority of the directivity records have $T_p \leq$10 s.

5.5 Scenario SHA-based ground motion selection in the near-fault region

5.5.1 Scenarios considered

Before examining ground motion properties for a PSHA-based seismic hazard where directivity effects can be caused by multitude of nearby ruptures, it is insightful to first understand the salient trends for the simpler case of a single rupture scenario-based seismic hazard. Ground motions selected based on single scenario ruptures can also be utilised to assess the seismic performance of engineered system against the occurrence of a given scenario rupture (FEMA-P58, 2012). 78 rupture scenarios presented in Table 5.4 were considered to empirically investigate the characteristics of the selected pulse-like and non-pulse-like ground motions. These scenarios encompass a wide range of causal parameters (*i.e.,* M_w=6.0-7.5; R_{rup}=5-30km; strike-slip and dip-slip faulting mechanisms) and site conditions (*i.e.,* V_{s30}=200, 400, and 800 m/s). The rupture length (Rup_l) for the strike-slip faults, and rupture width (Rup_w) for dip-slip faults were obtained from the empirical model of Leonard (2014). As shown in Figure 5.6, the considered rupture scenarios encompass a wide range of directivity pulse occurrence probability, from 0.05 to 0.8. In addition, as noted previously, multiple realisation of the hypocentre along the strike and dip directions are considered in calculating the rupture directivity probability based Mai et al. (2005). The site conditions considered represent typical soft soil, stiff soil, and soft rock conditions, approximately corresponding to NEHRP site classes D, C, and A/B, respectively (NEHRP, 2003).

A total of 20 ground motion records were selected using 10 replicate selection

(a)

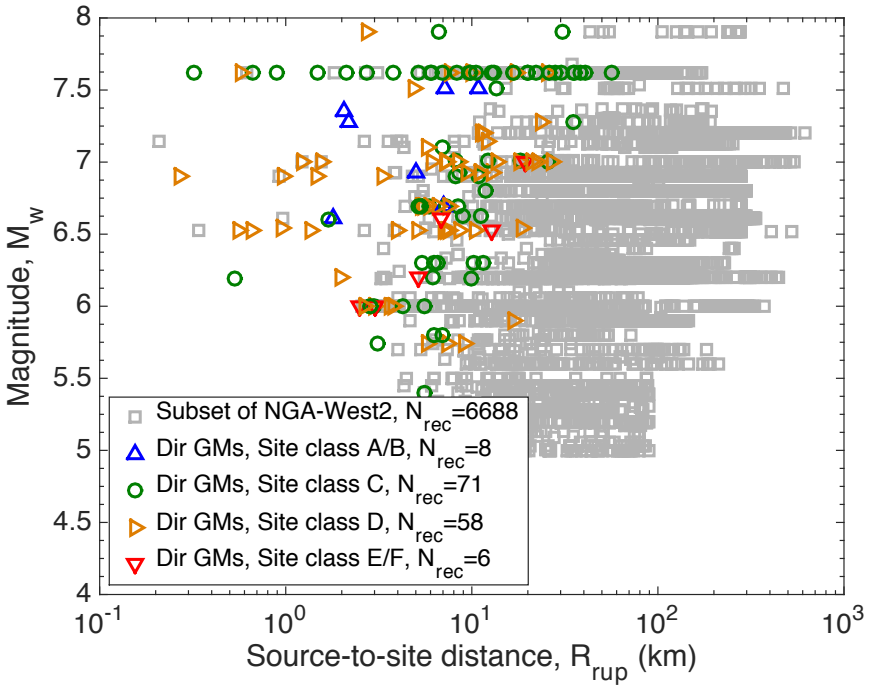

(b)

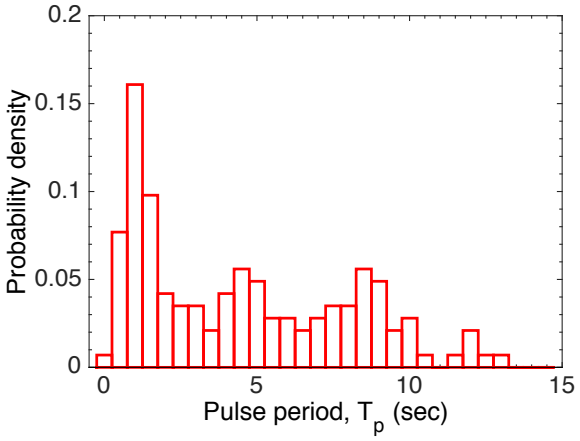

Figure 5.5: (a) $M_w - R_{rup}$ distribution of the considered ground motion records along with the NEHRP (2003) site classification (*i.e.,* A/B, C, D, E/F) for the directivity ground motions; and (b) pulse period distribution of the directivity ground motions.

Table 5.4: Characteristics of the 78 scenario ruptures and site conditions considered for scenario-based ground motion selection

Magnitude, M_w	Rupture, mechanism	Rupture length/width[1], Rup_l/Rup_w (km)	Source-to-site distance, R_{rup} (km)	Site condition, V_{s30} (km)
6.0	Strike-slip Dip-slip	13 9	5, 10, 20	200, 400, 800
6.5	Strike-slip Dip-slip	25 14	5, 10, 20	200, 400, 800
7.0	Strike-slip Dip-slip	54 22	5, 10, 20	200, 400, 800
7.5	Strike-slip Dip-slip	170 35	5, 10, 20 30	200, 400, 800

[1]Note: Rupture length (Rup_l) for strike-slip and rupture width (Rup_w) for dip-slip mechanism.

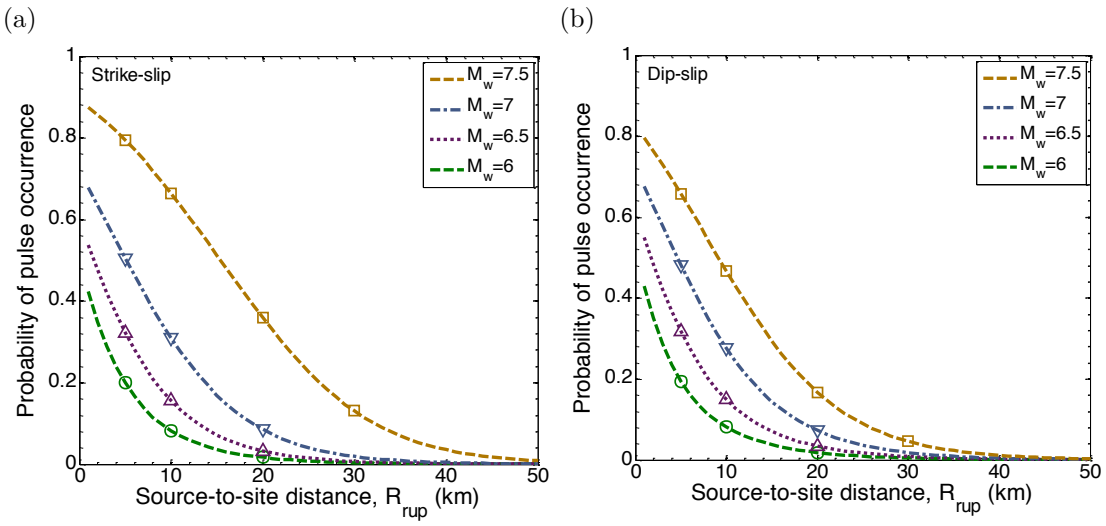

Figure 5.6: Directivity pulse probability for scenario ruptures: (a) strike-slip; (b) dip-slip. Points indicate the considered scenarios.

iterations (Bradley, 2012c; Tarbali and Bradley, 2015b) to obtain an ensemble with the lowest misfit to the target (*i.e.,* smallest global residual from Equation 5.15). In order to investigate the variability in the number of pulse-like ground motions within the selected ensemble of records and the variation in their characteristics, 20 different ensembles are selected for each rupture scenario.

5.5.2 Selected ground motions and their properties

5.5.2.1 Explicit IMs

Figure 5.7 illustrates the SA ordinates of the selected ground motions based on the case 1-4 weight vectors in Table 5.3 (from the specific ensemble with the median number of directivity ground motions, N_{Dir}, among the 20 replicate ensembles) and their corresponding 16^{th}, 50^{th}, and 84^{th} percentiles for a M_w=6.5 strike-slip scenario rupture with R_{rup}=5 km and V_{s30}=400 m/s. The response spectra of ground motion records classified as 'directivity ground motions' according to Shahi and Baker (2014a) are shown as a different colour, with the proportion of such selected records (N_{Dir}/N_{gm}) noted in the figure inset as well as the predicted directivity pulse probability, P_{Dir}.

As shown by the similarity of the target (GCIM) spectra and selected ensemble percentiles in Figure 5.7, the selected records appropriately represent the target SA hazard for all cases considered. Figure 5.7a illustrates that several of the selected ground motions for case 1 contain notable directivity effects as evident from their long period spectral peaks, even though directivity effects are not explicitly incorporated in the target spectrum for this case. Note that conventional GMM predictions in the near-fault region are implicitly influenced by directivity records in empirical ground motion databases. Figure 5.7b-d also illustrate that considering directivity effects in the determination of the target spectra (cases 2-4) along with non-SA IMs (cases 3-4) in the selection process, in general, results in a larger number of directivity ground motions (*i.e.,* increases in N_{Dir}/N_{gm} from

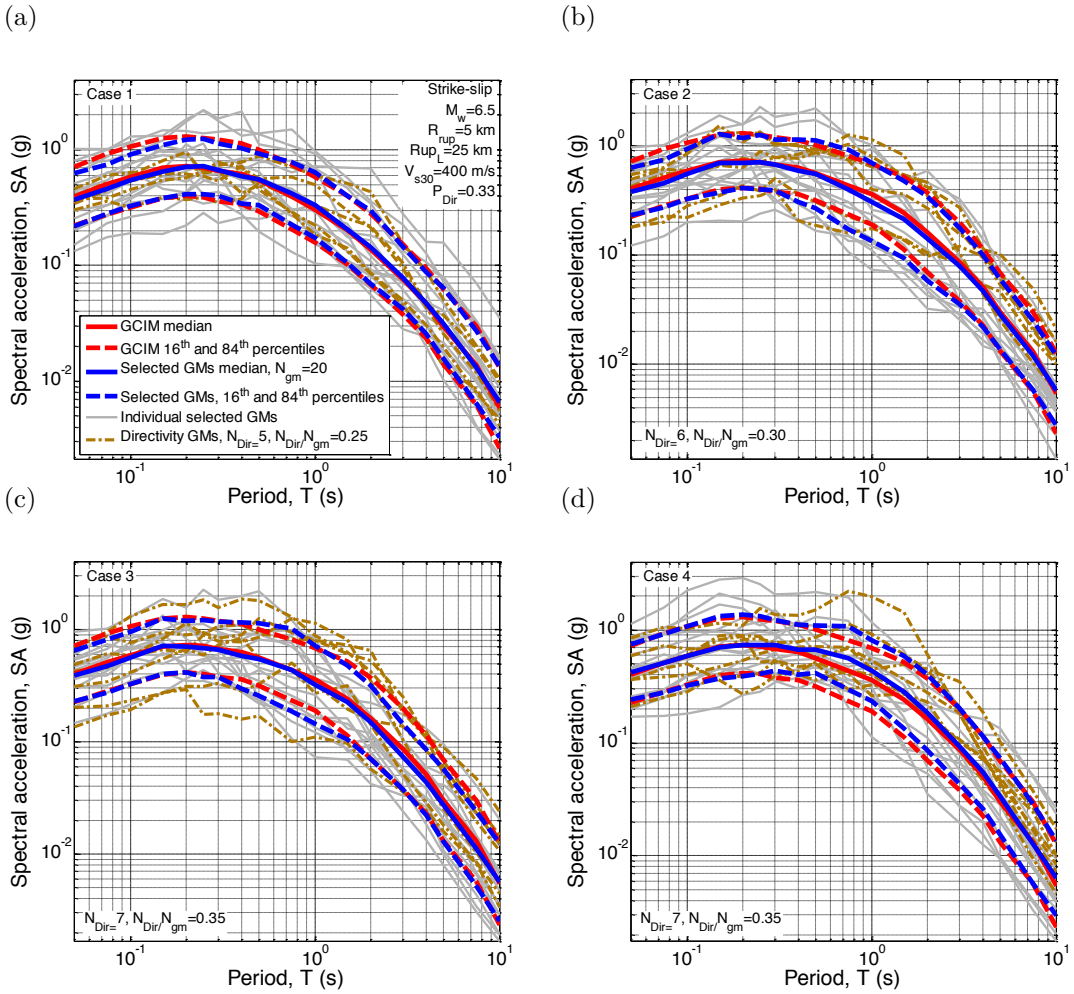

Figure 5.7: Comparison between the SA ordinates of selected records and the target hazard for an illustrative scenario (M_w=6.5, R_{rup}=5km, and V_{s30}=400 m/s): (a)-(b) selection based on only SA ordinates without and with directivity modifications, respectively; (c) selection based on SA, D_{s575}, and D_{s595} with directivity modifications; and (d) selection based on SA, D_{s575}, D_{s595}, and CAV with directivity modifications.

0.25-0.35), and also that N_{Dir}/N_{gm} in such cases is consistent with the scenario directivity probability of 0.33. In contrast, Figure 5.8 presents the results for a M_w=7.0 strike-slip scenario rupture with R_{rup}=5 km and V_{s30}=400 m/s in which it can be seen that N_{Dir}/N_{gm} (ranging from 0.3-0.40) for all four cases is small relative to the predicted directivity probability of P_{Dir}=0.51. Despite this incompatibility in the proportion of selected directivity motions with P_{Dir}, it can be seen that the selected ground motion ensembles have an appropriate representation of the target SA.

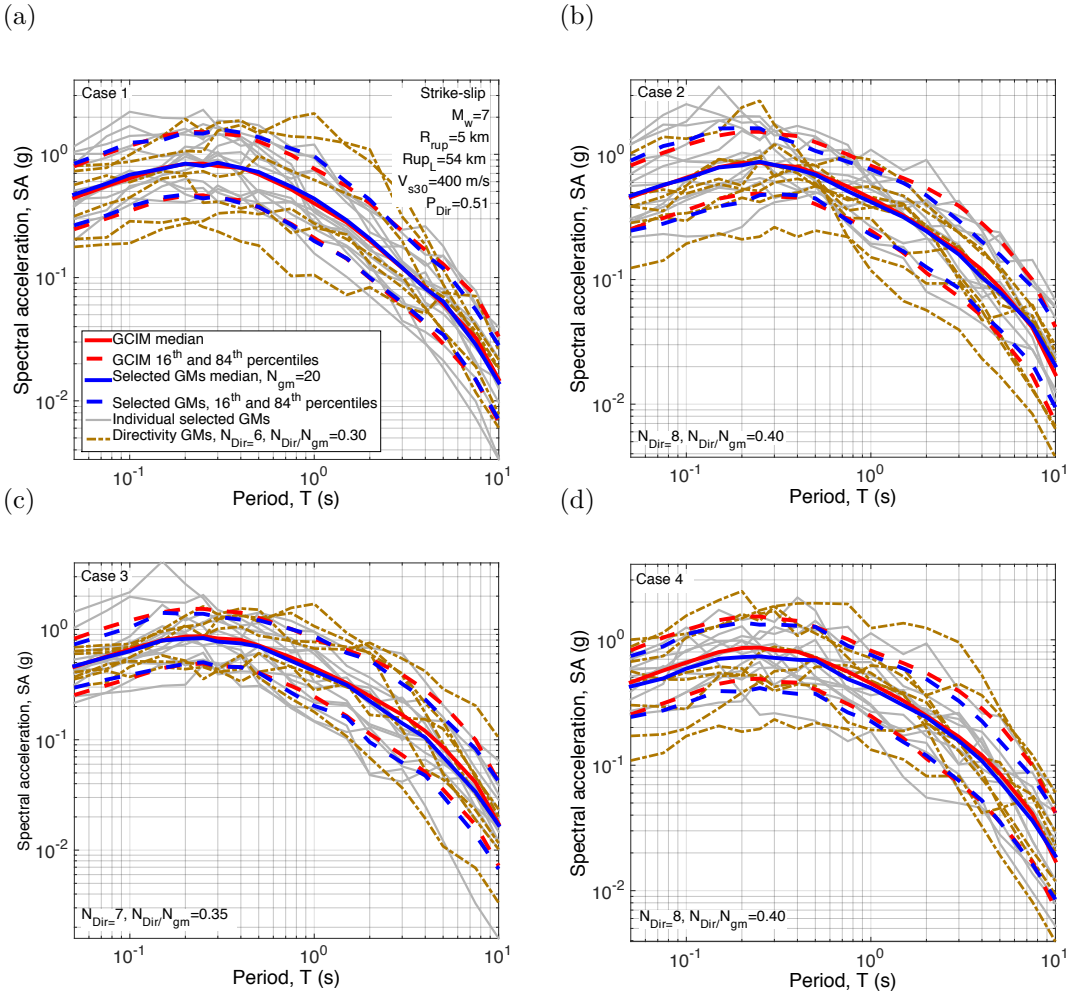

Figure 5.8: Comparison between the SA ordinates of selected records and the target hazard for an illustrative scenario (M_w=7.0, R_{rup}=5km, and V_{s30}=400 m/s): (a)-(b) selection based on only SA ordinates without and with directivity modifications, respectively; (c) selection based on SA, D_{s575}, and D_{s595} with directivity modifications; and (d) selection based on SA, D_{s575}, D_{s595}, and CAV with directivity modifications.

The ground motions depicted in Figures 5.7a-b and Figures 5.8a-b are selected based on considering only SA ordinates in the selection process. This may result in a biased representation for other important ground motion characteristics such as duration and cumulative IMs. As illustrated in Figures 5.9a and 5.9e for the same rupture scenario as in Figure 5.7, and as an example among other scenarios and IMs, statistically significant bias is present in the D_{s575} and AI distributions of these ground motions selected based on only SA ordinates for case 1. The bias is indicated by the empirical distribution of the ensemble lying 'outside' the Kolmogorov-Smirnov (KS) goodness-of-fit test bounds. Note that the D_{s575}, CAV, and AI distributions of the records from case 2 and 3 are also close to the KS bounds. This bias can be resolved by including such IMs in the selection process using an appropriate weight vector in the GCIM ground motion selection methodology (Bradley, 2012c; Tarbali and Bradley, 2015b). This is shown in Figures 5.9a and 5.9e for the ground motion ensembles selected based on cases 3-4, for which, in addition to SA, duration and cumulative IMs are also included in the selection process. As illustrated in Figures 5.9b, d, and f for D_{s575}, D_{s595}, and CAV, while ignoring non-SA IMs might not result in a statistically biased distribution for some non-SA IMs, considering such non-SA IMs in the selection process will improve their representativeness in the selected ensembles. As shown in Figures 5.9b, d, and f, selected records based on the case 4 weight vector have closer empirical distributions to the target IM distributions, compared with the case 1-3 ensembles.

5.5.2.2 Directivity properties of selected ground motions: Number of directivity ground motions

The proportion of directivity ground motions, N_{Dir}/N_{gm}, in the selected ensemble of records is considered important when selecting ground motion ensembles in the near-fault region (NEHRP, 2011). In order to compare the number of directivity ground motions among the 20 replicate ensembles selected, Figure 5.10 presents the proportion of directivity records in each ensemble for the considered

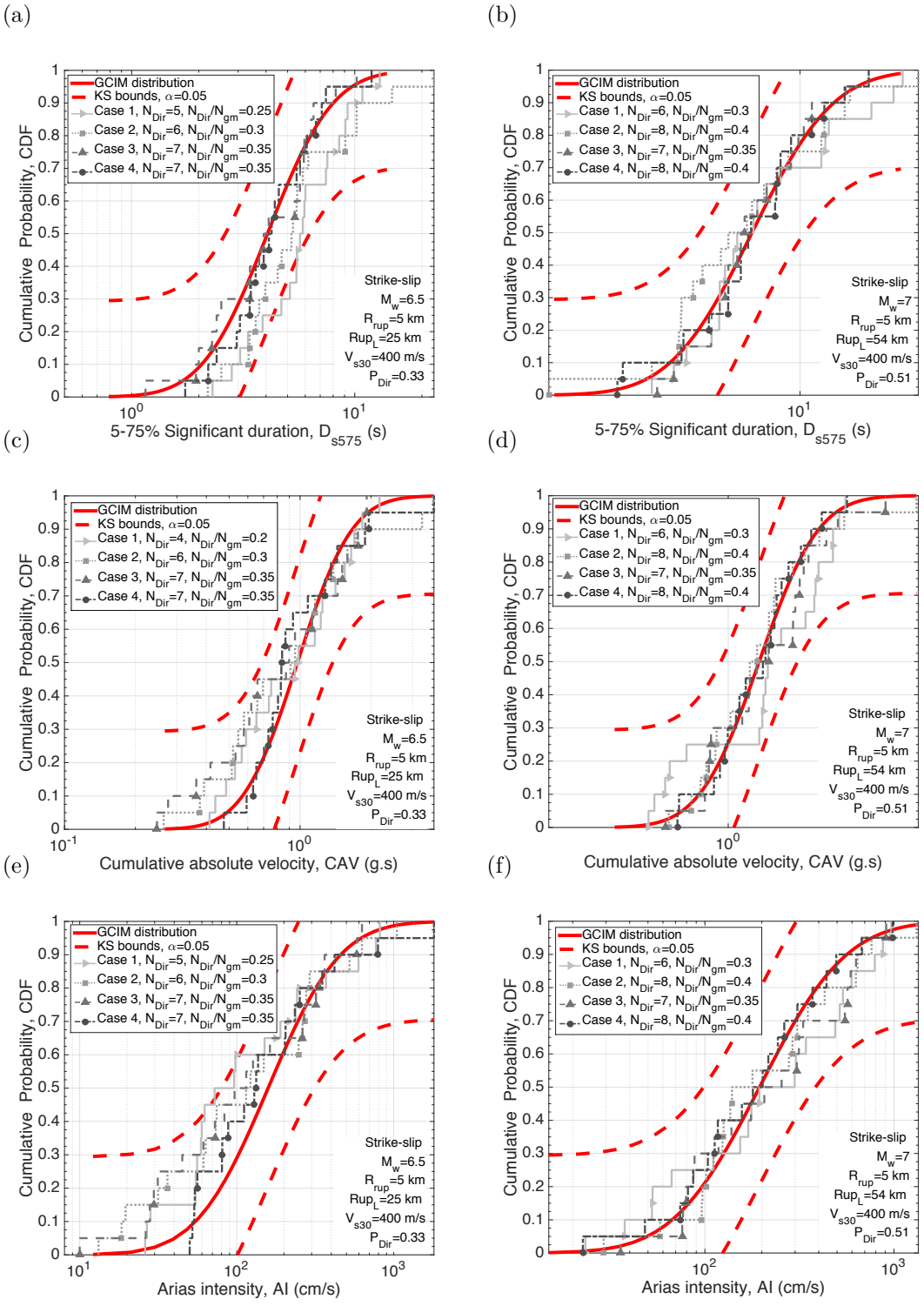

Figure 5.9: Comparison between the non-SA IM distributions for two illustrative rupture scenario (M_w=6.5 and 7.0, R_{rup}=5 km, and V_{s30}=400 m/s): (a)-(b) Ds575; (c)-(d) CAV; and (e)-(f) AI. The marked points in the empirical distributions of the ensembles indicate the IMs of the directivity ground motions.

strike-slip rupture scenarios. The box-and-whisker plots illustrate the variation in the proportion of directivity records across the 20 selected ensembles for each scenario. For comparison, the predicted directivity probability (P_{Dir}) for each rupture scenario is also shown (Shahi and Baker, 2014a). Note that for all four ground motion selection cases considered, the directivity properties (*i.e.,* P_{Dir} and T_p distribution) are not considered in the ground motion selection process itself, and the selection process is conducted based solely on the target IM distributions. The presented results in Figure 5.10 illustrate that the decreasing trend of P_{Dir} with the increase in R_{rup} is reflected in the selected proportion of pulse-like ground motions. While considering duration and cumulative measures (*i.e.,* case 3-4 results) generally yields ensembles with a larger number of directivity ground motions, the N_{Dir}/N_{gm} values of the selected ensembles for rupture scenarios with P_{Dir} >0.5 is lower than the predicted value (*e.g.,* the M_w=7.0 and 7.5, R_{rup}=5 km scenarios). It is critically important to note however that there is uncertainty associated with the calculated P_{Dir} based on Shahi and Baker (2014a) model for such rupture scenarios, as the existing empirical database used to develop the model contains a small number of records with R_{rup} ≤10 km and M_w ≥7.0.

Visual comparisons between the results presented for the V_{s30}=800 m/s cases (Figure 5.10c) with those for V_{s30}=200 and 400 m/s cases (Figures 5.10a-b) also shows that, in general, the proportion of directivity ground motions selected for the V_{s30}=800 m/s site condition is relatively smaller. In order to investigate the effects of the empirical ground motion database characteristics after the application of causal parameter bounds (Table 5.2), Figure 5.11 presents the number of available directivity and non-directivity (*i.e.,* 'ordinary') ground motions (*i.e.,* N_{Dir} and N_{Ord}, respectively) in the database for the V_{s30}=200, 400, and 800 m/s site conditions. It is shown that both N_{Dir} and N_{Ord} are greater for V_{s30}=400 m/s scenarios than for V_{s30}=200 and 800 m/s. Note that, in addition to the number of available records, the proportion of directivity ground motions selected depends on the properties of the available records in terms of their explicit IMs. For instance, while N_{Dir} and N_{Ord} for the M_w=7.0 and 7.5 scenarios at R_{rup}=5 km

(a)

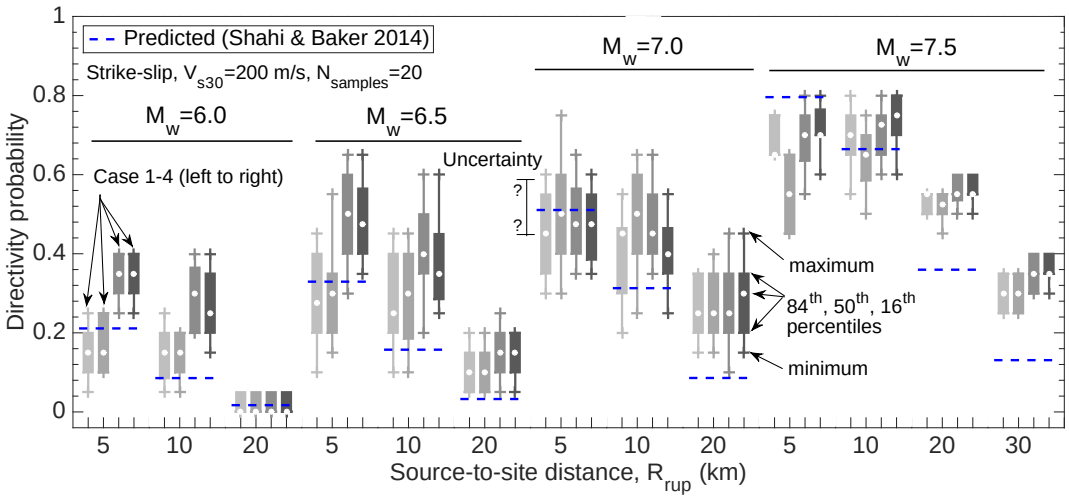

(b)

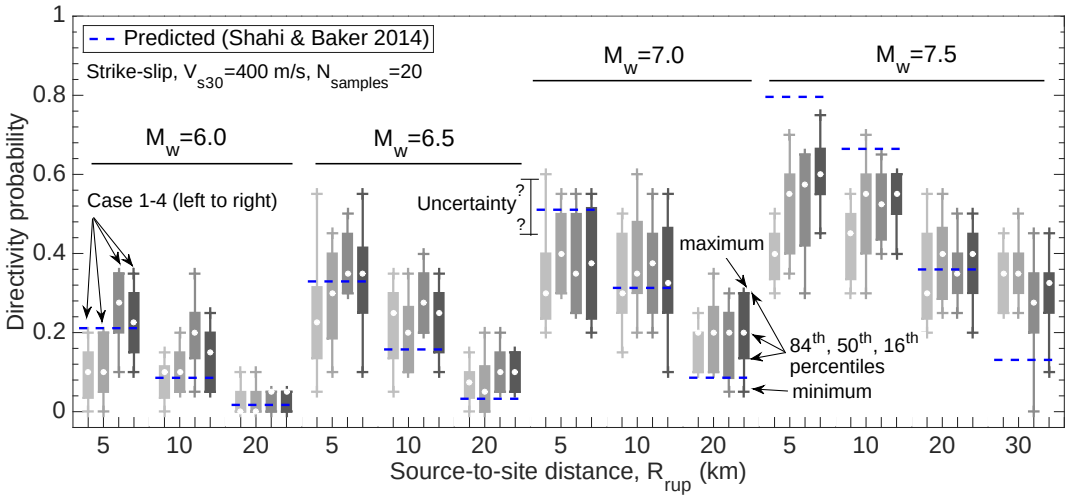

Figure 5.10: Directivity probability represented by the selected ground motion ensembles for the considered strike-slip rupture scenarios: (a)-(b) V_{s30}=200 and 400 m/s, respectively. The results for case 1-4 are shown by separate box-and-whisker colors as annotated.

(c)

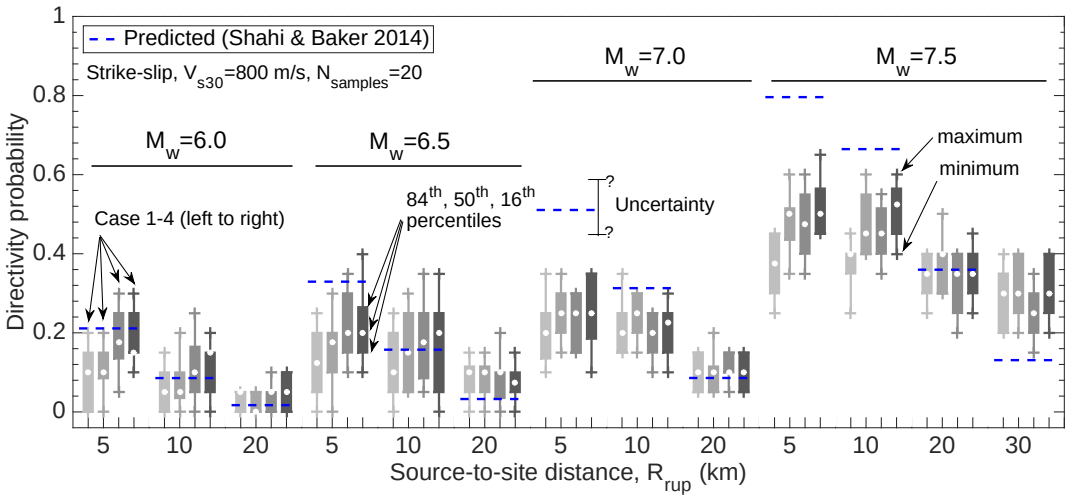

Figure 5.10: *(continued)* Directivity probability represented by the selected ground motion ensembles for the considered strike-slip rupture scenarios: (c) V_{s30}= 800 m/s, respectively. The results for case 1-4 are shown by separate box-and-whisker colors as annotated.

are smaller for the V_{s30}=200 m/s site condition than those for V_{s30}=400 m/s, the selected records for the V_{s30}=200 m/s site condition have closer representation of P_{Dir} than those selected for V_{s30}=400 m/s (see Figure 5.10), because the available records have a better representation of the hazard at a V_{s30}=200 m/s site. In general, it can be expected that having larger N_{Dir} and N_{Ord} allows for a more appropriate representation of P_{Dir}. This is, for example, shown for the M_w=6.5 rupture at R_{rup}=5 km, as relatively larger N_{Dir} and N_{Ord} for the V_{s30}=400 m/s site condition assists in representing P_{Dir} almost exactly by the ensemble with the median N_{Dir} (Figure 5.10), as opposed to the V_{s30}=200 and 800 m/s site conditions for which there are smaller N_{Dir} and N_{Ord}.

5.5.2.3 Directivity properties of selected ground motions: Pulse period

In addition to the proportion of directivity ground motions, pulse period (T_p) is also noted as an important factor to consider in the near-fault ground motion selection (NEHRP, 2011). Figure 5.12 illustrates the T_p distribution of the pulse-

(a)

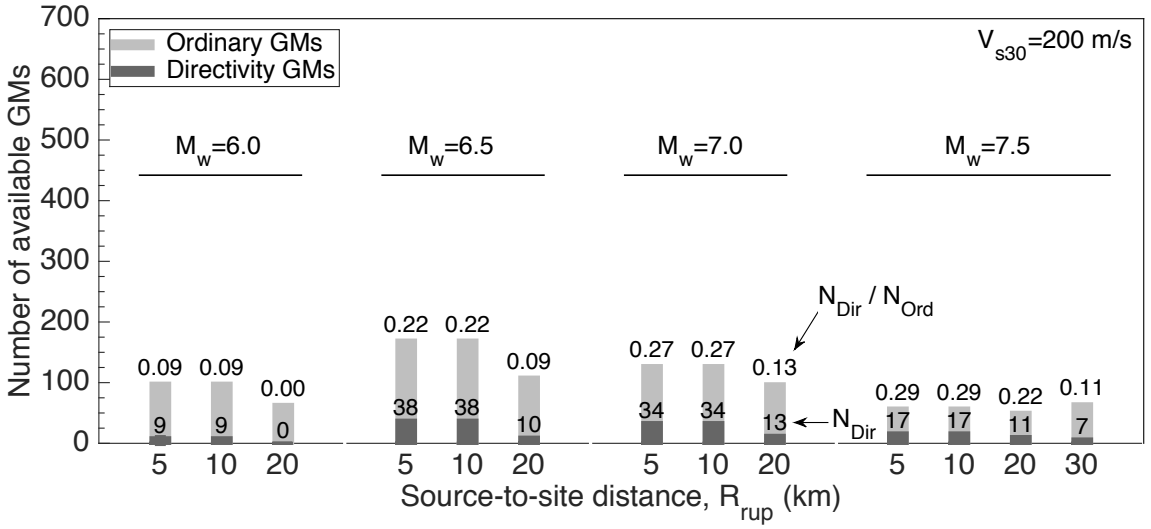

(b)

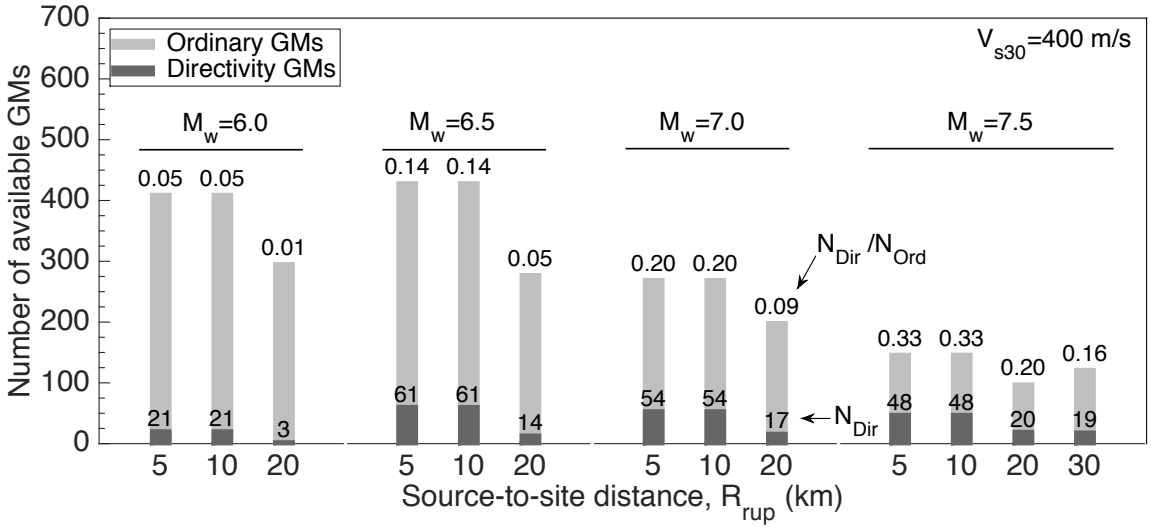

Figure 5.11: Number of the available directivity and non-directivity (*i.e.,* 'ordinary') ground motions in the database after the application of causal parameters bounds of Table 2. (a)-(b) V_{s30}=200 and 400 m/s, respectively.

(c)

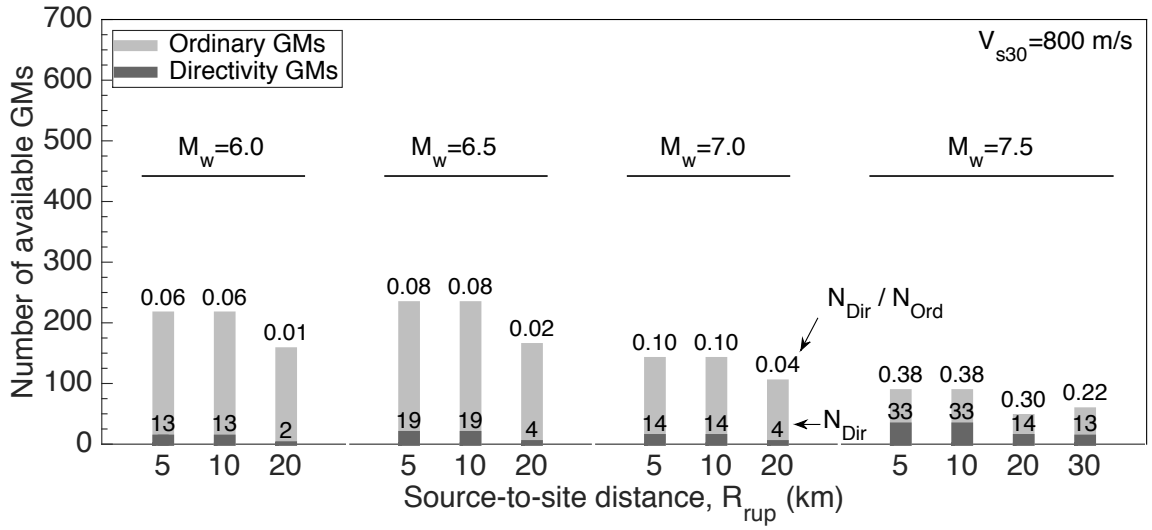

Figure 5.11: *(continued)* Number of the available directivity and non-directivity (*i.e.,* 'ordinary') ground motions in the database after the application of causal parameters bounds of Table 2. (c) V_{s30}= 800 m/s, respectively.

like motions for cases 1-4 from the ensemble with the median number of directivity ground motions in comparison to the predicted T_p distribution from Shahi and Baker (2014a) for three illustrative rupture scenarios with small, medium, and large P_{Dir} values (*i.e.,* M_w=6.5, 7.0, and 7.5 strike-slip ruptures with R_{rup}=5 km and P_{Dir}=0.33, 0.51, and 0.80, respectively). The results are presented for the V_{s30}=400 and 800 m/s site conditions. As shown, the selected directivity ground motions for both site conditions have an appropriate representation of the predicted distribution within the statistical rejection bounds. This holds true for the other considered scenario and site conditions. It is reiterated that no *ad hoc* criterion was enforced for selecting directivity records in the selection process. As noted previously, selecting ground motion records based on explicit IMs, which are themselves affected by any forward directivity effects, can result in ensembles with an appropriate representation of the target IM-based hazard and the other implicit parameters including T_p, without the need to directly enforce that the ground motion ensembles have a specific proportion of pulse-like motions or specific T_p distributions.

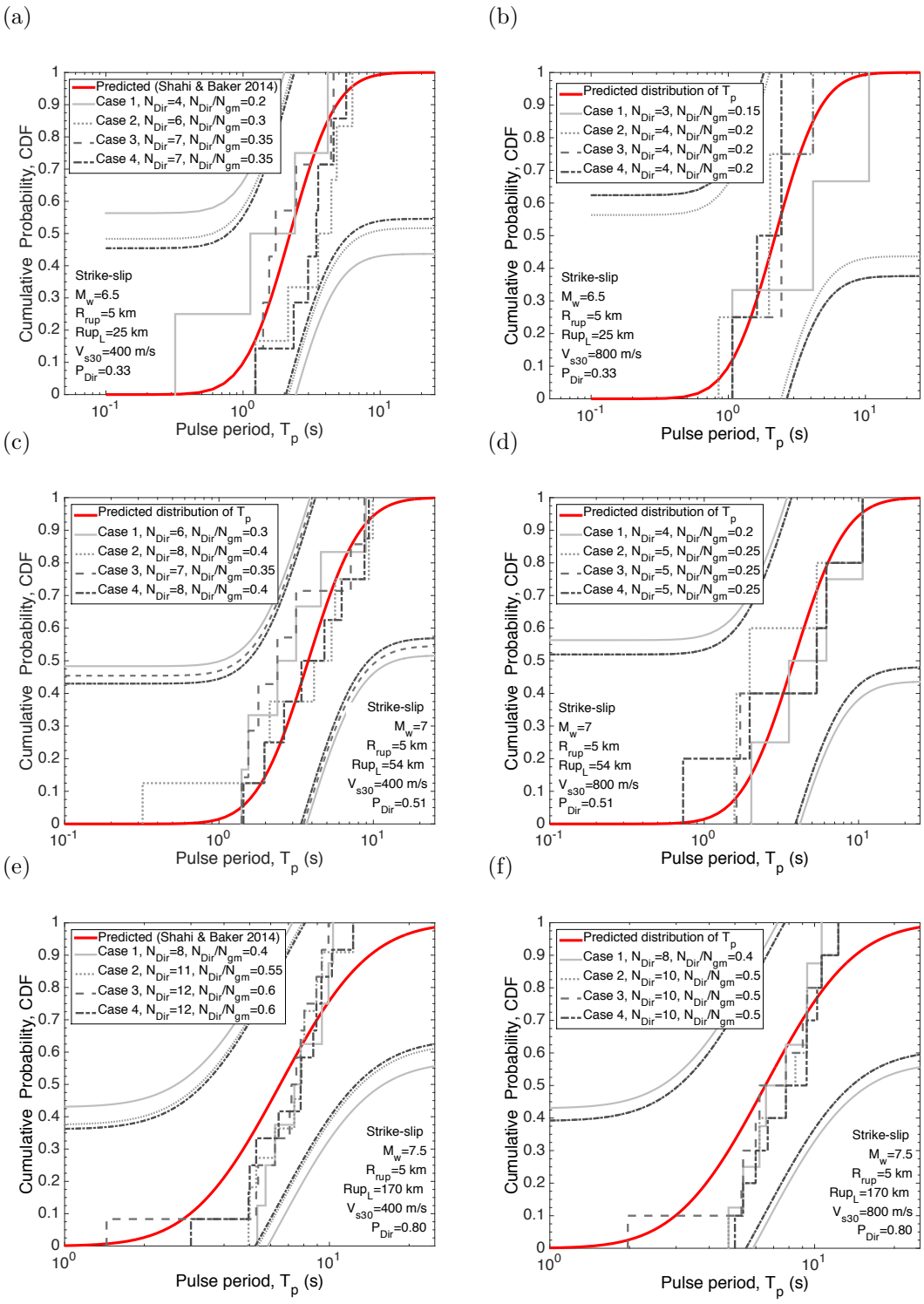

Figure 5.12: Comparison between the pulse period distributions of the selected ensembles with the predicted distribution for three illustrative rupture scenarios with small, medium, and large P_{Dir}: (a)-(b) M_w=6.5, R_{rup}=5km, P_{Dir}=0.33; (c)-(d) M_w=7.0, R_{rup}=5km, P_{Dir}=0.51; and (e)-(f) M_w=7.5, R_{rup}=5km, P_{Dir}=0.80. The results are presented for two site conditions with V_{s30}= 400 m/s and 800 m/s.

5.5.2.4 Causal parameters and their effect on selected directivity ground

In addition to explicit IMs, causal parameters such as M_w and R_{rup} are commonly examined for the selected ensemble of ground motions in comparison to the target scenario of interest. Figure 5.13 presents the $M_w - R_{rup}$ distribution of the ground motion ensembles selected for M_w=6.5 and 7.5 strike-slip ruptures with R_{rup}=5 and 20 km. As shown, the selected ground motions have an appropriate representation of the scenario M_w and R_{rup}, with both pulse-like and non-pulse-like ground motions encompassing the target scenario. This is mainly due to the fact that considering wide bounds on the causal parameters, as in Table 5.2, facilitates selecting ground motions that have an appropriate representation of the target rupture in terms of causal parameters, in addition to having an appropriate representation of the target explicit IMs, as discussed thoroughly by Tarbali and Bradley (2015a, 2016).

In order to investigate how causal parameter bounds affect the selection of pulse-like motions, ground motions are selected without considering the bounds presented in Table 5.2 and the proportion of directivity ground motions among the 20 replicate ensembles are compared with the predicted value. Figure 5.14 presents the results for the same scenario as in Figure 5.10, which illustrates that the number of pulse-like ground motions selected for scenarios with M_w=7.5 is significantly smaller when causal parameter bounds are not considered. This illustrates the positive influence of causal parameters bounds in selecting ground motion ensembles for the near-fault scenarios, in addition to those mentioned for Figure 5.13.

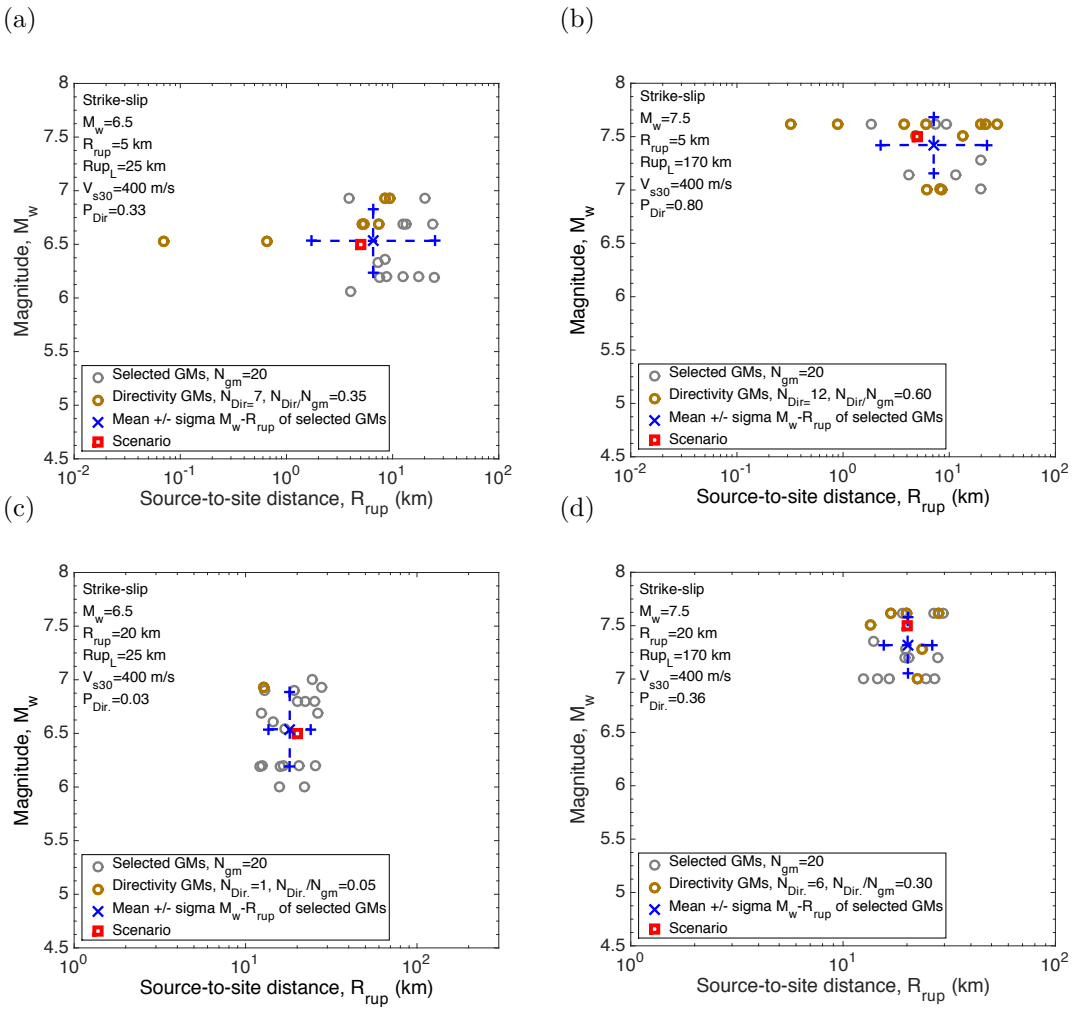

Figure 5.13: $M_w - R_{rup}$ distribution of the selected ground motion compared with the target scenario with V_{s30}=400 m/s site condition: (a) M_w=6.5, R_{rup}=5 km; (b) M_w=7.5, R_{rup}=5 km; (c) M_w=6.5, R_{rup}=20 km; (d) M_w=7.5, R_{rup}=20 km.

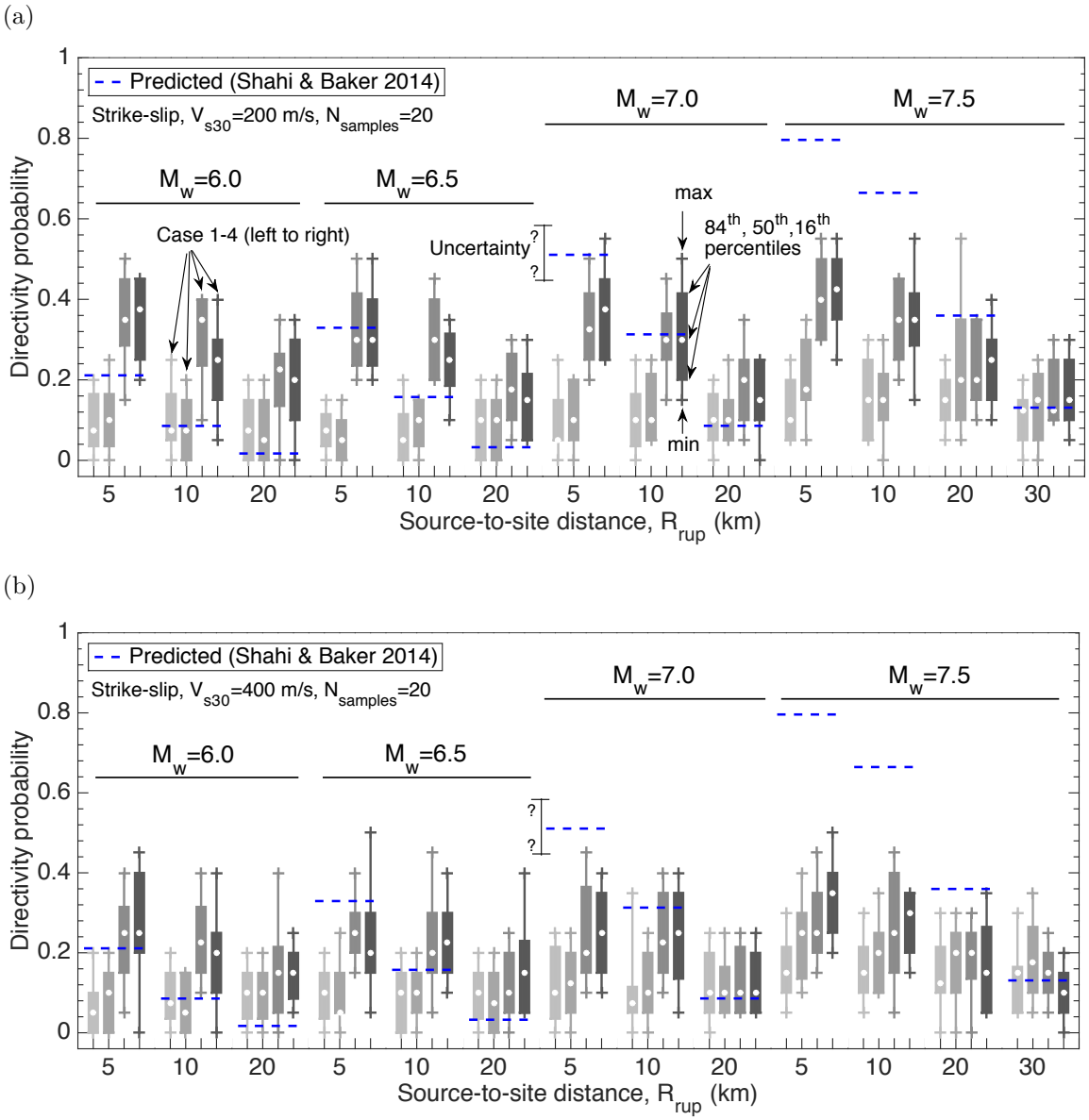

Figure 5.14: Directivity probability represented by the ground motion ensembles selected without using the causal parameter bounds of Table 2 for the considered strike-slip rupture scenarios: (a)-(c) V_{s30}= 200 and 400 m/s, respectively. The results for case1-4 are shown by separate box-and-whisker colors as annotated.

(c)

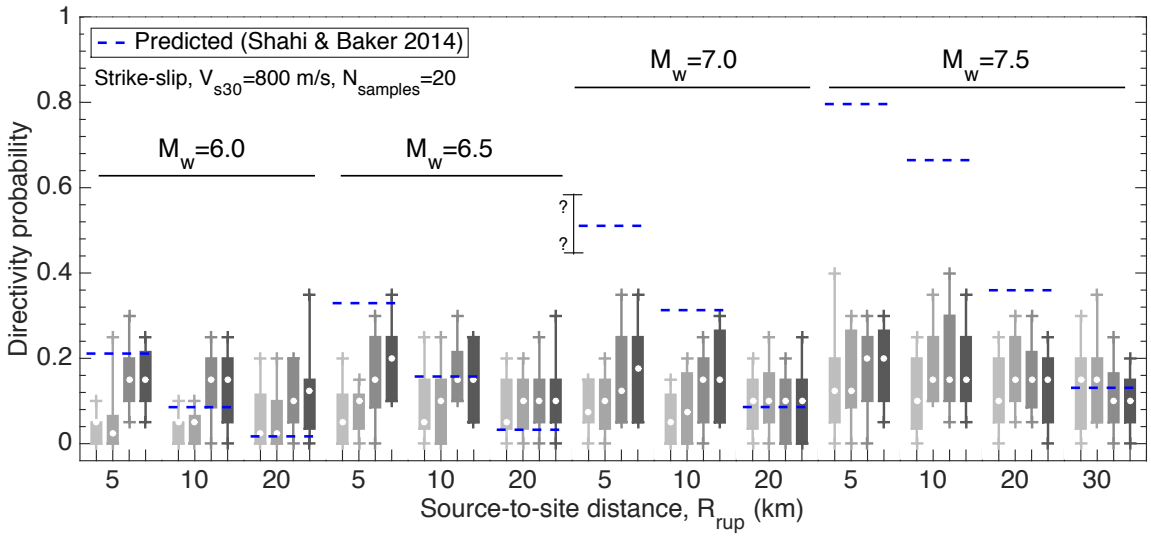

Figure 5.14: *(continued)* Directivity probability represented by the ground motion ensembles selected without using the causal parameter bounds of Table 2 for the considered strike-slip rupture scenarios: (c) V_{s30}= 800 m/s, respectively. The results for case1-4 are shown by separate box-and-whisker colors as annotated.

5.5.3 Scenario seismic demand distribution based on selected ground motions

5.5.3.1 Response analyses considered

From the ground motion selection perspective, while the 20 replicate ensembles selected for each scenario case contain a varying number of directivity ground motions and different T_p distributions, they are considered equally valid in representing the target hazard in terms of explicit IMs. In order to investigate the difference among the 20 replicate ensembles in terms of the resulting seismic demand distributions, three inelastic single-degree-of-freedom (SDOF) systems with strength and stiffness degradations (Ibarra et al., 2005; Lignos and Krawinkler, 2012) are subjected to the selected ground motion ensembles and their demand distributions are compared. The SDOF systems considered have fundamental vibration periods, T_n, of 1, 3, and 5 s, representing engineered systems that may be susceptible to the range of vibration periods affected by the directivity pulse periods. Figure 5.15 presents the backbone curves of the considered SDOF systems.

The collapse limit for these systems are defined based on a nominal displacement to height ratio, specifically, 0.06, 0.05, and 0.025 for the T_n=1, 3, and 5 s SDOF systems, corresponding to 4.25, 3, and 2.3 displacement ductility values, respectively.

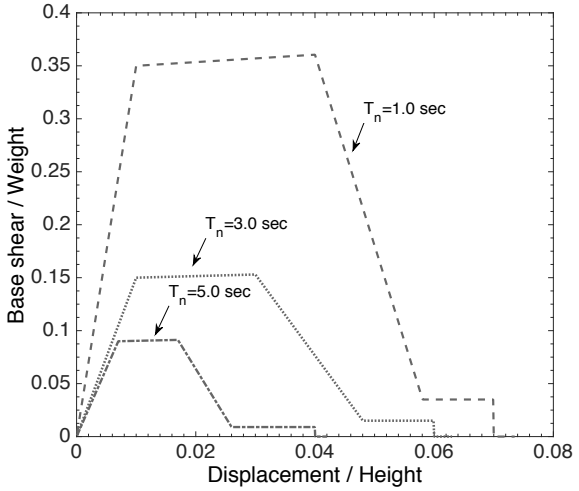

Figure 5.15: Backbone curves of the three inelastic SDOF systems considered for seismic response analysis.

5.5.3.2 Seismic demand distributions

Figure 5.16 presents the maximum displacement distributions for the SDOF systems with T_n =3.0 and 5.0 for sample scenario ruptures ranging from a small to large P_{Dir}=[0.33-0.8]. This figure shows the maximum displacement from individual ensembles and also indicates the ensembles containing the maximum, median, and minimum number of directivity ground motions, along with the predicted P_{Dir}.

Figure 5.16 illustrates that the various replicate ground motion ensembles result in similar seismic demand distributions, as expected based on the fact that they have been selected to represent the same target ground motion IMs. In addition, it can be seen that the varying N_{Dir} among the replicate ensembles does not have an noticeable effect on the demand distribution. As shown, the ensembles with the maximum N_{Dir} may not necessarily result in the largest seismic demands compared to the ensembles with the median or minimum N_{Dir} (or other selected

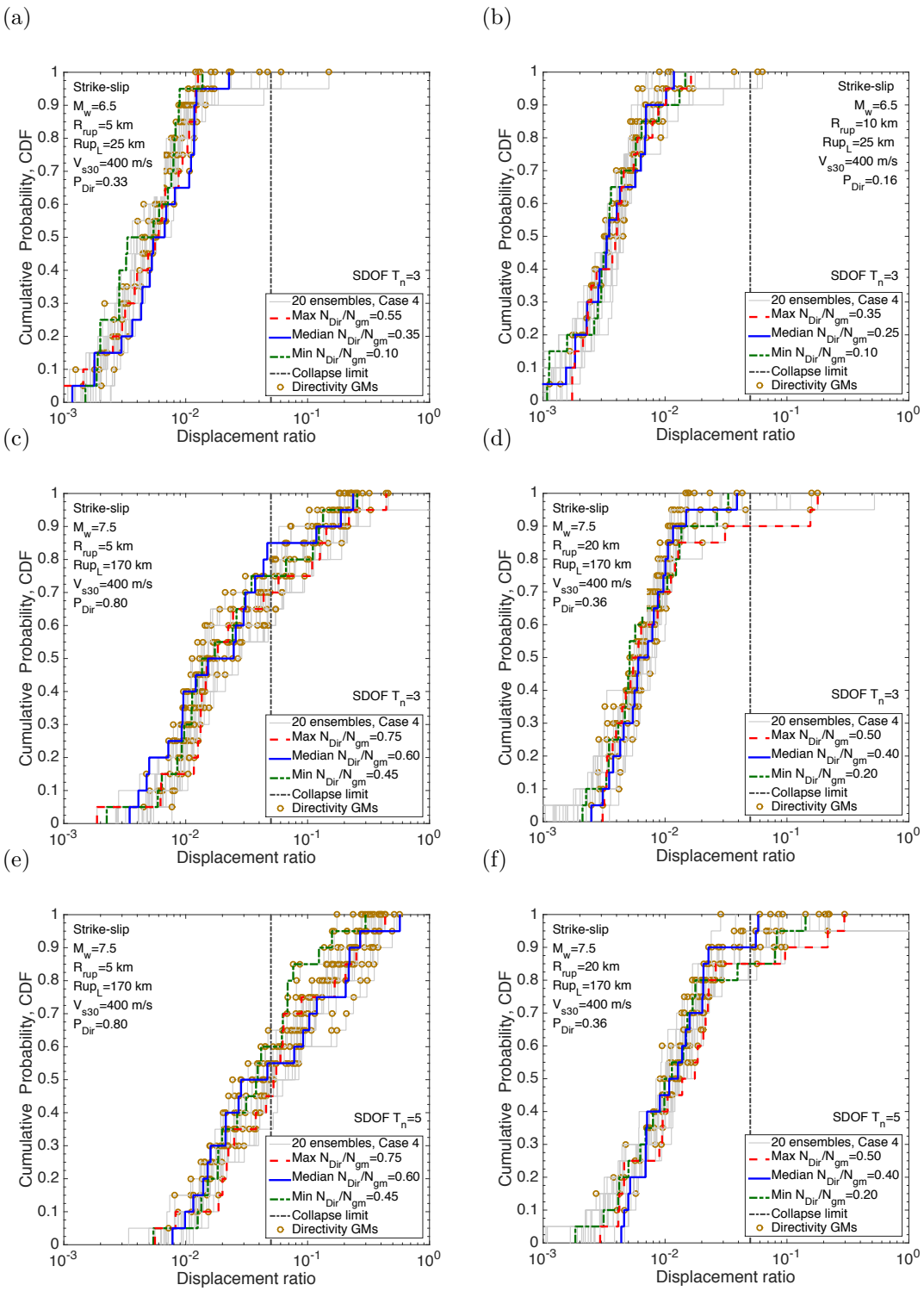

Figure 5.16: Distribution of the maximum displacement ratio from the 20 replicate ensembles selected for sample scenarios: (a)-(d) T_n=3 s SDOF system; (e)-(f) T_n=5 s SDOF system.

ensembles). It can also be seen that ground motions with directivity pulses result in seismic demands both above and below the median demand, although there is a slight tendency for directivity ground motions to produce seismic demands towards the upper tail of the distribution. Figure 5.16 also shows that the proportion of the records resulting in exceedance of the collapse limit (defined in section 5.5.3.1) is similar between the 20 replicate ensembles.

The results in Figure 5.16 indicate that variability in the computed seismic demand distributions among the selected ensembles can be attributed to inherent record-to-record variability rather than to any systematic dependence on the proportion of pulse-like ground motions in the selected ensemble. As a result, these analyses indicate that the selection of ground motions in the near-fault region based on IM properties alone can result in an appropriate representation of the target hazard and demand distributions, and there is no need to prescribe the proportion and T_p distribution of the directivity records.

5.6 PSHA-based ground motion selection in the near-fault region

5.6.1 Hazard analysis cases considered

In order to empirically investigate the characteristics of selected ground motion ensembles representing PSHA results, hazard analyses were conducted for numerous SA periods and sites in California, using the open-source seismic hazard analysis software, OpenSHA (Field et al., 2003). The UCERF2 earthquake rupture forecast (ERF) of Field et al. (2009) and empirical GMMs and correlation models presented in section 5.4 were used to conduct PSHAs and obtain the target distributions of the considered IMs for ground motion selection. Table 5.5 presents the details of the considered PSHA cases, including the location, site condition, conditioning IM (IM_j), and hazard levels (*i.e.,* exceedance probabilities

(EPs) in 50 years). These PSHA cases are intentionally chosen to span a wide range of deaggregation conditions (*i.e.,* rupture scenarios) and directivity probabilities. All ruptures from finite and distributed seismic sources within 200 km of the sites are considered in the calculations. As noted previously for the scenario rupture cases, multiple realisations of the hypocentre location for each rupture are also considered in the PSHA calculations, and the hazard from each realisation is adjusted by the occurrence probability of the hypocentre in the specified location using Mai et al. (2005). In order to consider hypocentre location for the distributed seismicity sources, they are converted to finite faults using UCERF2 distributed source modelling options. Number of the hypocentres long the strike and dip directions are determined based on the dimensions of the rupture surface, specifically at 20 km and 5 km intervals long the strike and dip directions, respectively. Three hypocentres with an equal distance from each other along the strike at a constant down-dip depth (0.6 times the down-dip width) are considered for ruptures with lengths and widths smaller than 20 and 5 km, respectively. In order to account for the inherent variability in the predicted T_p value in determining the directivity-included SA distributions, the full T_p distribution is integrated over for each considered rupture, as outlined in Table 5.1.

5.6.2 PSHA results with directivity effects

5.6.2.1 Hazard curves and the uniform hazard spectrum

Figure 5.17 compares the SA(3.0 s) hazard curves[2] of the considered PSHA cases with and without incorporating directivity effects for the V_{s30}=400 m/s site condition. As shown, depending on the hazard level and the location of the site (*i.e.,* surrounding seismic sources), directivity effects influences the hazard curve differently at the various sites. While IM values increase for EPs less than 20%

[2]Note that the PSHA formulation in OpenSHA is based on the probability of exceedance (Field et al., 2003). If the utilized ERF is time-independent, such as UCERF2 ERF (Field et al., 2009) utilized here, $P = 1 - e^{(-\lambda.T_{forecast})}$ can be used to convert between probability- and frequency-based results.

Table 5.5: Characteristics of the considered 36 PSHA cases for ground motion selection and seismic demand hazard calculations

PSHA case	Site	Latitude, Longitude	Site condition, V_{s30}(m/s)	Conditioning IM, SA ($T = t$), (s)	Hazard level, exceedance probabilities in 50 years (%)
1	Los Angeles	34.05, -118.25	200, 400, 800	1.0, 3.0, 5.0	1, 2, 4, 6, 8, 10, 50
2	Stanford	37.4225, -122.1653	200, 400, 800	1.0, 3.0, 5.0	1, 2, 4, 6, 8, 10, 50
3	San Francisco	37.7833, -122.4167	200, 400, 800	1.0, 3.0, 5.0	1, 2, 4, 6, 8, 10, 50
4	Davis	38.5539, -121.7381	200, 400, 800	1.0, 3.0, 5.0	1, 2, 4, 6, 8, 10, 50

for SA(3.0s) hazard in Los Angeles, the significant difference between the conventional and directivity-included hazard curves for Stanford and San Francisco occur between 1%-30% EPs (in 50 years). As shown in Figure 5.17d, considering directivity effects might not change the PSHA results for some locations (*e.g.,* Davis). The reasons for these differences are discussed subsequently.

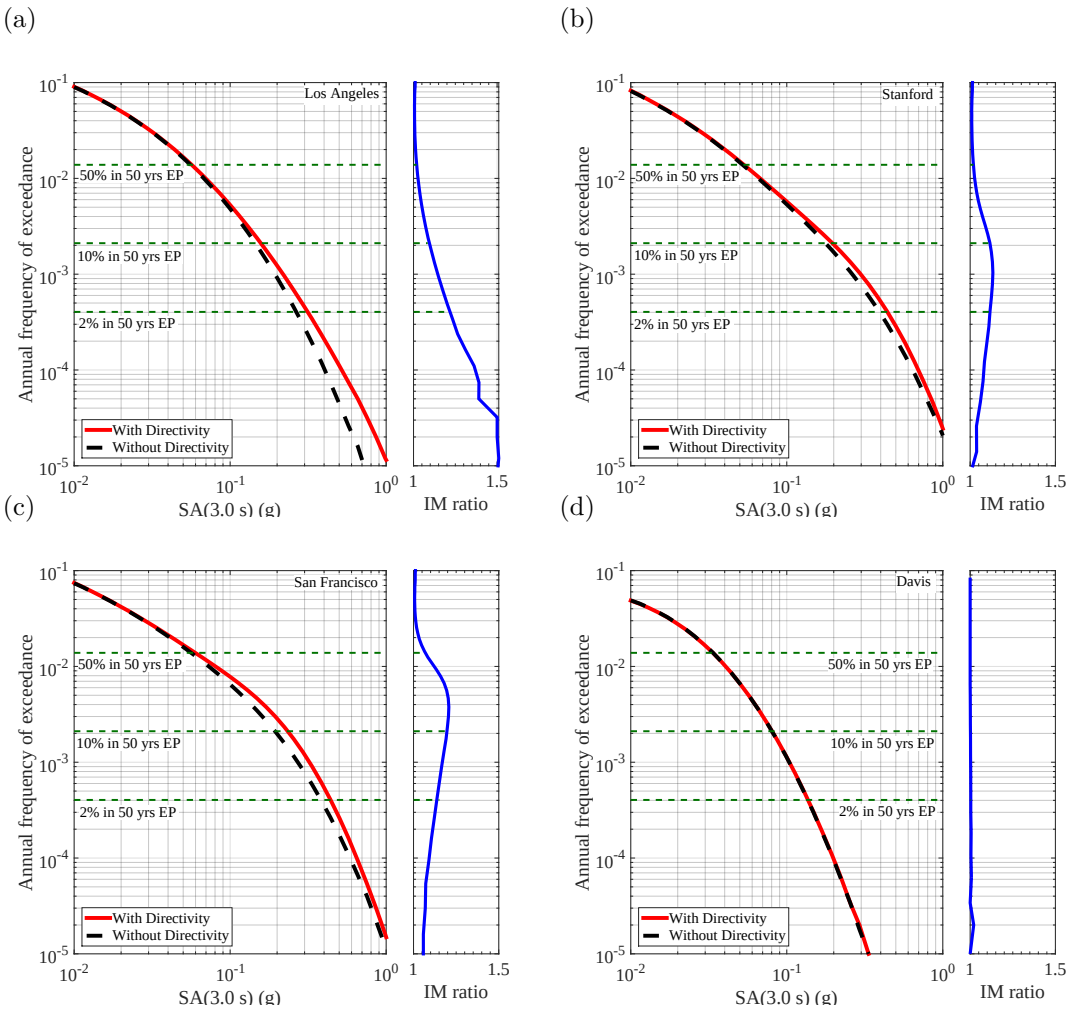

Figure 5.17: Comparison between the directivity-included and conventional hazard curves of the considered PSHA cases for SA(3.0 s) with V_{s30}=400 m/s site condition: (a) Los Angeles; (b) Stanford; (c) San Francisco; (d) Davis.

In order to illustrate the change in the IM values due to considering directivity effects for a board range of vibration periods, Figure 5.18 presents the uniform hazard spectrum (UHS) at 0.1%, 2%, 10%, and 50% EPs for the four sites considered. It can be seen that the Los Angeles UHS increases for a broad range of

vibration periods (T >1.0s), while the increase in the IM level occurs for T >3.0 s for the Stanford and San Francisco sites.

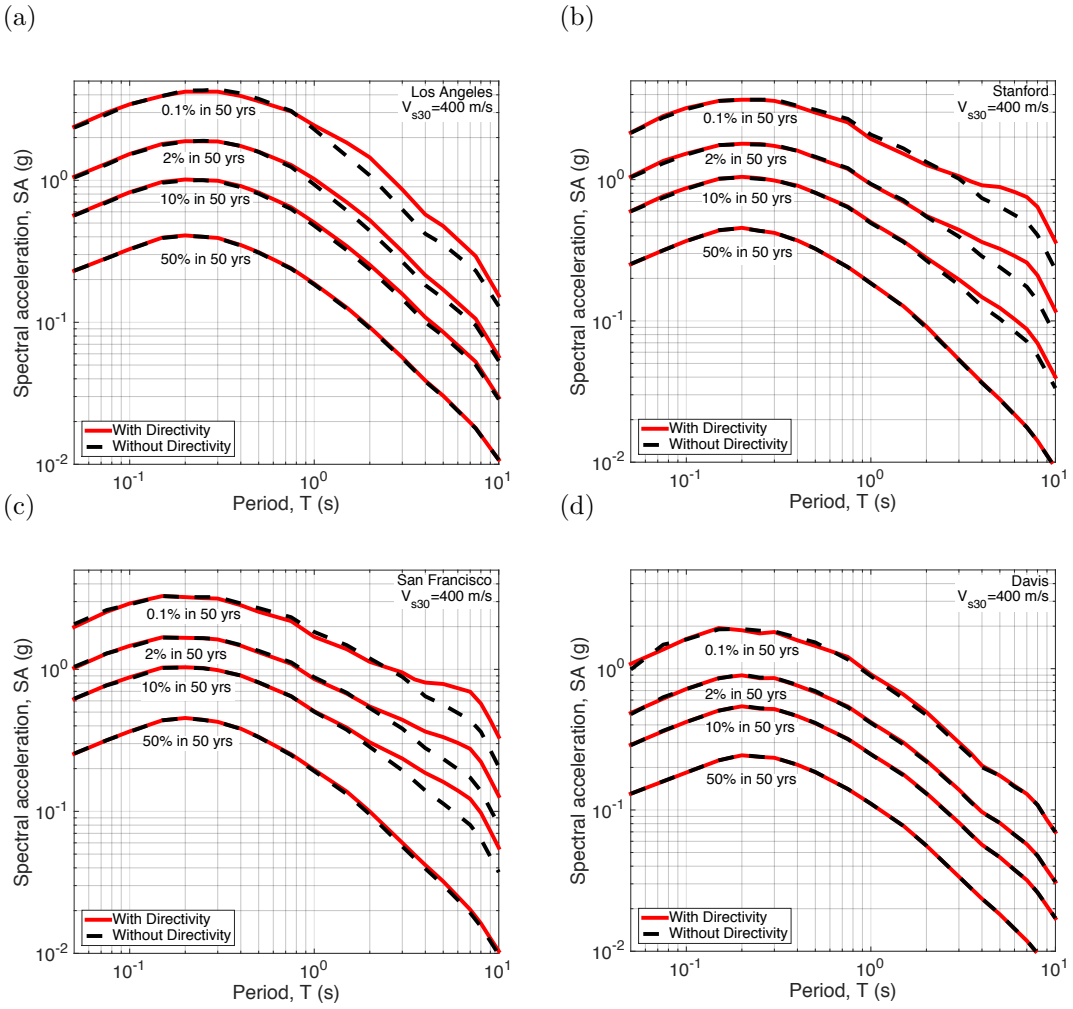

Figure 5.18: Uniform hazard spectrum with and without considering directivity effects for the considered PSHA cases: (a) Los Angeles; (b) Stanford; (c) San Francisco; and (d) Davis.

5.6.2.2 Contributing scenario ruptures and their directivity properties

In order to investigate the reason for the varying differences between the conventional and directivity-included hazard curves at different hazard levels, it is insightful to examine the deaggregation contribution of different sources to the IM hazard value with respect to their rupture magnitude (M_w) and directivity probability (P_{Dir}). Note that the calculated deaggregation contributions corre-

spond to the occurrence of IM level (*i.e.,* occurrence deaggregation), and not their exceedance (McGuire, 1995; Bazzurro and Cornell, 1999; Fox et al., 2015). The occurrence deaggregation is calculated using Equation 5.16:

$$P_{Rup|IM_j}\left(rup_k|IM_j = im_j\right) \approx \frac{P_{Rup|IM_j}\left(rup_k|im_j\right)\lambda_{IM_j}\left(im_j\right) - P_{Rup|IM_j}\left(rup_k|im_j + \delta im_j\right)\lambda_{IM_j}\left(im_j + \delta im_j\right)}{\lambda_{IM_j}\left(im_j\right) - \lambda_{IM_j}\left(im_j + \delta im_j\right)} \tag{5.16}$$

where $P_{Rup|IM_j}\left(rup_k|IM_j = im_j\right)$ is the contribution of rup_k to the occurrence of $IM_j = im_j$; $P_{Rup|IM_j}\left(rup_k|im_j\right)$ and $P_{Rup|IM_j}\left(rup_k|im_j + \delta im_j\right)$ are the contributions of rup_k to the exceedance of IM at im_j and $im_j + \delta im_j$ levels, respectively; and $\lambda_{IM_j}\left(im_j\right)$ and $\lambda_{IM_j}\left(im_j + \delta im_j\right)$ are the annual exceedance frequencies for $IM_j > im_j$ and $IM > im + \delta im_j$ from the calculated hazard curve [3], respectively. Note that Equation 5.16 becomes exact in the limit as $\delta im_j \to 0$. Contributions of rup_k to the exceedance of im_j, *i.e.,* $P_{Rup|IM_j}\left(rup_k|im_j\right)$, is calculated using Equation 5.17:

$$P_{Rup|IM_j}\left(rup_k|IM_j > im_j\right) = \frac{P_{IM_j|Rup}\left(IM_j > im_j|rup_k\right)\lambda_{Rup}\left(rup_k\right)}{\lambda_{IM_j}\left(im_j\right)} \tag{5.17}$$

where $P_{IM_j|Rup}\left(IM_j > im_j|rup_k\right)$ is the exceedance probability of im_j given rup_k from the utilized GMM; and $\lambda_{Rup}\left(rup_k\right)$ is the annual frequency of rup_k from the ERF.

Figure 5.19, presents the occurrence deaggregation distribution with respect to P_{Dir} and M_w for the Los Angeles site at 50%, 10%, 2%,and 0.1% EPs. As shown in Figures 5.19a-b, rupture scenarios dominating the hazard at 50% and 10% EPs have smaller P_{Dir}, hence a negligible change in the corresponding IM level (as shown in Figure 5.17a. In contrast, rupture scenarios contributing significantly to the hazard at 2% and 0.1% EPs, shown in Figures 5.19b-c, have large P_{Dir}

[3] $\lambda_{IM_j}\left(im_j\right) = \sum_{n=1}^{N_{rup}} P_{IM_j|Rup}(IM_j > im_j|rup_n)\ \lambda_{Rup}(rup_n)$, where $P_{IM_j|Rup}(IM_j > im_j|rup_n)$ is the probability of $IM > im$ given a scenario rupture (rup_n) from a GMM, and $\lambda_{Rup}(rup_n)$ is the annual frequency of rup_n.

with moderate M_w (*i.e.,* large rupture occurrence probability, $P_{Rup}\left(rup_k\right)$). This results in a large increase in the IM hazard value due to the directivity effects compared to the conventional hazard curve for the 2% and 0.1% EPs for Los Angeles.

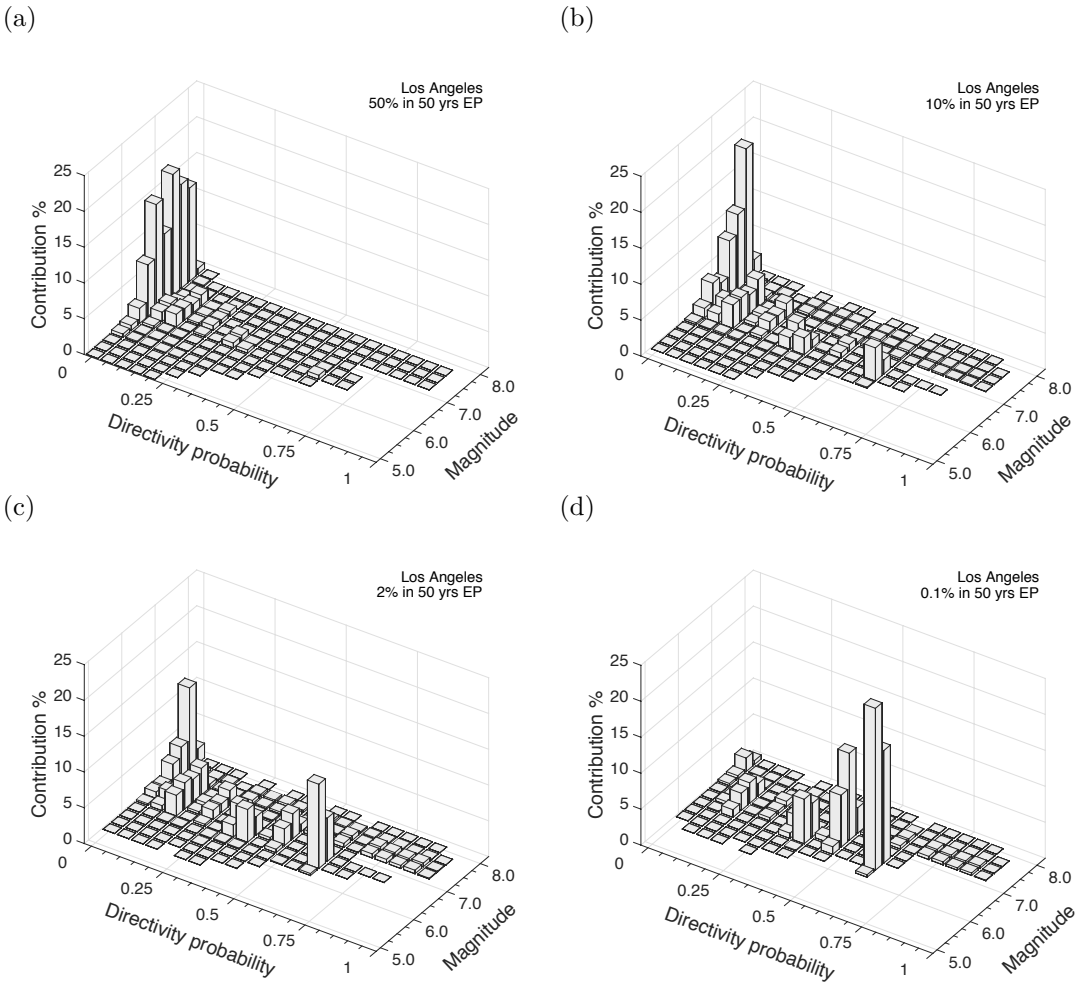

Figure 5.19: P_{Dir} – M_w distribution of the directivity-included SA(3.0s) hazard for Los Angeles (with V_{s30}=400 m/s site condition). Results for (a) 50%; (b) 10%; (c) 2%; and (d) 0.1% EPs in 50 years.

In contrast to Figure 5.19, which focused on various EPs for one location, in order to investigate the varying influence of directivity effects across the considered locations, Figure 5.20 presents the $P_{Dir} - M_w$ distribution of the directivity-included SA(3.0 s) hazard at 2% EP (for the considered four locations (with V_{s30}=400 m/s site condition). As shown in Figure 5.20a, the hazard at 2% EP

for Los Angeles is affected by ruptures with large P_{Dir} and moderate M_w (*i.e.*, $6.0 \leq M_w \leq 7.0$), which results in an increase for SA ordinates in a wide range of vibration period (see Figure 5.18). In contrast, Figures 5.20b-c illustrate that, while the dominant scenarios for Stanford and San Francisco have large P_{Dir}, they have $M_w > 7.0$, which can affect the long period SA ordinates significantly. As shown in Figures 5.18b-c for Stanford and San Francisco, the increase in the SA ordinates for $T > 3.0$ s is greater than that for SA(3.0s). Finally as shown in Figure 5.20d, the contributing scenarios for Davis mostly have P_{Dir}=0.0 (as they are in the far field region shown in Figure 5.21), hence no difference in the hazard curve is observed when directivity effects are considered for this site.

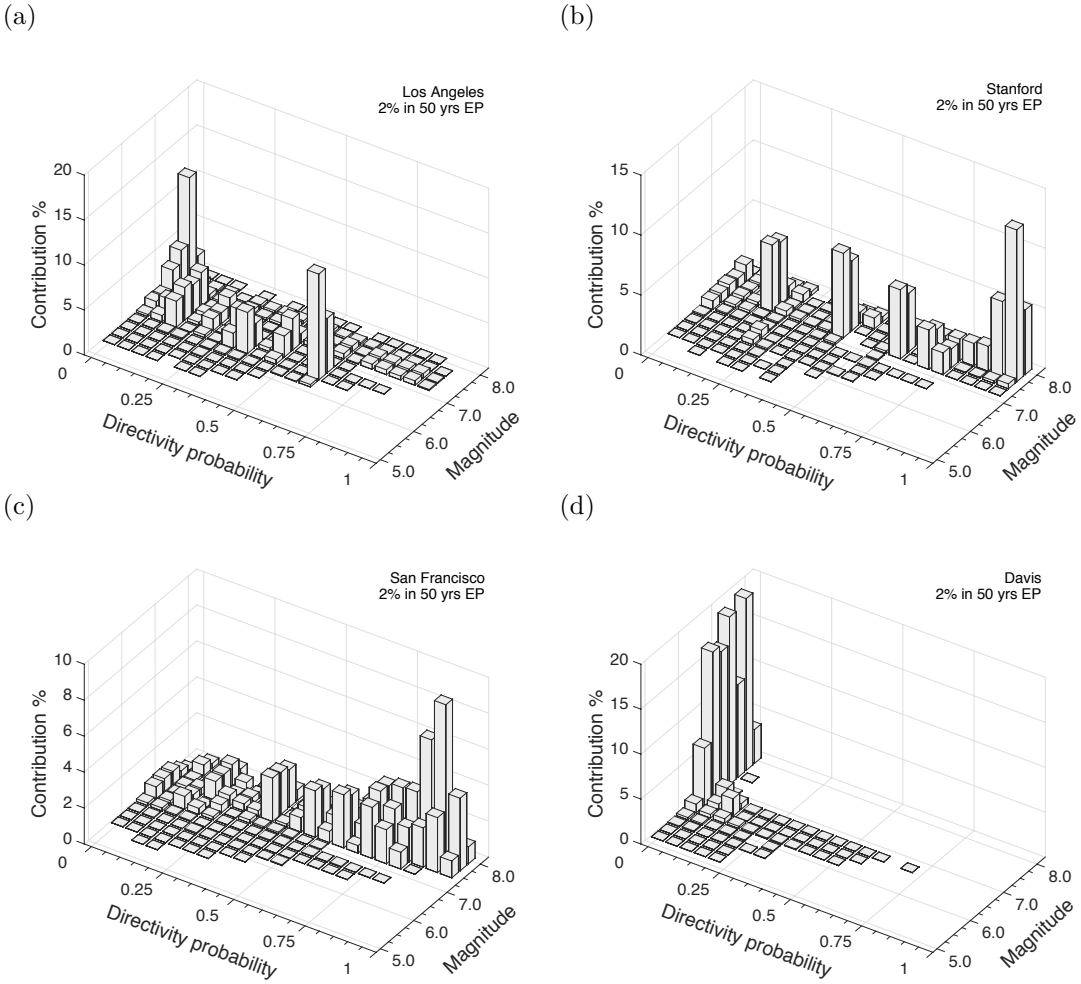

Figure 5.20: P_{Dir} – M_w distribution of the directivity-included SA(3.0s) hazard for 2% EP for the considered PSHA cases (with V_{s30}=400 m/s site condition): (a) Los Angeles; (b) Stanford; (c) San Francisco; (d) Davis.

In order to investigate the change in the contribution of rupture scenarios before and after considering directivity effects, and compare them in terms of causative M_w and R_{rup} values across the considered sites, Figure 5.21 presents the exceedance deaggreagtion contribution (*i.e.,* $P_{Rup|IM_j}(rup_k|IM_j > im_j)$) and the epsilon value ($\varepsilon-$the number of standard deviations that the obtained IM level from the hazard curve is above the median value for each scenario rupture) for the SA(3.0 s) hazard at 2% EP for the four considered sites. As shown in Figure 5.21b for Los Angeles, there is an increase in the contribution of rupture scenarios close to the site compared to the corresponding non-directivity deaggregation (shown in Figure 5.21a), which is due to the high P_{Dir} of the ruptures close to the site. Figures 5.21c-f illustrate the change in the deggregation distribution for Stanford and San Francisco, for which the seismic hazard is dominated only by the nearby scenarios. As shown, the contribution of some of the nearby scenarios has increased when the directivity effects are included, which consequently leads to a decrease in the contribution of other nearby scenarios. This is partially due to the difference in the P_{Dir} of the nearby sources based on their source-to-site geometry (as illustrated in Figure 5.1 and Equation 5.9), and their rupture properties (*i.e.,* M_w and $P_{Rup}(rup_k)$). Figure 5.21g-h illustrates no difference in the exceedance deaggregation for the Davis site.

Comparison between ε values of the contributing scenarios shown in Figures 5.21a-b (and similar results for other hazard levels and IMs considered) indicates that ε value for some contributing scenarios may decrease when directivity effects are included, which may have implications in terms of calculating conditional IM distributions for ground motion selection (discussed subsequently). The change in ε values is due to the fact that including directivity effects results in an increase in the median IM values for some scenario rupture relative to the calculated IM from PSHA, resulting in smaller ε values.

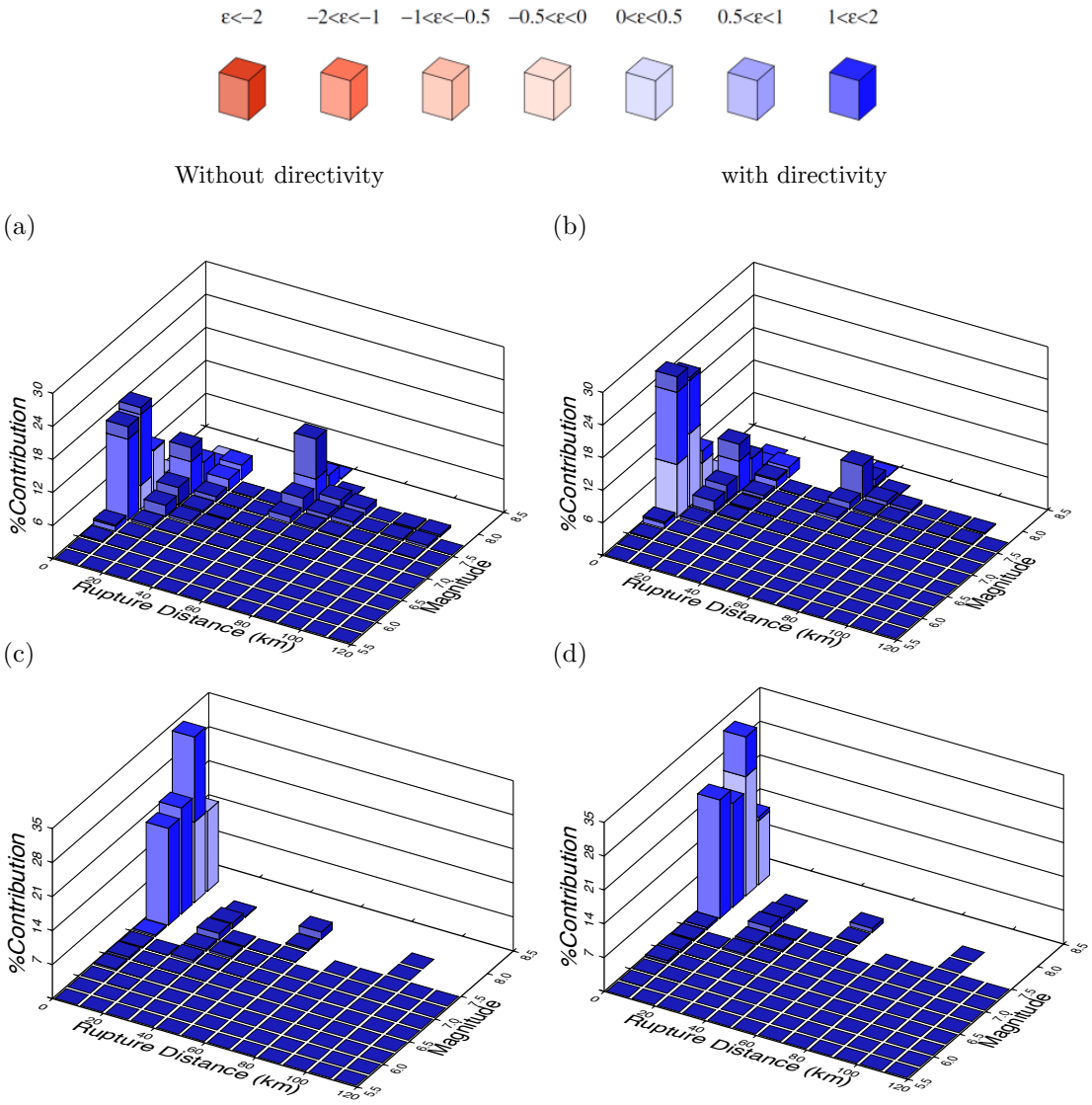

Figure 5.21: Exceedance deaggregation for SA(3.0s) hazard with V_{s30}=400 m/s at 2% EP, with and without considering directivity effects: (a)-(b) Los Angeles; (c)-(b) Stanford.

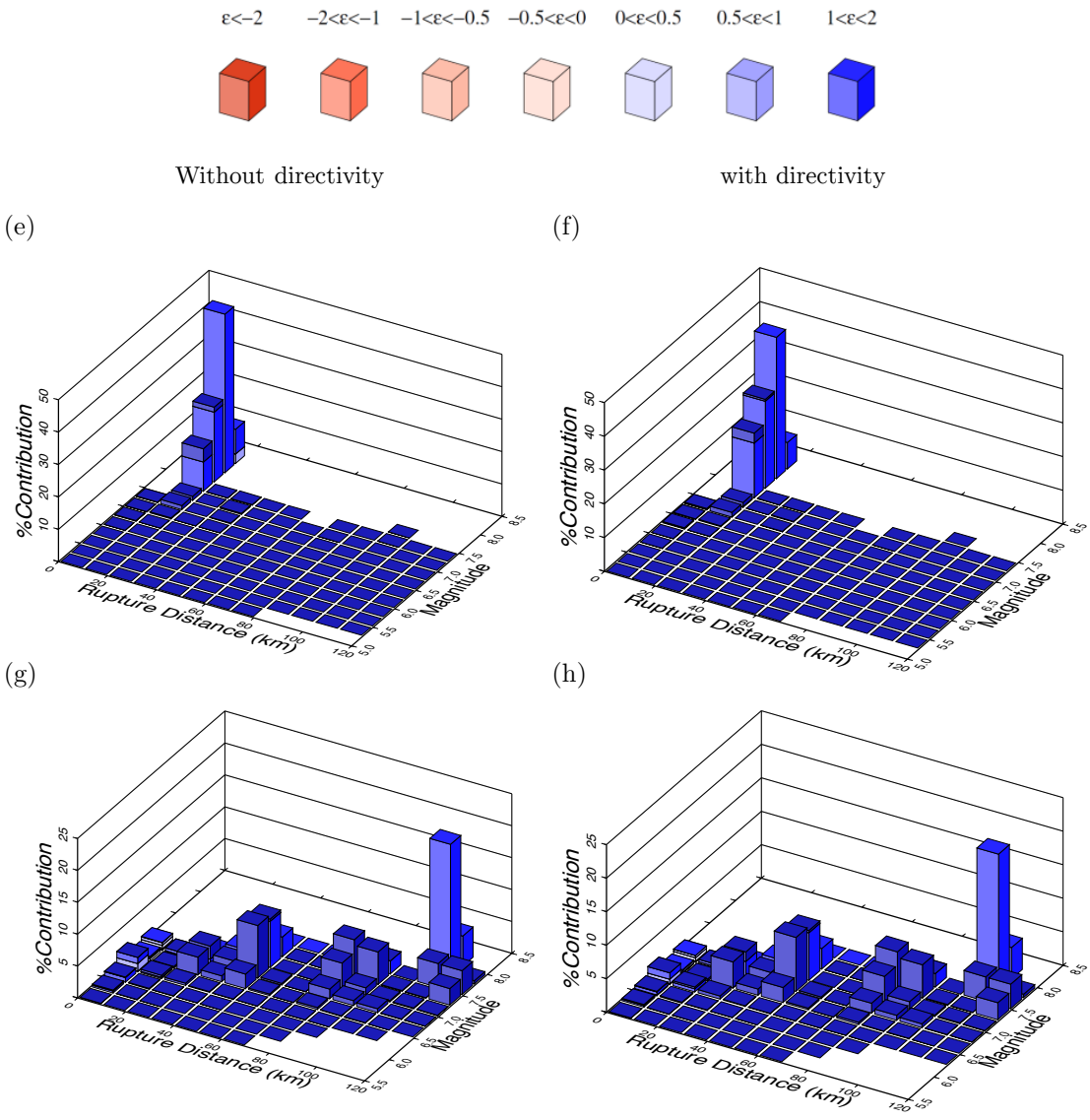

Figure 5.21: *(continued)* Exceedance deaggregation for SA(3.0s) hazard with V_{s30}=400 m/s at 2% EP, with and without considering directivity effects: (e)-(f) San Francisco; (g)-(h) Davis.

5.6.2.3 Mean directivity probability for ground motion selection

In order to integrate the P_{Dir} of the contributing rupture scenarios to obtain a single measure which can be used in ground motion selection process to compare the proportion of the directivity records selected (as discussed in section 5.6.3.2), P_{Dir} of causative ruptures are multiplied by their occurrence deaggregation contribution and summed over all the contributing ruptures. This yields the mean directivity probability for a given IM level, denoted as $\overline{P_{Dir}}$, as presented in Equation (17):

$$\overline{P_{Dir}} = \sum_{k=1}^{N_{rup}} P_{Rup|IM_j}\left(rup_k|IM_j = im_j\right) P_{Dir}^{rup_k} \tag{5.18}$$

where $P_{Dir}^{rup_k}$ is the directivity probability associated with rup_k given the source-to-site geometry (using Equation 5.9), and $P_{Rup|IM_j}\left(rup_k|IM_j = im_j\right)$ is the contribution of rup_k to the occurrence of $IM_j = im_j$ (using Equation 5.16). Figure 5.22 presents the calculated $\overline{P_{Dir}}$ for the SA(3.0 s) hazard at 2% EP for the four sites considered, along with the contribution of the surrounding ruptures to the obtained $\overline{P_{Dir}}$, *i.e.,* $P_{Rup|IM_j}\left(rup_k|IM_j = im_j\right).P_{Dir}^{rup_k}$ product of the causative ruptures. As shown in Figure 5.22, $\overline{P_{Dir}}$varies between the considered sites, depending on the contribution of the ruptures and their corresponding $P_{Dir}^{rup_k}$. The reason for the large $\overline{P_{Dir}}$ for the San Francisco and Stanford sites is the fact that hazard for these sites are dominated by large M_w ruptures which have large $P_{Dir}^{rup_k}$ (Shahi and Baker, 2014a), implications of which are discussed in section 5.6.3.2.

5.6.2.4 Conditional IM distributions for ground motion selection

In addition to the conditioning IM, (*i.e.,* IM_j), the target distribution of other IMs (referred to collectively as IM_i) may also be affected by considering directivity effects due to the increase in the IM_j value and the change in the contribution of the various causative ruptures affecting the hazard at the site. The extend of the change in the conditional IM_i distribution depends on the correla-

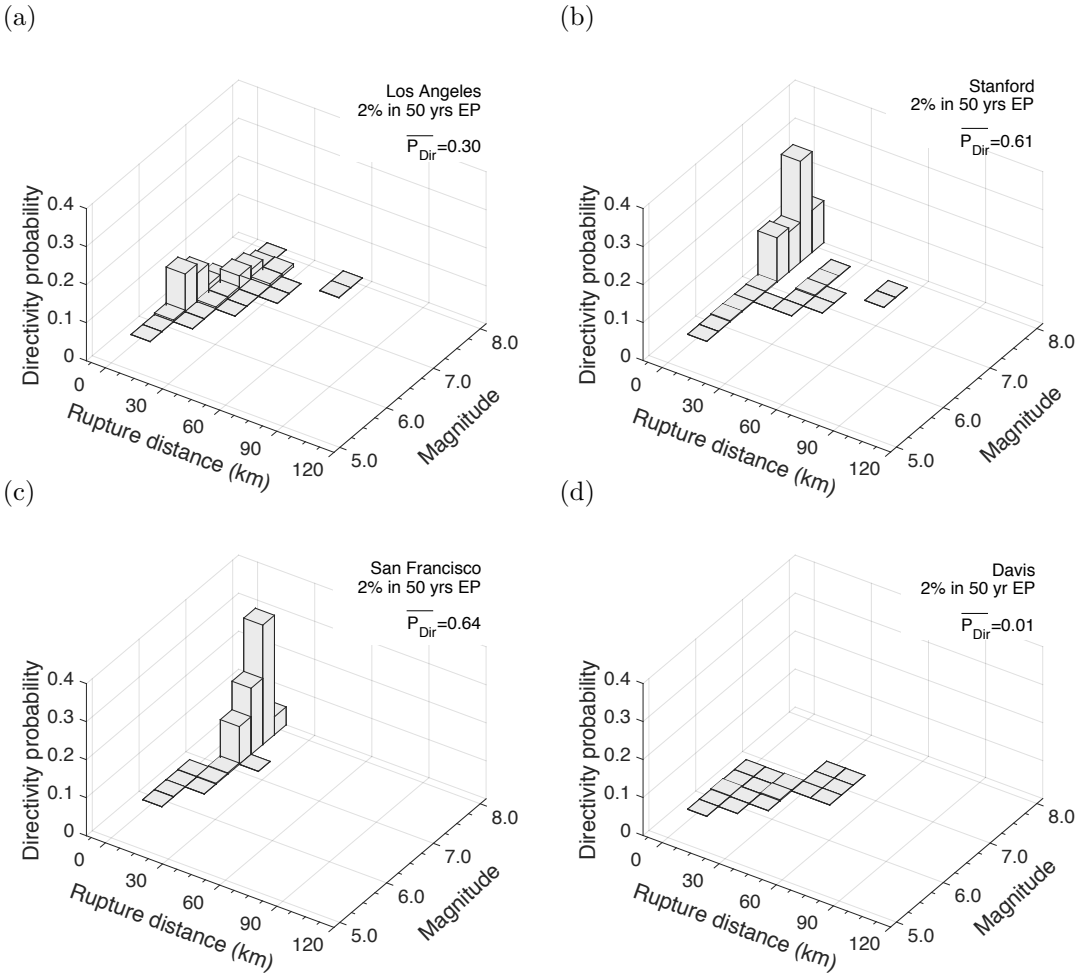

Figure 5.22: $\overline{P_{Dir}}$ calculated for SA(3.0 s) hazard at 2% EP and the relative contribution of the causative ruptures: (a) Los Angeles; (b) Stanford; (c) San Francisco; (d) Davis.

tion between the specific IM_i and IM_j. In order to investigate the conditional distribution of different IMs representing various characteristics of ground motion (*i.e.,* amplitude, frequency content, duration, and cumulative effects), SA for 18 vibration periods (T= 0.05-10.0 s), along with CAV, D_{s575}, and D_{s595} were calculated for the considered PSHA cases (see section 5.4.2 for the adopted GMMs). Figure 5.23 illustrates the conditional response spectrum for Los Angeles and San Francisco, conditioned on the SA(3.0 s) hazard at 2% EP, along with the conditional distribution for D_{s575}, CAV, PGA, and PGV. As shown in Figure 5.23a, in addition to the increase in the conditioning IM value (*i.e.,* IM_j=SA(3.0 s)) (shown previously in Figure 5.17), SA values at other vibration periods have also increased for the Los Angeles case, especially for T <3.0 periods. This is due to the fact that, as shown in Figures 5.20 and 5.21, directivity effects from rupture scenarios with moderate M_w (*i.e.,* 6.0≤ M_w ≤7.0) is more pronounced for this site which results in influencing SA at short periods. This indicates the importance of considering all the contributing rupture scenarios in establishing the target IM distributions for ground motion selection as opposed to simply using a single (*e.g.,* mean) rupture parameters (Almufti et al., 2013), which is one of the advantages of using the GCIM methodology (Bradley, 2010b, 2012c). Having a larger SA for shorter vibration periods may have a significant effect on the seismic response of the engineered systems susceptible to the higher mode effects, for example.

Regarding IMs other than SA, Figures 5.23c-d illustrate a decrease in the median D_{s575}, and an increase in the median CAV for the Los Angeles 2% EP hazard when directivity effects are considered. This is mainly caused by the increase in the contribution of nearby ruptures with M_w ≤7.0 to the IM_j=SA(3.0 s) hazard for Los Angeles (as shown in Figures 5.21a-b). Since the correlation between SA and IM_i= D_{s575} and CAV are close to zero for IM_j=SA(3.0 s) (Bradley, 2011a, 2012a), the correlation between IM_j and IM_i does not have a significant effect in the change for the D_{s575} and CAV conditional distributions for the Los Angeles site. In contrast, the change in the PGA and PGV conditional distributions, shown in Figures 5.23e-f, have been influenced by the correlation between IM_j

and IM_i (Bradley, 2011b, 2012b), in addition to the change in the contribution of the causative ruptures.

In contrast to the Los Angeles PSHA results, directivity effects for San Francisco are dominated by large M_w scenarios (*i.e.,* $M_w > 7.0$), with a relatively smaller change in the IM_j value with respect to the non-directivity PSHA (*i.e.,* $\sim$ 1.1 times larger SA(3.0 s) at 2% EP for San Francisco in contrast to 1.2 for Los Angeles, as shown in Figure 5.17). This results in a negligible increase for T <3.0 s SA ordinates in San Francisco along with a negligible change in the target distribution of the other IMs shown in Figures 5.23c-f However, due the strong correlation between the long period SA ordinates (Baker and Jayaram, 2008) and the dominance of large M_w ruptures for San Francisco (which will result in pulse periods greater than 3.0 s, as shown in Figure 5.30), there is a greater increase in the T >3.0 s SA ordinates for San Francisco compared to Los Angeles (see Figure 5.23b).

In addition to the changes in the contribution of the causative rupture and the conditioning IM value, changes in the ε values of causative ruptures due to the consideration of directivity effects (as shown in Figure 5.21) may influence the IM_i conditional distributions presented in Figure 5.23. In general, for low EPs where ε values are mostly positive (as shown in Figure 5.21), a decrease in the ε value (as a result of an increase in the median SA due to directivity effects) diminishes the effect of the increase in IM_j when calculating the conditional distribution of an IM_i that has a positive correlation with IM_j. This results in a smaller increase in their target distribution (see Equations 10-11 in Bradley (2010b) for further clarifications). Note that having a smaller negative ε values, which is common for large EPs such as 50% in 50 years, results in larger values for the median IM_i that have a negative correlations with IM_j (Burks and Baker, 2012).

From the above discussion it is clear that even though directivity effects are not explicitly considered in establishing the target distribution for non-SA IMs (due to the lack of GMMs addressing directivity effects for a wider range

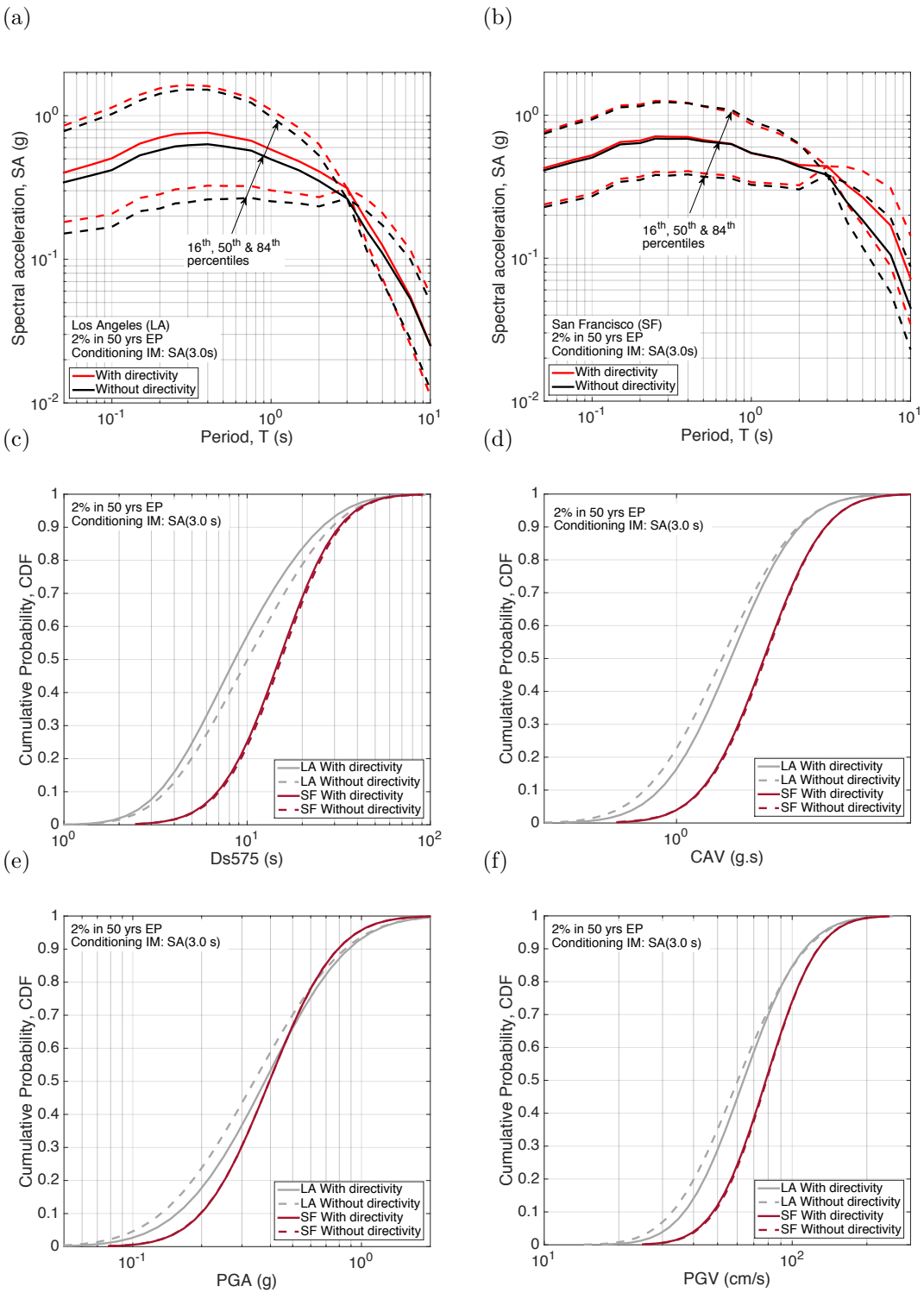

Figure 5.23: Comparison between the IM distribution with and without directivity effects conditioned on the SA(3.0) hazard at 2% EP for Los Angeles (LA) and San Francisco (SF): (a)-(b) SA; (c) D_{s575}; (d) CAV; (e) PGA; and (f) PGV.

of IMs), considering the changes in the contribution of causative ruptures and their ε values, along with the correlation between the considered IM_i and the directivity-included IM_j (*i.e.,* SA) results in the conditional distribution of IM_i that reflects the directivity effects, albeit in a broad sense.

5.6.3 Selected ground motions and their properties

5.6.3.1 Explicit IMs

Ground motion ensembles were selected representing the hazard for the considered PSHA cases in Table 5.5, using the four target IM distributions presented in Table 5.3. It is reiterated that a total of 20 ground motion records were selected using 10 replicate selection iterations (Bradley, 2012c; Tarbali and Bradley, 2015b) to obtain an ensemble with the lowest misfit to the target (*i.e.,* smallest global residual from Equation 5.15). In order to investigate the variability in the number of pulse-like ground motions within the selected ensemble of records and the variation in their characteristics, 20 replicate ensembles were selected for each PSHA case.

Figure 5.24 illustrates the SA ordinates of the selected ground motions based on case 1-4 targets (from the specific ensemble with the median number of directivity ground motions, N_{Dir}, among the 20 replicate ensembles) and their corresponding 16^{th}, 50^{th}, and 84^{th} percentiles for the Los Angeles site conditioned on SA(3.0 s) hazard at 2% EP level. Ground motion records classified as directivity records according to Shahi and Baker (2014a) are shown as a different colour, with the proportion of such selected records noted in the inset text in the figure legend, in addition to $\overline{P_{Dir}}$ calculated based on Equation 5.18 representing the mean directivity probability for the site (given the conditioning IM and the chosen EP level).

As shown in Figure 5.24a for the ground motions selected based on the case 1 weight vector (*i.e.,* without SA modification and non-SA IMs), although directiv-

ity effects are not explicitly included in the PSHA calculations, selected ensembles contain a small number of directivity records. As mentioned before for the case of scenario-based ground motion selection, this is due to the fact that the ground motion estimates from conventional GMMs in the near-fault region are implicitly influenced by the directivity motions, and the realisations of the target IM distributions reflect such effects. Figures 5.24b-d illustrate the selected ensembles for cases 2-4 respectively, for which the directivity effects are explicitly considered in the PSHA calculations. As shown, including directivity effects in the target distribution results in a larger N_{Dir} in the selected ensembles. Similar results are presented in Figures 5.7 and 5.8 (in section 5.5.2) for ground motion ensembles representing single scenario ruptures. Properties of the directivity ground motion in the selected ensembles are discussed in the next section.

Although the ground motions presented in Figures 5.24b-d have an appropriate representation of the target hazard (by having their SA percentiles close to the GCIM target), exclusion of duration and cumulative IMs from the ground motion selection process (as done for case 2-3) may result in a biased distribution for those IMs. As illustrated in Figure 5.25 for the Los Angeles and San Francisco cases, as an example among others, statistically significant bias exists in the D_{s575} and CAV distributions of the selected ground motions in cases 1-2 in Figure 5.25a, case 2 in Figure 5.25b, and case 3 in Figure 5.25c, as indicated by the empirical distribution of the ensemble lying 'outside' the Kolmogorov-Smirnov (KS) test bounds. Such biases can be resolved by including non-SA IMs in the selection process using an appropriate weight vector in the GCIM methodology (Bradley, 2012c; Tarbali and Bradley, 2015b). This is shown for case 4 in Figure 5.25 for which, in addition to SA ordinates, D_{s575}, D_{s595}, and CAV are also included in the selection process.

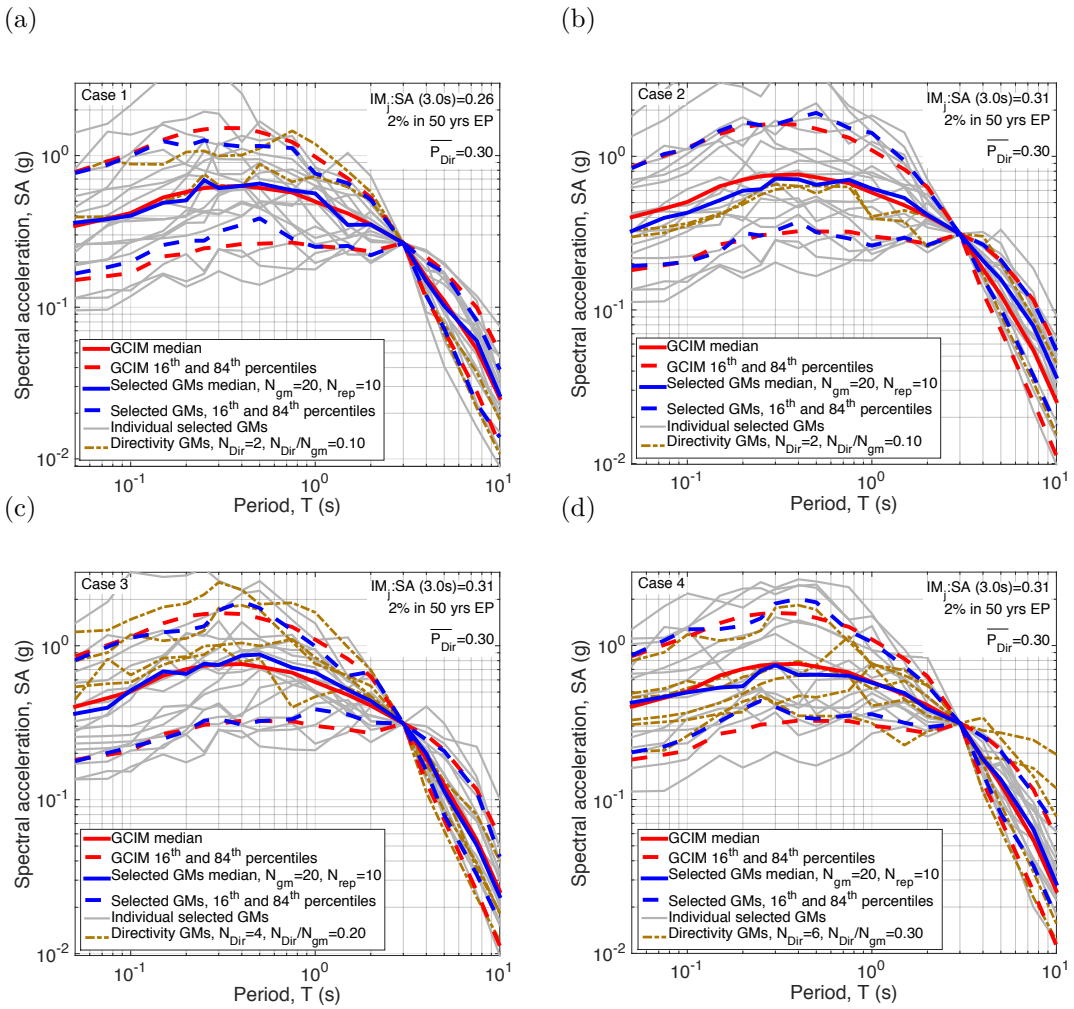

Figure 5.24: Comparison between the SA ordinates of the selected records and the target distribution for the Los Angeles SA(3.0 s) hazard with 2% EP and $V_{s30} = 400$ m/s: (a)-(b) selection based on only SA ordinates without and with directivity modifications, respectively; (c) selection based on SA, D_{s575}, and D_{s595} with directivity modifications; and (d) selection based on SA, D_{s575}, D_{s595}, and CAV with directivity modifications.

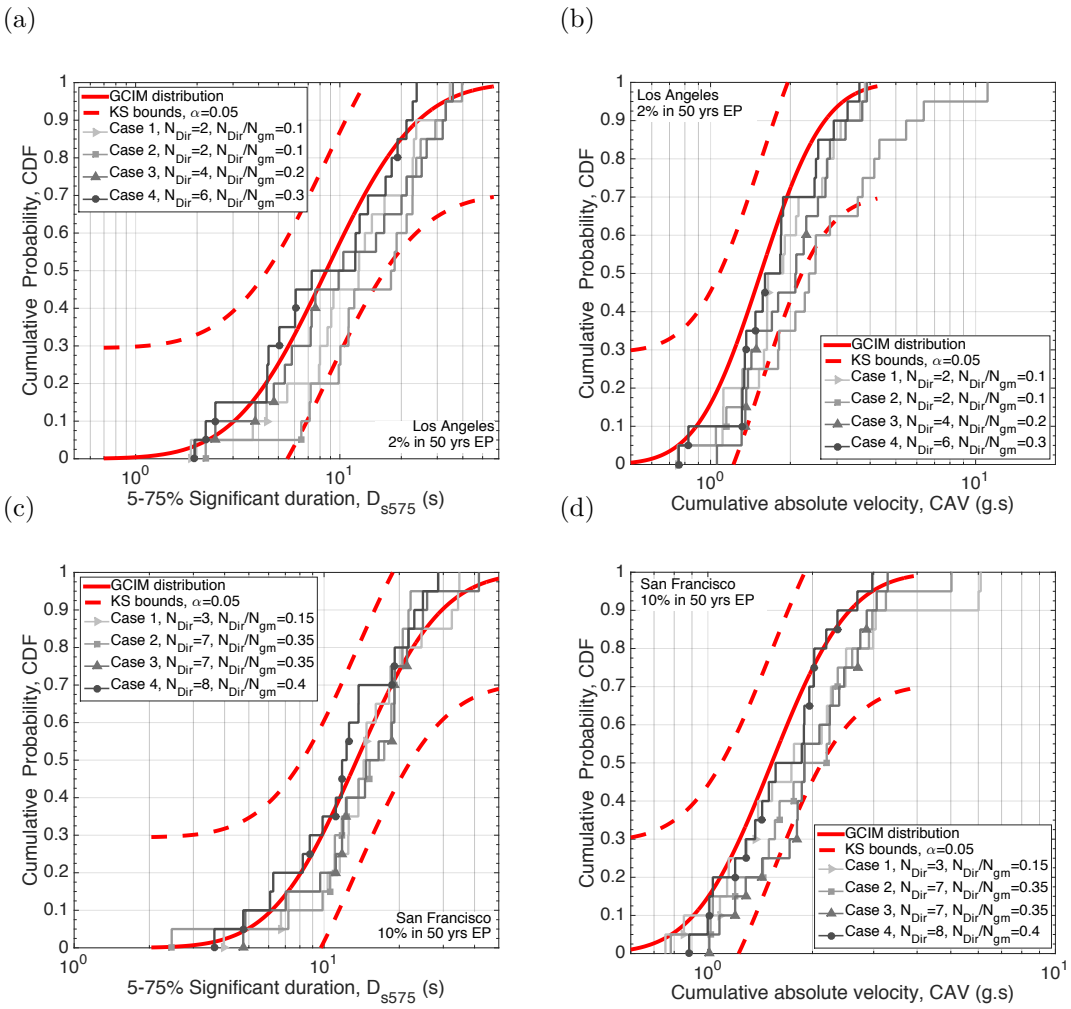

Figure 5.25: Comparison between the non-SA IM distributions of the selected ground motions based on case1-4 weight vectors (with $V_{s30} = 400$ m/s): (a)-(b) Los Angeles SA(3.0 s) hazard at 2% EP; and (c)-(d) San Francisco SA(3.0 s) hazard at 10% EP. The points indicated the IMs of the directivity ground motions.

5.6.3.2 Directivity properties of selected ground motions: Number of directivity ground motions

As mentioned before, the proportion of directivity ground motions in the selected ensemble of records is considered important when selecting ground motion ensembles in the near-fault region (NEHRP, 2011). In order to compare the number of directivity ground motions among the 20 replicate ensembles selected, Figure 5.26 presents the SA ordinates of the selected ground motions based on case 4 weight vector for the San Francisco SA(3.0 s) hazard at 1%, 2%, and 10% EPs from the two ensembles with the median and maximum N_{Dir} among the 20 replicate ensembles. As shown, while selected records have an appropriate representation of the GCIM target, with the exception of the slight deviation of the 16^{th} and 50^{th} SA ordinate percentiles at $0.2 \leq T \leq 2$ from the target distribution, the number of directivity ground motions both in the median and maximum N_{Dir} ensembles is lower than the calculated $\overline{P_{Dir}}$ =0.65, 0.64, and 0.58 for 1%, 2%, and 10% EPs, respectively. In contrast, as shown before in Figure 5.24d, the selected ground motion ensemble (which has the median N_{Dir} among the 20 replicate ensembles) can appropriately represent the $\overline{P_{Dir}}$ =0.3 for the Los Angeles SA(3.0 s) hazard at 2% EP. It is important to note that that the number of available directivity records in the near-fault region from large M_w ruptures is limited (see Figure 5.5), which results in a small number of directivity records for PSHA cases such as the San Francisco site (with seismic hazard dominated by large M_w). Implications of the number of directivity ground motions within the selected ensemble of records in terms of the demand hazard is investigated in section 5.6.4.

It is worth examining the effect of target IM distribution on the N_{Dir} variation within the 20 replicate ground motion ensembles selected. Figure 5.27 presents the directivity probability from the selected ground motions based on case 1-4 target distributions (in Table 5.3) for the SA(3.0 s) hazard (of the considered four locations with V_{s30}=400 m/s site condition). For comparison, the corresponding

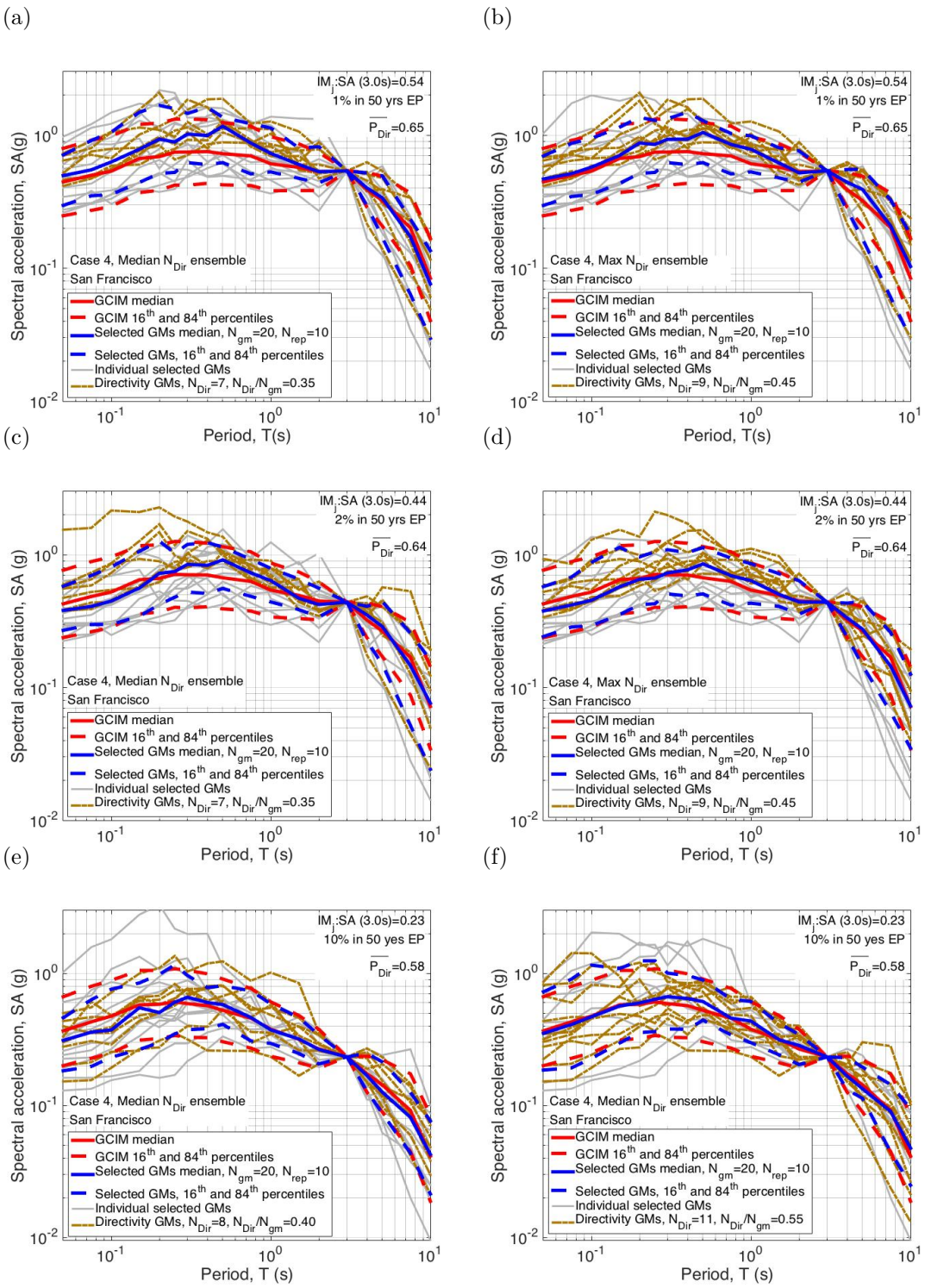

Figure 5.26: Comparison between the SA ordinates of the selected records for the San Francisco SA(3.0 s) hazard (with $V_{s30} = 400$ m/s) from two ensembles with the median and maximum N_{Dir} among the 20 replicate ensembles selected: (a)-(b) 1% EP, (c)-(d) 2% EP; (e)-(f) 10% EP.

$\overline{P_{Dir}}$ is also shown for each PSHA case. It is important to reiterate that $\overline{P_{Dir}}$ is not considered directly in the ground motion selection process itself, and the selection is conducted only based on the target IM distributions. As shown in Figure 5.27, considering duration and cumulative IMs (*i.e.,* case 4) generally results in larger median directivity probabilities that are therefore consistent with the 'target' $\overline{P_{Dir}}$ from the hazard deaggregation-based prediction using the model of Shahi and Baker (2014a) (in addition to alleviating the possible bias in their distributions with respect to their target conditional distributions). It can be seen in Figure 5.27 that the directivity probability represented by the selected ground motion ensembles for PSHA cases with $\overline{P_{Dir}} \geq 0.4$ is lower than the predicted value from Shahi and Baker (2014a). In order to investigate the reason for this, Figure 5.28 presents the number of available directivity and non-directivity (*i.e.,* 'ordinary') ground motions in the database (*i.e.,* N_{Dir} and N_{Ord}, respectively) after the application of causal parameters bounds in Table 5.2.

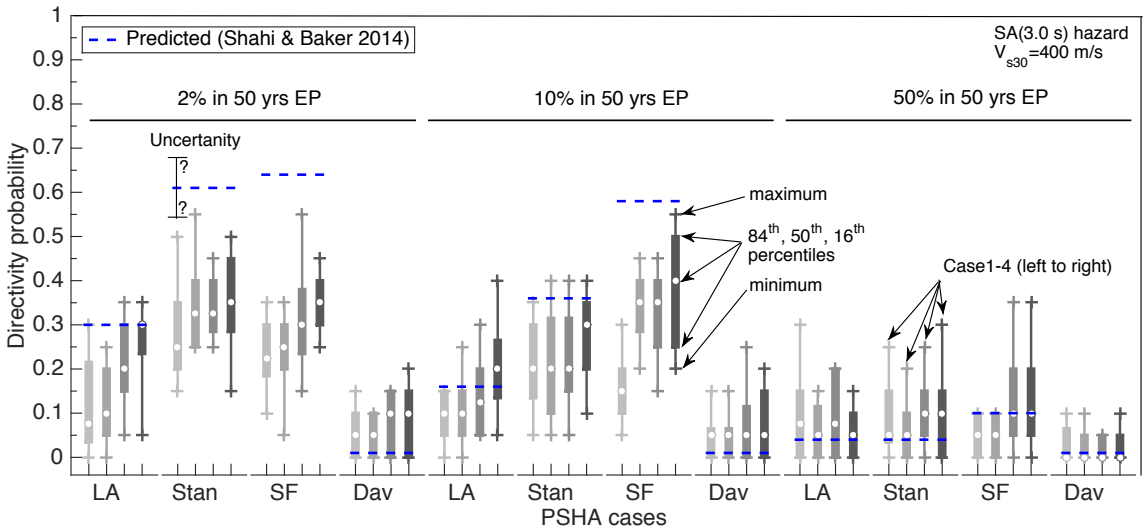

Figure 5.27: Directivity probability represented by the selected ground motion ensembles for SA(3.0 s) hazard for the four sites considered. The results for case1-4 targets for ground motion selection are shown by separate box-and-whisker colors as annotated.

As shown in Figure 5.28, there is a smaller number of directivity motions available for the 2% and 10% EPs for Stanford and San Francisco than for Los Angeles. This is due to the fact that hazard and the calculated $\overline{P_{Dir}}$ for these

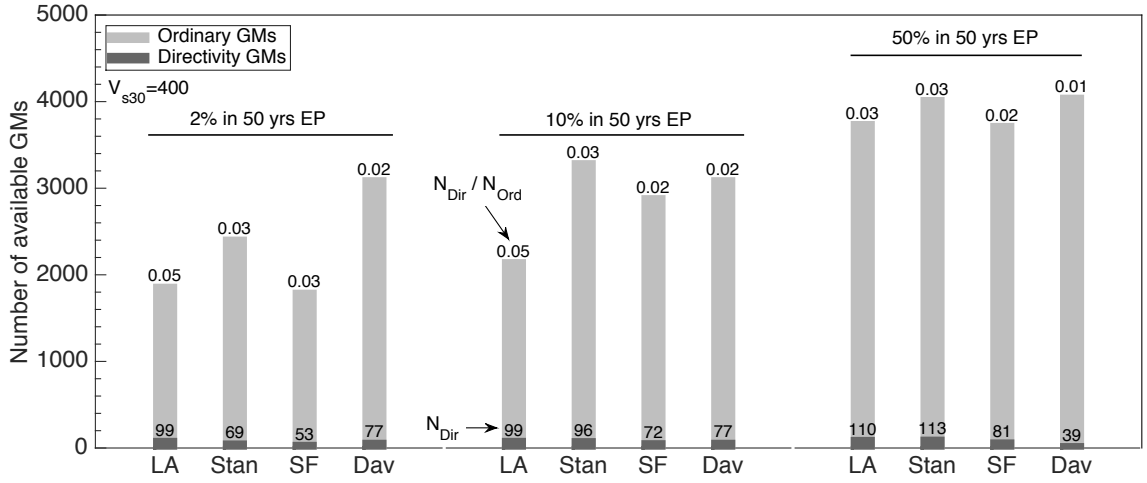

Figure 5.28: Number of the available directivity and non-directivity (*i.e.,* 'ordinary') ground motions in the database after the application of causal parameters bounds in Table 5.2.

two locations, as shown in Figures 5.21 and 5.22, are dominated by ruptures with $M_w \geq$7.5 and $R_{rup} \leq$20 km, for which there is a smaller number of records available for ground motion selection. The paucity of recorded ground motions from large magnitude ruptures in the near fault region (shown in Figure 5.5) has also affected the calculated $\overline{P_{Dir}}$, as Shahi and Baker (2014a) model is developed based on the limited number of records available from such ruptures. As a result there is an uncertainty associated with the calculated $\overline{P_{Dir}}$, which is annotated symbolically in Figure 5.27. Therefore, the dashed blue line in Figure 5.27 should not be considered as the definitive target for ground motion selection but merely an indication.

Since the finite number of ground motions selected may affect the median and maximum N_{Dir} in the ground motion ensembles discussed previously, Figure 5.29 examines the median and maximum N_{Dir}/N_{gm} for the ensembles with 10, 20, 50, and 100 ground motions (selected based on case 4 target distribution). The results correspond to 50%, 10% and 2% EPs for the Los Angeles and San Francisco SA(3.0 s) hazard cases, and are compared with the corresponding $\overline{P_{Dir}}$. Figure 5.29 shows that both the median and maximum N_{Dir}/N_{gm} from the selected ensembles are not changing significantly with the increase in the number of replicate selections,

implying that the median and maximum N_{Dir} from 20 ensembles (presented in the previous results) are stable estimates for these values. While Figure 5.29 shows that the median and maximum directivity probability represented in the selected ensembles are smaller than the predicted $\overline{P_{Dir}}$ for PSHA cases with $\overline{P_{Dir}} \geq 0.4$ (*e.g.*, 10% and 2% EPs for San Francisco), it is noted that there is an unquantified uncertainty associated with the predicted $\overline{P_{Dir}}$ as shown symbolically in Figure 5.29.

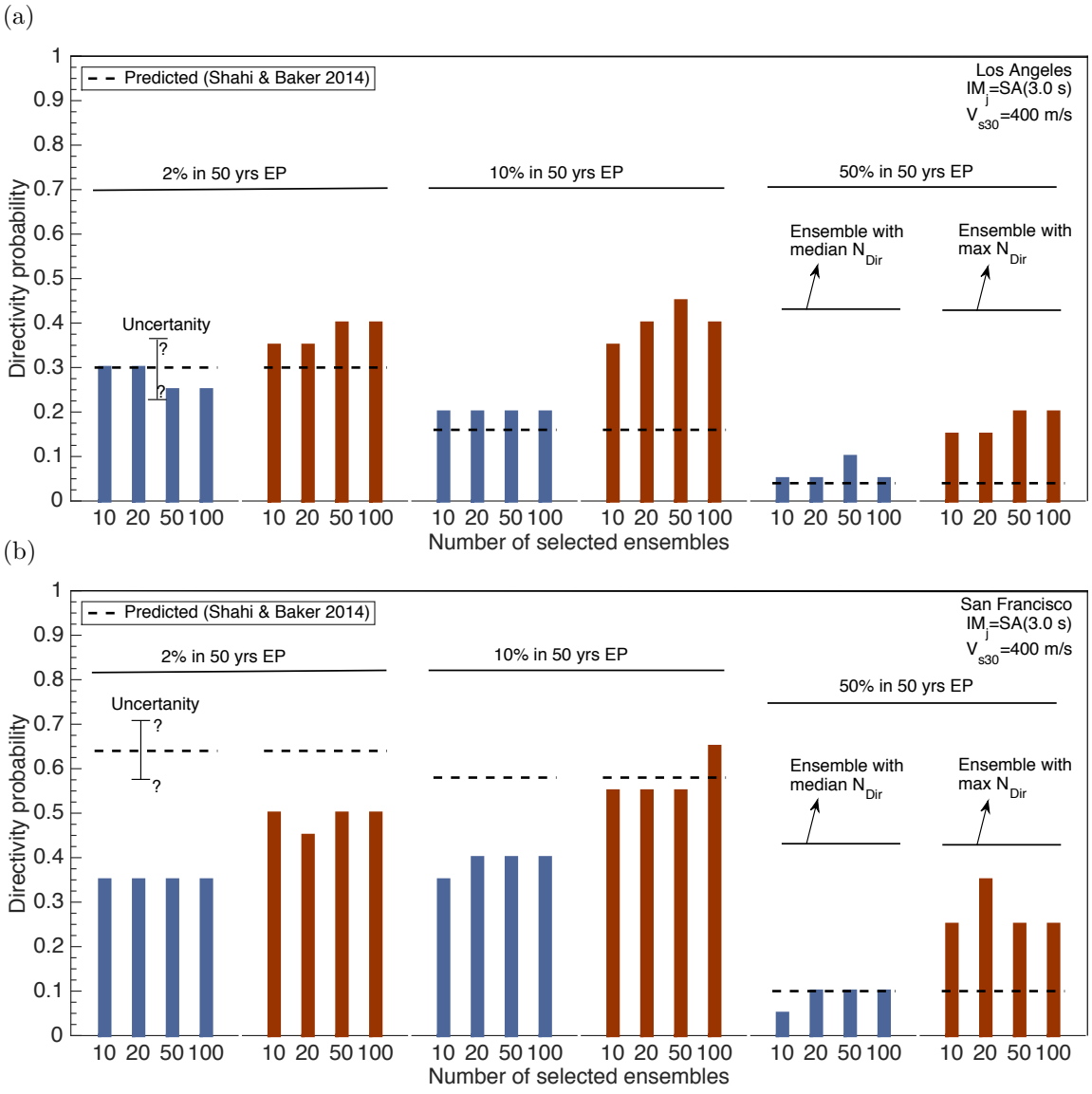

Figure 5.29: Comparison between the directivity probability represented by the selected ground motion ensembles with the corresponding $\overline{P_{Dir}}$ calculated at three EPs for the SA(3.0 s) hazard: (a) Los Angeles; (b) San Francisco.

5.6.3.3 Directivity properties of selected ground motions: Pulse period

In addition to the proportion of directivity ground motions, pulse period (T_p) is also noted as an important factor to consider in the near-fault ground motion selection (NEHRP, 2011). Since PSHA represents the effect of all causative ruptures in the vicinity of the site, T_p distribution based on PSHA results is not a function of a single scenario rupture. Therefore, the contribution of all the causative ruptures is considered in establishing the target T_p distribution ($f_{T_p}^{total}(t_p)$), as presented in Equation 5.19:

$$f_{T_p}^{total}(t_p|im_j) = \sum_{k=1}^{N_{rup}} f_{T_p}(t_p|rup_k)\, P_{Rup|IM_j}(rup_k|IM_j = im_j) \tag{5.19}$$

where $f_{T_p}(t_p|rup_k)$ is the T_p distribution from rup_k based on Equations 5.10 and 5.11 (Shahi and Baker, 2014a) summed over all the contributing ruptures to the occurrence of target conditioning IM; and $P_{Rup|IM_j}(rup_k|IM_j = im_j)$ is the contribution of rup_k to the occurrence of $IM_j = im_j$ using Equation 5.16.

Figure 5.30 presents the T_p distribution of the pulse-like motions from the ensembles with the median N_{Dir} for the Los Angeles and San Francisco SA(3.0 s) hazard at 2% and 10% EPs in comparison to the corresponding target T_p distributions. As shown, the selected directivity ground motions have an appropriate representation of the corresponding $f_{T_p}^{total}(t_p)$, with their empirical distributions lying inside the KS statistical rejection bounds. This holds true for the other PSHA cases considered. As noted previously, no *ad hoc* criterion in terms of T_p was enforced to select directivity records and the selection process is based on only explicit IMs, which are themselves affected by any forward directivity effects (such as T_p). As demonstrated in Figure 5.30, this approach results in ensembles with an appropriate representation of T_p as an implicit parameter of ground motion severity.

Figure 5.30 also illustrates that the ground motions selected based on case

4 target distribution (*i.e.,* considering both SA and non-SA IMs in the selection process) have, in general, a closer T_p distribution to $f_{T_p}^{total}(t_p)$. The paucity of recorded pulse-like ground motions (from large magnitude ruptures) with T_p values larger than 10 s, as shown in Figure 5.5b, is the reason for not having selected ground motions with large T_p corresponding to the upper tail of the $f_{T_p}^{total}(t_p)$; however, in general, the selected records can accurately represent the median T_p values. Selecting records from simulated ground motion ensembles (Bradley et al., 2015) can potentially resolve these shortcomings in the empirical databases for ground motion selection once predictive confidence in simulated ground motions is developed through validations (Galasso et al., 2012, 2013). In terms of PSHA cases for which the hazard is dominated by a single scenario, it was shown previously in Figure 5.12 (section 5.5.2.2) that the selected records based on case 4 weight vector have an appropriate representation of the T_p distribution for scenario ruptures.

5.6.3.4 Causal parameters and their effect on selected directivity ground motions

In addition to explicit IMs, causal parameters such as M_w and R_{rup} (as the implicit measures of ground motion severity) are commonly examined for the selected ground motion ensembles in comparison to the distribution of scenario ruptures contributing to the hazard at the site. Figure 5.31 presents the M_w and R_{rup} distributions of the records from the ensembles with the median N_{Dir} representing the Los Angeles and San Francisco SA(3.0 s) hazard at 2% EP, compared to the marginal distribution from the corresponding occurrence deaggregation results. As shown, M_w and R_{rup} distributions of the selected records cannot precisely represent the deaggregation distribution, partially due to the small number of ground motions available with $M_w \geq 6.5$ and $R_{rup} \leq 30$ km recorded on site conditions compatible with the V_{s30} bounds applied (Table 5.2). Despite the discrepancies noted with respect to Figure 5.31, it is noted that causal parameters of the selected records (*e.g.,* M_w and R_{rup}) are not of a primary concern in comparison to their explicit IMs when selecting ground motions. As shown by Tarbali and

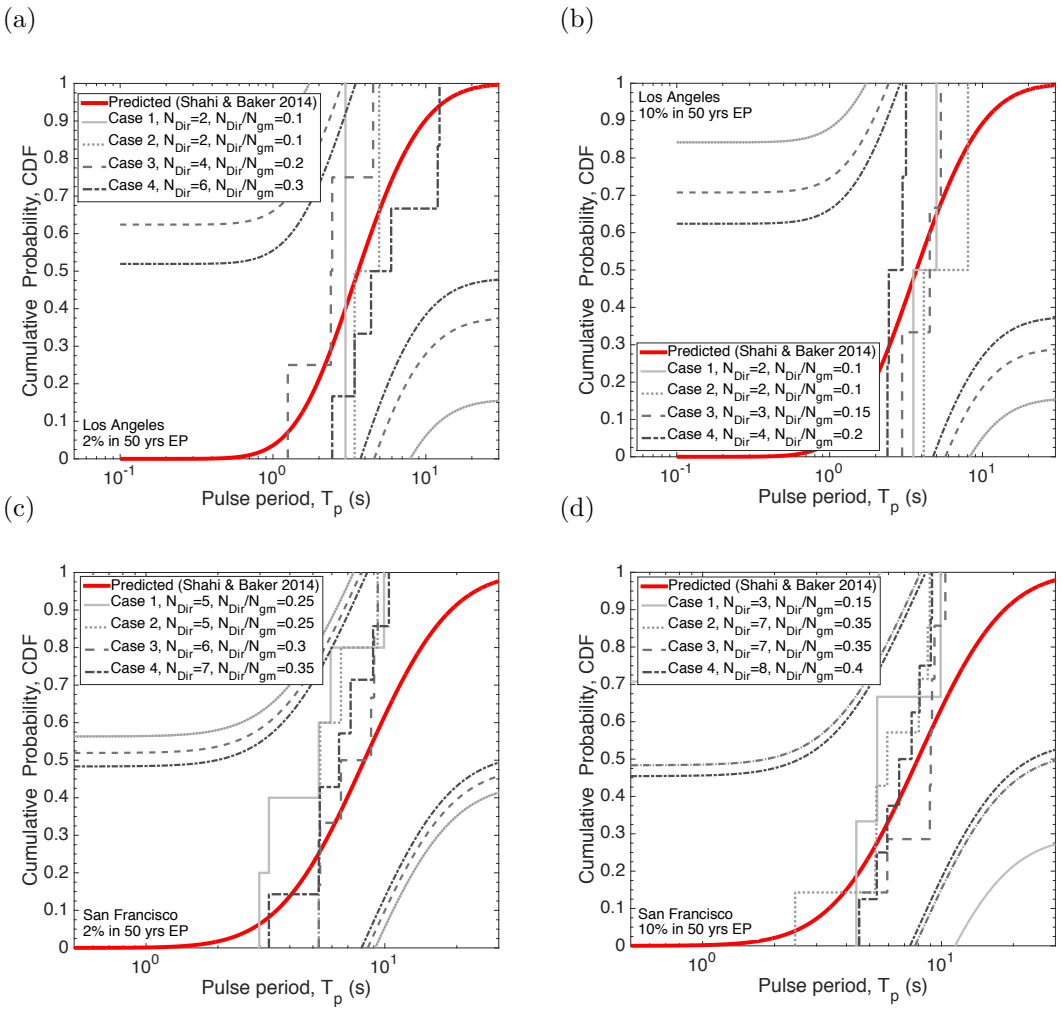

Figure 5.30: Comparison between the pulse period distributions of selected ground motion ensembles with the calculated target distribution for the SA(3.0 s) hazard at 2% and 10% EPs: (a)-(b) Los Angeles; (c)-(d) San Francisco.

Bradley (2015a, 2016), although applying narrow bounds will result in selecting records with M_w and R_{rup} distributions close to the deaggregation results, it will come with a degraded representation of the target hazard in terms of explicit IMs, typically as a result of an insufficient number of prospective ground motions.

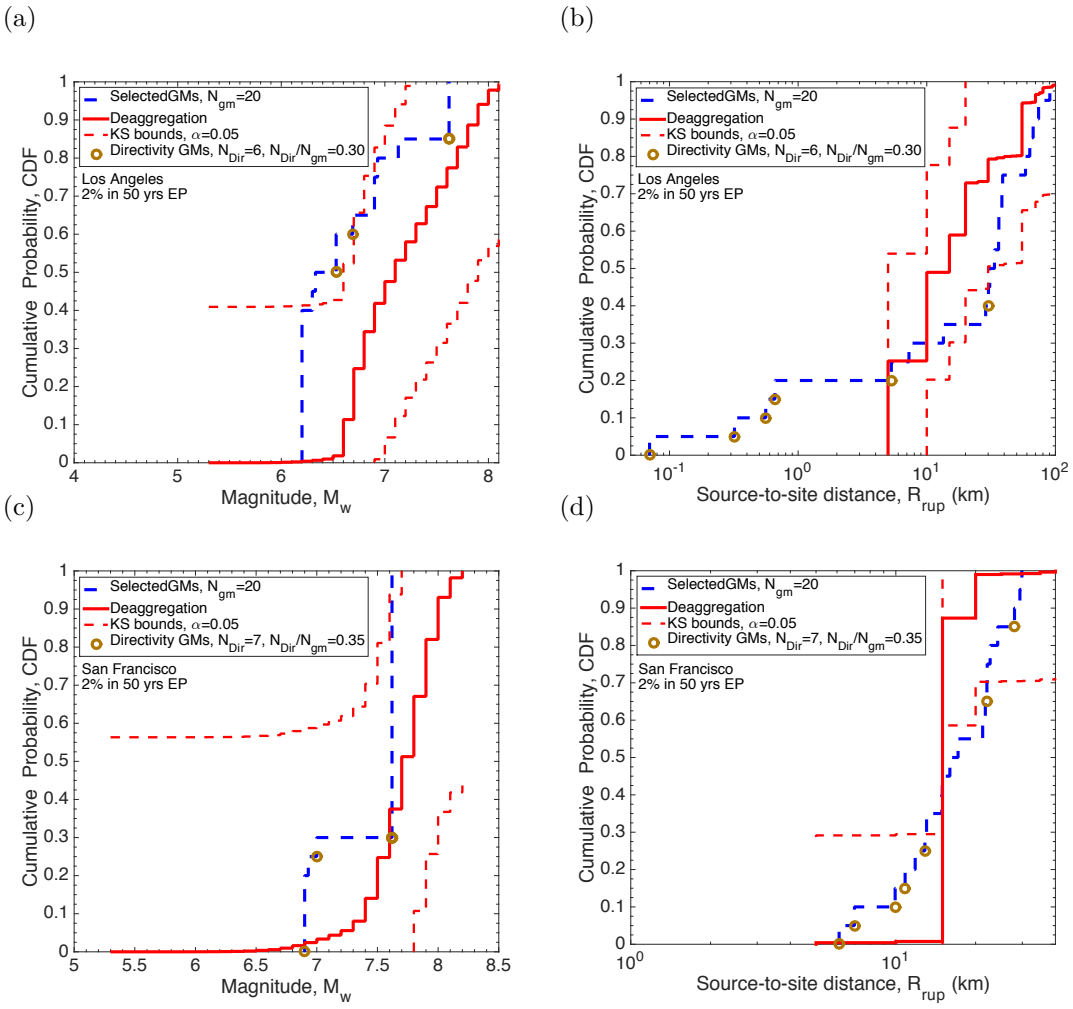

Figure 5.31: M_w and R_{rup} distributions of the selected ground motions compared with the marginal deaggregation distributions for the SA(3.0 s) hazard at 2% EP: (a) Los Angeles; (b) San Francisco.

It is also noted that using appropriate causal parameter bounds (*e.g.,* Table 5.2), in contrast to using no bounds, effectively removes ground motions with drastically different characteristics with respect to the target hazard and results in an improved representation of the explicit IM distributions and the causal parameters (Tarbali and Bradley, 2015a, 2016). In order to investigate this notion

in terms of selecting pulse-like ground motions in the near-fault region, Figure 5.32 presents results similar to those in Figure 5.27 with the exception that the records are selected without using causal parameter bounds of Table 5.2. As shown, ignoring the bounds results in lower median directivity probabilities, for most cases, specifically for Los Angeles, Stanford, and San Francisco at 2% EP, and Stanford and San Francisco at 10% EP levels. Similar results were also obtained for the selected ground motions representing single scenario ruptures (as presented in Figure 5.16). Hence, the consideration of 'wide' causal parameters (Tarbali and Bradley, 2015a, 2016) leads to a more consistent selection of ground motions from the prospective of directivity, without being overly restrictive.

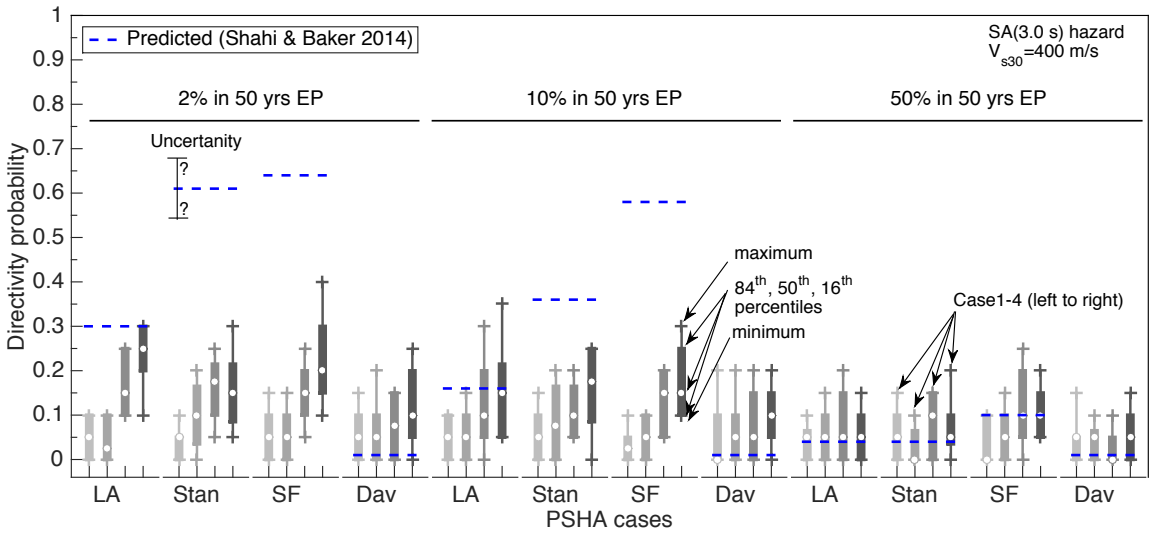

Figure 5.32: Directivity probability represented by the ground motion ensembles selected without using the causal parameter bounds of Table 2 for SA(3.0 s) hazard. The results for case1-4 targets for ground motion selection are shown by separate box-and-whisker colors as annotated.

5.6.3.5 The effect of narrow causal parameter bounds on the number of directivity ground motion selected

For PSHAs such as the Stanford and San Francisco cases considered, for which the $\overline{P_{Dir}}$ of the selected ground motion ensembles are smaller than the calculated $\overline{P_{Dir}}$ (*e.g.,* Figures 5.29 and 5.27), narrower bounds on M_w and R_{rup} can be utilised to constrain the database to a range in which a larger number of directivity records

are available. Figure 5.37 illustrates the M_w-R_{rup} distribution of the available records based on M_w=[6.5, 8.0] and R_{rup}=[0, 20 km] bounds, referred to as the 'narrow' bounds hereafter. As shown, directivity records comprise 36% of the total records available for ground motion selection.

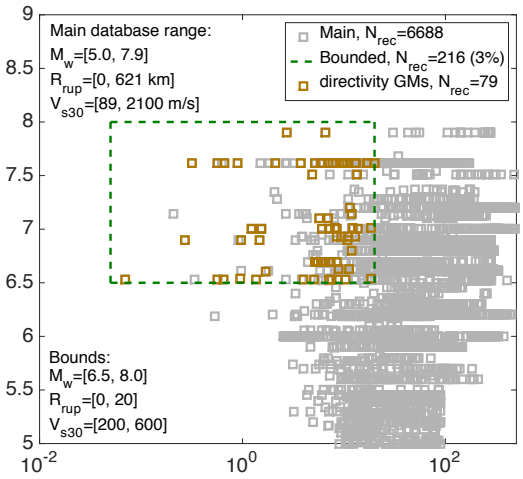

Figure 5.33: M_w-R_{rup} distribution of the available ground motions after the application of 'narrow' causal parameter bounds.

Figure 5.34 presents the SA ordinates of the ground motions selected based on the narrow bounds (from the ensemble with the median N_{Dir} among the 20 replicate ensembles), and their corresponding 16$^{\text{th}}$, 50$^{\text{th}}$, and 84$^{\text{th}}$ percentiles for the Los Angeles, Stanford, and San Francisco SA(3.0) hazards at 2% and 10% EPs. As shown in Figures 5.34a-b, the N_{Dir} of the selected ensemble for the Los Angeles case is larger than the corresponding $\overline{P_{Dir}}$ (ensembles selected based on the wide bounds presented in Table 5.2 had an accurate representation of the $\overline{P_{Dir}}$ for the Los Angeles case as shown in Figures 5.24 and 5.27). In contrast, the selected records based on the narrow bounds have an almost exact representation of the calculated $\overline{P_{Dir}}$ for the Stanford and San Francisco cases. This improved representation of the $\overline{P_{Dir}}$ comes with a degraded quality for the selected records in terms of representing the target explicit IMs. As shown in Figures 5.34c and 5.34e, 16$^{\text{th}}$ and 50$^{\text{th}}$ percentiles of the selected records are larger than the target distribution for the 2% EP hazard for T <3.0 s.

The degraded representation of the target hazard in terms of explicit IMs,

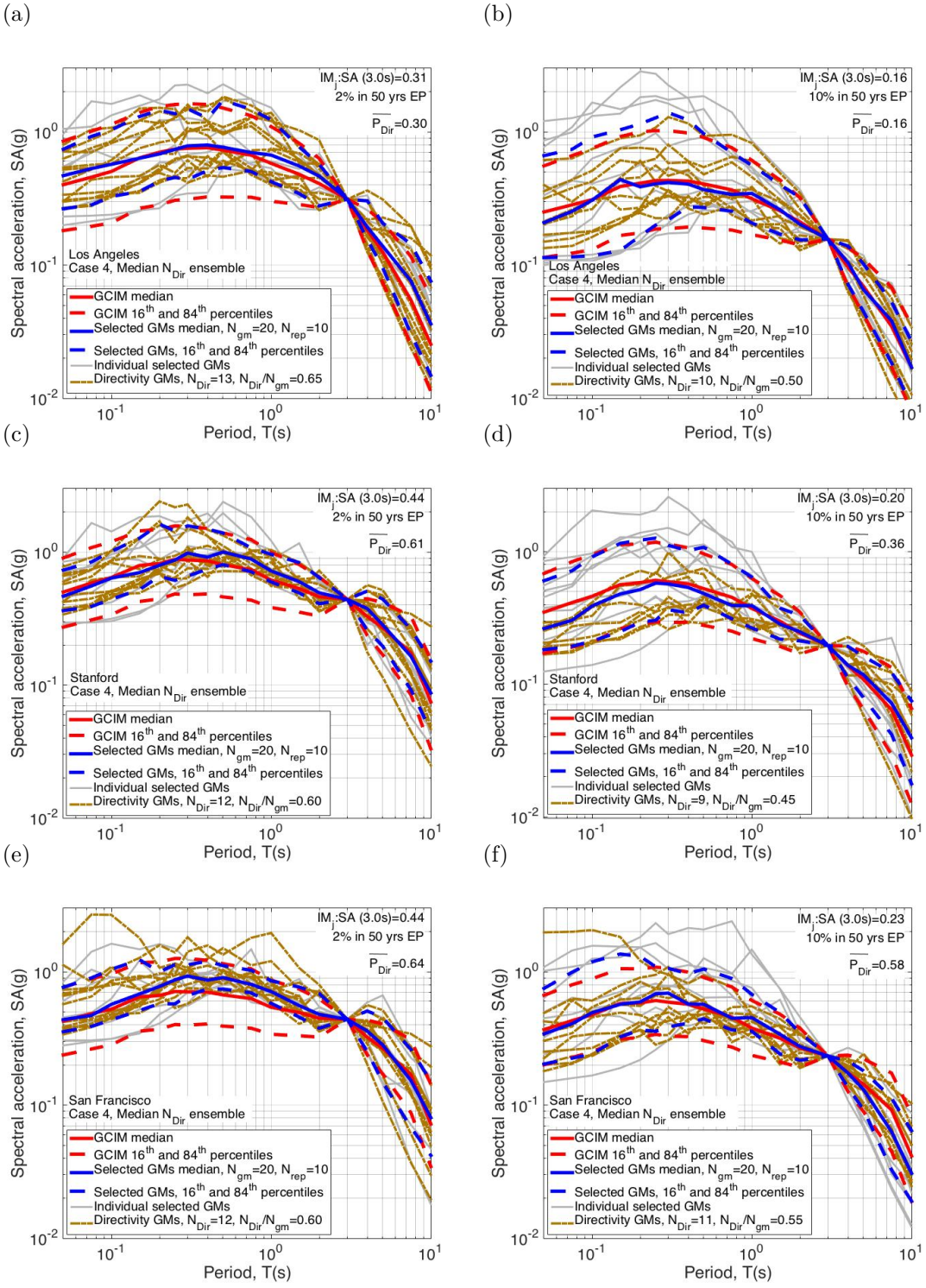

Figure 5.34: Comparison between the SA ordinates of the selected records based on the narrow causal parameter bounds and the target distribution for SA(3.0 s) hazard at 2% and 10% EPs: (a)-(b) Los Angeles; (c)-(d) Stanford; (e)-(f) San Francisco.

typically as a result of an insufficient number of prospective ground motions due to the utilisation of excessive narrow bounds, is discussed by (Tarbali and Bradley, 2015a, 2016) in more details. It is noted here that causal parameters of the selected records (*e.g.*, M_w, R_{rup}, and directivity versus non-directivity calcification) are not of a primary concern in comparison to the explicit IMs when selecting ground motion records.

Figure 5.35 compares the directivity probability represented by the ground motion ensembles selected based on the narrow and wide causal parameter bounds (using case 4 weight vector) for the Los Angeles, Stanford, and San Francisco sites. As shown, the median N_{Dir} from the ensembles selected based on the narrow bounds have an appropriate representation of the $\overline{P_{Dir}}$ for the San Francisco site at 2% and 10% EPs, and for the Stanford site at 2% EP. However, utilising the narrow bounds results in over-representation of the $\overline{P_{Dir}}$ for the Los Angeles site at 2% and 10% EPs, along with all cases at the 50% EP hazard.

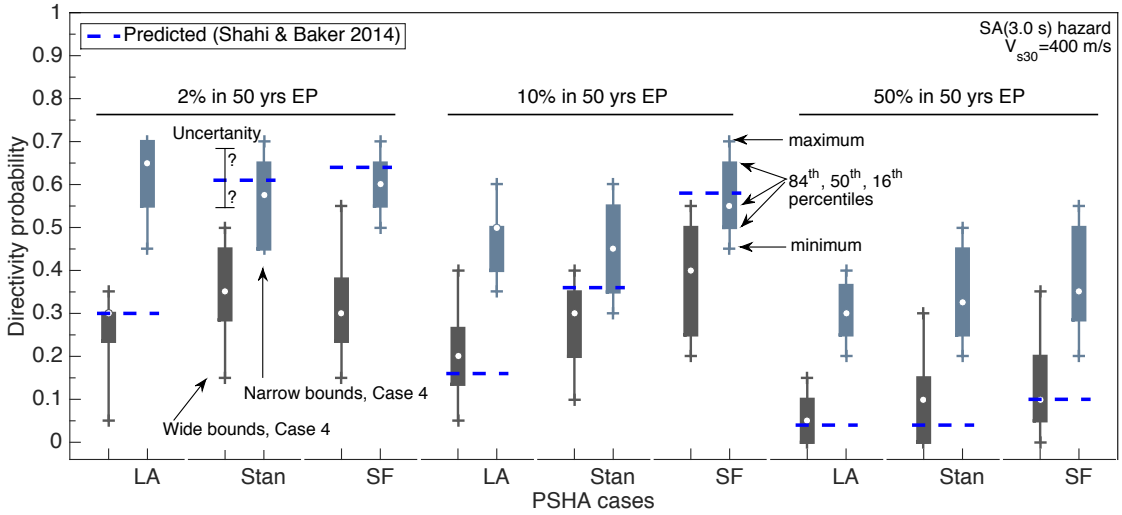

Figure 5.35: Comparison between the directivity probabilities represented by ground motion ensembles selected based on the narrow and wide causal parameter bounds for the SA(3.0 s) hazard at the Los Angeles, Stanford, and San Francisco sites. The results for the different bounds are shown by separate box-and-whisker colors as annotated.

Figure 5.36 compares the T_p distribution of the selected ground motions based on the narrow and wide bounds for the Stanford and San Francisco sites at 2% and 10% EP hazards. As shown, utilising the narrow causal parameter bounds

does not significantly affect the T_p distribution of the selected ground motions, as the T_p distributions from the narrow and wide bounds are similar (with empirical distributions within the statistical rejection bounds with respect to the target T_p distribution).

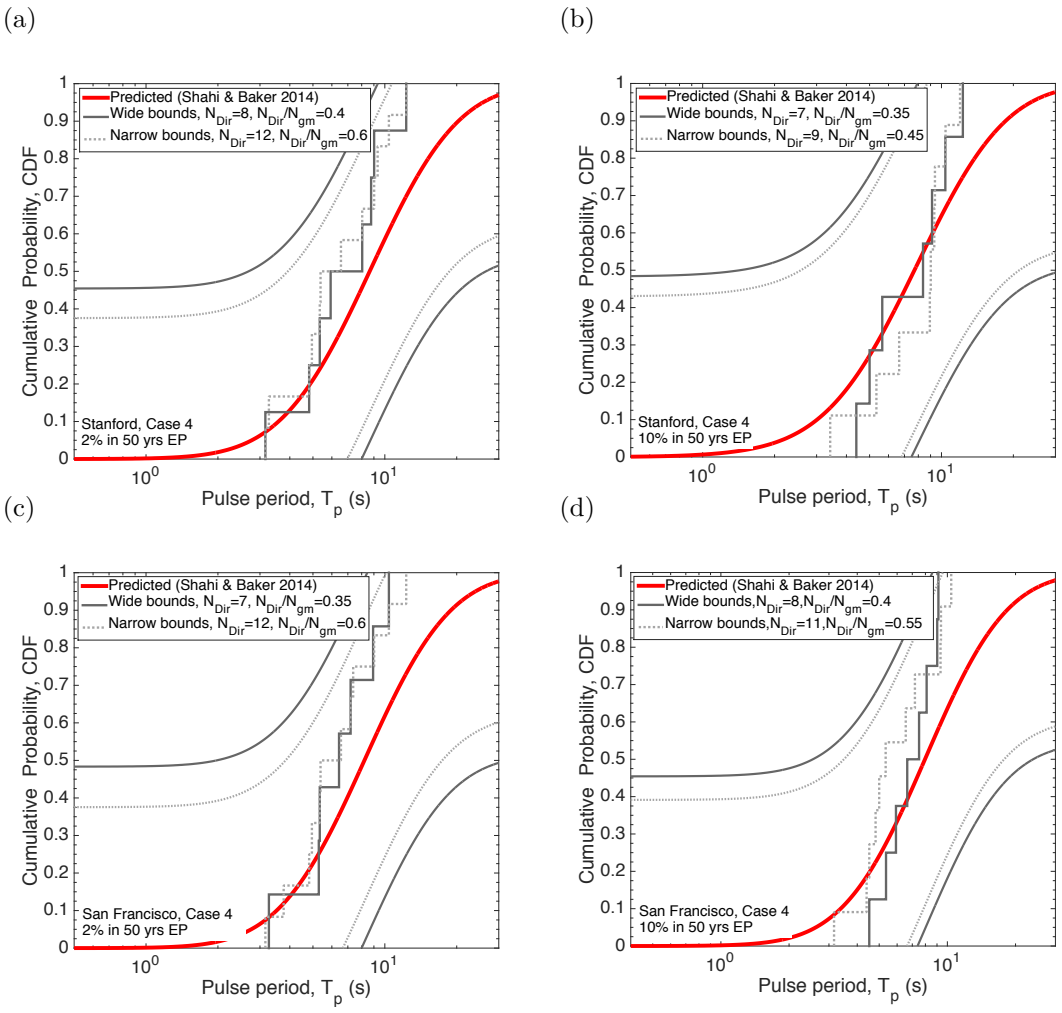

Figure 5.36: Comparison between the pulse period distributions of selected ground motions based on the narrow and wide bounds for the SA(3.0 s) hazard at 2% and 10% EPs: (a)-(b) Los Angeles; (c)-(d) San Francisco.

5.6.4 Influence of selected ground motions on seismic demand hazard

5.6.4.1 Seismic demand hazard

In order to investigate the demand-based seismic performance of the considered SDOF systems subjected ground motions selected based on the PSHA results, the seismic demand hazard is calculated using Equation 5.20 (Shome and Cornell, 1999; Krawinkler and Miranda, 2004):

$$\lambda_{EDP}\left(edp\right) = \int_0^\infty G_{EDP|IM_j}\left(edp|im_j\right)\left|\frac{\mathrm{d}\lambda_{IM_j}\left(im_j\right)}{\mathrm{d}IM_j}\right|\mathrm{d}IM_j \tag{5.20}$$

where $G_{EDP|IM_j}\left(edp|im_j\right)$ is the probability that the system will experience an engineering demand parameter (EDP) larger than edp given $IM_j = im_j$; and $\mathrm{d}\lambda_{IM_j}\left(im_j\right)/\mathrm{d}IM_j$ is the derivative of the hazard curve with respect to IM. $G_{EDP|IM_j}\left(edp|im_j\right)$ is calculated by separating the collapse and non-collapse cases at the considered IM levels, as in Equation 5.21:

$$G_{EDP|IM_j}\left(edp|im_j\right) = G_{EDP|IM_j,NC}\left(edp|im_j\right)\left(1 - P_{C|IM_j}\left(im_j\right)\right) + P_{C|IM_j}\left(im_j\right) \tag{5.21}$$

where $G_{EDP|IM_j,NC}\left(edp|im_j\right)$ is the probability of $EDP > edp$ given $IM_j = im_j$ calculated from the non-collapse (NC) responses; and $P_{C|IM_j}\left(im_j\right)$ is the probability of having collapse in the system given $IM_j = im_j$. $P_{C|IM_j}\left(im_j\right)$ is calculated based on the proportion of ground motions causing collapse within the selected ensemble of records for a given IM level. In general, a lognormal distribution is fitted to the empirical collapse data (Baker, 2015).

The maximum displacement of three inelastic SDOF systems with strength and stiffness degradations (Ibarra et al., 2005; Lignos and Krawinkler, 2012) is chosen as the EDP of interest and the demand hazard is calculated for the selected 20 replicate ground motion ensembles. As previously presented in section 5.5.3.1, the SDOF systems considered have fundamental vibration periods (T_n) of 1, 3,

and 5 s, representing engineered systems that may be susceptible to the range of vibration periods affected by the directivity pulse periods (see Figure 5.15 for the backbone curves). Seven IMs at 1%, 2%, 4%, 6%, 8%, 10%, and 50% in 50 years seismic hazard EPs are chosen to select ground motion ensembles and conduct nonlinear response history analyses on the considered SDOF systems (two more IM levels corresponding to 0.25% and 0.5% EPs were also added to these seven IM levels only for the Los Angeles case, in order to constrain the extrapolation error for the corresponding collapse fragility curves). In order to estimate the demand hazard for IM values between the considered levels, a linear relationship between $ln(EDP)$ and $ln(IM)$ is used to interpolate between non-collapse responses (Bradley, 2013e). The maximum likelihood approach of Baker (2015) is used to establish the collapse fragility function. As mentioned previously in section 5.5.3.1, the collapse limit for the considered SDOF systems are defined based on a nominal displacement to height ratio, specifically, 0.06, 0.05, and 0.025 for the T_n=1, 3, and 5 s SDOF systems, corresponding to 4.25, 3, and 2.3 displacement ductilities, respectively.

Figure 5.37 presents the demand hazard for the T_n= 3 s SDOF system using 20 replicate ground motion ensembles at each IM level for the four sites considered. As shown, replicate ground motion ensembles result in similar hazard curves for demand hazard annual exceedance frequencies greater than 0.005. The difference increases for demand hazard levels smaller than 0.005 as the number of collapse cases increases (with the exception of the Davis case, *i.e.,* Figure 5.37d, for which the demand is below the collapse limit). In order to investigate the effect of N_{Dir} on the demand hazard variation, demand hazard curves corresponding to the maximum, minimum, and median N_{Dir} ensembles are calculated. The maximum (median, or minimum) N_{Dir} demand hazard curves are calculated based on the ensembles that have the maximum (median, or minimum) number of directivity motions among the 20 replicate ensembles at all IM levels.

As shown in Figure 5.37a for the Los Angeles site, the maximum N_{Dir} curve has the largest demand hazards at the near-collapse EDP levels. In contrast,

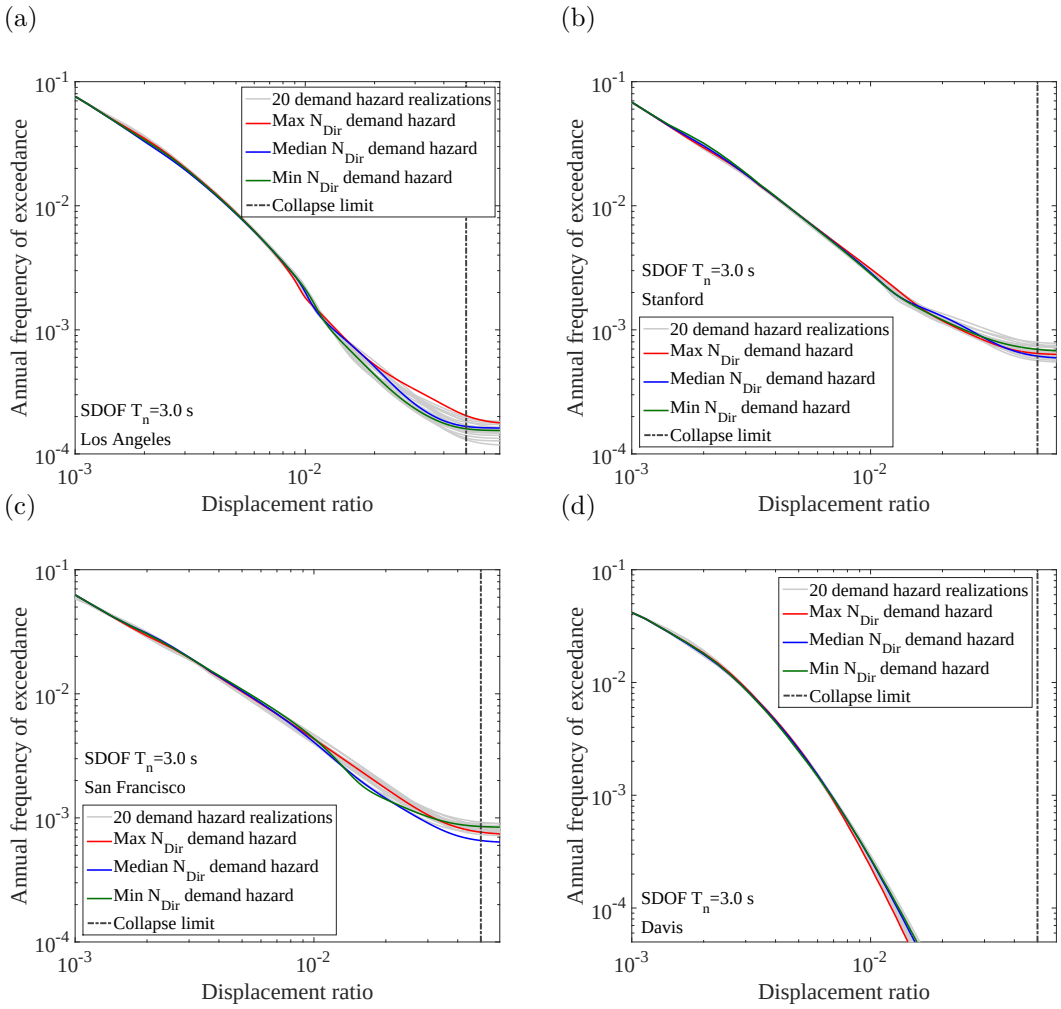

Figure 5.37: Demand hazard curves from the 20 replicate ground motion ensembles for the T_n=3 s SDOF system: (a) Los Angeles; (b) Stanford; (c) San Francisco; (d) Davis.

as shown in Figure 5.37b for the Stanford site, the demand hazard curves with the maximum, minimum, and median N_{Dir} are very close to each other. Figure 5.37c also shows that, for the San Francisco site, the minimum N_{Dir} demand hazard is larger at near-collapse EDP levels compared to the maximum and median N_{Dir} demand hazards. The reasons behind such differences are elaborated on, subsequently.

Figure 5.38 presents the dispersion (*i.e.,* standard deviation of the natural logarithm) of the demand hazards from the 20 replicate ensembles for the T_n= 3 s SDOF system, which is significantly smaller than the dispersion in the demand hazard due to epistemic uncertainties in seismic hazard analysis and ground motion selection discussed in Tarbali et al. (2017).

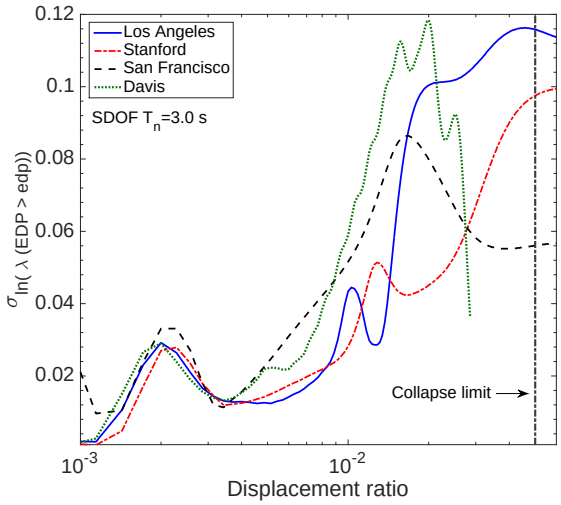

Figure 5.38: Dispersion of the demand hazards from the 20 replicate ground motion ensembles for the T_n=3 s SDOF system.

5.6.4.2 Collapse fragility

In order to investigate the reason for the variability in the demand hazard at the near-collapse EDP levels with respect to the N_{Dir}, Figure 5.39 presents the collapse fragility functions calculated for the Los Angeles, Stanford, and San Francisco sites from the 20 replicate ground motion ensembles (collapse for Davis was not observed at the lowest seismic hazard level considered (*i.e.,* 0.1% EP in 50

years). Figure 5.39a illustrates that for the rare ground motion levels (*i.e.,* SA(3.0) $\geq$ 0.4 g corresponding to seismic hazard EP$\leq$1% in 50 years − see Figure 5.17), the collapse probabilities corresponding to the maximum N_{Dir} fragility curve is lower than those corresponding to the median and minimum N_{Dir} curves. However, Since rare IM levels have low probability of occurrence, the demand hazard is not significantly affected by the difference in the collapse probabilities at the rare IM levels. In contrast, for IMs smaller than 0.4 g, the maximum N_{Dir} collapse fragility curve results in higher collapse probabilities compared to the median and minimum N_{Dir} curves. This determines the larger annual exceedance frequency for the maximum N_{Dir} demand hazard compared to the other demand hazard curves for the Los Angeles site (shown in Figure 5.37a). In contrast to the Los Angeles site, as shown in Figure 5.39c for the San Francisco site, the minimum N_{Dir} collapse fragility curve results in higher collapse probabilities for SA(3.0) $\leq$ 0.4 g (corresponding to seismic hazard EP>2% in 50 years − see Figure 5.17) compared to the median and maximum N_{Dir} fragility curves, which results in higher demand hazards at the near collapse EDP levels for the San Francisco site (shown in Figure 5.37c). These examples illustrate how the variation in the collapse probability at IM levels with higher probability of occurrence governs the variation in the demand hazard curve at the near-collapse EDP levels.

In order to investigate the dependency of the collapse probability on the N_{Dir}, Figure 5.40 illustrates the collapse probabilities from 20 replicate collapse fragility functions versus the corresponding N_{Dir} of the selected ground motion ensembles at different hazard levels. In addition, collapse probabilities from the fragility functions corresponding to the maximum, minimum, and median N_{Dir} ensembles are also presented. The p-values calculated for the slope of the relationship between the collapse probability and N_{Dir} is utilised to determine the dependency between these two parameters. The p-value gives the probability that there is no relationship between these two parameters (*i.e.,* the null hypothesis), and conventionally a p-value smaller than 0.05 is considered as a threshold to reject this hypothesis. As shown in Figure 5.40, with the exception of the 0.5%

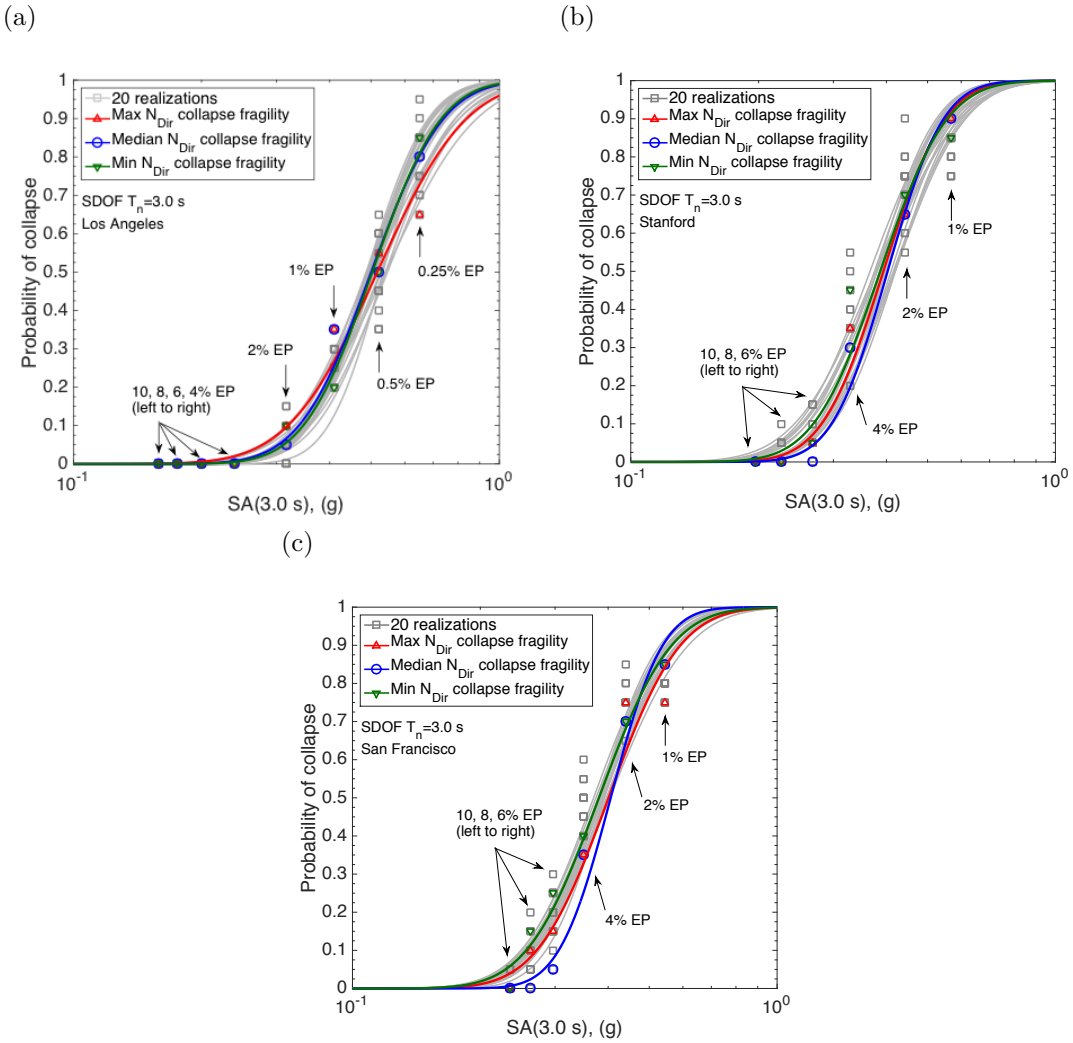

Figure 5.39: Collapse fragility curves of the T_n=3 s SDOF system based on the 20 replicate ground motion ensembles: (a) Los Angeles; (b) Stanford; (c) San Francisco. The points indicate the proportion of the records within each ensemble that has caused collapse in the system at specific seismic hazard EPs in 50 years.

EP for the Los Angeles and 8% EP for Stanford sites, the calculated p-values are well above the 0.05 threshold, indicating that the a relationship between the collapse probability and N_{Dir} cannot be accepted. Figure 5.40 also illustrates that there is no clear trend between the collapse probability and N_{Dir}, especially for EP$\geq$2% seismic hazard levels which significantly influence the demand hazard at the near-collapse EDP levels (as discussed in Figures 5.37 and 5.39). In addition, the collapse probabilities from the maximum N_{Dir} fragility curve are not necessarily the largest values among the replicate ensembles considered, and the ensembles with smaller N_{Dir} may result in higher collapse probabilities.

From the above discussion it is clear that the variability in the collapse probability related to the record-to-record variability is the main reason for the variation in the demand hazard rather than the difference in the N_{Dir} of selected ground motion ensembles. Hence, it is advocated that the selection of ground motions in the near-fault region based on the explicit IM properties alone is preferred to that in which the proportion of directivity ground motions within the selected ensembles is specified *a priori* as a strict criterion for ground motion selection.

5.7 Conclusion

An approach was presented to consider the forward directivity velocity pulse effect in seismic hazard analysis, adapted based on Shahi and Baker (2011) method. However, instead of separating the seismic hazard calculations for pulse-like and non-pulse-like ground motions, the 'total' pseudo-acceleration distribution is assumed to be lognormal in the presented approach, with the mean and standard deviation accounting for pulse-like and non-pulse-like ground motions. This results in a single target hazard at the site for ground motion selection and is a surrogate for future ground motion models that will explicitly address the effect of directivity pulses in a rigorous manner instead of using *post hoc* correction models.

(a)

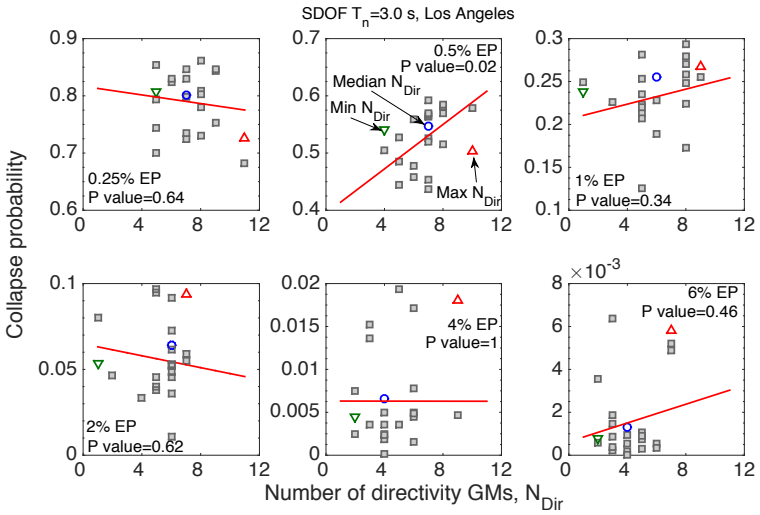

(b)

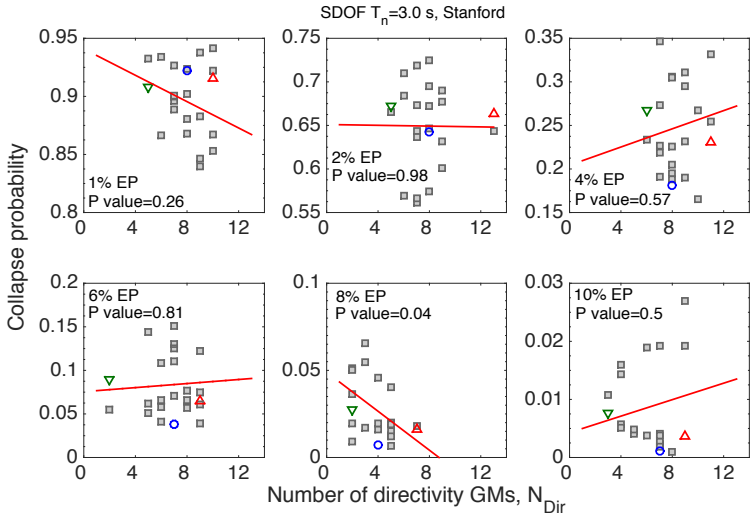

Figure 5.40: Collapse probabilities versus the corresponding N_{Dir} from the 20 replicate collapse fragility curves at specific seismic hazard EPs in 50 years: (a) Los Angeles; (b) Stanford.

(c)

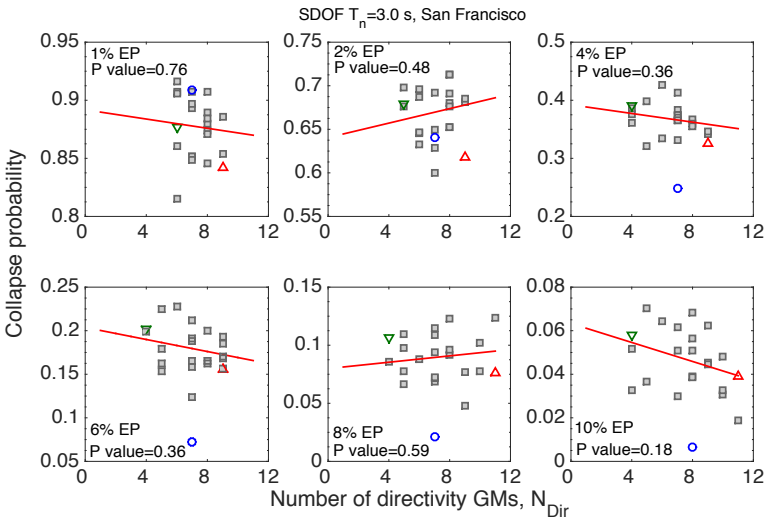

Figure 5.40: *(continued)* Collapse probabilities versus the corresponding N_{Dir} from the 20 replicate collapse fragility curves at specific seismic hazard EPs in 50 years: (c) San Francisco.

The ability of ground motion selection methods to appropriately select records containing forward directivity pulse motions in the near-fault region was examined. Particular attention was given to ground motion selection which is explicitly based on ground motion intensity measures (IMs), including pseudo-acceleration response spectrum, duration, and cumulative measures; rather than a focus on implicit parameters (*i.e.,* distance, and pulse or non-pulse classifications) that are conventionally used to heuristically distinguish between the near-fault and far-field records. The selection process is based on the generalised conditional intensity measure (GCIM) approach which addresses the shortcomings of existing methods for selecting forward directivity ground motions. Forward directivity effects were considered in the target IM distributions for ground motion selection by incorporating such effects in the seismic hazard analysis process. No *ad hoc* criterion in terms of the number of directivity ground motions and their pulse periods was enforced for selecting pulse-like records. Example applications were presented for scenario and probabilistic seismic hazard analysis cases with different rupture characteristics, source-to-site geometry, and site conditions. Seismic demand on degrading inelastic single-degree-of-freedom systems subjected to the

selected ground motions were examined, and the effect of the number of directivity ground motion, N_{Dir}, was discussed. The results indicated that considering the directivity pulse effects in the target IM distributions and utilising multiple IMs in the selection process based on the GCIM approach results in ground motion ensembles with an accurate representation of the target hazard. It was shown that the selected ground motion ensembles can appropriately represent the total directivity probability at the site for a given hazard level if the available database of ground motion records have sufficient number of records in the near-fault region. It was also demonstrated that causal parameter bounds can be utilised to constrain the database of records for more accurate representation of the directivity probability. Moreover, the selected records can appropriately represent the target pulse period distribution. The conditional demand distribution, collapse fragility, and demand hazard calculated based on the selected replicate ground motion ensembles with varying N_{Dir} did not show a systematic dependency of these demand measures on the N_{Dir}. It was advocated that the selection of ground motions in the near-fault region based on IM properties alone is preferred to that in which the proportion of 'pulse-like' motions and their pulse periods are specified *a priori* as strict criteria for ground motion selection.

5.8 Software

Seismic hazard analysis, deaggregation, and the conditional IM distributions incorporating the directivity effects were performed using computer programs written for this study within the openSHA software source code. The programs enable the analyst to generate multiple realisations of the causative ruptures with different hypocentre locations along the strike and dip directions, calculate the directivity geometric parameters utilised in the directivity-included PSHA, conduct hazard analysis based on the RotD100, RotD50, and RotDI50 definitions for the SA ordinates, and consider multiple GMMs and ERFs in order to address seismic hazard epistemic uncertainty. The programs are published in the

following web address in order to provide the research community with means to conduct directivity-included PSHAs using advanced ERFs and recently developed GMMs implemented in the openSHA software: `https://sites.google.com/site/brendonabradley/software/ground-motion-selection-gcim`.

Chapter 6

Consideration and propagation of ground motion selection epistemic uncertainties to seismic performance metrics

Tarbali, K., Bradley, B. A., and Baker, J. W. (2017). Consideration and propagation of ground motion selection epistemic uncertainties to seismic performance metrics. *(Submitted to Earthquake Spectra)*.

6.1 Summary

This chapter investigates various approaches to propagate the effect of epistemic uncertainty in seismic hazard and ground motion selection to seismic performance metrics. Specifically, three approaches with different levels of rigour are presented for establishing the conditional distribution of intensity measures considered for ground motion selection, selecting ground motion ensembles, and performing nonlinear response history analyses to probabilistically characterise seismic response. The mean and distribution of the seismic demand hazard is

used as the principal means to compare the various results. An example application illustrates that, for seismic demand levels significantly below the collapse limit, epistemic uncertainty in seismic response resulting from ground motion selection can generally be considered as small relative to the uncertainty in the seismic hazard itself. In contrast, uncertainty resulting from ground motion selection appreciably increases the uncertainty in the seismic demand hazard for near-collapse demand levels.

6.2 Introduction

Uncertainty in the seismic performance of engineered systems is conventionally addressed by separating uncertainty rooted from a lack of knowledge, known as 'epistemic uncertainty', from that due to apparent variability in the natural processes according to the considered mathematical model, known as 'apparent aleatory variability' (Marzocchi and Jordan, 2014). Epistemic uncertainty in the modelled characteristics of causative rupture scenarios, resulting ground motions, and the seismic response of the engineered system of interest are important steps in addressing uncertainty in seismic performance. Time-domain response history analyses (RHAs) are usually conducted to estimate the distribution of engineering demand parameters characterising the seismic demand of the system. Conducting RHAs requires an appropriate representation of the seismic hazard at the site, which can be achieved by selecting ground motion time series recorded during past earthquakes and/or from an ensemble of simulated ground motions. While various methods have been proposed to select ground motions for seismic response analysis (*e.g.,* McGuire, 1995; Shome et al., 1998; Bommer and Acevedo, 2004; Kottke and Rathje, 2008; Baker, 2011; Jayaram et al., 2011; Wang, 2011; Bradley, 2012c) and address epistemic uncertainty in seismic hazard (*e.g.,* Kulkarni et al., 1984; Abrahamson and Bommer, 2005; McGuire et al., 2005; Bommer et al., 2005; Musson, 2005; Cotton et al., 2006; Bommer and Scherbaum, 2008; Bradley, 2009; Bommer et al., 2010; Atkinson et al., 2014), the only past study concerned with

the explicit consideration of seismic hazard epistemic uncertainty in the selection of ground motions is by Lin et al. (2013), which focused on epistemic uncertainty in empirical ground motion models (GMMs) and the subsequent computation of conditional pseudo spectral acceleration as the target for the ground motion selection process.

In the present study, we extend beyond Lin et al. (2013) to propagate epistemic uncertainty in both earthquake rupture forecast (ERF) and GMM aspects of probabilistic seismic hazard analysis (PSHA) to the conditional distribution of multiple intensity measures, $\boldsymbol{IM}$, utilised in ground motion selection. Different ground motion ensembles are then selected based on the epistemic uncertainty in $\boldsymbol{IM}$ to represent the seismic hazard epistemic uncertainty. Three different approaches are presented to propagate epistemic uncertainty in seismic hazard analysis and consequent ground motion selection to seismic performance measures, specifically the mean and distribution of the seismic demand hazard.

In the next sections, the main components of the seismic performance assessment procedure, and three approaches to propagate epistemic uncertainty are presented, as well as an example application to illustrate the pertinent implications.

6.3 Seismic performance assessment procedure

The PEER framework formula considers four calculation stages to assess the seismic performance of engineered systems, including seismic hazard, response, damage, and loss assessment (Deierlein et al., 2003). Epistemic uncertainty in the performance of a system can originate from the modelling assumptions utilised at each one of these four stages. This study focuses on the consideration of, and methods to propagate, epistemic uncertainties from seismic hazard analysis and ground motion selection results to demand-based seismic performance measures by calculating the seismic demand hazard of the system (*i.e.,* probability of

exceeding a seismic demand metric). That is, we exclude discussion of epistemic uncertainty in damage and loss assessment calculations, for which the reader is referred elsewhere (Taghavi and Miranda, 2003; Aslani and Miranda, 2005; Bradley, 2010a).

Computation of demand-based seismic performance measures, such as the seismic demand hazard, entails four key steps as explained in the following subsections. In this section we suppress the notational conditioning on the adopted GMM and ERF (*i.e.,* sources of seismic hazard epistemic uncertainties) which are presented in the following section explicitly based on three alternative approaches for epistemic uncertainty propagation.

6.3.1 Step 1: Seismic hazard analysis

PSHA quantifies the annual exceedance frequency[1] of a ground motion IM considering the characteristics of all causative rupture scenarios in the vicinity of the site based on an ERF as presented in Equation 6.1:

$$\lambda_{IM}\left(im\right) = \sum_{n=1}^{N_{rup}} P_{IM|Rup}(IM > im|rup_n)\ \lambda_{Rup}(rup_n) \tag{6.1}$$

where $P_{IM|Rup}(IM > im|rup_n)$ is the probability of $IM > im$ given a scenario rupture (rup_n), and $\lambda_{Rup}(rup_n)$ is the annual frequency of rup_n. As presented in Equation 6.1, the PSHA formulation takes into account apparent aleatory variability in the occurrence of rupture scenarios and the corresponding ground motions. Although not explicitly denoted here, the hazard curve defined via Equation 6.1 is conditioned on the adopted GMM and ERF, which will be later generalised for the case of multiple models representing epistemic uncertainty.

[1]Note that the seismic hazard can be defined based on the probability of exceedance (Field et al., 2003), which enables the time-dependent seismic hazard analysis utilised for the example application in this chapter.

6.3.2 Step 2: Ground motion selection

Selecting ground motion ensembles consistent with seismic hazard analysis provides the connection between seismic hazard and seismic response analyses. The severity of a ground motion is, in general, a function of amplitude, frequency content, duration, and cumulative effects. Therefore, it is pertinent to consider multiple ground motion IMs in order to take into account the salient characteristics of ground motion to accurately obtain the seismic demand distribution for the system of interest (Kramer, 1996; Bommer et al., 2004; Hancock and Bommer, 2005; Villaverde, 2007; Bradley, 2010b; Tarbali and Bradley, 2015b; Chandramohan et al., 2016). Since the seismic hazard is the aggregation of the threat from all seismic sources, it is also necessary to consider all causal ruptures when calculating the conditional distribution of IMs. Among several proposed methods for ground motion selection (*e.g.,* McGuire, 1995; Shome et al., 1998; Bommer and Acevedo, 2004; Kottke and Rathje, 2008; Baker, 2011; Jayaram et al., 2011; Wang, 2011; Bradley, 2012c), the generalised conditional intensity measure (GCIM) approach (Bradley, 2010b, 2012c), as the extension of the conditional mean spectrum (CMS) (Baker and Cornell, 2006a; Baker, 2011), provides the required framework to address the abovementioned points. Implementing the GCIM methodology requires deaggregating the seismic hazard curve and calculating the conditional distribution of IMs considered in the ground motion selection process (as elaborated on subsequently)

6.3.2.1 Deaggregating the seismic hazard curve

Establishing the conditional distribution of various IMs requires deaggregating the seismic hazard curve to obtain the contribution of causative ruptures at a given IM level, referred to as the 'conditioning IM' (and denoted as IM_j). The contribution of a given rupture (rup_n) to the occurrence of an IM value (denoted as $IM_j = im_j$) is known as the 'occurrence' deaggregation contribution (as opposed to the exceedance deaggregation representing the contribution of scenarios

to $IM_j > im_j$), and is calculated using Equation 6.2 (McGuire, 1995; Bazzurro and Cornell, 1999; Fox et al., 2015)[2]:

$$P_{Rup|IM_j}\left(rup_n|IM_j = im_j\right) \approx [P_{Rup|IM_j}\left(rup_n\middle|IM_j > im_j\right)\lambda_{IM}\left(IM_j > im_j\right) - P_{Rup|IM_j}\left(rup_n|IM_j > im_j + \delta im_j\right)\lambda_{IM}\left(IM_j > im_j + \delta im_j\right)]/[\lambda_{IM}\left(IM_j > im_j\right) - \lambda_{IM}\left(IM_j > im_j + \delta im_j\right)] \tag{6.2}$$

where $\lambda_{IM}\left(IM_j > im_j\right)$ and $\lambda_{IM}\left(IM_j > im_j + \delta im_j\right)$ are the annual exceedance frequencies corresponding to im_j and $im_j + \delta im_j$ values obtained from the seismic hazard curve, respectively; and $P_{Rup|IM_j}\left(rup_n\middle|IM_j > im_j\right)$ is the contribution of rup_n to the exceedance of IM_j at im_j level, calculated using Equation 6.3:

$$P_{Rup|IM_j}\left(rup_n\middle|IM_j > im_j\right) = \frac{P_{IM_j|Rup}(IM_j > im_j|rup_n)\ \lambda_{Rup}\left(rup_n\right)}{\lambda_{IM}\left(IM_j > im_j\right)} \tag{6.3}$$

where $P_{IM_j|Rup}(IM_j > im_j|rup_n)$ is the exceedance probability for im_j value given rup_n obtained from the implemented GMM, $\lambda_{Rup}\left(rup_n\right)$ is the annual frequency of rup_n from the ERF, and $\lambda_{IM}\left(IM_j > im_j\right)$ is the annual exceedance frequency of im_j from the seismic hazard curve.

6.3.2.2 Conditional distribution of IMs considered in ground motion selection

The target for ground motion selection in the GCIM methodology is the conditional multivariate distribution of the considered vector of IMs, $\boldsymbol{IM} = \{IM_1, IM_2, \ldots, IM_i, \ldots\}$, which accounts for various aspects of ground motion severity. The marginal conditional distribution of a single IM_i in the $\boldsymbol{IM}$ vector is obtained based on Equation 6.4 (Bradley, 2010b), considering the contribution of all causal ruptures to the seismic hazard at the conditioning IM level

[2]Note that Equation 6.2 becomes exact in the limit as $\delta im \to 0$.

$(IM_j = im_j)$:

$$f_{IM_i|IM_j}(im_i|im_j) = \sum_{n=1}^{N_{rup}} f_{IM_i|Rup,IM_j}(im_i|rup_n, im_j)\ P_{Rup|IM_j}(rup_n|IM_j = im_j) \tag{6.4}$$

where $f_{IM_i|Rup,IM_j}(im_i|rup_n, im_j)$ is the marginal distribution of IM_i from a single scenario rupture, rup_n, conditioned on the IM_j level considered for deaggregating the seismic hazard curve; $P_{Rup|IM_j}(rup_n|IM_j = im_j)$ is the contribution of rup_n to the occurrence of $IM_j = im_j$ obtained from Equation 6.2; and N_{rup} is the number of ruptures considered in the vicinity of the site. The obtained marginal IM_i distributions are used to generate realisations of the multivariate $\boldsymbol{IM}$ distribution considering the correlation between the considered IMs (see Bradley (2012c) for further details), which are then used to assess the appropriateness of the candidate ground motions (as elaborated on in the next subsection).

6.3.2.3 Selecting ground motions

In order to select an ensemble of N_{gm} ground motions, a database of prospective (recorded and/or simulated) ground motions is searched to find ground motions that fit the generated realisations of the $\boldsymbol{IM}$ distribution (Jayaram et al., 2011; Bradley, 2012c; Wang, 2011; Baker and Lee, 2017). A so-called weight vector, w_i, is used to prescribe the relative importance of the considered IM_i and calculate the misfit of each prospective ground motion with respect to the target distribution (Bradley, 2012c; Tarbali and Bradley, 2015b). Bounds on causal parameters (*e.g.,* magnitude, source-to-site distance, site condition) of prospective ground motions can also be considered prior to conducting IM-based ground motion selection (see Tarbali and Bradley (2016) and references therein).

6.3.3 Step 3: Seismic response analysis

Ground motion ensembles selected at different IM_j levels can be utilised to conduct RHAs of the system to calculate the distributions of engineering demand

parameters (EDPs) pertinent to characterise the behaviour of the system (Jalayer and Cornell, 2009). This requires separating the results of ground motions causing collapse in the response history analysis from those resulting in non-collapse responses (Shome and Cornell, 1999). A collapse fragility function, characterising the probability of collapse for a given IM_j value, $P_{C|IM_j}(im_j)$, is established based on the proportion of ground motions resulting in collapse within the ensemble of selected records. Baker (2015) presents a maximum likelihood approach that can be used to fit a collapse fragility function to the collapse responses. Finally, when RHAs are performed for a discrete set of IM_j levels for which ground motions have been selected, interpolation is needed to develop the EDP-IM relationship. Here, linear relationships are used for $ln(EDP)$ and $\sigma_{ln(EDP)}$ with $ln(IM_j)$ to establish non-collapse response distributions (Bradley, 2013e).

The exceedance probability for the EDP of interest conditioned on an IM_j value is then obtained from Equation 6.5 (Shome and Cornell, 1999):

$$G_{EDP|IM_j}(edp|im_j) = G_{EDP|IM_j,NC}(edp|im_j)\left(1 - P_{C|IM_j}(im_j)\right) + P_{C|IM_j}(im_j) \tag{6.5}$$

where $G_{EDP|IM_j,NC}(edp|im_j)$ is the probability of $EDP > edp$ given $IM_j = im_j$ calculated from the non-collapse (NC) responses; and $P_{C|IM_j}(im_j)$ is the probability of collapse given $IM_j = im_j$ (based on the established collapse fragility function).

6.3.4 Step 4: seismic demand hazard

The seismic demand hazard is calculated from (Shome and Cornell, 1999; Krawinkler and Miranda, 2004):

$$\lambda_{EDP}(edp) = \int_0^\infty G_{EDP|IM_j}(edp|im_j)\left|\frac{\mathrm{d}\lambda_{IM_j}(im_j)}{\mathrm{d}IM_j}\right|\mathrm{d}IM_j \tag{6.6}$$

where $\mathrm{d}\lambda_{IM}(im_j)/\mathrm{d}IM_j$ is the derivative of the considered seismic hazard curve with respect to IM_j; and $G_{EDP|IM_j}(edp|im_j)$ is the seismic response exceedance

probability obtained from Equation 6.5.

Note that the distribution of EDPs of interest conditioned on a single IM_j value are conventionally utilised in seismic design guidelines (*e.g.,* NZS1170.5, 2004; ASCE/SEI7-10, 2010) to characterise the seismic performance. However, this approach neglects the fact that: (i) a certain EDP level can be exceeded at different IM_j levels; and (ii) the EDP distribution is a function of the considered IM_j (i.e., hazard) level (Bradley, 2013a). The use of the seismic demand hazard overcomes these shortcomings by taking into account the likelihood of different IM_j levels and the distribution of EDPs (conditioned on a given IM_j level), providing a more robust approach to assess the demand-based seismic performance of the system (Bradley, 2012d, 2013a).

6.4 Propagation of epistemic uncertainty

Epistemic uncertainty in the PSHA results is conventionally addressed by considering alternative GMMs and ERFs using the logic tree method[3] (Kulkarni et al., 1984; Reiter, 1991; Bommer et al., 2005), which results in alternative plausible seismic hazard curves for the site of interest. The effect of seismic hazard epistemic uncertainty can be reflected in seismic demand measures by considering the full distribution of seismic hazard, or a single representative such as the mean or certain percentiles of the alternative hazard curves (Abrahamson and Bommer, 2005; McGuire et al., 2005; Musson, 2005). Table 6.1 compares the three approaches presented in the next section for propagation of seismic hazard and ground motion selection epistemic uncertainties based on the four-step demand-based seismic performance assessment procedure outlined in the previous section. As presented in Table 6.1, the specifics of the ground motion selection and response analysis steps, which constitute the computationally demanding steps of the process, depend on how the seismic hazard epistemic uncertainty is addressed

[3]The discussions to follow are equally applicable if Monte Carlo simulation is used to sample seismic hazard epistemic uncertainties.

(*i.e.,* via the full distribution of seismic hazard or simply the mean hazard). Note that Approach 2 and 3 aim to approximate the distribution and the mean demand measures from Approach 1 (*i.e.,* the exact approach). The main components of these approaches are presented in the following sections. As elaborated upon in the discussion section, since attention in this chapter is focused on epistemic uncertainties in ground motion selection, then epistemic uncertainty in the seismic response of the considered engineered system is omitted, however it should be considered in practical applications.

6.4.1 Approach one: Exact approach

In the exact approach, each seismic hazard curve from the logic tree branches is treated separately as one possible answer to 'what is the true seismic hazard at the site?'. Therefore, the selected ground motion ensembles, corresponding RHAs, EDP distributions, and demand hazard curve are obtained specifically for each alternative seismic hazard curve. This process results in N_{models} demand hazard curves, where N_{models} is the number of models considered to represent epistemic uncertainties in the seismic hazard.

Establishing the target distribution of IMs specific to the k^{th} logic tree branch of the seismic hazard curve requires deaggregating them at the considered conditioning IM levels. In order to have a consistent basis to establish the conditional distribution of IMs and EDP-IM relationships representing the alternative hazard curves, and compare them with those representing the mean hazard (utilised in the two approximate approaches elaborated upon subsequently), all the seismic hazard curves are deaggregated at the same conditioning IM levels. Although not strictly necessary, these IM levels may correspond to certain exceedance probabilities of the mean hazard (see Figure 6.1 for schematic illustration). Equations 6.2 and 6.3 are utilised for deaggregating the hazard curves for each logic tree branch resulting in the contribution of causative rupture scenario to the occurrence of $IM_j = im_j$ conditioned on the k^{th} model characteristics, *i.e.,* $P^k_{Rup|IM_j}(rup_n|im_j)$.

Table 6.1: Comparison of three approaches to propagate the effect of epistemic uncertainties in seismic hazard analysis and ground motion selection to demand-based seismic performance measures

Step	**Approach 1: Exact**	**Approach 2:Approximate full distribution**	**Approach 3: Approximate mean**
1. Seismic hazard analysis	Complete seismic hazard distribution (all logic tree branches)		Mean hazard
2. Ground motion selection	A different GM set for every logic tree branch	One GM set corresponding to the mean hazard	
3. Seismic response analysis	Different seismic response analyses for each GM set	One set of seismic response analyses corresponding to the one GM set	
4. Seismic demand hazard	Exact distribution of the seismic demand hazard	Approximate distribution of the seismic demand hazard	Approximate mean seismic demand hazard

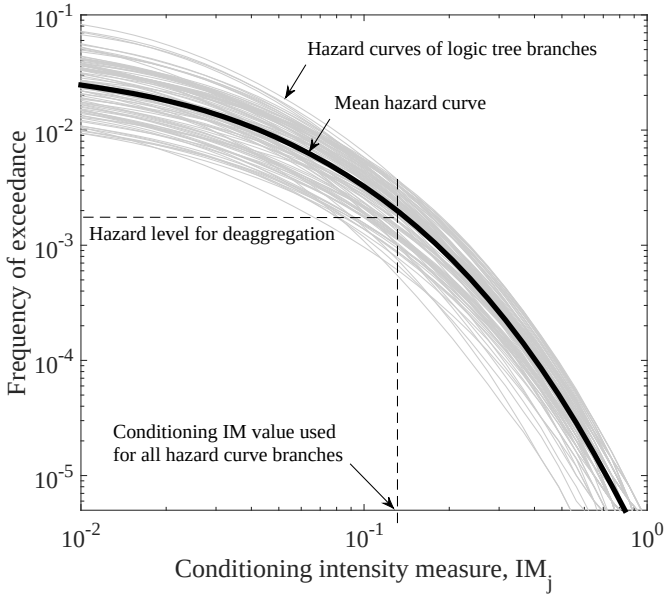

Figure 6.1: Schematic illustration of deaggregating the seismic hazard curve branches to establish the conditional IM distributions for ground motion selection.

The marginal conditional distribution of IM_i pertaining to the k^{th} model ($f^k_{IM_i|IM_j}(im_i|im_j)$) is calculated based on Equation 6.4. Ground motion ensembles are then selected to represent the k^{th} seismic hazard curve. By conducting RHAs of the system subjected to the selected ground motions, the EDP-IM relationship specific to the k^{th} model is obtained using Equation 6.5. The obtained relationship is conditioned on the selected ground motion ensembles, which are themselves conditioned on the choice of GMM and ERF for the k^{th} model. The seismic demand hazard specific to the k^{th} model (*i.e.,* $\lambda^k_{EDP}(edp)$) is then calculated using Equation 6.6. It is emphasised that this 'exact' approach requires the selection of N_{models} different ground motion ensembles as well as performing RHAs for each and every one of these ensembles, and is therefore very computationally demanding (often prohibitively so).

The distribution of the resulting seismic demand hazard at a given EDP level, in the form of cumulative probability function, is obtained using Equation 6.7:

$$F_{\lambda_{EDP}}[l|edp] = \sum_{k=1}^{N_{models}} I(\lambda^k_{EDP}(edp) \geq l)\ W_k \tag{6.7}$$

where $I(\lambda_{EDP}^{k}(edp) \geq l)$ is the indicator function taking the value of one for the k^{th} hazard curve resulting in a demand hazard exceedance frequency larger than or equal to l and zero otherwise; and W_k is the epistemic uncertainty weight of the k^{th} model, normalised such that $\sum_{k=1}^{N_{models}} W_k = 1$. Assuming that the considered models represent a robust set of applicable models to characterise the seismic hazard at the site, the resulting demand hazard from this exact approach can be assumed to represent the centre, body, and range in epistemic uncertainty of the seismic performance of the system due to seismic hazard and ground motion selection epistemic uncertainties.

6.4.2 Approach two: Approximate full distribution

Considering the significant computational burden of selecting multiple ground motion ensembles and performing RHAs of the system for every branch of the seismic hazard logic tree in the exact approach, a simplification can be applied by considering only a single EDP-IM relationship. This single EDP-IM relationship is derived based on the response of the system when subjected to ground motions representative of the mean seismic hazard. This single EDP-IM relationship can then be integrated with the alternative branches of the seismic hazard, resulting in the N_{models} demand hazard curves which tend to approximate the demand hazard distributions from the exact approach. The assumption of this approach is that the uncertainty in the EDP-IM relationship, as a result of uncertainty in the selected ground motion ensembles, is small relative to the uncertainty in the seismic hazard itself. As elaborated upon via example in Section 6.5.2, ground motion ensembles selected to represent the mean hazard may also be appropriate to represent the target IM distributions of logic tree branches. Hence, they can be utilised as a surrogate for branch-specific ground motion ensembles to obtain an approximation for the EDP-IM relationship. Note that Lin et al. (2013) also recommend selecting ground motion ensembles representing a single target (*i.e.,* mean hazard or variants of it); however, its integration with the mean or branches

of the hazard curve logic tree was not directly discussed.

This approximate approach requires calculating the mean seismic hazard, $\overline{\lambda_{IM}}\left(im_j\right)$, which is given by:

$$\overline{\lambda_{IM_j}}\left(im_j\right) = \sum_{k=1}^{N_{models}} \lambda_{IM_j}^{k}\left(im_j\right) W_k \tag{6.8}$$

where $\lambda_{IM_j}^{k}\left(im_j\right)$ is the seismic hazard curve pertaining to the k^{th} logic tree branch with the corresponding weight of W_k. Note that the calculation of the mean hazard is for a specific $IM_j = im_j$ value, *i.e.,* it is a mean annual exceedance frequency, and the notion of a mean IM value for a given exceedance frequency does not have a methodological meaning (Bommer and Scherbaum, 2008).

6.4.2.1 Deaggregating the mean hazard

In order to establish the conditional distribution of IMs (considered for ground motion selection), the mean hazard curve is deaggregated with respect the contributing alternative models. The contribution of the k^{th} model to the mean hazard at a given IM level, $P_{model}^{k}\left(im_j|\overline{\lambda_{IM_j}}\left(im_j\right)\right)$, is calculated using Equation 6.9:

$$P_{model}^{k}\left(im_j|\overline{\lambda_{IM_j}}\left(im_j\right)\right) = \frac{\lambda_{IM_j}^{k}\left(im_j\right) W_k}{\overline{\lambda_{IM_j}}\left(im_j\right)} \tag{6.9}$$

The model weight in Equation 6.9, W_k, can be considered as the prior probability in the Bayesian statistics context, with $P_{model}^{k}\left(im_j|\overline{\lambda_{IM_j}}\left(im_j\right)\right)$ as the posterior probability obtained based on the likelihood function of $\lambda_{IM_j}^{k}\left(im_j\right)/\overline{\lambda_{IM_j}}\left(im_j\right)$. The IM distributions representing the mean hazard can be calculated based on this posterior probability (as elaborated upon in Equation 6.12).

The contribution of causative rupture scenarios at the conditioning IM level, $IM_j = im_j$, to the mean hazard, $\overline{P_{Rup|IM_j}}(rup_n|IM_j = im_j)$, is then calculated

based on Equation 6.10:

$$\overline{P_{Rup|IM_j}}(rup_n|IM_j = im_j) = \sum_{k=1}^{N_{models}} P^k_{Rup|IM_j}\left(rup_n\middle|IM_j = im_j\right) P^k_{model}\left(im_j|\overline{\lambda_{IM_j}}\left(im_j\right)\right) \tag{6.10}$$

where $P^k_{Rup|IM_j}\left(rup_n\middle|IM_j = im_j\right)$ is the contribution of a given scenario rupture (rup_n) to the k^{th} hazard curve obtained based on Equations 6.2 and 6.3.

6.4.2.2 Conditional distribution of IMs in the approximate approach

Following Equation 6.4, the conditional distribution of IMs in the approximate approach is calculated using Equation 6.11:

$$\overline{f_{IM_i|IM_j}}\left(im_i|im_j\right) = \sum_{n=1}^{N_{rup}} f_{IM_i|Rup,IM_j}(im_i|rup_n, im_j)\overline{P_{Rup|IM_j}}(rup_n|IM_j = im_j) \tag{6.11}$$

where $f_{IM_i|Rup,IM_j}(im_i|rup_n, im_j)$ is the marginal distribution of IM_i from a single scenario rupture conditioned on the IM_j level, and $\overline{P_{Rup|IM_j}}$ is obtained from Equation 6.10.

Alternatively to Equation 6.11, in the case where conditional distribution of IMs are already calculated for each alternative model (as, for example, in the OpenSHA software (Field et al., 2003)), these distributions can simply be combined using Equation 6.12 to obtain the IM distribution representing the mean hazard:

$$\overline{f_{IM_i|IM_j}}\left(im_i|im_j\right) = \sum_{n=1}^{N_{models}} f^k_{IM_i|IM_j}\left(im_i|im_j\right) P^k_{model}\left(im_j|\overline{\lambda_{IM_j}}\left(im_j\right)\right) \tag{6.12}$$

where $f^k_{IM_i|IM_j}\left(im_i|im_j\right)$ is the conditional distribution of IM_i pertaining to the k^{th} model obtained based on Equation 6.4. Equation 6.11 or 6.12 therefore enables the calculation of conditional IM_i distributions which provide the target for selecting ground motion ensembles representing the mean hazard curve (refer to Section 6.3.2.3 for further details on the ground motion selection process).

6.4.2.3 Seismic demand hazard

By conducting RHAs of the system subjected to the selected ground motion ensembles representing the mean hazard, the EDP-IM relationship specific to the mean hazard curve, $\overline{G_{EDP|IM_j}}\,(edp|im_j)$, is obtained based on Equation 6.5. The uncertainty in the seismic hazard can then be propagated by integrating each logic tree seismic hazard branch with the mean hazard-based EDP-IM relationship using Equation 6.13:

$$\widetilde{\lambda^k_{EDP}}\,(edp) = \int_0^\infty \overline{G_{EDP|IM_j}}\,(edp|im_j) \left| \frac{\mathrm{d}\lambda^k_{IM_j}\,(im_j)}{\mathrm{d}IM_j} \right| \mathrm{d}IM_j \tag{6.13}$$

where $\sim$ is used to denote the approximation of $\lambda^k_{EDP}(edp)$ via the use of $\overline{G_{EDP|IM_j}}$ in place of $G^k_{EDP|IM_j}$ in the exact approach.

The distribution of demand hazards at a given EDP level from the approximate method can be calculated in the same manner as the exact approach using Equation 6.8.

6.4.3 Approach three: Approximate mean

The most simplified approach to calculate the demand-based seismic performance measure when addressing epistemic uncertainties in the seismic hazard and ground motion selection is to integrate the EDP-IM relationship corresponding to the mean seismic hazard (as developed in the previous subsection) with the mean seismic hazard curve (*i.e.,* Equation 6.8), as shown in Equation 6.14:

$$\overline{\lambda_{EDP}}\,(edp) = \int_0^\infty \overline{G_{EDP|IM_j}}\,(edp|im_j) \left| \frac{\mathrm{d}\overline{\lambda_{IM_j}}\,(im_j)}{\mathrm{d}IM_j} \right| \mathrm{d}IM_j \tag{6.14}$$

This approach, denoted as the 'approximate mean approach', results in a single demand hazard curve that aims to approximate the mean value of the demand hazard curves obtained from the exact approach. It deviates from the second

approach in that individual branches of the seismic hazard are not considered.

6.5 Example application

The San Francisco Bay Area is chosen to conduct PSHA and demonstrate the presented methodologies to propagate the effect of epistemic uncertainties, because it is a well-studied region in terms of uncertainties associated with the ERF component of PSHA, including: time-dependent nature of characteristic ruptures, magnitude-frequency distributions, magnitude-area relationships, seismogenic thickness, seismic and aseismic slip rates, distributed seismicity, fault segmentation, among others (WGCEP02, 2003). PSHA was conducted using the open-source seismic hazard analysis software OpenSHA (Field et al., 2003). Epistemic uncertainty in the ERF was considered using 100 logic tree branches of WGCEP02 (and thus each and every ERF branch has a weight of 1/100). Note that since WGCEP02 ERF is a time-dependent model, the results presented for the example application are based on exceedance probability rather than exceedance frequency[4].

Four empirical ground motion models for pseudo spectral acceleration (SA) developed as part of the next generation attenuation (NGA) project were considered in the PSHA and calculating conditional IM distributions, namely, Boore and Atkinson (2008); Chiou and Youngs (2008); Campbell and Bozorgnia (2008) and Abrahamson and Silva (2008) (referred to as BA08, CY08, CB08, and AS08, respectively). Each model is given an equal weight of 1/4 hence, in total, there exist 400 logic tree branches considering the ERF and GMM model combinations. The selected GMMs provide sufficiently appropriate tools to demonstrate the purpose of this chapter.

[4]Due to the incompactness of the probability-based PSHA formulation (Field et al., 2003), the three methodologies presented for epistemic uncertainty prorogation are based on exceedance frequency. If the utilized ERF is time-independent, $P = 1 - e^{(-\lambda . T_{forecast})}$ can be used to convert between probability- and frequency-based results.

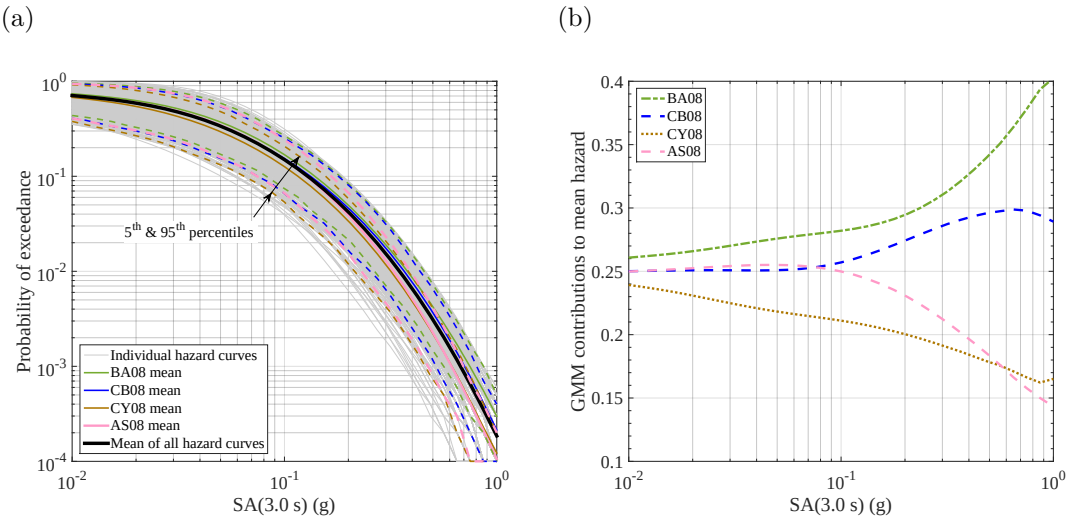

Figure 6.2: (a) Branch and the mean SA(3.0 s) hazard curves for a site with V_{s30}=400 m/s in San Francisco; (b) contribution of the considered GMMs to the mean hazard.

6.5.1 PSHA results

The effect of epistemic uncertainties in the considered GMM and ERF branches are first illustrated through the obtained hazard curve and the deaggregation results. Figure 6.2a presents the hazard curves from 400 logic tree branches corresponding to SA at T =3 s vibration period, SA(3.0), obtained for a site with a V_{s30} of 400 m/s located in San Francisco (Lat 37.7833°, Long -122.4167°). Considering the time-dependent ERF of WGCEP02, PSHAs were conducted for a 30-year time period starting from 2002. Note that all the ERF branches and the considered GMMs have equal weights (of 1/400). Figure 6.2a shows a large range of variation in the seismic hazard due to epistemic uncertainties in the ERF (shown in grey) and GMM (shown in four colors). Figure 6.2b presents the contribution of the considered four GMMs to the mean hazard (*i.e.,* GMM deaggregation) calculated using Equation 6.9. Figure 6.2b shows large differences in the contribution of the considered GMMs to the mean hazard from the prior equal weight of 0.25 as the IM level increases (Lin et al., 2013).

The IM levels corresponding to 50%, 10%, 8%, 6%, 4%, 2%, 1%, 0.5%, 0.25%, 0.1%, 0.05%, 0.02% exceedance probabilities of the mean hazard curve are chosen

(a) (b)

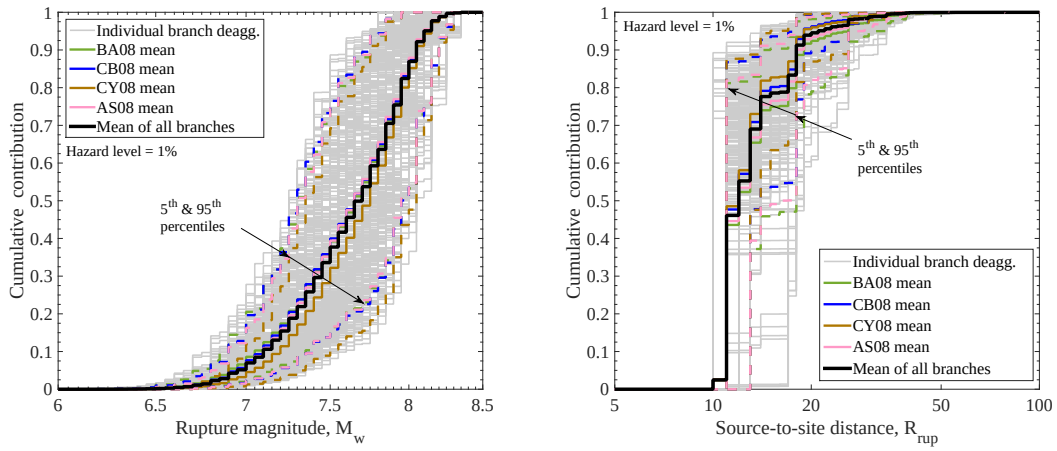

Figure 6.3: Cumulative contribution of causative ruptures to the IM level with 1% exceedance probability: (a) rupture magnitude; (b) source-to-site distance.

as the conditioning IMs to deaggregate hazard curves (see Figure 6.1). As an illustration of variation in deaggregation results, Figure 6.3 presents the occurrence deaggregation contribution of the causative rupture scenarios to the conditioning IM level corresponding to 1% exceedance probability of the mean hazard (shown in the form of cumulative distribution). As shown, there is a large variation in the deaggregation contribution from alternative ERF and GMM branches with the median magnitude and source-to-site distance having ranges of [7.2-8.1] and [10-20 km], respectively (note that the considered site is dominated by near-source scenarios, hence a small range of variation for source-to-site distances). The variation in the deaggregation contribution of the causative rupture scenarios will propagate to the conditional distribution of IMs considered for ground motion selection and the resulting ground motion ensembles selected (as illustrated in the next section).

6.5.2 Conditional IM distributions and selected ground motion ensembles

The following IMs were considered in the ground motion selection process: SA ordinates for 18 vibration periods (T=0.05, 0.075, 0.1, 0.15, 0.2, 0.25, 0.3, 0.4, 0.5, 0.75, 1.0, 1.5, 2.0, 3.0, 4.0, 5.0, 7.5, and 10.0 s); cumulative absolute velocity (CAV); and 5-75% and 5-95% Significant Durations (D_{s575} and D_{s595}, respectively). These IMs represent various aspects of ground motions including amplitude, frequency content, duration, and cumulative effects, and their selection is based on other research on suitable IMs for ground motion selection (Bradley, 2012c; Tarbali and Bradley, 2015b; Chandramohan et al., 2016). The marginal distributions of SA ordinates were obtained using the corresponding GMMs utilised for the PSHA (*i.e.,* BA08, CY08, CB08, AS08). The Campbell and Bozorgnia (2010) and Kempton and Stewart (2006) GMMs were used for CAV and Significant Duration IMs, respectively. Correlations between the considered IMs were obtained based on existing empirical models (Baker and Jayaram, 2008; Bradley, 2011a, 2012a). For the reasons elaborated upon subsequently in Section 6.6.3, epistemic uncertainties in choosing the IM correlation models and GMMs to obtain the conditional distribution of CAV, D_{s575}, and D_{s595} were not considered in this study. An ensemble of 20 ground motions was selected separately at each conditioning IM level using the GCIM methodology. A weight vector with 70% of the total weight distributed equally over the SA ordinates and 30% (equally) over CAV, D_{s575}, and D_{s595} was utilised in the ground motion selection process, which provides an appropriate weight distribution for general ground motion selection cases (Bradley, 2012c; Tarbali and Bradley, 2015b, 2016, 2015a). A subset of NGA-West2 empirical ground motion database (Ancheta et al., 2013) constrained by the causal parameter bounds recommended by Tarbali and Bradley (2016) were utilised to provide the available set of prospective records for ground motion selection.

Figure 6.4a presents the 16^{th}, 50^{th}, and 84^{th} percentiles of the conditional SA distributions representing the SA(3.0 s) hazard at the conditioning IM level

corresponding to 1% exceedance probability of the mean hazard curve. The conditional IM distributions representing the D_{s575} and CAV, and the target distributions representing the mean hazard are also presented in Figures 6.4c and 6.4e, respectively. The empirical IM_i distributions of the selected ground motion ensembles based on the IM distributions are shown in Figures 6.4b, d, and f. In these figures, the statistical rejections bounds based on the Kolmogorov-Smirnov (KS) test (Ang and Tang, 1975) are presented. As shown in Figures 6.4a, c, and e, there is a large variation in the target IM distributions due to the significant epistemic uncertainty in the PSHA results (shown in Figures 6.2 and 6.3), which are duly reflected in the properties of the selected ground motions.The selected ground motion ensembles might not in some cases properly represent the target hazard (*e.g.,* biased representation shown in Figure 6.4e for some of the CAV distributions as the empirical IM distributions lay outside the KS test bounds). This is due to the paucity of appropriate ground motions in the empirical database to collectively represent all the considered IMs in the selection process.

As shown in Figures 6.4b, d, and f, although there is a large variation, the selected ground motion ensemble corresponding to the mean hazard appears to be an appropriate ensemble to represent the target IM distributions of logic tree branches (*i.e.,* the corresponding empirical distribution lies within the KS test bounds of the target IM distributions for logic tree branches). Hence, in order to approximate the demand hazard distribution, the EDP-IM relationship obtained based on the ground motion ensembles representing the mean seismic hazard can be integrated with the seismic hazard curves from the logic tree branches (*i.e.,* the essence of the approximate full distribution approach presented previously).

6.5.3 Response history analysis

An inelastic single-degree-of-freedom (SDOF) system with strength and stiffness degradation (Ibarra et al., 2005; Lignos and Krawinkler, 2012), and a fundamental vibration period of T_n=3 s was subjected to the selected ground motion

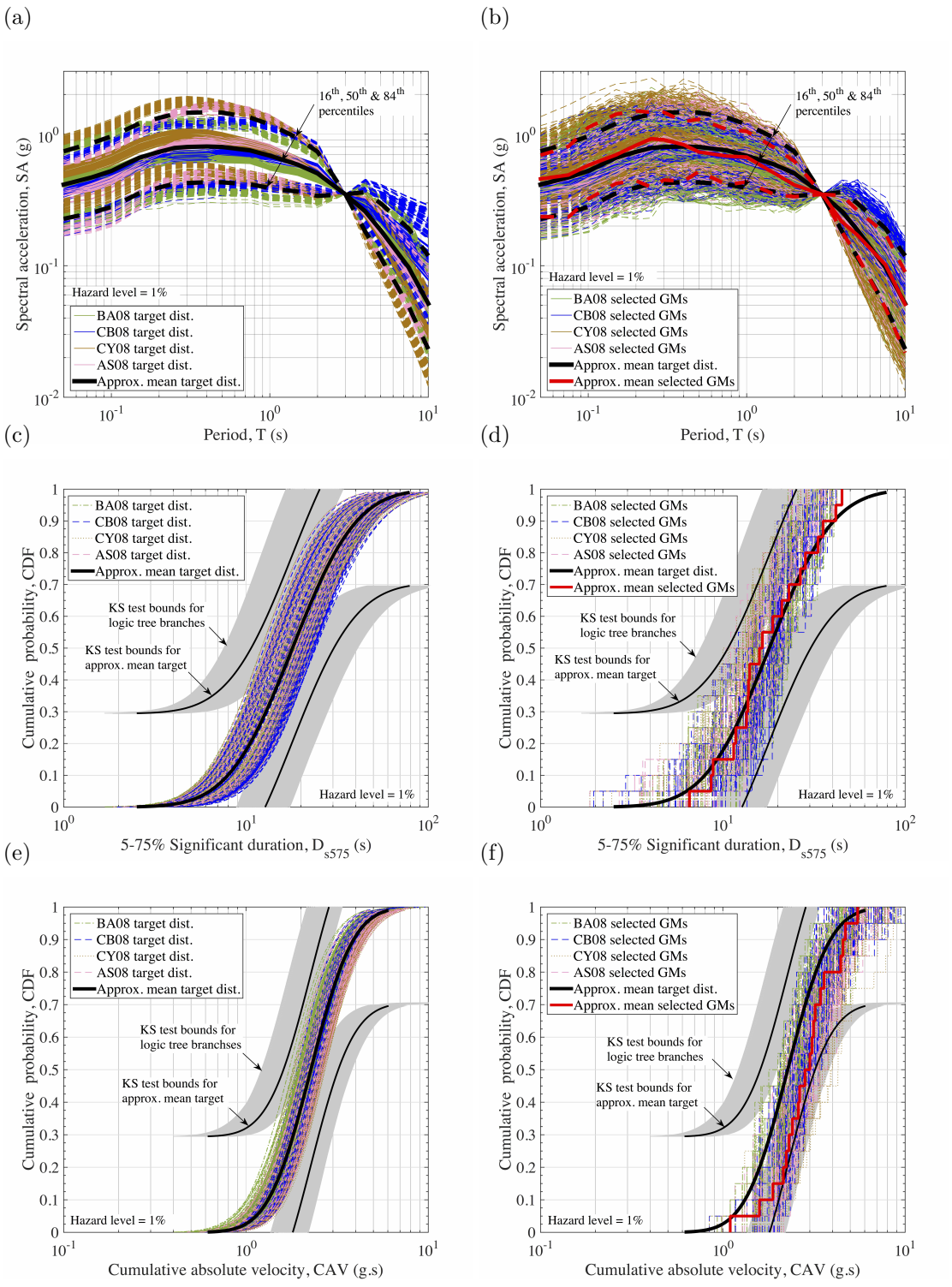

Figure 6.4: Conditional IM and selected ground motion distributions corresponding to the IM level with 1% exceedance probability: (a)-(b) SA ordinates; (c)-(d) Ds575; (e)-(f) CAV. The back and red lines present the target and selected ground motion distributions representing the mean seismic hazard. The coloured lines and the grey bands illustrate selected ground motion ensembles representing each and every seismic hazard branch and their corresponding KS test bounds.

ensembles previously discussed. The maximum displacement of the system was chosen as the EDP of interest and the collapse limit is defined based on a nominal displacement to height ratio, specifically, 0.05, corresponding to a displacement ductility of 3.0. As noted previously, a linear relationship between ln(EDP) and ln(IM) is used to interpolate between the considered conditional IM values for the non-collapse responses (Bradley, 2013e). The maximum likelihood approach of Baker (2015) is used to establish the collapse fragility curve.

6.5.4 Propagation of epistemic uncertainty in seismic performance assessment

Figure 6.5a presents the EDP-IM relationship of the SDOF system for the non-collapse responses from ground motion ensembles that are specifically selected to represent every branch of the seismic hazard curves (*i.e.,* the exact approach). The mean of the results from the exact approach and the results from the approximates approaches (for which the demand distribution is obtained based on the ground motions selected to represent the mean hazard—see Table 6.1), are also presented. A large variation in the EDP-IM relationship is evident especially at ground motion levels for which the response of the system is beyond the elastic response (approximately SA(3.0)>0.3 g). Note that the results from the approximate mean approach (shown in black), is close to the logarithmic mean from the exact approach (shown in solid red). Figure 6.5a also illustrates that while the 50^{th} percentile of the non-collapse responses has an increasing trend, there might be large variations in the distribution of non-collapse responses indicated by the non-increasing trend in the 16^{th} and 84^{th} percentiles, due to the change in the proportion of ground motions causing collapse in the system for various IM levels.

Figure 6.5b presents the collapse fragility curves obtained based on the exact approach (*i.e.,* the branch-specific ground motion ensembles), separately indicated based on the GMM from the corresponding logic tree branch and their mean value, along with the results from the approximate mean approach. As shown, there is

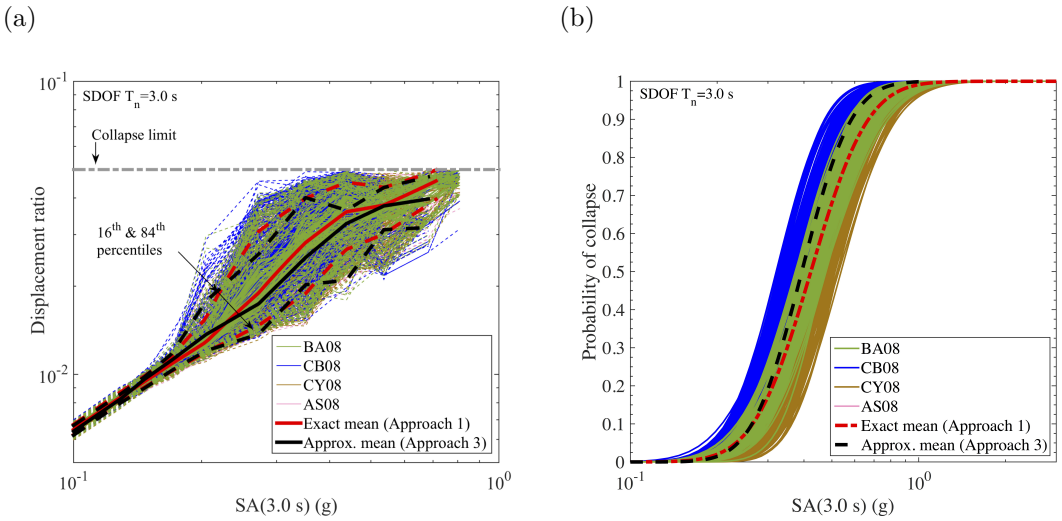

Figure 6.5: (a) EDP-IM relationship of the non-collapse responses; and (b) collapse fragility curves, for the T_n=3.0s SDOF system considered. The black lines illustrate the EDP and collapse probability under the mean hazard. The red lines present the mean and percentiles from the exact approach. The coloured lines illustrated the DEP and collapse probability of the system under each and every seismic hazard branch.

a large variation in the collapse probability for the complete IM (*i.e.,* SA(3.0 s)) range. The reason for larger approximate mean collapse probabilities from Approach 3 (for $P_{C|IM} > 0.25$) in comparison to the exact mean probabilities is the larger proportion of collapse responses (as shown in Figure 6.5a with a smaller median for non-collapse responses in comparison to the exact approach).

Figure 6.6 presents the obtained demand hazard curves from the exact (*i.e.,* Approach 1), approximate distribution (*i.e.,* Approach 2), and approximate mean (*i.e.,* Approach 3) methods, and their corresponding 1$^{\text{th}}$, 16$^{\text{th}}$, 50$^{\text{th}}$, 84$^{\text{th}}$, and 99$^{\text{th}}$ percentiles. As shown in Figure 6.6a, the exact mean demand hazard curve (from Approach 1) is appropriately estimated by the approximate mean (Approach 3). Note that the mean of the results from Approach 2 (*i.e.,* the demand distribution representing the mean hazard integrated with every branch of the seismic hazard curves) is the same as that from Approach 3 (*i.e.,* the demand distribution representing the mean hazard integrated with the mean hazard). As shown in Figure 6.6b, while the differences between the exact and approximate distribution results are more pronounced for near-collapse EDP levels, the approximate method can

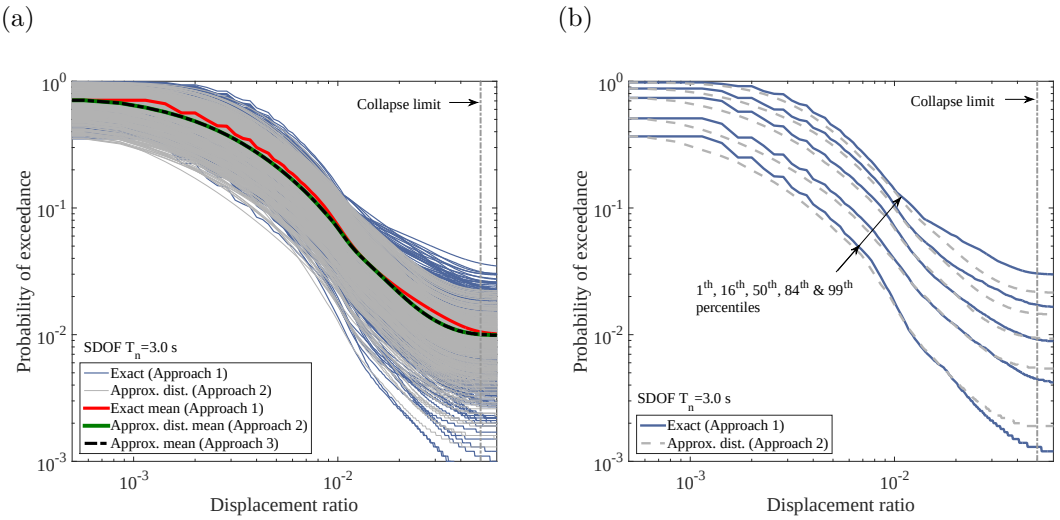

Figure 6.6: (a) Demand hazard curves from the three presented methodologies; (b) percentiles of the demand hazard distributions from the exact (*i.e.,* Approach 1) and approximate distribution (*i.e.,* Approach 2) methods.

appropriately estimate the demand hazard percentiles of the exact method in the whole range of EDP considered.

The presented results indicate that in cases where the objective is to obtain the mean demand hazard, it may be sufficient to integrate the mean seismic hazard with the demand distribution representing the mean hazard (*i.e.,* the approximate mean — Approach 3). Also, if the aim is to only have an approximation for the demand hazard distribution of the system, the approximate distribution (*i.e.,* Approach 2) might provide appropriate results. However, accurate assessment of epistemic uncertainties from seismic hazard and ground motion selection for demand levels near collapse likely requires the exact computation (*i.e.,* Approach 1).

6.6 Discussion

6.6.1 Comparison of demand hazard variability

Given the presented results, it is insightful to examine the relative contribution of: (i) seismic hazard, and (ii) ground motion selection uncertainties on the uncertainty in the seismic demand hazard and their dependence on the propagation approach. Figure 6.7a presents the lognormal standard deviation (*i.e.,* dispersion) of the seismic hazard exceedance probability, $\sigma_{ln(P_{IM}(im))}$[5]. The results are shown for the seismic hazard curves from individual GMMs and all the seismic hazard curves combined. The dispersion of the demand hazard exceedance probability, $\sigma_{ln(P_{EDP}(edp))}$[6], is also presented in Figure 6.7b. As shown, the dispersions both tend to increase with increasing IM and EDP levels, respectively. Firstly, it can be seen in Figure 6.7b that the dispersion in the seismic demand hazard for small EDP levels is equal to the dispersion of the seismic hazard at small IM levels. This is the result of the fact that the demand hazard for small EDPs is governed by small IMs, and that the EDP-IM relationship has small uncertainty at these IM levels (shown in Figure 6.5a). As the EDP level increases, the uncertainty in the EDP-IM relationship increases (due to the variability in the selected ground motion properties and increasing nonlinear response (see Figure 6.5a), which consequently increases the dispersion in the demand hazard. Secondly, while the demand hazard dispersion from the exact and approximate approaches is somewhat similar at small EDP levels, it is significantly different at larger (near-collapse) EDP levels.

Note that the difference between the exact and approximate approaches for estimating the dispersion in Figure 6.7b is simply the result of the difference in the properties of ground motions selected to represent individual logic tree branches compared to those selected to represent only the mean hazard. Because only a single ground motion ensemble is used in the approximate approaches (*i.e.,* a single

[5] $\sigma_{ln(\lambda_{IM}(im))}$ for frequency-based calculations
[6] $\sigma_{ln(\lambda_{EDP}(edp))}$ for frequency-based calculations

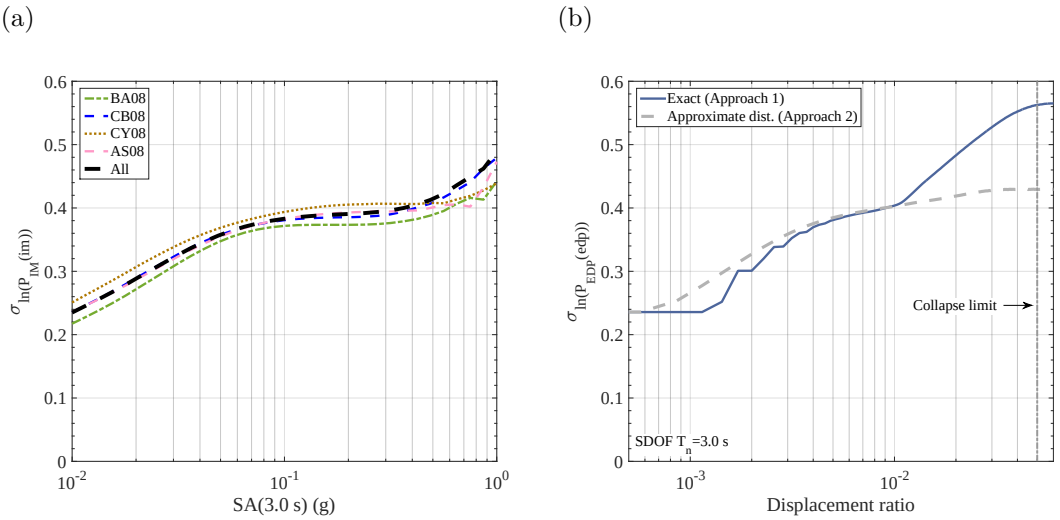

Figure 6.7: Dispersion of the exceedance probabilities for: (a) seismic hazard; and (b) demand hazard for the example case considered.

EDP-IM relationship and collapse fragility curve representing the response of the system under the mean hazard), uncertainty in the collapse probability distribution and EDP is not considered in the approximate approaches. In aggregate, as indicated in Figure 6.7b, it can be seen that ground motion selection uncertainty, leading to the EDP-IM and collapse fragility uncertainty, is significant at highly-nonlinear near-collapse seismic response levels (noting that, for example, large demand hazard dispersions of 0.56 and 0.43 in Figure 6.7b represent a variance ratio of 1.7 — *i.e.*, 70% increase).

6.6.2 Comparison of the computational burden

The exact and approximate approaches for estimating the demand hazard can be compared in terms of the computational cost of propagating seismic hazard and ground motion selection epistemic uncertainties. For (i) N_{models} seismic hazard logic tree branches, (ii) deaggregated at N_{iml} IM levels, and (iii) N_{gm} ground motion selected for each ensemble; $N_{models} \times N_{iml}$ ground motion selection tasks and $N_{models} \times N_{iml} \times N_{gm}$ RHAs of the system need to be performed for the exact method. In contrast, for the approximate distribution and mean approaches these numbers are reduced to N_{iml} and $N_{iml} \times N_{gm}$, respectively (*i.e.*, a ratio of

N_{models} fewer). As a typical example, considering N_{models}=100, N_{iml}=12, and N_{gm}=20, the exact approach requires 1200 ground motion selections and 24000 RHAs, whereas these numbers reduce to 12 and 240, respectively, for the two approximate approaches. Thus, given the significantly lower computational cost of the approximate approaches, it is expected that their accuracy in estimating the demand hazard will likely be deemed sufficient in many cases.

6.6.3 Additional sources of epistemic uncertainty not considered in this study

Given a GMM model utilised in seismic hazard analysis for the conditioning IM, the GMM implemented to obtain the conditional distribution of IM_i (considered in ground motion selection) can also be chosen from a set of existing models, which results in an additional level of epistemic uncertainty to consider. Note that while there is a relatively large number of GMMs to obtain SA ordinates (Douglas, 2011; Stewart et al., 2015), there is a limited number of GMMs available for other IMs, which may prevent the analyst from an appropriate representation of this additional epistemic uncertainty (Cotton et al., 2006; Bommer et al., 2010; Atkinson et al., 2014).

In addition to the epistemic uncertainty in the adopted GMMs for the considered IMs, various correlation models can be utilised in calculating the multivariate distribution of IMs considered in the ground motion selection process. In contrast to the significant differences in the IM mean and standard deviation from different GMMs (*e.g.,* Abrahamson et al., 2008; Douglas, 2011; Gregor et al., 2014; Stewart et al., 2015), different correlation models yield, in general, similar results (Baker and Bradley, 2017). Also, as illustrated by Baker and Bradley (2017), epistemic uncertainty due to the choice of GMMs to calculate the conditional distribution of IM (which will be utilised in the ground motion selection process) is significantly larger than the effect of variations in the correlation coefficients. While being another source of epistemic uncertainty in the process of seismic perfor-

mance assessment, it is expected that a single correlation model will be sufficient for practical cases.

Although not considered in this chapter, uncertainties in the modelling assumptions and the input parameters to create the numerical model of the system, in contrast to the two abovementioned uncertainties, is significantly important in addressing epistemic uncertainty in seismic performance assessment (Liel et al., 2009; Bradley, 2013b; Terzic et al., 2015; Gokkaya et al., 2016). These uncertainties can be addressed by considering them in the logic tree approach alongside the uncertainties from seismic hazard analysis and ground motion selection.

6.6.4 The effect of model selection

Selecting appropriate GMMs that can represent the center, body, and range of ground motions from causative rupture scenarios for a specific region requires a rigorous approach (Cotton et al., 2006; Bommer et al., 2010; Atkinson et al., 2014). Given the fact that the NGA models utilised for the example application in this chapter were developed based on similar ground motion databases and interactions between the developers, epistemic uncertainties obtained from a suite of GMMs with independent development processes can be higher for the site considered in this study (Al Atik and Youngs, 2014). It is important to note that alternative ERFs and GMMs implemented in any PSHA calculation represent the range of available models rather than the range of 'true' epistemic uncertainty for the site of interest (Abrahamson, 2006). As a result, a region that is not well-studied might falsely have a smaller epistemic uncertainty due to the lack of appropriate models. Since the example region chosen in this study is a well-studied region, it is expected that the effect of epistemic uncertainty on properties of the selected ground motions and seismic performance measures will be more severe for regions with greater uncertainties.

6.7 Conclusion

In this chapter, three approaches are presented to propagate the effect of ground motion selection epistemic uncertainties to seismic performance metrics. These approaches differ in the level of rigor considered to propagate epistemic uncertainty to the conditional distribution of IMs utilised in ground motion selection, selected ground motion ensembles, and the number of response history analyses (RHAs) performed to obtain the distribution of engineering demand parameters (EDPs). In the exact approach, the EDP-IM relationship and demand hazard is calculated specifically for each seismic hazard curve from the logic tree. Assuming that the considered models represent a robust set of applicable models to characterise the seismic hazard at the site, the resulting demand hazards from the exact approach can be assumed to represent the centre, body, and range in epistemic uncertainty of seismic performance of the system. In contrast, an approximate distribution approach utilises the EDP-IM relationship and collapse fragility curve obtained based on ground motion ensembles representing only the mean seismic hazard curve, which is then integrated with hazard curves from the logic tree branches to obtain an approximation to the demand hazard obtained from the exact approach. This approach has a significantly lower computational cost compared to the exact approach due to the smaller number of RHAs and ground motion selection tasks performed. The third (*i.e.,* approximate mean) approach integrates the EDP-IM relationship and collapse fragility curve representing the mean hazard with the mean seismic hazard curve, resulting in a demand hazard which aims to approximate the mean from the exact approach.

The three presented approaches were compared for an example in the San Francisco Bay Area considering epistemic uncertainties in the earthquake rupture forecast and ground motion models. The presented results indicate that considering the significantly lower computational cost of utilising the approximate distribution approach, this approach can appropriately approximate the distribution of the demand hazards from the exact approach. In addition, if the aim is

to obtain the mean demand hazard, it is sufficient to integrate the mean seismic hazard with the EDP-IM relationship and collapse fragility curve representing the mean seismic hazard. Also, it was observed that, for seismic demand levels below the collapse limit, epistemic uncertainty in ground motion selection is a smaller uncertainty contributor relative to the uncertainty in the seismic hazard itself. In contrast, uncertainty in ground motion selection process increases the uncertainty in the seismic demand hazard for near-collapse demand levels.

Chapter 7

Conclusions

Ground motion selection provides the connection between seismic hazard and seismic response analysis steps in seismic performance assessment process, hence, selected ground motions should appropriately represent the seismic hazard (at the site of interest) in order to provide a means to obtain an unbiased distribution of the system's seismic response. This dissertation focused on several issues in selecting ground motion time series for seismic response analysis which are not adequately addressed in the existing literature. Key contributions of this dissertation and the recommendations for future work are summarised here.

7.1 Key contributions

7.1.1 Ground motion selection representing scenario earthquake ruptures

While seismic hazard is frequently defined based on probabilistic seismic hazard analysis, understanding the anticipated seismic performance of engineered systems due to the occurrence of specific 'scenario' earthquake ruptures is also of interest, which requires ensembles of ground motion time series to performance seismic response analysis (FEMA-P58, 2012). Since scenario-based ground mo-

tion selection methods (*e.g.,* Kottke and Rathje (2008); Baker (2011); Jayaram et al. (2011); Wang (2011)) have considered only spectral amplitudes in the selection process, there is a need for adequate consideration of the joint distribution of multiple intensity measure (IM) types.

The generalised conditional intensity measure (GCIM) methodology (Bradley, 2010b, 2012c) was extended to scenario-based ground motion selection. The ground motion selection algorithm is based on generating random realisations of the considered IM distributions for a specific rupture scenario and then finding the prospective ground motions which best fit the realisations based on an optimal amplitude scale factor. Using different rupture scenarios and site conditions, two important aspects of the GCIM methodology were scrutinised: (i) different weight vectors for the various IMs considered; and (ii) quantifying the importance of replicate selections for ensembles with different numbers of desired ground motions.

Performing ground motion selection based on multiple IM types requires considering the relative importance of them in the selection process using a weight vector (Bradley, 2012c). It is important to identify an appropriate weight distribution on IMs that represent the salient features of ground motion (*i.e.,* amplitude, frequency content, duration, and cumulative effects) to obtain an unbiased response of the system of interest. It was demonstrated that considering only spectral acceleration (SA) ordinates in the selection process, as is common in many conventional selection procedures, may result in selected motions with a biased representation for duration and cumulative ground motion effects. In contrast, considering IMs other than SA ordinates (in particular, Significant Duration, cumulative absolute velocity, and Arias Intensity) results in ensembles with an appropriate representation of these IMs, without a practically significant effect on SA ordinates. A minimum of 60% weighting across all spectral ordinates is recommended. The reason for having a large portion of the total weight on SA ordinates, compared to other IMs, is due to the fact that SA ordinates represent the amplitude and frequency content of the ground motion and are therefore of

primary importance. In order for cumulative- and duration-related responses to become important, a ground motion's amplitude and frequency content must first be large enough to induce nonlinear response. It was also demonstrated that some IMs provide largely redundant information and therefore their joint consideration is largely ineffective in ground motion selection. For example, it was shown that ground motion selection which considers SA amplitudes over a wide period range will also typically yield ground motion ensembles with an unbiased distribution of ASI, SI, and DSI.

Another important aspect of the GCIM-based ground motion selection is to conduct replicate selections to obtain an ensemble of motions with the 'best' representation for the considered seismic hazard (*i.e.,* lowest global residual). The need for replicate selection is a result of the fact that random realisations of the target multivariate distribution of considered IMs is used in the selection process, meaning that each replicate may result in a different ground motion ensemble. The number of the replicate selections to reach to a stable result is dependent upon the number of the selected motions. It was demonstrated that conducting several replicate selections has generally a positive effect on obtaining a set of motions with a smaller global residual, compared with using one replicate. Since conducting an excessive number of replicate selections can result in unnecessary computational burden, a minimum number of replicates is suggested for different ground motion ensemble sizes.

7.1.2 Representative ground-motion ensembles for several major earthquake scenarios in New Zealand

As an application of the developed scenario-based ground motion selection method, ground motion ensembles were selected to represent several major earthquake scenarios in New Zealand that pose a significant seismic hazard, namely, Alpine, Hope and Porters Pass ruptures for Christchurch city; and Wellington, Ohariu, and Wairarapa ruptures for Wellington city. Sets of 20 and 7 ground

motions were selected to represent the predicted distribution of various IMs considered for amplitude, frequency content, duration, and cumulative effects. These scenario-based ground motion sets can be used to complement ground motions which are often selected in conjunction with probabilistic seismic hazard analysis, in order understand the performance of structures for the question 'what if this fault ruptures?' (FEMA-P58, 2012). It was also shown that a paucity of recorded motions from events with large magnitudes and short source-to-site distances in existing strong ground motion databases impedes selecting motions for large magnitude small source-to-site distance rupture scenarios and also consequently requires the use of large amplitude scale factors to scale available prospective ground motions.

7.1.3 Causal parameter bounds in scenario- and PSHA-based ground motion selection

The primary reason for using causal parameter bounds stems from the fact that considering SA ordinates as the only explicit IMs does not account for an accurate representation of ground motion duration and cumulative effects which are not explicitly considered. Although using bounds on the causal parameters of prospective ground motions (*e.g.,* magnitude, source-to-site distance, and site condition) is common practice in conventional approaches for ground motion selection (Katsanos et al., 2010), there is presently no consistent approach for setting these bounds as a function of the seismic hazard at the site. A rigorous basis was developed and sensitivity analyses performed for the consideration of bounds on magnitude, source-to-site distance, and site condition. In order to empirically illustrate the effects of various causal parameter bounds on the characteristics of selected ground motions, 78 and 36 cases of scenario seismic hazard analysis (scenario SHA) and probabilistic seismic hazard analysis (PSHA) were considered, which cover a wide range of causal parameters and seismic hazard/site conditions. The effect of causal parameter bound selection on both the number of available

prospective ground motions from an initial empirical as-recorded database, and the statistical properties of IMs of selected ground motions were examined.

It was demonstrated that using causal parameter bounds is not a reliable approach to implicitly account for ground motion duration and cumulative effects when selection is based on only spectral acceleration ordinates. It was also shown that the application of relatively 'wide' bounds on causal parameters can effectively remove ground motions with drastically different characteristics with respect to the target seismic hazard and consequently improve the causal parameter distributions of selected ground motions with respect to the target scenario rupture and deaggregation results. In contrast, the use of excessively narrow bounds can lead to ground motion ensembles with a poor representation of the target IM distributions, as a result of the narrow bounds resulting in a small database of prospective ground motions relative to the size of the ground motion ensemble desired. It was heuristically evaluated that the subset of prospective ground motions after the application of causal parameter bounds should be more than three times the size of the desired ground motion ensemble.

It was shown that implementing causal parameter bounds results in smaller scaling factors for the selected ground motions due to the fact that by restricting the prospective ground motions to those records with causal parameters close to characteristics of the causal ruptures affecting the seismic hazard at the site, only a small change in amplitude of as-recorded motions is required to represent the target distribution of IMs. It was shown that having small amplitude scaling factors does not necessarily imply a higher quality in terms of representing the target distribution (both mean and variability) of the considered explicit IMs.

Since selecting ground motions to represent target distribution of IMs for a scenario SHA requires calculating optimum amplitude scaling factors for all prospective ground motions included in the database (Tarbali and Bradley, 2015b), it was shown that reducing the number of prospective ground motions by considering causal parameter bounds significantly increases the computational efficiency

of the ground motion selection process for scenario ruptures. Although causal parameter bound consideration also lowers the computational time of ground motion selection for PSHA cases, it was demonstrated that the computational time for PSHA-based ground motion selection is significantly lower in comparison to the scenario-based ground motion selection (*i.e.,* in the order of few seconds as compared to tens of minutes).

Specific causal parameter bounding criteria were recommended for general use as a 'default' bounding criterion in scenario- and PSHA-based ground motion selection, with possible adjustments from the analyst based on problem-specific preferences.

7.1.4 Seismic hazard analysis and ground motion selection in the near-fault region

Ground motions in the near-fault region may exhibit characteristics such as forward directivity velocity pulses that are not observed in the far-field ground motions. The occurrence of such characteristics have been long recognised and numerous studies conducted to illustrate the effect of such ground motions on seismic response of engineered systems (*e.g.,* Bertero et al., 1978; Anderson and Bertero, 1987; Hall et al., 1995; Alavi and Krawinkler, 2001; Luco and Cornell, 2007; Champion and Liel, 2012). Accurately assessing seismic performance of engineered systems in the near-fault region requires considering the forward directivity effects in seismic hazard analysis and ground motion selection.

An approach was presented to consider the forward directivity velocity pulse effect in seismic hazard analysis, which was adapted from Shahi and Baker (2011) method. However, instead of separating the hazard calculations for pulse-like and non-pulse-like ground motions, the 'total' SA distribution is assumed to be lognormal in the presented approach, with the mean and standard deviation accounting for pulse-like and non-pulse-like ground motions. This results in a single target hazard at the site for ground motion selection and is a surrogate for future ground

motion models (GMMs) that will explicitly address the effect of directivity pulses in a rigorous manner instead of using *post hoc* correction models.

The ability of ground motion selection methods to appropriately select records containing forward directivity pulse motions in the near-fault region was examined. Particular attention was given to ground motion selection which is explicitly based on ground motion IMs, including SA, duration, and cumulative measures; rather than a focus on implicit parameters (*i.e.,* distance, and pulse or non-pulse classifications) that are conventionally used to heuristically distinguish between the near-fault and far-field records. Forward directivity effects were considered in the target IM distributions for ground motion selection by incorporating such effects in the seismic hazard analysis process. No *ad hoc* criterion in terms of the number of directivity ground motions and their pulse periods was enforced for selecting pulse-like records. Example applications were presented for scenario and PSHA cases with different rupture characteristics, source-to-site geometry, and site conditions. The implications of the selected records, in terms of the conditional demand distribution and the demand hazard, were discussed.

The analyses undertaken indicate that considering directivity pulse effects in the target IM distributions and utilising multiple IMs in the selection process results in ground motion ensembles with an accurate representation of the target hazard. It was shown that the selected ground motion ensembles can appropriately represent the total directivity probability at the site for a given hazard level if the available database of ground motion records have sufficient number of records in the near-fault region. It was also demonstrated that causal parameter bounds can be utilised to constrain the database of records for more accurate representation of the directivity probability. Moreover, the selected records can appropriately represent the target pulse period distribution.

The conditional demand distribution, collapse fragility, and demand hazard calculated based on the selected replicate ground motion ensembles with the varying number of directivity ground motions did not show a systematic dependency

of these demand measures on the number of directivity ground motions. It was advocated that the selection of ground motions in the near-fault region based on IM properties alone is preferred to that in which the proportion of pulse-like motions and their pulse periods are specified *a priori* as strict criteria for ground motion selection.

7.1.5 Correlation between IMs of directivity ground motions

Correlation coefficients are utilised in the GCIM (Bradley, 2012c) and similar ground motion selection methods (*e.g.,* Jayaram et al., 2011; Wang, 2011) in order to generate realisations of the conditional multivariate distribution of a considered vector of IMs for ground motion selection. Due to the different characteristics of near-fault ground motions, such as forward directivity velocity pulses which are not observed in the far-field records, the empirical correlation between different IMs were calculated specifically for ground motions containing forward directivity pulses. Uncertainty due to the use of different GMMs and the limited number of ground motions were considered in the calculations. The obtained correlation coefficients are compared with those from a 'general' database of ground motions utilised in the past studies (containing both pulse-like and non-pulse-like ground motions). It was observed that the difference between the SA correlation coefficients of the directivity and general database of ground motions is within the range of differences among the correlation coefficients developed by various researchers using different ground motion databases. In addition, the differences between the correlation coefficients of the non-SA IMs with each other and with SA ordinates is small, and in comparison to the significant changes in the conditional IM distribution due to epistemic uncertainty in the utilised GMMs, they generally have slight effect on the target for ground motion selection.

7.1.6 Directionality of directivity ground motions

Directionality of ground motions containing forward directivity pulses were examined for SA ordinates. The RotD100/RotD50 ratios from the directivity ground motions are compared with the model developed by Shahi and Baker (2014b) based on the general database of NGA-West2 project (Ancheta et al., 2013) including directivity and non-directivity ground motions. As shown, the median RotD100/RotD50 ratio of the directivity motions are greater than the Shahi and Baker (2014b) median values due to the fact that the velocity pulses of directivity ground motions generally result in higher long-period SA ordinates (*e.g.,* Archuleta and Hartzell, 1981; Somerville et al., 1997; Aagaard et al., 2004; Bray and Rodriguez-Marek, 2004; Shahi and Baker, 2011). The 84^{th} percentile of the RotD100/RotD50 ratio is also greater for the whole range of SA ordinates. This observation is important as it implies that when computing the ground motion hazard for sites at which directivity is of consideration, not only do directivity ground motions result in an increase in the RotD50 amplitudes around the pulse period (Shahi and Baker, 2011), but they also increase the polarity of the ground motion (meaning that the resulting RotD100 value will be the product of these two factors, both of which increase for directivity ground motions).

7.1.7 Consideration and propagation of seismic hazard and ground motion selection epistemic uncertainties to seismic performance metrics

Epistemic uncertainty in the modelled characteristics of causative rupture scenarios and resulting ground motions (along with the modelling assumptions for seismic response analysis) are important components in addressing uncertainty in the seismic performance of engineered systems. Performing time-domain response history analyses (RHAs) to estimate the distribution of engineering demand parameters (EDPs) requires an appropriate representation of the seismic hazard at

the site, which can be achieved by selecting ground motion time series recorded during past earthquakes and/or from an ensemble of simulated ground motions. Hence, epistemic uncertainty in seismic hazard analysis needs to be propagated to the conditional distribution of IMs utilised in ground motion selection, and then the selected ground motion ensembles.

Three methods were presented to propagate the effect of seismic hazard and ground motion selection epistemic uncertainties to seismic performance metrics. These methods are different in the level of rigor considered to propagate the epistemic uncertainty effects to conditional distribution of IMs utilised in ground motion selection, selected ground motion ensembles, and the number of RHAs performed to obtain the distribution of EDPs. In the exact approach, the EDP-IM relationship and demand hazard is calculated based on ground motion ensembles selected specifically to represent each alternative seismic hazard curve. Assuming that the considered models represent a robust set of applicable models to characterise the seismic hazard at the site, the resulting demand hazards from the exact approach can be assumed to represent the center, body, and range in epistemic uncertainty of seismic performance of the system. In contrast, the approximate distribution approach utilises the EDP-IM relationship and collapse fragility curve obtained based on ground motion ensembles representing only the mean seismic hazard curve, which is then integrated with the epistemic uncertainty in the seismic hazard to obtain an approximation to the demand hazard obtained from the exact approach. This approach has a significantly lower computational cost compared to the exact approach due to the smaller number of RHAs and ground motion selection tasks performed. The third approach integrates the EDP-IM relationship and collapse fragility curve representing the mean hazard with the mean seismic hazard curve, resulting in a demand hazard which tends to approximate the mean of the demand hazard from the exact approach.

These three epistemic uncertainty propagation methods were compared for an example case in the San Francisco Bay Area considering epistemic uncertainties in the earthquake rupture forecast and ground motion models. The presented results

indicate that considering the significantly lower computational cost of utilising the approximate distribution approach, this approach can appropriately approximate the distribution of the demand hazards from the exact approach. In addition, if the aim is to obtain the mean demand hazard, it is sufficient to integrate the mean seismic hazard with the EDP-IM relationship and collapse fragility curve representing the mean seismic hazard. Also, it was observed that, for seismic demand levels below the collapse limit, epistemic uncertainty in ground motion selection is a small uncertainty contributor relative to the uncertainty in the seismic hazard itself. In contrast, uncertainty in ground motion selection process appreciably increases the uncertainty in the seismic demand hazard for near-collapse demand levels.

7.2 Recommendations for future work

Considering the limitations of this dissertation and the existing literature, following recommendations are made for future work in the field of ground motion selection.

7.2.1 Ground motion selection for subduction ruptures

Ground motion selection conducted in this dissertation utilised example case studies where the seismic hazard is dominated by shallow crustal events. However, the occurrence of major subduction zone earthquakes (both interface and slab) should also be considered in ground motion selection for regions prone to this type of earthquakes (such as Wellington in New Zealand, Oregon, British Columbia, and Alaska in North America, among others) (Tarbali and Bradley, 2014b). At present, routine ground motion selection for subduction zone events is hindered by a lack of a comprehensive database of strong ground motions recorded from subduction zone events and appropriate subduction zone GMMs and correlation equations for various ground motions IMs. The development of these necessary

models will allow appropriate ground motion selection for regions affected by multiple tectonic regimes. The consideration of 'proportion of records from a specific tectonic type' is a causal parameter which is likely important in ground motion selection for sites affected by ruptures from different tectonic regimes.

7.2.2 Bidirectional and vertical ground motion selection

It has been long recognised that vertical and torsional response of engineered systems can cause significant damage during earthquakes for certain systems (Fischer and Seeber, 1988; Saadeghvariri and Foutch, 1991; Papazoglou and Elnashai, 1996; De Stefano and Pintucchi, 2008). A comprehensive approach to select ground motion ensembles for three dimensional seismic response analysis should be based on selecting three components of recorded and/or simulated ground motions that conforms to the target seismic hazard. Such an approach requires GMMs for various IMs in three (*i.e.,* two translational and one vertical) directions (Gülerce and Abrahamson, 2010, 2011; Gülerce et al., 2016), in addition to correlation models for various IMs in all directions. Such models should be developed (or thoroughly examined) for ground motions in different tectonic regimes (*i.e.,* shallow crustal, subduction, stable continental).

7.2.3 Epistemic uncertainty in ground motion selection

Uncertainty in seismic hazard analysis and ground motion selection due to alternative GMMs utilised for seismic hazard analysis is discussed in this dissertation. Alternative GMMs can also be used for IMs other than the conditioning IM when calculating their conditional distribution for ground motion selection, which depends on the availability of such models. It would be insightful to investigate the effect of utilising alternative models for all IMs considered in ground motion selection (in terms of seismic performance metrics), in comparison to the case where alternative models are considered only for the conditioning IM.

It is also of practical interest to discern the effect of epistemic uncertainty in seismic response analysis of engineered systems due to modelling assumptions in comparison to epistemic uncertainty in seismic hazard analysis and ground motion selection.

7.2.4 Ground motion selection in conjunction with site response analysis

Seismic performance assessment of engineered systems on soft soils can be performed by selecting ground motion ensembles representing the target IM distributions on soft soil from conventional seismic hazard analysis. An alternative, an arguably more accurate, approach is to perform seismic hazard and ground motion selection for the bedrock condition (or suitable reference condition in the case of deep sedimentary soils), then conduct site response analysis under the selected records to obtain ground motions on soft soil. Considering the variability in the selected ground motion properties on soft soil and bed rock conditions, and uncertainty in the modelling assumption of the soil profile, comparisons are needed to be made between properties of the resulting ground motion on the soil surface from site response analysis with the IM distributions obtained from the conventional ground motion selection. Also, the distribution of EDPs for various superstructures subjected to both types of input motions should be compared.

7.2.5 Mainshock-aftershock ground motion selection

Following major earthquakes causing significant damage in engineered systems, aftershocks can cause further damage or collapse in the severely affected systems. Post-disaster management after a major earthquake and reducing the possible loss due to aftershocks requires seismic hazard analysis and ground motion selection methods which consider the coupled mainshock and aftershock seismicity in the region. Considering the shortcoming of existing approaches to select

aftershock ground motions (*i.e.,* mainly based on amplitude scaling of mainshock ground motions neglecting the differences in their frequency contents and durations), a consistent methodology is needed to select mainshock-aftershock sequence ground motion ensembles representing the corresponding seismic hazards. Research on time-dependent aftershock seismic hazard analysis is also warranted.

7.2.6 Seismic hazard analysis and ground motion selection in the near-fault region

Seismic hazard analysis and ground motion selection in the near-fault region requires GMMs for various IMs (representing amplitude, frequency content, duration, and cumulative effects) that consider the near-fault effects in a direct fashion (*e.g.,* Shahi, 2013; Chiou and Youngs, 2014), rather than *post hoc* modifications (*e.g.,* Somerville et al., 1997; Abrahamson, 2000; Somerville, 2003; Tothong et al., 2007; Spudich and Chiou, 2008; Shahi and Baker, 2011; Spudich et al., 2014).

Further investigations on the correlation between various IMs and directionality of near-fault ground motion is warranted. In addition to seismic hazard analysis and ground motion selection, such investigations can serve seismic design codes (*e.g.,* NZS1170.5, 2004) in updating the parameters utilised for incorporating near-fault effects in the design process.

Considering the paucity of directivity ground motions from large magnitude ruptures in the empirical ground motion databases, selecting records from simulated ground motion ensembles with directivity characteristics needs to be examined in terms of their IM properties and resulting demand distributions for different engineered systems, once predictive confidence in simulated ground motions is developed through validations (Galasso et al., 2012, 2013; Bradley et al., 2015).

7.2.7 Comparison between code-based and other ground motion selection methodologies

Comparisons are needed to be made between properties of ground motion ensembles selected based on methods with rigorous bases (*e.g.,* Baker, 2011; Jayaram et al., 2011; Wang, 2011; Bradley, 2012c; Tarbali and Bradley, 2015b) and those selected based on seismic design codes. Distribution of various EDPs from these ground motion ensembles should also be compared in order identify potential biases in code-based ground motion selection procedures.

7.3 Concluding remarks

This dissertation was an attempt to address some of the shortcomings in the current methodologies for ground motion selection. Further work is warranted in the addressed topics in this dissertation and those outlined in the recommendation section to improve the practice of ground motion selection and provide engineers with rigorous methods to perform ground motion selection in seismic design and performance assessment processes.

Appendix A

Tabulated characteristics of the ground motions selected for several major earthquake scenarios in New Zealand

Presented is the NGA ID number (Chiou et al., 2008) of the 20 ground motions and their corresponding amplitude scale factors, selected for the scenario rupture of the Alpine, Hope, and Porters Pass faults for Christchurch city (Tables A1-A3), and Wellington, Wairarapa, and Ohariu faults for Wellington city (Tables A4-A6). Subsets of 7 ground motions from these 20 motions are presented in Tables A7-A9 and for Christchurch city, and Tables A10-A12 for Wellington city.

It is important to note that the ground-motion selection has been conducted based on the geometric mean of the intensity measures of motion. Presented ground-motion time series are the as-recorded motions in two horizontal directions and the vertical direction (which have file names with suffix '_1', '_2', and '_3' for the two horizontal and vertical components; accessible at `https://sites.google.com/site/brendonabradley/research/ground-motion-selection`). Geometric mean of peak ground acceleration (PGA) and peak ground velocity

(PGV) of the two as-recorded horizontal motions are presented in the tables below. These motions are also accessible at `http://peer.berkeley.edu/nga/`, using the NGA ID number.

Table A.1: Selected 20 ground motions representing the Alpine fault scenario rupture for Christchurch city

NGA#	Event	Year	Station	M_w	Mechanism	R_{rup}(km)	V_{s30}(m/s)	PGA (g)	PGV (cm/s)	Scale factor
836	Landers	1992	Baker Fire Station	7.28	Strike-Slip	87.9	271.4	0.11	9.85	1.18
842	Landers	1992	Brea - S Flower Av	7.28	Strike-Slip	137.4	308.6	0.04	10.50	2.74
860	Landers	1992	Hemet Fire Station	7.28	Strike-Slip	68.7	338.5	0.09	5.60	0.74
869	Landers	1992	LA - N Westmoreland	7.28	Strike-Slip	159.1	315.1	0.04	3.55	4.41
888	Landers	1992	San Bernardino - E & Hospitality	7.28	Strike-Slip	79.8	271.4	0.08	17.16	0.68
895	Landers	1992	Tarzana - Cedar Hill	7.28	Strike-Slip	175.7	257.2	0.05	7.07	1.10
1188	Chi-Chi- Taiwan	1999	CHY016	7.62	Reverse-Oblique	66.7	200.9	0.10	16.14	0.88
1192	Chi-Chi- Taiwan	1999	CHY023	7.62	Reverse-Oblique	81.3	279.8	0.05	9.08	1.04
1217	Chi-Chi- Taiwan	1999	CHY060	7.62	Reverse-Oblique	68.9	228.9	0.05	14.82	0.88
1223	Chi-Chi- Taiwan	1999	CHY067	7.62	Reverse-Oblique	83.6	228	0.06	10.33	0.66
1342	Chi-Chi- Taiwan	1999	ILA055	7.62	Reverse-Oblique	90.3	266.8	0.07	25.00	0.85
1415	Chi-Chi- Taiwan	1999	TAP010	7.62	Reverse-Oblique	101.3	226.4	0.10	22.80	0.85
1599	Duzce- Turkey	1999	Ambarli	7.14	Strike-Slip	188.7	175	0.03	5.59	2.55
1790	Hector Mine	1999	Huntington Beach - Lake St	7.13	Strike-Slip	184	370.8	0.02	10.02	3.34
1814	Hector Mine	1999	Newhall - Fire Sta	7.13	Strike-Slip	198.1	269.1	0.02	4.63	2.87
1823	Hector Mine	1999	Salton City	7.13	Strike-Slip	123.2	324.5	0.05	7.93	2.56
1837	Hector Mine	1999	Valyermo Forest Fire Station	7.13	Strike-Slip	135.8	345.4	0.06	6.36	1.37
2109	Denali- Alaska	2002	Fairbanks - Ester Fire Station	7.9	Strike-Slip	139.8	274.5	0.05	4.00	1.12
2115	Denali- Alaska	2002	TAPS Pump Station #11	7.9	Strike-Slip	126.4	376.1	0.08	11.52	0.67
2116	Denali- Alaska	2002	TAPS Pump Station #12	7.9	Strike-Slip	164.7	338.6	0.04	4.39	1.05

Table A.2: Selected 20 ground motions representing the Hope fault scenario rupture for Christchurch city

NGA#	Event	Year	Station	M_w	Mechanism	R_{rup}(km)	V_{s30}(m/s)	PGA (g)	PGV (cm/s)	Scale factor
82	San Fernando	1971	Port Hueneme	6.61	Reverse	68.8	297.9	0.03	5.43	1.18
742	Loma Prieta	1989	Bear Valley #1- Fire Station	6.93	Reverse-Oblique	61.7	338.5	0.07	5.87	1.52
832	Landers	1992	Amboy	7.28	Strike-Slip	69.2	271.4	0.13	19.00	0.55
887	Landers	1992	Riverside Airport	7.28	Strike-Slip	96	370.8	0.04	3.05	2.70
1068	Northridge-01	1994	San Bernardino - Co Service Bldg -Freefield	6.69	Reverse	107.7	271.4	0.04	4.65	2.25
1147	Kocaeli- Turkey	1999	Ambarli	7.51	Strike-Slip	69.6	175	0.21	36.67	0.28
1220	Chi-Chi- Taiwan	1999	CHY063	7.62	Reverse-Oblique	72.2	246.9	0.06	8.56	0.94
1332	Chi-Chi- Taiwan	1999	ILA042	7.62	Reverse-Oblique	85.7	209.4	0.08	16.67	0.75
1344	Chi-Chi- Taiwan	1999	ILA059	7.62	Reverse-Oblique	86.3	236.8	0.07	15.39	0.33
1433	Chi-Chi- Taiwan	1999	TAP047	7.62	Reverse-Oblique	84.5	400.3	0.06	15.20	1.28
1559	Chi-Chi- Taiwan	1999	TTN003	7.62	Reverse-Oblique	95	262.6	0.02	3.10	2.11
1766	Hector Mine	1999	Baker Fire Station	7.13	Strike-Slip	64.8	271.4	0.11	8.44	0.52
1773	Hector Mine	1999	Cabazon	7.13	Strike-Slip	76.9	345.4	0.04	7.40	0.80
1783	Hector Mine	1999	Fort Irwin	7.13	Strike-Slip	65.9	345.4	0.13	10.06	0.53
1813	Hector Mine	1999	Morongo Valley	7.13	Strike-Slip	53.2	345.4	0.08	16.52	1.94
1821	Hector Mine	1999	Pomona - 4th & Locust FF	7.13	Strike-Slip	143.4	229.8	0.04	6.42	0.60
1822	Hector Mine	1999	Riverside Airport	7.13	Strike-Slip	123.8	370.8	0.02	2.96	1.59
1823	Hector Mine	1999	Salton City	7.13	Strike-Slip	123.2	324.5	0.05	7.93	1.74
2089	Nenana Mountain- Alaska	2002	Fairbanks - Ester Fire Station	6.7	Strike-Slip	146.3	274.5	0.02	1.69	1.59
2115	Denali- Alaska	2002	TAPS Pump Station #11	7.9	Strike-Slip	126.4	376.1	0.08	11.52	0.59

Table A.3: Selected 20 ground motions representing the Porters Pass fault scenario rupture for Christchurch city

NGA#	Event	Year	Station	M_w	Mechanism	R_{rup}(km)	V_{s30}(m/s)	PGA (g)	PGV (cm/s)	Scale factor
51	San Fernando	1971	2516 Via Tejon PV	6.61	Reverse	55.2	280.6	0.03	3.43	1.67
93	San Fernando	1971	Whittier Narrows Dam	6.61	Reverse	39.5	298.7	0.12	9.30	2.02
176	Imperial Valley-06	1979	El Centro Array #13	6.53	Strike-Slip	22	249.9	0.13	14.23	2.71
190	Imperial Valley-06	1979	Superstition Mtn Camera	6.53	Strike-Slip	24.6	362.4	0.14	6.79	0.82
191	Imperial Valley-06	1979	Victoria	6.53	Strike-Slip	31.9	274.5	0.13	7.79	1.66
287	Irpinia- Italy-01	1980	Bovino	6.9	Normal	46.2	274.5	0.04	2.69	5.96
729	Superstition Hills-02	1987	Wildlife Liquef. Array	6.54	Strike-Slip	23.9	207.5	0.20	27.82	0.66
761	Loma Prieta	1989	Fremont - Emerson Court	6.93	Reverse-Oblique	39.9	284.8	0.16	13.57	0.79
762	Loma Prieta	1989	Fremont - Mission San Jose	6.93	Reverse-Oblique	39.5	367.6	0.14	11.36	1.01
850	Landers	1992	Desert Hot Springs	7.28	Strike-Slip	21.8	345.4	0.16	20.42	2.55
880	Landers	1992	Mission Creek Fault	7.28	Strike-Slip	27	345.4	0.12	12.63	1.00
900	Landers	1992	Yermo Fire Station	7.28	Strike-Slip	23.6	353.6	0.22	36.40	0.83
1026	Northridge-01	1994	Lawndale - Osage Ave	6.69	Reverse	39.9	361.2	0.12	8.25	1.09
1059	Northridge-01	1994	Port Hueneme - Naval Lab.	6.69	Reverse	51.8	271.4	0.09	8.09	2.70
1215	Chi-Chi- Taiwan	1999	CHY058	7.62	Reverse-Oblique	59.8	237.6	0.06	12.11	1.67
1228	Chi-Chi- Taiwan	1999	CHY076	7.62	Reverse-Oblique	42.2	169.8	0.08	19.56	0.60
1258	Chi-Chi- Taiwan	1999	HWA005	7.62	Reverse-Oblique	47.6	489.2	0.14	14.34	0.81
1279	Chi-Chi- Taiwan	1999	HWA030	7.62	Reverse-Oblique	47	487.4	0.07	12.25	1.63
1762	Hector Mine	1999	Amboy	7.13	Strike-Slip	43	271.4	0.20	23.90	1.42
1776	Hector Mine	1999	Desert Hot Springs	7.13	Strike-Slip	56.4	345.4	0.07	8.83	2.56

Table A.4: Selected 20 ground motions representing the Wellington fault scenario rupture for Wellington city

NGA#	Event	Year	Station	M_w	Mechanism	R_{rup}(km)	V_{s30}(m/s)	PGA (g)	PGV (cm/s)	Scale factor
161	Imperial Valley-06	1979	Brawley Airport	6.53	Strike-Slip	10.4	208.7	0.18	35.97	3.70
173	Imperial Valley-06	1979	El Centro Array #10	6.53	Strike-Slip	6.2	202.8	0.20	42.95	4.40
175	Imperial Valley-06	1979	El Centro Array #12	6.53	Strike-Slip	17.9	196.9	0.13	19.64	3.09
179	Imperial Valley-06	1979	El Centro Array #4	6.53	Strike-Slip	7	208.9	0.41	55.89	1.74
183	Imperial Valley-06	1979	El Centro Array #8	6.53	Strike-Slip	3.9	206.1	0.53	50.23	1.35
723	Superstition Hills-02	1987	Parachute Test Site	6.54	Strike-Slip	0.9	348.7	0.38	72.74	2.64
729	Superstition Hills-02	1987	Wildlife Liquef. Array	6.54	Strike-Slip	23.9	207.5	0.20	27.82	1.55
776	Loma Prieta	1989	Hollister - South & Pine	6.93	Reverse-Oblique	27.9	370.8	0.29	48.34	2.71
806	Loma Prieta	1989	Sunnyvale - Colton Ave.	6.93	Reverse-Oblique	24.2	267.7	0.20	34.42	1.86
880	Landers	1992	Mission Creek Fault	7.28	Strike-Slip	27	345.4	0.12	12.63	2.73
900	Landers	1992	Yermo Fire Station	7.28	Strike-Slip	23.6	353.6	0.22	36.40	2.82
1084	Northridge-01	1994	Sylmar - Converter Sta	6.69	Reverse	5.3	251.2	0.69	110.25	1.73
1176	Kocaeli- Turkey	1999	Yarimca	7.51	Strike-Slip	4.8	297	0.29	59.27	2.40
1194	Chi-Chi- Taiwan	1999	CHY025	7.62	Reverse-Oblique	19.1	277.5	0.16	42.59	3.57
1244	Chi-Chi- Taiwan	1999	CHY101	7.62	Reverse-Oblique	10	258.9	0.41	96.39	1.38
1499	Chi-Chi- Taiwan	1999	TCU060	7.62	Reverse-Oblique	8.5	495.8	0.15	39.86	2.28
1503	Chi-Chi- Taiwan	1999	TCU065	7.62	Reverse-Oblique	0.6	305.9	0.69	101.37	1.83
1528	Chi-Chi- Taiwan	1999	TCU101	7.62	Reverse-Oblique	2.1	504.4	0.23	60.18	1.12
1547	Chi-Chi- Taiwan	1999	TCU123	7.62	Reverse-Oblique	14.9	241.7	0.15	39.01	1.58
2114	Denali- Alaska	2002	TAPS Pump Station #10	7.9	Strike-Slip	2.7	329.4	0.30	107.63	1.41

Table A.5: Selected 20 ground motions representing the Wairarapa fault scenario rupture for Wellington city

NGA#	Event	Year	Station	M_w	Mechanism	R_{rup}(km)	V_{s30}(m/s)	PGA (g)	PGV (cm/s)	Scale factor
850	Landers	1992	Desert Hot Springs	7.28	Strike-Slip	21.8	345.4	0.16	20.42	1.84
864	Landers	1992	Joshua Tree	7.28	Strike-Slip	11	379.3	0.28	34.15	3.28
880	Landers	1992	Mission Creek Fault	7.28	Strike-Slip	27	345.4	0.12	12.63	3.07
881	Landers	1992	Morongo Valley	7.28	Strike-Slip	17.3	345.4	0.16	18.15	4.34
882	Landers	1992	North Palm Springs	7.28	Strike-Slip	26.8	345.4	0.13	12.76	4.15
900	Landers	1992	Yermo Fire Station	7.28	Strike-Slip	23.6	353.6	0.22	36.40	2.62
1158	Kocaeli- Turkey	1999	Duzce	7.51	Strike-Slip	15.4	276	0.33	52.60	1.09
1194	Chi-Chi- Taiwan	1999	CHY025	7.62	Reverse-Oblique	19.1	277.5	0.16	42.59	2.49
1201	Chi-Chi- Taiwan	1999	CHY034	7.62	Reverse-Oblique	14.8	378.8	0.31	38.37	2.94
1203	Chi-Chi- Taiwan	1999	CHY036	7.62	Reverse-Oblique	16.1	233.1	0.26	38.07	2.73
1209	Chi-Chi- Taiwan	1999	CHY047	7.62	Reverse-Oblique	24.1	291.9	0.18	21.27	1.59
1244	Chi-Chi- Taiwan	1999	CHY101	7.62	Reverse-Oblique	10	258.9	0.41	96.39	2.18
1484	Chi-Chi- Taiwan	1999	TCU042	7.62	Reverse-Oblique	26.3	424	0.20	43.68	2.33
1491	Chi-Chi- Taiwan	1999	TCU051	7.62	Reverse-Oblique	7.7	467.5	0.19	43.65	1.74
1495	Chi-Chi- Taiwan	1999	TCU055	7.62	Reverse-Oblique	6.4	447.8	0.22	39.03	1.38
1499	Chi-Chi- Taiwan	1999	TCU060	7.62	Reverse-Oblique	8.5	495.8	0.15	39.86	2.99
1503	Chi-Chi- Taiwan	1999	TCU065	7.62	Reverse-Oblique	0.6	305.9	0.69	101.37	1.58
1513	Chi-Chi- Taiwan	1999	TCU079	7.62	Reverse-Oblique	11	364	0.54	54.50	1.80
1528	Chi-Chi- Taiwan	1999	TCU101	7.62	Reverse-Oblique	2.1	504.4	0.23	60.18	2.10
1553	Chi-Chi- Taiwan	1999	TCU141	7.62	Reverse-Oblique	24.2	209.2	0.09	35.36	2.62

Table A.6: Selected 20 ground motions representing the Ohariu fault scenario rupture for Wellington city

NGA#	Event	Year	Station	M_w	Mechanism	R_{rup}(km)	V_{s30}(m/s)	PGA (g)	PGV (cm/s)	Scale factor
162	Imperial Valley-06	1979	Calexico Fire Station	6.53	Strike-Slip	10.4	231.2	0.24	18.47	2.16
165	Imperial Valley-06	1979	Chihuahua	6.53	Strike-Slip	7.3	274.5	0.27	28.65	1.73
169	Imperial Valley-06	1979	Delta	6.53	Strike-Slip	22	274.5	0.28	27.01	1.22
172	Imperial Valley-06	1979	El Centro Array #1	6.53	Strike-Slip	21.7	237.3	0.14	12.97	3.62
176	Imperial Valley-06	1979	El Centro Array #13	6.53	Strike-Slip	22	249.9	0.13	14.23	5.07
187	Imperial Valley-06	1979	Parachute Test Site	6.53	Strike-Slip	12.7	348.7	0.16	16.06	1.61
192	Imperial Valley-06	1979	Westmorland Fire Sta	6.53	Strike-Slip	15.2	193.7	0.09	15.54	4.09
721	Superstition Hills-02	1987	El Centro Imp. Co. Cent	6.54	Strike-Slip	18.2	192.1	0.26	43.30	1.41
725	Superstition Hills-02	1987	Poe Road (temp)	6.54	Strike-Slip	11.2	207.5	0.34	29.46	2.01
728	Superstition Hills-02	1987	Westmorland Fire Sta	6.54	Strike-Slip	13	193.7	0.22	28.62	3.12
776	Loma Prieta	1989	Hollister - South & Pine	6.93	Reverse-Oblique	27.9	370.8	0.29	48.34	1.51
778	Loma Prieta	1989	Hollister Diff. Array	6.93	Reverse-Oblique	24.8	215.5	0.29	42.56	1.53
803	Loma Prieta	1989	Saratoga - W Valley Coll.	6.93	Reverse-Oblique	9.3	370.8	0.32	65.43	3.95
900	Landers	1992	Yermo Fire Station	7.28	Strike-Slip	23.6	353.6	0.22	36.40	2.43
1176	Kocaeli- Turkey	1999	Yarimca	7.51	Strike-Slip	4.8	297	0.29	59.27	1.35
1244	Chi-Chi- Taiwan	1999	CHY101	7.62	Reverse-Oblique	10	258.9	0.41	96.39	1.65
1499	Chi-Chi- Taiwan	1999	TCU060	7.62	Reverse-Oblique	8.5	495.8	0.15	39.86	2.72
1502	Chi-Chi- Taiwan	1999	TCU064	7.62	Reverse-Oblique	16.6	357.5	0.11	43.94	2.45
1537	Chi-Chi- Taiwan	1999	TCU111	7.62	Reverse-Oblique	22.1	237.5	0.12	45.32	4.12
2114	Denali- Alaska	2002	TAPS Pump Station #10	7.9	Strike-Slip	2.7	329.4	0.30	107.63	0.88

Table A.7: Selected 7 ground motions representing the Alpine fault scenario rupture for Christchurch city

NGA#	Event	Year	Station	M_w	Mechanism	R_{rup}(km)	V_{s30}(m/s)	PGA (g)	PGV (cm/s)	Scale factor
888	Landers	1992	San Bernardino - E & Hospitality	7.28	Strike-Slip	79.8	271.4	0.08	17.16	1.07
895	Landers	1992	Tarzana - Cedar Hill	7.28	Strike-Slip	175.7	257.2	0.05	7.07	1.97
1188	Chi-Chi- Taiwan	1999	CHY016	7.62	Reverse-Oblique	66.7	200.9	0.10	16.14	0.87
1223	Chi-Chi- Taiwan	1999	CHY067	7.62	Reverse-Oblique	83.6	228	0.06	10.33	0.88
1823	Hector Mine	1999	Salton City	7.13	Strike-Slip	123.2	324.5	0.05	7.93	0.61
2109	Denali- Alaska	2002	Fairbanks - Ester Fire Station	7.9	Strike-Slip	139.8	274.5	0.05	4.00	1.56
2115	Denali- Alaska	2002	TAPS Pump Station #11	7.9	Strike-Slip	126.4	376.1	0.08	11.52	0.90

Table A.8: Selected 7 ground motions representing the Hope fault scenario rupture for Christchurch city

NGA#	Event	Year	Station	M_w	Mechanism	R_{rup}(km)	V_{s30}(m/s)	PGA (g)	PGV (cm/s)	Scale factor
887	Landers	1992	Riverside Airport	7.28	Strike-Slip	96	370.8	0.04	3.05	1.40
1147	Kocaeli- Turkey	1999	Ambarli	7.51	Strike-Slip	69.6	175	0.21	36.67	0.29
1332	Chi-Chi- Taiwan	1999	ILA042	7.62	Reverse-Oblique	85.7	209.4	0.08	16.67	0.95
1344	Chi-Chi- Taiwan	1999	ILA059	7.62	Reverse-Oblique	86.3	236.8	0.07	15.39	0.43
1766	Hector Mine	1999	Baker Fire Station	7.13	Strike-Slip	64.8	271.4	0.11	8.44	0.82
1813	Hector Mine	1999	Morongo Valley	7.13	Strike-Slip	53.2	345.4	0.08	16.52	0.55
1823	Hector Mine	1999	Salton City	7.13	Strike-Slip	123.2	324.5	0.05	7.93	1.59

Table A.9: Selected 7 ground motions representing the Porters Pass fault scenario rupture for Christchurch city

NGA#	Event	Year	Station	M_w	Mechanism	R_{rup}(km)	V_{s30}(m/s)	PGA (g)	PGV (cm/s)	Scale factor
93	San Fernando	1971	Whittier Narrows Dam	6.61	Reverse	39.5	298.7	0.12	9.30	0.94
729	Superstition Hills-02	1987	Wildlife Liquef. Array	6.54	Strike-Slip	23.9	207.5	0.20	27.82	0.46
761	Loma Prieta	1989	Fremont - Emerson Court	6.93	Reverse-Oblique	39.9	284.8	0.16	13.57	1.31
762	Loma Prieta	1989	Fremont - Mission San Jose	6.93	Reverse-Oblique	39.5	367.6	0.14	11.36	2.37
880	Landers	1992	Mission Creek Fault	7.28	Strike-Slip	27	345.4	0.12	12.63	1.50
1026	Northridge-01	1994	Lawndale - Osage Ave	6.69	Reverse	39.9	361.2	0.12	8.25	0.57
1228	Chi-Chi- Taiwan	1999	CHY076	7.62	Reverse-Oblique	42.2	169.8	0.08	19.56	0.74

Table A.10: Selected 7 ground motions representing the Wellington fault scenario rupture for Wellington city

NGA#	Event	Year	Station	M_w	Mechanism	R_{rup}(km)	V_{s30}(m/s)	PGA (g)	PGV (cm/s)	Scale factor
173	Imperial Valley-06	1979	El Centro Array #10	6.53	Strike-Slip	6.2	202.8	0.20	42.95	3.17
175	Imperial Valley-06	1979	El Centro Array #12	6.53	Strike-Slip	17.9	196.9	0.13	19.64	1.96
729	Superstition Hills-02	1987	Wildlife Liquef. Array	6.54	Strike-Slip	23.9	207.5	0.20	27.82	2.24
806	Loma Prieta	1989	Sunnyvale - Colton Ave.	6.93	Reverse-Oblique	24.2	267.7	0.20	34.42	3.62
880	Landers	1992	Mission Creek Fault	7.28	Strike-Slip	27	345.4	0.12	12.63	4.71
1176	Kocaeli- Turkey	1999	Yarimca	7.51	Strike-Slip	4.8	297	0.29	59.27	2.33
1194	Chi-Chi- Taiwan	1999	CHY025	7.62	Reverse-Oblique	19.1	277.5	0.16	42.59	2.13

Table A.11: Selected 7 ground motions representing the Wairarapa fault scenario rupture for Wellington city

NGA#	Event	Year	Station	M_w	Mechanism	R_{rup}(km)	V_{s30}(m/s)	PGA (g)	PGV (cm/s)	Scale factor
850	Landers	1992	Desert Hot Springs	7.28	Strike-Slip	21.8	345.4	0.16	20.42	4.69
880	Landers	1992	Mission Creek Fault	7.28	Strike-Slip	27	345.4	0.12	12.63	5.41
882	Landers	1992	North Palm Springs	7.28	Strike-Slip	26.8	345.4	0.13	12.76	3.21
900	Landers	1992	Yermo Fire Station	7.28	Strike-Slip	23.6	353.6	0.22	36.40	3.97
1495	Chi-Chi- Taiwan	1999	TCU055	7.62	Reverse-Oblique	6.4	447.8	0.22	39.03	1.25
1503	Chi-Chi- Taiwan	1999	TCU065	7.62	Reverse-Oblique	0.6	305.9	0.69	101.37	0.58
1513	Chi-Chi- Taiwan	1999	TCU079	7.62	Reverse-Oblique	11	364	0.54	54.50	0.77

Table A.12: Selected 7 ground motions representing the Ohariu fault scenario rupture for Wellington city

NGA#	Event	Year	Station	M_w	Mechanism	R_{rup}(km)	V_{s30}(m/s)	PGA (g)	PGV (cm/s)	Scale factor
172	Imperial Valley-06	1979	El Centro Array #1	6.53	Strike-Slip	21.7	237.3	0.14	12.97	2.16
176	Imperial Valley-06	1979	El Centro Array #13	6.53	Strike-Slip	22	249.9	0.13	14.23	3.49
187	Imperial Valley-06	1979	Parachute Test Site	6.53	Strike-Slip	12.7	348.7	0.16	16.06	5.01
776	Loma Prieta	1989	Hollister - South & Pine	6.93	Reverse-Oblique	27.9	370.8	0.29	48.34	3.25
778	Loma Prieta	1989	Hollister Diff. Array	6.93	Reverse-Oblique	24.8	215.5	0.29	42.56	1.63
1244	Chi-Chi- Taiwan	1999	CHY101	7.62	Reverse-Oblique	10	258.9	0.41	96.39	1.18
1537	Chi-Chi- Taiwan	1999	TCU111	7.62	Reverse-Oblique	22.1	237.5	0.12	45.32	2.36

Appendix B

Correlation between various intensity measures of ground motions containing forward directivity pulses

B.1 Summary

Correlation coefficients are utilized in the generalized conditional intensity measure (GCIM) methodology in order to generate realizations of the conditional multivariate distribution of a considered vector of IMs for ground motion selection (Bradley, 2010b). Due to the different characteristics of near-fault ground motions, such as forward directivity velocity pulses which are not observed in the far-field records, the empirical correlation between different IMs are calculated here specifically for ground motions containing forward directivity pulses. The obtained correlation coefficients are compared with those based on a 'general' database of ground motions utilized in the past studies (containing both pulse-like and non-pulse-like ground motions). The practical implications of the observed differences between the directivity ground motions and general database

correlation coefficients are discussed.

B.2 Methodology and database

The Pearson correlation coefficient, which measures the linear dependence between two variables (Ang and Tang, 1975), is calculated to obtain the empirical correlation between two given IMs (*e.g.,* Baker and Jayaram, 2008; Bradley, 2011b; Wang and Du, 2012). Due to the linear relationship between the total residual and the median prediction from a ground motion model (GMM), correlation coefficients are calculated between the residuals of given IMs, mainly by separating the between-event and within-even residuals (refer to Bradley (2012b) for further details).

A range of IMs are considered in this study to adequately examine the correlation between different characteristics of ground motion, namely, amplitude, frequency content, duration, and cumulative effects. Specifically, these IMs include pseudo-spectral acceleration (SA) for 18 vibration periods (T=0.05, 0.075, 0.1, 0.15, 0.2, 0.25, 0.3, 0.4, 0.5, 0.75, 1.0, 1.5, 2.0, 3.0, 4.0, 5.0, 7.5, and 10.0 s); peak ground acceleration (PGA); peak ground velocity (PGV); acceleration spectrum intensity (ASI); spectrum intensity (SI); displacement spectrum intensity (DSI); cumulative absolute velocity (CAV); Arias intensity (AI); and 5-75% and 5-95% significant durations (D_{s575} and D_{s595}, respectively). Table B.1 presents the list of IMs, the number of GMMs (N_{GMMs}), and their corresponding abbreviated names considered in this study.

There is uncertainty associated with the adopted GMMs to calculate the median and standard deviation of a given IM which is addressed by utilizing different GMMs for each IM. Note that with the exception of a large number of GMMs for SA (Douglas, 2011; Stewart et al., 2015), there are very few GMMs published for IMs such as AI, CAV, and Significant Duration. Given a lack of evidence to do otherwise, equal weights were assigned to each and every GMM for

Table B.1: List of IMs and the corresponding GMMs considered in the analyses

IM	N_{GMMs}	GMMs
SA, PGA, PGV	4	Boore and Atkinson (2008) – BA08 Chiou and Youngs (2008) – CY08 Campbell and Bozorgnia (2008) – CB08 Abrahamson and Silva (2008) – AS08
ASI	4	Bradley (2010) using BA08, CY08, CB08, and AS08
SI	4	Bradley et al. (2009) using BA08, CY08, CB08, and AS08
DSI	4	Bradley (2011c) using BA08, CY08, CB08, and AS08
CAV	1	Campbell and Bozorgnia (2010)
AI	3	Travasarou et al. (2003) Foulser-Piggott and Stafford (2012) Campbell and Bozorgnia (2012)
D_{s575} and D_{s595}	2	Kempton and Stewart (2006) Bommer et al. (2009)

a specific IM. The number of correlation coefficient relationships obtained from two different IMs with N_{GMM_i} and N_{GMM_j} GMMs for each is equal to $N_{\text{GMM}_i} \times N_{\text{GMM}_j}$(*e.g.,* 12 estimated correlation coefficients are obtained for the correlation coefficients between AI and SA ordinates in this study — see Table B.1).

Having a finite number of ground motions to calculate the correlation coefficient is another source of uncertainty which is addressed by using the Fisher Z transformation and bootstrap sampling (Ang and Tang, 1975) in order to estimate the variance of the correlation coefficients from a finite number of ground motions (Bradley, 2012b).

Considering the above sources of uncertainty due to the use of different GMMs, and also the limited number of ground motions, results in a distribution for the estimated correlation coefficients. This distribution is explicitly represented here, as well as the mean value of the distribution.

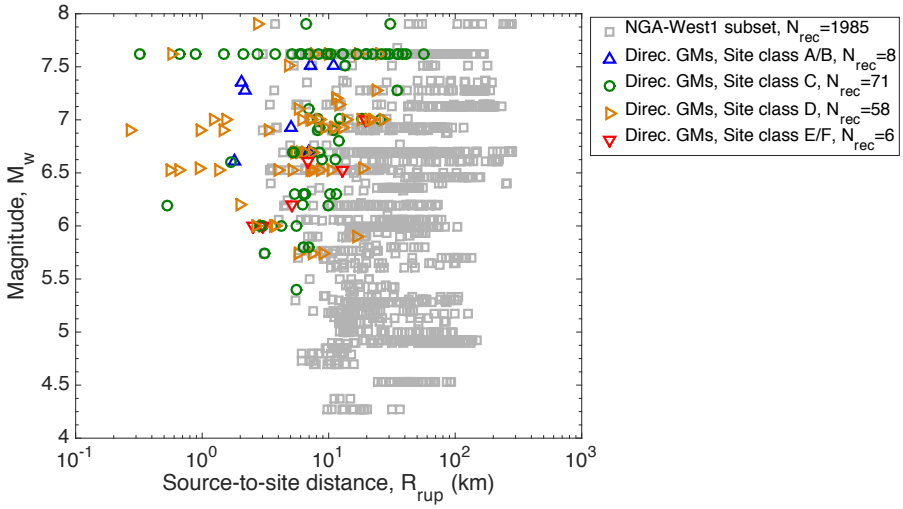

Figure B.1: $M_w - R_{rup}$ distribution of the directivity and general database of ground motions.

Ground motions identified by Shahi and Baker (2014a) as containing velocity pulses caused by forward directivity effects are used as the directivity ground motion records. The directivity effect in the predicted IM median and standard deviation is calculated based on the method proposed in this study (see Table 1 of this chapter). A subset of the empirical ground motion database of the NGA-West1 project (Chiou et al., 2008) is used as the general database, which includes directivity and non-directivity records. Figure 1 presents the magnitude (M_w) and source-to-site distance (R_{rup}) distribution of the utilized ground motions, along with the site classification of the directivity records according to NEHRP (2003). Note that this subset of NGA-West1 database was previously utilized to derive correlation coefficient models for various IMs (*e.g.,* Bradley (2011b, 2012b,a, 2015)). SA ordinates for the considered vibration periods are calculated considering the usable range of periods for a ground motion record.

B.3 IM correlation results

Figure 2 presents the correlation of SA ordinates from 0.01 to 10 s periods with SA(0.2), SA(2.0), D_{s575} , and CAV for the considered directivity ground motions.

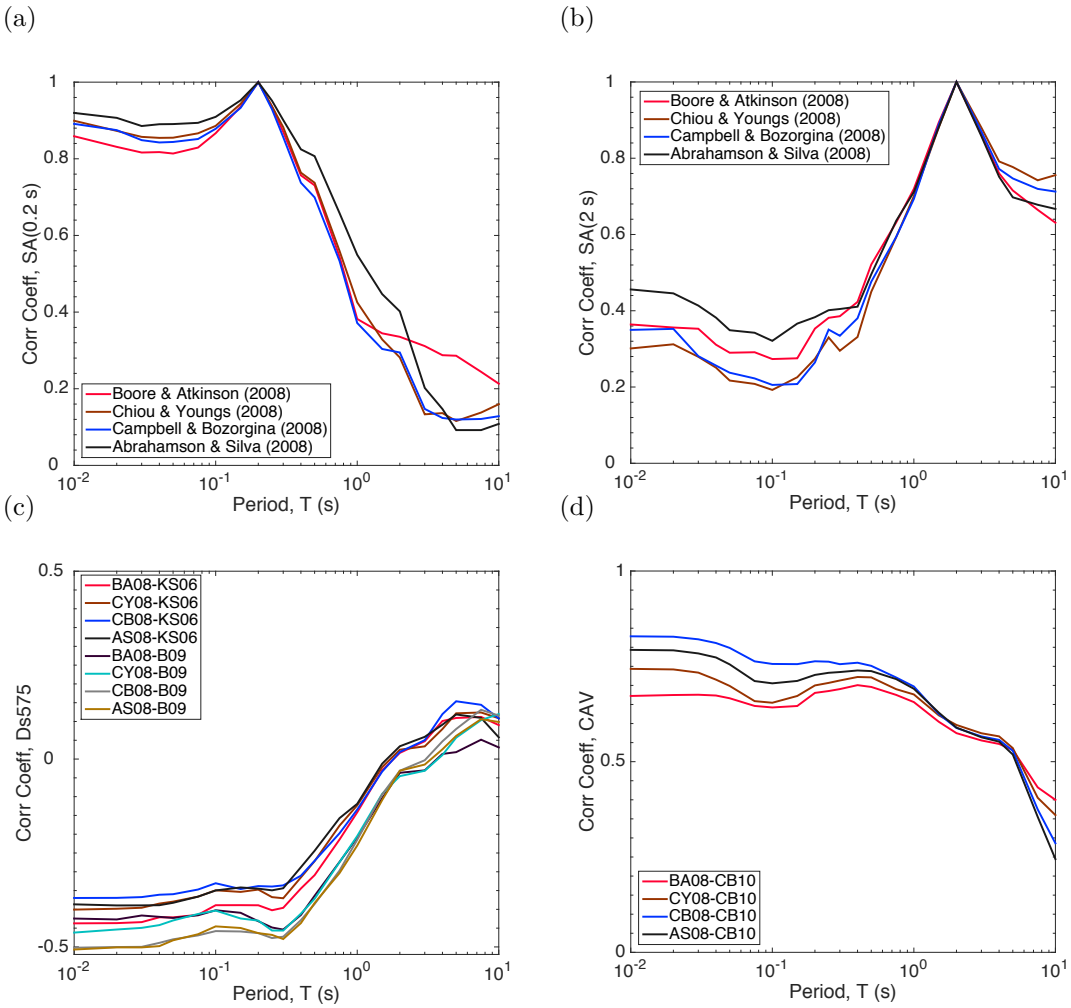

Figure B.2: Correlation of SA ordinates from 0.01 to 10s periods with SA(0.2s), SA(2.0s), D_{s575} , and CAV for directivity ground motions.

These figures are intended to illustrate the variation in the correlation coefficients with respect to the epistemic uncertainty in the chosen GMMs (i.e. for clarity, the effect of finite sample uncertainty is not shown).

B.3.1 Directivity vs. general database of ground motions

Figure B.3 compares the correlation coefficients of the SA ordinates (i.e., T= 0.01 to 10 s) for the directivity and general database of ground motions, and Figure B.4 and Figure B.5 compare the correlation of PGA, PGV, AI, CAV, D_{s575}, D_{s595}, ASI, SI, and DSI with the SA ordinates. The presented results illustrate a

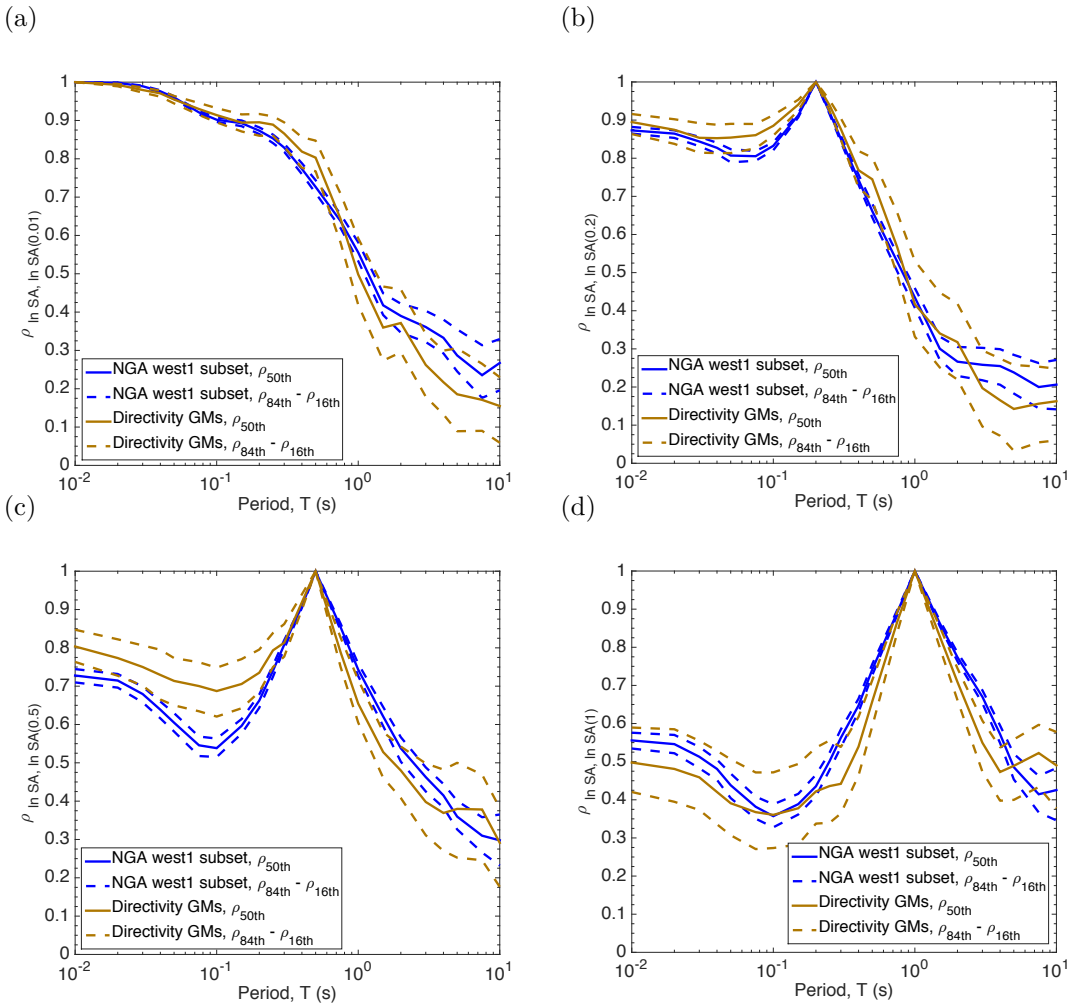

Figure B.3: Correlation of SA ordinates with SA(0.01s), SA(0.2s), SA(0.5s), SA(1.0s), SA(2.0s), and SA(4.0s).

general similarity between these correlation coefficients.

Figure B.6 and Figure B.7 compare the correlation of non-SA IMs considered (i.e., PGA, PGV, AI, CAV, D_{s575}, D_{s595}, ASI, SI, and DSI) for the directivity and general databases. As shown, the median correlation coefficients are generally close, with a larger variation for the directivity ground motions (due to the significantly small number of directivity ground motions and also the large variability in the characteristics of ground motions identified as directivity records).

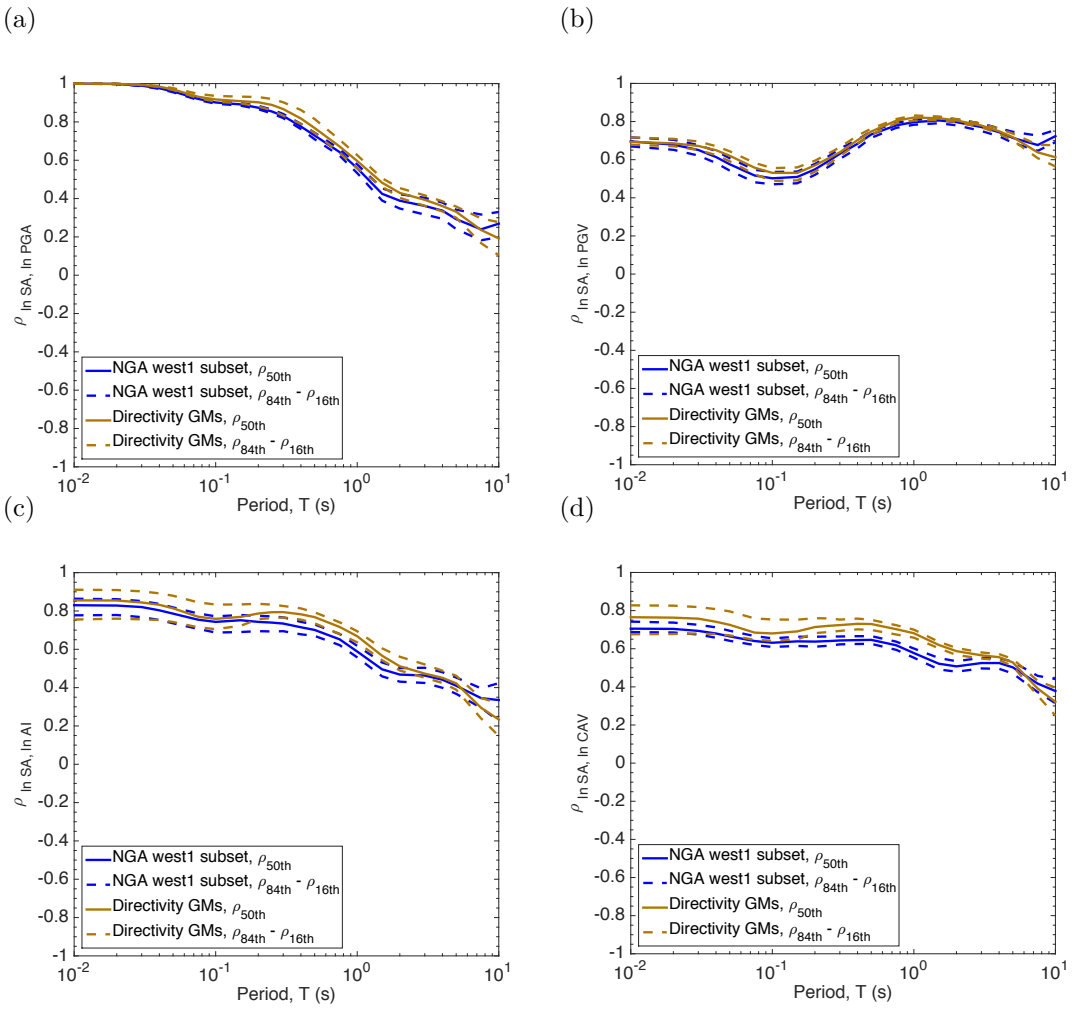

Figure B.4: Correlation of SA ordinates with PGA, PGV, AI, CAV, D_{s575} and D_{s595}.

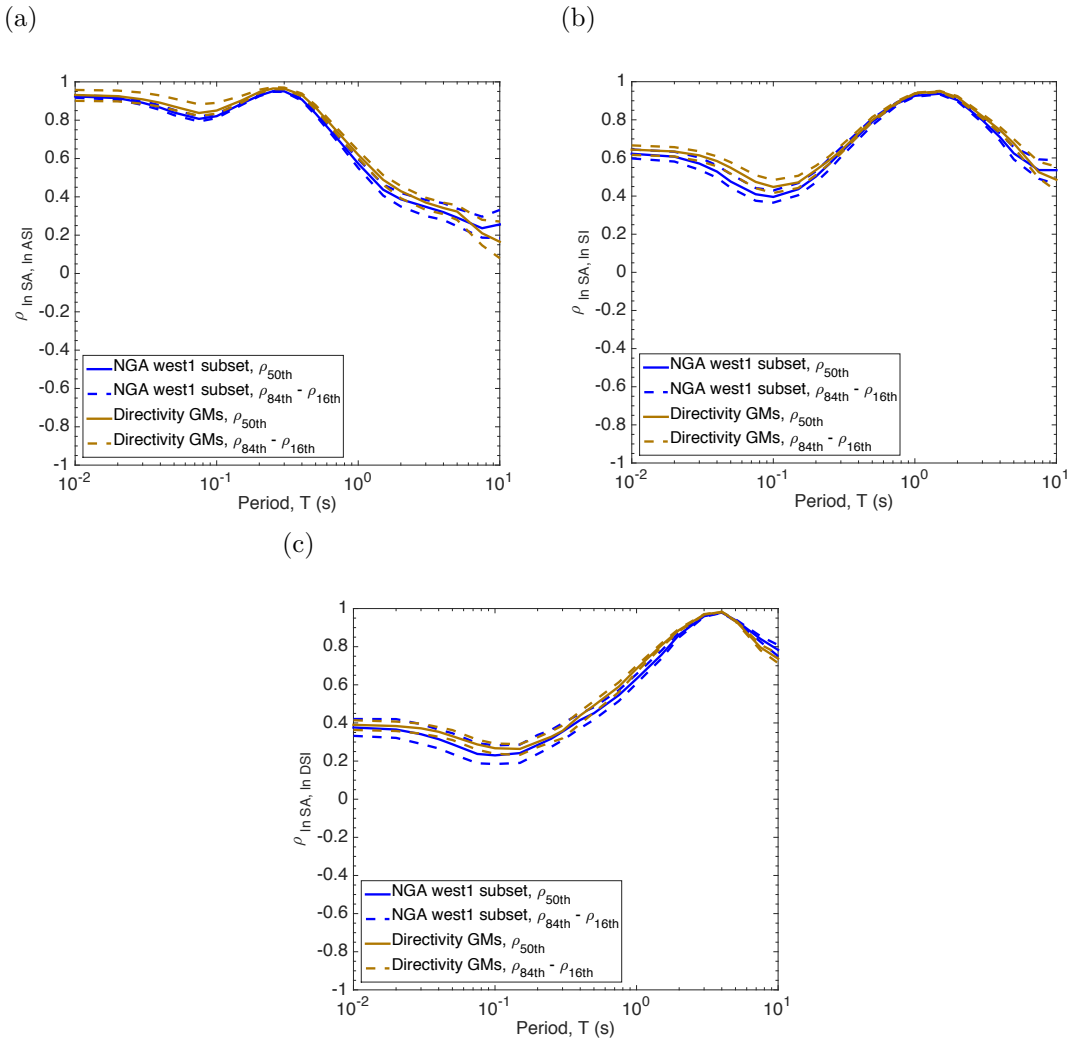

Figure B.5: Correlation of SA ordinates with ASI, SI, and DSI.

(a)

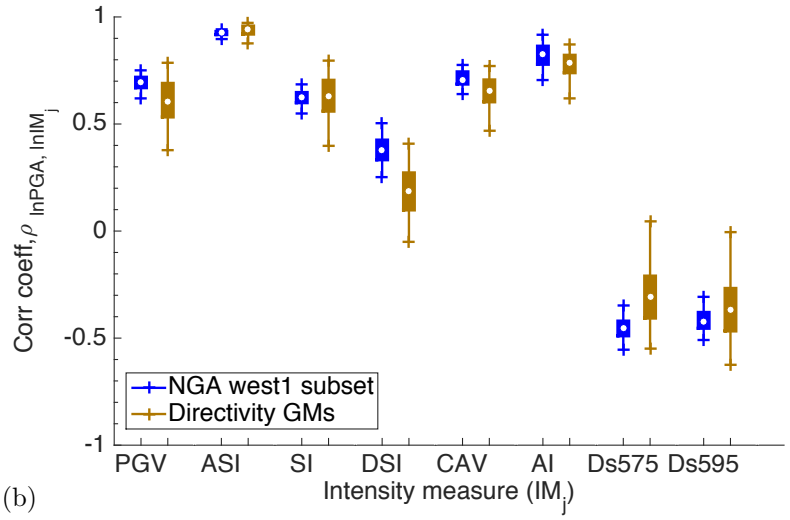

(b)

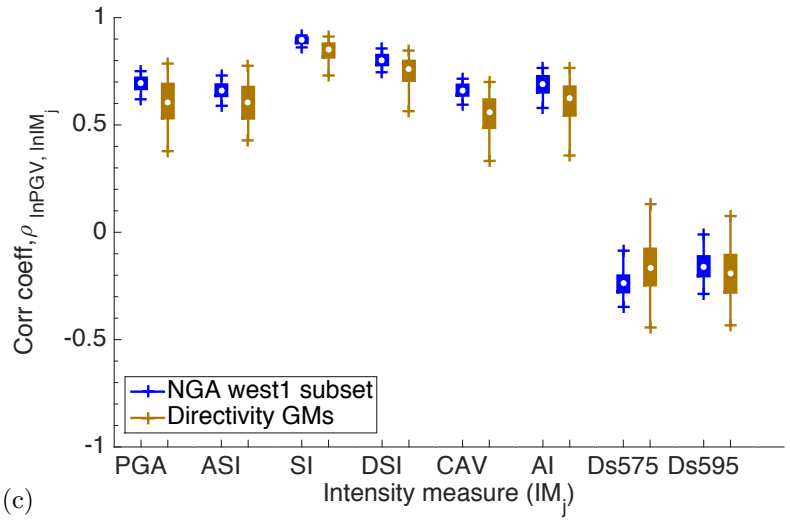

(c)

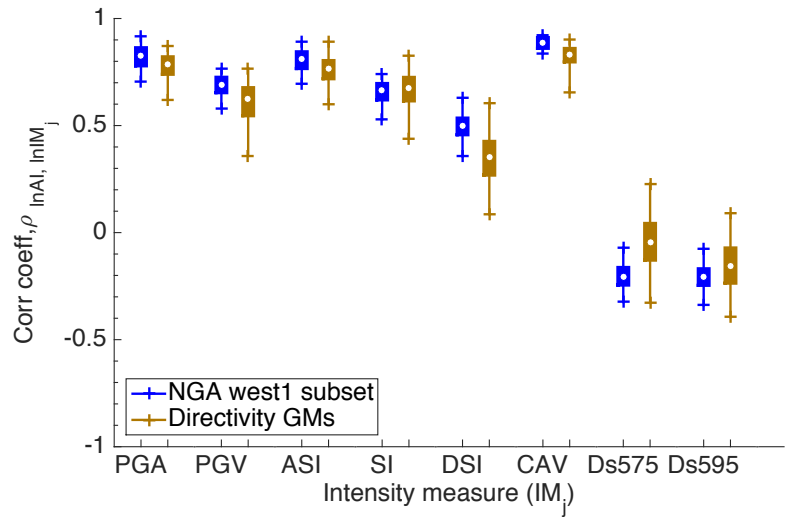

Figure B.6: Correlation of non-SA IMs: (a) PGA; (b) PGV; and (c) AI.

(d)

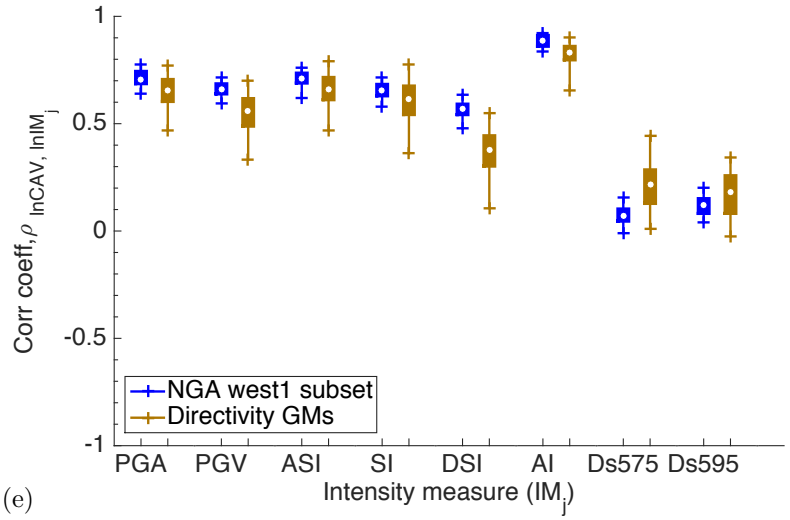

(e)

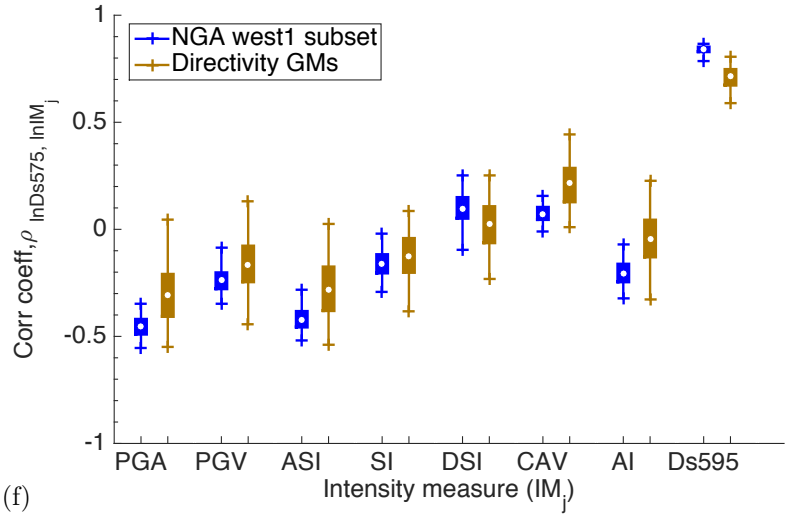

(f)

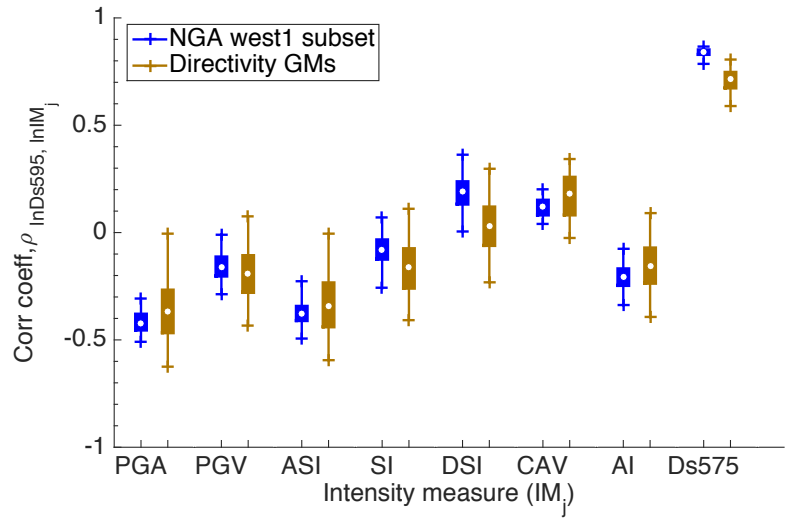

Figure B.6: *(continued)* Correlation of non-SA IMs: (d) CAV; (e) D_{s575}; and (f) D_{s595}.

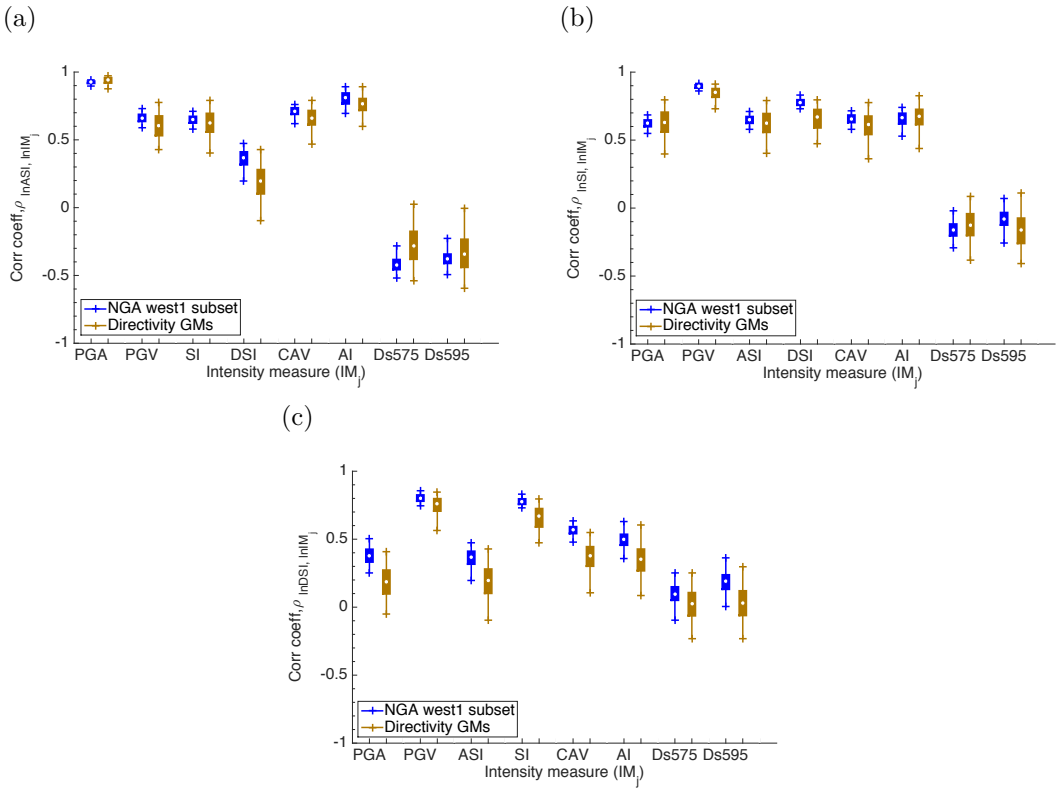

Figure B.7: Correlation of non-SA IMs: (a) ASI; (b) SI; and (c) DSI.

B.4 Discussion

The difference between the SA correlation coefficients of the directivity and general database of ground motions is within the range of differences among the various correlation coefficients developed by other researchers using different ground motion databases (refer to Baker and Bradley 2016 for further details). In addition, as illustrated by Baker and Bradley (2016) (in Figure 6), epistemic uncertainty due to the choice of GMMs to calculate the conditional distribution of SA ordinates (which will be utilized in the ground motion selection process) is significantly larger than the effect of slight variations in the correlation coefficients.

Since the differences between the correlation coefficients of the non-SA IMs with each other and with SA ordinates (illustrated in this Appendix) is small, it is also expected that slight variations in the correlation coefficients will not have significant effects on the conditional distribution of non-SA IMs compared to the

effect of uncertainty in the chosen GMMs.

Appendix C

Directionality in ground motions containing forward directivity pulses

C.1 Summary

Directionality of ground motions containing directivity pulses are examined for pseudo-spectral acceleration ordinates. The results are compared with those from a general database of records containing directivity and non-directivity ground motions.

C.2 Introduction

Intensity measures (IMs) of earthquake ground motions in the horizontal plane are determined based on the chosen orientation of the applied motion. While some ground motions tend to be polarized in a certain orientation, others may approximately have the same IM values in most orientations. Also, polarization of different IMs (*e.g.,* spectral acceleration at two different vibration periods) may

be different for a given ground motion record.

While ground motion IM definitions such as the median amplitude over the non-redundant directions of motion (i.e., RotD50) or other rotation-independent or rotation-dependent median responses are conventionally used to develop ground motion models (GMMs) and select ground motions for seismic response analysis (Baker and Cornell, 2006b; Beyer and Bommer, 2006; Boore et al., 2006; Power et al., 2008; Bozorgnia et al., 2014), engineers might consider the maximum response over all directions (i.e., RotD100) to design engineered systems (BSSC, 2009). The relationship between the maximum and median IMs (i.e., RotD100 / RotD50) can be utilized to examine the directionality of ground motions and provide a means to use a consistent IM definition in different stages of seismic performance assessment (from seismic hazard analysis to ground motion selection and seismic response analysis).

In addition to the RotD100/RotD50 ratio, the orientation at which the maximum IM occurs is also of interest in design and assessment of engineered systems. For example, various studies have examined the maximum IM orientation for near-fault ground motions, demonstrating that depending on the rupture mechanism and the distance from the source, the strike-normal component of the near-fault ground motions may not necessarily represent the strongest orientation of the near-fault ground motion (Howard et al., 2005; Watson-Lamprey and Boore, 2007; Huang et al., 2009; Shahi and Baker, 2014b).

This appendix examines the directionality of the directivity ground motions and compares the results with a published model based on a general database containing directivity and non-directivity ground motions.

C.3 Analysis results

The RotD100 and RotD50 (Beyer and Bommer, 2006; Boore et al., 2006) IMs are calculated for spectral pseudo-acceleration (SA) ordinates for 18 vibration

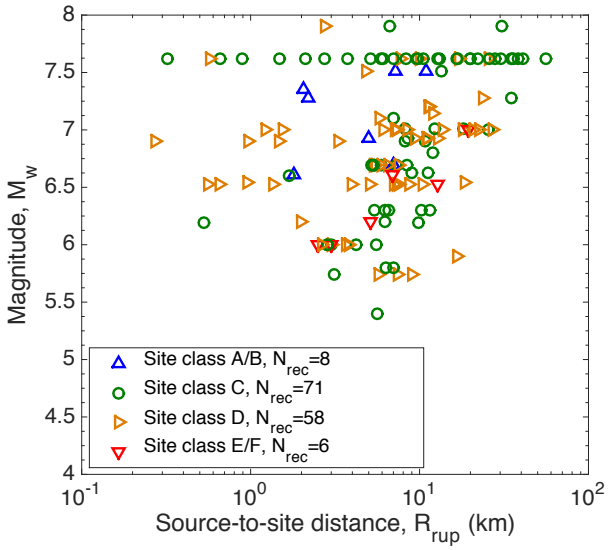

Figure C.1: $M_w - R_{rup}$ distribution of the directivity ground motions considered.

periods (T= 0.05, 0.075, 0.1, 0.15, 0.2, 0.25, 0.3, 0.4, 0.5, 0.75, 1.0, 1.5, 2.0, 3.0, 4.0, 5.0, 7.5, and 10.0 s). The ground motions identified by Shahi and Baker (2014a) as containing forward directivity pulses are utilized in this study. Figure C.1 presents the magnitude (M_w) and source-to-site distance (R_{rup}) of these ground motions, along with their site classification according to NEHRP (2003).

Figure C.2 a presents the normalized displacement response of a linear elastic oscillator with the vibration period of 0.05 s (shown in black solid line) subjected to the as-recorded orthogonal components of a directivity ground motion with the NGA ID number of 143. In addition, the normalized maximum response of the oscillator in all horizontal directions (shown in dashed blue line), and the directions of median, maximum, and minimum responses are presented in Figure C.2a. As shown, this ground motion is not significantly polarized in any orientation with respect to the SA(0.05 s) response. Figure C.2b presents similar results for the response of another oscillator with the vibration period of 3.0 s (i.e., SA(3.0s) response) subjected to the same ground motion.

In contrast to Figure C.2, Figure C.3 presents the response of 0.05 and 3.0 s oscillators to another directivity ground motions with the NGA ID of 983, illustrating significantly polarized responses for both short and long period oscillators.

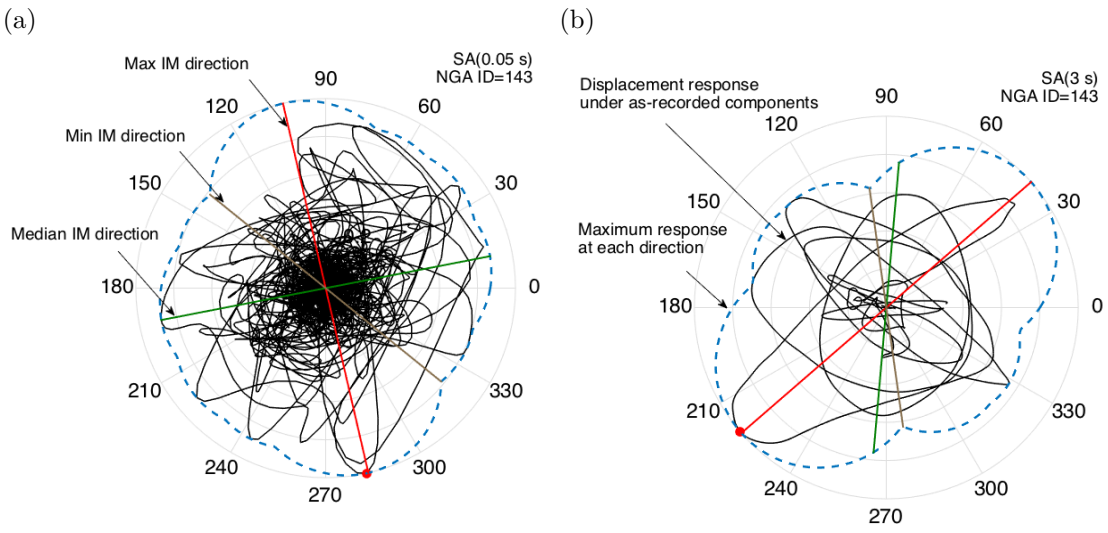

Figure C.2: Normalized displacement response, maximum response of the oscillator in all horizontal orientation, and the orientation of median, maximum, and minimum responses for a ground motion with the NGA ID number of 143: (a) T= 0.05 s oscillator; (b) T= 3.0 s oscillator. This record does not have significantly polarized motion with respect to the SA(0.05) and SA(3.0s) responses.

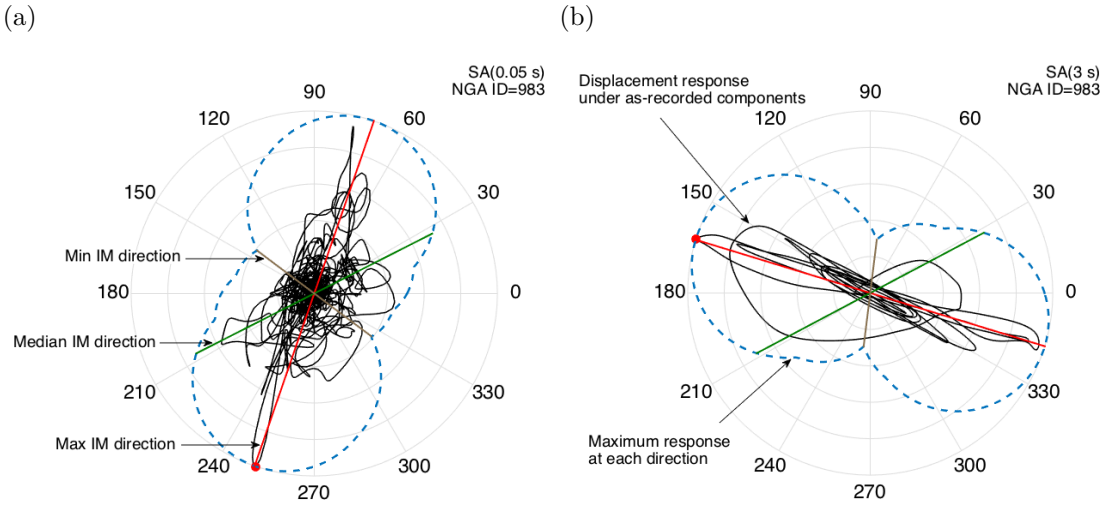

Figure C.3: Normalized displacement response, maximum response of the oscillator in all horizontal directions, and the direction of median, maximum, and minimum responses for a ground motion with the NGA ID number of 983: (a) T= 0.05 s oscillator; (b) T= 3.0 s oscillator. This record has a significant polarization with respect to the SA(0.05) and SA(3.0s) responses.

In order to examine the directionality of the directivity ground motions for the range of SA ordinates considered, Figure C.4 presents the percentiles of the RotD100/RotD50 ratios from the directivity ground motions in comparison to the model developed by Shahi and Baker (2014b) based on the general database of the NGA-West2 project (Ancheta et al., 2013) including directivity and non-directivity ground motions. As shown, the median RotD100/RotD50 ratio of the directivity motions are greater than the Shahi and Baker (2014b) median values due to the fact that the velocity pulses of directivity ground motions generally result in higher long-period SA ordinates (*e.g.,* Archuleta and Hartzell, 1981; Somerville et al., 1997; Aagaard et al., 2004; Bray and Rodriguez-Marek, 2004; Shahi and Baker, 2011). The 84^{th} percentile of the RotD100/RotD50 ratio is also greater for the whole range of SA ordinates. This observation is important as it implies that when computing the ground motion hazard for sites at which directivity is of consideration, not only do directivity ground motions result in an increase in the RotD50 amplitudes around the pulse period (Shahi and Baker, 2011), but they also increase the polarity of the ground motion (meaning that the resulting RotD100 value will be the product of these two factors, both of which increase for directivity ground motions).

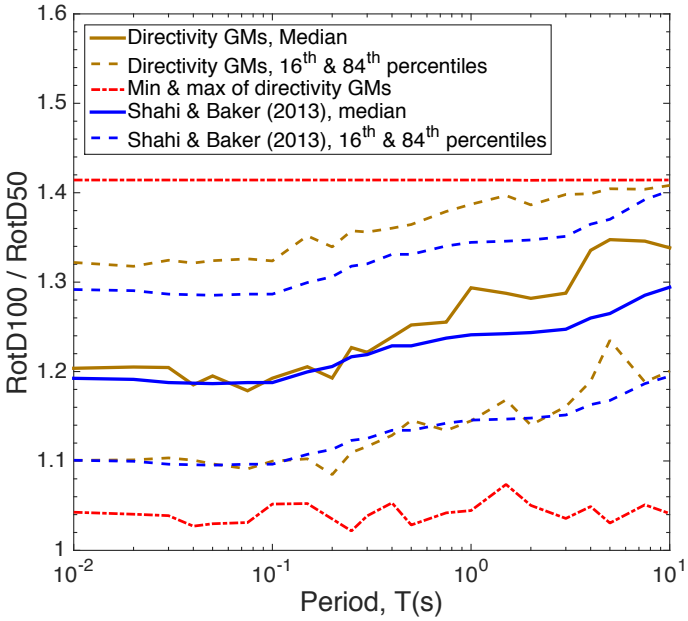

Figure C.4: Percentiles of the RotD100/RotD50 ratios from the directivity ground motions in comparison to the model developed by Shahi and Baker (2014b).

Bibliography

Aagaard, B. T., Hall, J. F., and Heaton, T. H. (2004). Effects of fault dip and slip rake angles on near-source ground motions: why rupture directivity was minimal in the 1999 chi-chi, taiwan, earthquake. *Bulletin of the Seismological Society of America*, 94(1):155–170.

Abrahamson, N. (2006). Seismic hazard assessment: problems with current practice and future developments. In *First European Conference on Earthquake Engineering and Seismology*, pages 3–8.

Abrahamson, N., Atkinson, G., Boore, D., Bozorgnia, Y., Campbell, K., Chiou, B., Idriss, I., Silva, W., and Youngs, R. (2008). Comparisons of the nga ground-motion relations. *Earthquake Spectra*, 24(1):45–66.

Abrahamson, N. and Silva, W. (2008). Summary of the abrahamson & silva nga ground-motion relations. *Earthquake spectra*, 24(1):67–97.

Abrahamson, N. A. (2000). Effects of rupture directivity on probabilistic seismic hazard analysis. In *Proceedings of the 6th International Conference on Seismic Zonation*, volume 1, pages 151–156. Palm Springs CA.

Abrahamson, N. A. and Bommer, J. J. (2005). Probability and uncertainty in seismic hazard analysis. *Earthquake Spectra*, 21(2):603–607.

Akkar, S., Yazgan, U., and GÃijlkan, P. (2005). Drift estimates in frame buildings subjected to near-fault ground motions. *Journal of Structural Engineering*, 131(7):1014–1024.

Al Atik, L. and Youngs, R. R. (2014). Epistemic uncertainty for nga-west2 models. *Earthquake Spectra*, 30(3):1301–1318.

Alavi, B. and Krawinkler, H. (2001). *Effects of Near-Field Ground Motion on Frame Structures*. Thesis.

Almufti, I., Motamed, R., Grant, D. N., and Willford, M. (2013). Incorporation of velocity pulses in design ground motions for response history analysis using a probabilistic framework. *Earthquake Spectra*.

Ambraseys, N. and Douglas, J. (2003). Near-field horizontal and vertical earthquake ground motions. *Soil dynamics and earthquake engineering*, 23(1):1–18.

Ancheta, T. D., Darragh, R., Stewart, J., Seyhan, E., Silva, W., Chiou, B., Wooddell, K., Graves, R., Kottke, A., and Boore, D. (2013). Peer nga-west2 database. *PEER Report 2013*, 3.

Anderson, J. C. and Bertero, V. V. (1987). Uncertainties in establishing design earthquakes. *Journal of Structural Engineering*, 113(8):1709–1724.

Ang, A. H. and Tang, W. H. (1975). *Probability concepts in engineering planning and design*. John Wiley & Sons, Inc., New York.

Archuleta, R. J. and Hartzell, S. H. (1981). Effects of fault finiteness on near-source ground motion. *Bulletin of the Seismological Society of America*, 71(4):939–957.

ASCE/SEI7-10 (2010). Minimum design loads for buildings and other structures, asce/sei 7-10. american society of civil engineers, reston, virginia.

Aslani, H. and Miranda, E. (2005). *Probabilistic earthquake loss estimation and loss disaggregation in buildings*. Thesis.

Atkinson, G. M., Bommer, J. J., and Abrahamson, N. A. (2014). Alternative approaches to modeling epistemic uncertainty in ground motions in probabilistic seismic-hazard analysis. *Seismological Research Letters*, 85(6):1141–1144.

Baker, J. W. (2007). Quantitative classification of near-fault ground motions using wavelet analysis. *Bulletin of the Seismological Society of America*, 97(5):1486–1501.

Baker, J. W. (2011). Conditional mean spectrum: Tool for ground-motion selection. *Journal of Structural Engineering*, 137(3):322–331.

Baker, J. W. (2015). Efficient analytical fragility function fitting using dynamic structural analysis. *Earthquake Spectra*, 31(1):579–599.

Baker, J. W. and Bradley, B. A. (2017). Intensity measure correlations observed in the nga-west2 database, and dependence of correlations on rupture and site parameters. *Earthquake Spectra*, 33(1):145–156.

Baker, J. W. and Cornell, A. C. (2006a). Spectral shape, epsilon and record selection. *Earthquake Engineering & Structural Dynamics*, 35(9):1077–1095.

Baker, J. W. and Cornell, C. A. (2006b). Which spectral acceleration are you using? *Earthquake Spectra*, 22(2):293–312.

Baker, J. W. and Jayaram, N. (2008). Correlation of spectral acceleration values from nga ground motion models. *Earthquake Spectra*, 24(1):299–317.

Baker, J. W. and Lee, C. (2017). An improved algorithm for selecting ground motions to match a conditional spectrum. *Journal of Earthquake Engineering*, pages 1–16.

Bazzurro, P. and Cornell, C. A. (1999). Disaggregation of seismic hazard. *Bulletin of the Seismological Society of America*, 89(2):501–520.

Bertero, V. V., Mahin, S. A., and Herrera, R. A. (1978). Aseismic design implications of near-fault san fernando earthquake records. *Earthquake engineering & structural dynamics*, 6(1):31–42.

Beyer, K. and Bommer, J. J. (2006). Relationships between median values and between aleatory variabilities for different definitions of the horizontal component of motion. *Bulletin of the Seismological Society of America*, 96(4A):1512–1522.

Bommer, J. J. (2002). Deterministic vs. probabilistic seismic hazard assessment: an exaggerated and obstructive dichotomy. *Journal of Earthquake Engineering*, 6(spec01):43–73.

Bommer, J. J. and Acevedo, A. B. (2004). The use of real earthquake accelerograms as input to dynamic analysis. *Journal of Earthquake Engineering*, 8(spec01):43–91.

Bommer, J. J., Douglas, J., Scherbaum, F., Cotton, F., Bungum, H., and Fah, D. (2010). On the selection of ground-motion prediction equations for seismic hazard analysis. *Seismological Research Letters*, 81(5):783–793.

Bommer, J. J., Douglas, J., and Strasser, F. O. (2003). Style-of-faulting in ground-motion prediction equations. *Bulletin of Earthquake Engineering*, 1(2):171–203.

Bommer, J. J., Hancock, J., and AlarcÃşn, J. E. (2006). Correlations between duration and number of effective cycles of earthquake ground motion. *Soil Dynamics and Earthquake Engineering*, 26(1):1–13.

Bommer, J. J., Magenes, G., Hancock, J., and Penazzo, P. (2004). The influence of strong-motion duration on the seismic response of masonry structures. *Bulletin of Earthquake Engineering*, 2(1):1–26.

Bommer, J. J. and Martinez-Pereira, A. (1999). The effective duration of earthquake strong motion. *Journal of Earthquake Engineering*, 3(2):127–172.

Bommer, J. J. and Scherbaum, F. (2008). The use and misuse of logic trees in probabilistic seismic hazard analysis. *Earthquake Spectra*, 24(4):997–1009.

Bommer, J. J., Scherbaum, F., Bungum, H., Cotton, F., Sabetta, F., and Abrahamson, N. A. (2005). On the use of logic trees for ground-motion prediction equations in seismic-hazard analysis. *Bulletin of the Seismological Society of America*, 95(2):377–389.

Bommer, J. J., Stafford, P. J., and AlarcÃşn, J. E. (2009). Empirical equations for the prediction of the significant, bracketed, and uniform duration of earthquake

ground motion. *Bulletin of the Seismological Society of America*, 99(6):3217–3233.

Boore, D. M. and Atkinson, G. M. (2008). Ground-motion prediction equations for the average horizontal component of pga, pgv, and 5and 10.0 s. *Earthquake Spectra*, 24(1):99–138.

Boore, D. M., Watson-Lamprey, J., and Abrahamson, N. A. (2006). Orientation-independent measures of ground motion. *Bulletin of the Seismological Society of America*, 96(4A):1502–1511.

Bozorgnia, Y., Abrahamson, N. A., Atik, L. A., Ancheta, T. D., Atkinson, G. M., Baker, J. W., Baltay, A., Boore, D. M., Campbell, K. W., and Chiou, B. S.-J. (2014). Nga-west2 research project. *Earthquake Spectra*, 30(3):973–987.

Bradley, B. A. (2009). Seismic hazard epistemic uncertainty in the san francisco bay area and its role in performance-based assessment. *Earthquake Spectra*, 25(4):733–753.

Bradley, B. A. (2010a). Epistemic uncertainties in component fragility functions. *Earthquake Spectra*, 26(1):41–62.

Bradley, B. A. (2010b). A generalized conditional intensity measure approach and holistic ground-motion selection. *Earthquake Engineering & Structural Dynamics*, 39(12):1321–1342.

Bradley, B. A. (2010c). Site-specific and spatially distributed ground-motion prediction of acceleration spectrum intensity. *Bulletin of the Seismological Society of America*, 100(2):792–801.

Bradley, B. A. (2011a). Correlation of significant duration with amplitude and cumulative intensity measures and its use in ground motion selection. *Journal of Earthquake Engineering*, 15(6):809–832.

Bradley, B. A. (2011b). Empirical correlation of pga, spectral accelerations and spectrum intensities from active shallow crustal earthquakes. *Earthquake Engineering & Structural Dynamics*, 40(15):1707–1721.

Bradley, B. A. (2011c). Empirical equations for the prediction of displacement spectrum intensity and its correlation with other intensity measures. *Soil Dynamics and Earthquake Engineering*, 31(8):1182–1191.

Bradley, B. A. (2012a). Empirical correlations between cumulative absolute velocity and amplitude-based ground motion intensity measures. *Earthquake Spectra*, 28(1):37–54.

Bradley, B. A. (2012b). Empirical correlations between peak ground velocity and spectrum-based intensity measures. *Earthquake Spectra*, 28(1):17–35.

Bradley, B. A. (2012c). A ground motion selection algorithm based on the generalized conditional intensity measure approach. *Soil Dynamics and Earthquake Engineering*, 40:48–61.

Bradley, B. A. (2012d). The seismic demand hazard and importance of the conditioning intensity measure. *Earthquake Engineering & Structural Dynamics*, 41(11):1417–1437.

Bradley, B. A. (2013a). A comparison of intensity-based demand distributions and the seismic demand hazard for seismic performance assessment. *Earthquake Engineering & Structural Dynamics*, 42(15):2235–2253.

Bradley, B. A. (2013b). A critical examination of seismic response uncertainty analysis in earthquake engineering. *Earthquake Engineering & Structural Dynamics*, 42(11):1717–1729.

Bradley, B. A. (2013c). *Ground motion selection for seismic risk analysis of civil infrastructures*. Woodhead Publishing Ltd., Cambridge.

Bradley, B. A. (2013d). A new zealand-specific pseudospectral acceleration ground-motion prediction equation for active shallow crustal earthquakes

based on foreign models. *Bulletin of the Seismological Society of America*, 103(3):1801–1822.

Bradley, B. A. (2013e). Practice-oriented estimation of the seismic demand hazard using ground motions at few intensity levels. *Earthquake Engineering & Structural Dynamics*, 42(14):2167–2185.

Bradley, B. A. (2015). Correlation of arias intensity with amplitude, duration and cumulative intensity measures. *Soil Dynamics and Earthquake Engineering*, 78:89–98.

Bradley, B. A., Araki, K., Ishii, T., and Saitoh, K. (2013). Effect of lattice-shaped ground improvement geometry on seismic response of liquefiable soil deposits via 3-d seismic effective stress analysis. *Soil Dynamics and Earthquake Engineering*, 48:35–47.

Bradley, B. A., Burks, L. S., and Baker, J. W. (2015). Ground motion selection for simulation-based seismic hazard and structural reliability assessment. *Earthquake Engineering & Structural Dynamics*, 44(13):2321–2340.

Bradley, B. A., Cubrinovski, M., MacRae, G. A., and Dhakal, R. P. (2009). Ground-motion prediction equation for si based on spectral acceleration equations. *Bulletin of the Seismological Society of America*, 99(1):277–285.

Bradley, B. A., Dhakal, R. P., MacRae, G. A., and Cubrinovski, M. (2010). Prediction of spatially distributed seismic demands in specific structures: Ground motion and structural response. *Earthquake Engineering & Structural Dynamics*, 39(5):501–520.

Bray, J. D. and Rodriguez-Marek, A. (2004). Characterization of forward-directivity ground motions in the near-fault region. *Soil Dynamics and Earthquake Engineering*, 24(11):815–828.

BSSC, B. S. S. (2009). Nehrp recommended seismic provisions for new buildings and other structures (fema p-750).

Burks, L. S. and Baker, J. W. (2012). Occurrence of negative epsilon in seismic hazard analysis deaggregation, and its impact on target spectra computation. *Earthquake Engineering & Structural Dynamics*, 41(8):1241–1256.

Campbell, K. W. and Bozorgnia, Y. (2008). Nga ground motion model for the geometric mean horizontal component of pga, pgv, pgd and 5ranging from 0.01 to 10 s. *Earthquake Spectra*, 24(1):139–171.

Campbell, K. W. and Bozorgnia, Y. (2010). A ground motion prediction equation for the horizontal component of cumulative absolute velocity (cav) based on the peer-nga strong motion database. *Earthquake Spectra*, 26(3):635–650.

Campbell, K. W. and Bozorgnia, Y. (2012). A comparison of ground motion prediction equations for arias intensity and cumulative absolute velocity developed using a consistent database and functional form. *Earthquake Spectra*, 28(3):931–941.

CEN (2005). Design of structures for earthquake resistance. part 1: General rules, seismic actions and rules for buildings.

Champion, C. and Liel, A. (2012). The effect of near-fault directivity on building seismic collapse risk. *Earthquake Engineering & Structural Dynamics*, 41(10):1391–1409.

Chandramohan, R., Baker, J. W., and Deierlein, G. G. (2015). Quantifying the influence of ground motion duration on structural collapse capacity using spectrally equivalent records. *Earthquake Spectra*.

Chandramohan, R., Baker, J. W., and Deierlein, G. G. (2016). Impact of hazard-consistent ground motion duration in structural collapse risk assessment. *Earthquake Engineering & Structural Dynamics*.

Chioccarelli, E. and Iervolino, I. (2010). Near-source seismic demand and pulse-like records: A discussion for l'aquila earthquake. *Earthquake Engineering & Structural Dynamics*, 39(9):1039–1062.

Chiou, B., Darragh, R., Gregor, N., and Silva, W. (2008). Nga project strong-motion database. *Earthquake Spectra*, 24(1):23–44.

Chiou, B.-J. and Youngs, R. R. (2008). An nga model for the average horizontal component of peak ground motion and response spectra. *Earthquake Spectra*, 24(1):173–215.

Chiou, B. S.-J. and Youngs, R. R. (2014). Update of the chiou and youngs nga model for the average horizontal component of peak ground motion and response spectra. *Earthquake Spectra*, 30(3):1117–1153.

Cotton, F., Scherbaum, F., Bommer, J. J., and Bungum, H. (2006). Criteria for selecting and adjusting ground-motion models for specific target regions: Application to central europe and rock sites. *Journal of Seismology*, 10(2):137–156.

De Stefano, M. and Pintucchi, B. (2008). A review of research on seismic behaviour of irregular building structures since 2002. *Bulletin of Earthquake Engineering*, 6(2):285–308.

Deierlein, G., Krawinkler, H., and Cornell, C. (2003). A framework for performance-based earthquake engineering. In *Pacific conference on earthquake engineering*, pages 1–8. Citeseer.

Douglas, J. (2011). *Ground-motion prediction equations 1964-2010*. Pacific Earthquake Engineering Research Center Berkeley, CA.

FEMA-P58 (2012). Seismic performance assessment of buildings: Vol. 1–methodology. Technical report, Applied Technology Council, Federal Emergency Management Agency, Washington, D.C.

Field, E. H., Dawson, T. E., Felzer, K. R., Frankel, A. D., Gupta, V., Jordan, T. H., Parsons, T., Petersen, M. D., Stein, R. S., and Weldon, R. (2009). Uniform california earthquake rupture forecast, version 2 (ucerf 2). *Bulletin of the Seismological Society of America*, 99(4):2053–2107.

Field, E. H., Jordan, T. H., and Cornell, C. A. (2003). Opensha: A developing community-modeling environment for seismic hazard analysis. *Seismological Research Letters*, 74(4):406–419.

Fischer, F. and Seeber, R. (1988). Dynamic response of vertically excited liquid storage tanks considering liquid-soil interaction. *Earthquake engineering & structural dynamics*, 16(3):329–342.

Fox, M. J., Stafford, P. J., and Sullivan, T. J. (2015). Seismic hazard disaggregation in performance-based earthquake engineering: occurrence or exceedance? *Earthquake Engineering & Structural Dynamics*.

Galasso, C., Zareian, F., Iervolino, I., and Graves, R. (2012). Validation of ground-motion simulations for historical events using sdof systems. *Bulletin of the Seismological Society of America*, 102(6):2727–2740.

Galasso, C., Zhong, P., Zareian, F., Iervolino, I., and Graves, R. W. (2013). Validation of ground-motion simulations for historical events using mdof systems. *Earthquake Engineering & Structural Dynamics*, 42(9):1395–1412.

Gokkaya, B. U., Baker, J. W., and Deierlein, G. G. (2016). Quantifying the impacts of modeling uncertainties on the seismic drift demands and collapse risk of buildings with implications on seismic design checks. *Earthquake Engineering & Structural Dynamics*, 45(10):1661–1683.

Gregor, N., Abrahamson, N. A., Atkinson, G. M., Boore, D. M., Bozorgnia, Y., Campbell, K. W., Chiou, B. S.-J., Idriss, I., Kamai, R., and Seyhan, E. (2014). Comparison of nga-west2 gmpes. *Earthquake Spectra*, 30(3):1179–1197.

Gülerce, Z. and Abrahamson, N. A. (2010). Vector-valued probabilistic seismic hazard assessment for the effects of vertical ground motions on the seismic response of highway bridges. *Earthquake Spectra*, 26(4):999–1016.

Gülerce, Z. and Abrahamson, N. A. (2011). Site-specific design spectra for vertical ground motion. *Earthquake Spectra*, 27(4):1023–1047.

Gülerce, Z., Kamai, R., Abrahamson, N. A., and Silva, W. J. (2016). Ground motion prediction equations for the vertical ground motion component based on the nga-w2 database. *Earthquake Spectra*.

Hall, J. F., Heaton, T. H., Halling, M. W., and Wald, D. J. (1995). Near-source ground motion and its effects on flexible buildings. *Earthquake spectra*, 11(4):569–605.

Hancock, J. and Bommer, J. J. (2005). The effective number of cycles of earthquake ground motion. *Earthquake engineering & structural dynamics*, 34(6):637–664.

Hayden, C. P., Bray, J. D., and Abrahamson, N. A. (2014). Selection of near-fault pulse motions. *Journal of Geotechnical and Geoenvironmental Engineering*, 140(7):04014030.

Howard, J. K., Tracy, C. A., and Burns, R. G. (2005). Comparing observed and predicted directivity in near-source ground motion. *Earthquake Spectra*, 21(4):1063–1092.

Huang, Y.-N., Whittaker, A. S., and Luco, N. (2009). Orientation of maximum spectral demand in the near-fault region. *Earthquake Spectra*, 25(3):707–717.

Ibarra, L. F., Medina, R. A., and Krawinkler, H. (2005). Hysteretic models that incorporate strength and stiffness deterioration. *Earthquake engineering & structural dynamics*, 34(12):1489–1511.

Jalayer, F. and Cornell, C. (2009). Alternative non-linear demand estimation methods for probability-based seismic assessments. *Earthquake Engineering & Structural Dynamics*, 38(8):951–972.

Jayaram, N., Lin, T., and Baker, J. W. (2011). A computationally efficient ground-motion selection algorithm for matching a target response spectrum mean and variance. *Earthquake Spectra*, 27(3):797–815.

Joshi, V. A. (2013). *Near-Fault Forward-Directivity Aspects of Strong Ground Motions in the 2010-11 Canterbury Earthquakes*. Thesis.

Katsanos, E. I., Sextos, A. G., and Manolis, G. D. (2010). Selection of earthquake ground motion records: A state-of-the-art review from a structural engineering perspective. *Soil Dynamics and Earthquake Engineering*, 30(4):157–169.

Kempton, J. J. and Stewart, J. P. (2006). Prediction equations for significant duration of earthquake ground motions considering site and near-source effects. *Earthquake spectra*, 22(4):985–1013.

Kottke, A. and Rathje, E. M. (2008). A semi-automated procedure for selecting and scaling recorded earthquake motions for dynamic analysis. *Earthquake Spectra*, 24(4):911–932.

Kramer, S. L. (1996). *Geotechnical earthquake engineering*. Pearson Education India.

Krawinkler, H. and Miranda, E. (2004). *Performance-based earthquake engineering*. CRC Press, Boca Raton, FL.

Kulkarni, R., Youngs, R., and Coppersmith, K. (1984). Assessment of confidence intervals for results of seismic hazard analysis. In *Proceedings of the Eighth World Conference on Earthquake Engineering*, volume 1, pages 263–270.

Kurzon, I., Vernon, F., Ben-Zion, Y., and Atkinson, G. (2014). Ground motion prediction equations in the san jacinto fault zone: significant effects of rupture directivity and fault zone amplification. *Pure and Applied Geophysics*, 171(11):3045–3081.

Leonard, M. (2014). Self-consistent earthquake fault-scaling relations: Update and extension to stable continental strike-slip faults. *Bulletin of the Seismological Society of America*.

Liel, A. B., Haselton, C. B., Deierlein, G. G., and Baker, J. W. (2009). Incorporating modeling uncertainties in the assessment of seismic collapse risk of buildings. *Structural Safety*, 31(2):197–211.

Lignos, D. G. and Krawinkler, H. (2012). Development and utilization of structural component databases for performance-based earthquake engineering. *Journal of Structural Engineering*, 139(8):1382–1394.

Lin, T., Harmsen, S. C., Baker, J. W., and Luco, N. (2013). Conditional spectrum computation incorporating multiple causal earthquakes and ground-motion prediction models. *Bulletin of the Seismological Society of America*, 103(2A):1103–1116.

Luco, N. and Cornell, C. A. (2007). Structure-specific scalar intensity measures for near-source and ordinary earthquake ground motions. *Earthquake Spectra*, 23(2):357–392.

Mai, P. M., Spudich, P., and Boatwright, J. (2005). Hypocenter locations in finite-source rupture models. *Bulletin of the Seismological Society of America*, 95(3):965–980.

Makris, N. and Black, C. J. (2004). Dimensional analysis of bilinear oscillators under pulse-type excitations. *Journal of Engineering Mechanics*, 130(9):1019–1031.

Marzocchi, W. and Jordan, T. H. (2014). Testing for ontological errors in probabilistic forecasting models of natural systems. *Proceedings of the National Academy of Sciences*, 111(33):11973–11978.

Mavroeidis, G., Dong, G., and Papageorgiou, A. (2004). Near-fault ground motions, and the response of elastic and inelastic single-degree-of-freedom (sdof) systems. *Earthquake Engineering & Structural Dynamics*, 33(9):1023–1049.

Mavroeidis, G. and Papageorgiou, A. (2002). Near-source strong ground motion:

characteristics and design issues. In *Proc. of the Seventh US National Conf. on Earthquake Engineering (7NCEE), Boston, Massachusetts*, volume 21, page 25.

Mavroeidis, G. P. and Papageorgiou, A. S. (2010). Effect of fault rupture characteristics on near-fault strong ground motions. *Bulletin of the Seismological Society of America*, 100(1):37–58.

McGuire, R. K. (1995). Probabilistic seismic hazard analysis and design earthquakes: closing the loop. *Bulletin of the Seismological Society of America*, 85(5):1275–1284.

McGuire, R. K., Cornell, C. A., and Toro, G. R. (2005). The case for using mean seismic hazard. *Earthquake Spectra*, 21(3):879–886.

Menun, C. and Fu, Q. (2002). An analytical model for near-fault ground motions and the response of sdof systems. *Earthquake Spectra*, pages 249–58.

Musson, R. (2005). Against fractiles. *Earthquake Spectra*, 21(3):887–891.

NEHRP (2003). Building seismic safety council, nehrp recommended provisions for seismic regulations for new buildings and other structures, part1: Provisions, fema 450, federal emergency management agency, washington, d.c.

NEHRP (2011). Selecting and scaling earthquake ground motions for performing response history analysis, nist/gcr 11-917-15, nehrp consultants joint venture for the national institute of standards and technology, gaithersburg, maryland.

NZS1170.5 (2004). Nzs1170.5:2004 structural design actions, part 5: Earthquake actions - new zealand.

Oyarzo-Vera, C. A., McVerry, G. H., and Ingham, J. M. (2012). Seismic zonation and default suite of ground-motion records for time-history analysis in the north island of new zealand. *Earthquake Spectra*, 28(2):667–688.

Papazoglou, A. and Elnashai, A. (1996). Analytical and field evidence of the damaging effect of vertical earthquake ground motion. *Earthquake Engineering and Structural Dynamics*, 25(10):1109–1138.

Petersen, M. D., Cao, T., Campbell, K. W., and Frankel, A. D. (2007). Time-independent and time-dependent seismic hazard assessment for the state of california: Uniform california earthquake rupture forecast model 1.0. *Seismological Research Letters*, 78(1):99–109.

Pitarka, A., Somerville, P., Fukushima, Y., Uetake, T., and Irikura, K. (2000). Simulation of near-fault strong-ground motion using hybrid green's functions. *Bulletin of the Seismological Society of America*, 90(3):566–586.

Power, M., Chiou, B., Abrahamson, N., Bozorgnia, Y., Shantz, T., and Roblee, C. (2008). An overview of the nga project. *Earthquake spectra*, 24(1):3–21.

Reiter, L. (1991). *Earthquake hazard analysis: issues and insights*. Columbia University Press.

Saadeghvariri, M. A. and Foutch, D. A. (1991). Dynamic behaviour of r/c highway bridges under the combined effect of vertical and horizontal earthquake motions. *Earthquake Engineering & Structural Dynamics*, 20(6):535–549.

Shahi, S. K. (2013). *A probabilistic framework to include the effects of near-fault directivity in seismic hazard assessment*. Thesis.

Shahi, S. K. and Baker, J. W. (2011). An empirically calibrated framework for including the effects of near-fault directivity in probabilistic seismic hazard analysis. *Bulletin of the Seismological Society of America*, 101(2):742–755.

Shahi, S. K. and Baker, J. W. (2014a). An efficient algorithm to identify strong-velocity pulses in multicomponent ground motions. *Bulletin of the Seismological Society of America*, 104(5):2456–2466.

Shahi, S. K. and Baker, J. W. (2014b). Nga-west2 models for ground motion directionality. *Earthquake Spectra*, 30(3):1285–1300.

Shome, N. and Cornell, C. (1999). probabilistic seismic demand analysis of non-linear structures. Report, Stanford University: Palo Alto, CA.

Shome, N., Cornell, C. A., Bazzurro, P., and Carballo, J. E. (1998). Earthquakes, records, and nonlinear responses. *Earthquake Spectra*, 14(3):469–500.

Somerville, P. G. (2003). Magnitude scaling of the near fault rupture directivity pulse. *Physics of the earth and planetary interiors*, 137(1):201–212.

Somerville, P. G., Smith, N. F., Graves, R. W., and Abrahamson, N. A. (1997). Modification of empirical strong ground motion attenuation relations to include the amplitude and duration effects of rupture directivity. *Seismological Research Letters*, 68(1):199–222.

Spudich, P. and Chiou, B. S. (2008). Directivity in nga earthquake ground motions: analysis using isochrone theory. *Earthquake Spectra*, 24(1):279–298.

Spudich, P., Rowshandel, B., Shahi, S. K., Baker, J. W., and Chiou, B. S.-J. (2014). Comparison of nga-west2 directivity models. *Earthquake Spectra*, 30(3):1199–1221.

Stewart, J. P., Chiou, S.-J., Bray, J. D., Graves, R. W., Somerville, P. G., and Abrahamson, N. A. (2001). Ground motion evaluation procedures for performance-based design. Report.

Stewart, J. P., Douglas, J., Javanbarg, M., Bozorgnia, Y., Abrahamson, N. A., Boore, D. M., Campbell, K. W., Delavaud, E., Erdik, M., and Stafford, P. J. (2015). Selection of ground motion prediction equations for the global earthquake model. *Earthquake Spectra*, 31(1):19–45.

Stirling, M., McVerry, G., Gerstenberger, M., Litchfield, N., Van Dissen, R., Berryman, K., Barnes, P., Wallace, L., Villamor, P., and Langridge, R. (2012). National seismic hazard model for new zealand: 2010 update. *Bulletin of the Seismological Society of America*, 102(4):1514–1542.

Taghavi, S. and Miranda, E. (2003). *Response assessment of nonstructural building elements*. Pacific Earthquake Engineering Research Center.

Tarbali, K. and Bradley, B. A. (2014a). Ground-motion selection for scenario ruptures using the generalized conditional intensity measure (gcim) approach and its application for several major earthquake scenarios in new zealand, department of civil and natural resources engineering, research report 2014-03, university of canterbury, new zealand, https://ir.canterbury.ac.nz/handle/10092/10566. Report.

Tarbali, K. and Bradley, B. A. (2014b). Representative ground-motion ensembles for several major earthquake scenarios in new zealand. *Bulletin of New Zealand Society of Earthquake Engineering*, 47(4):231–252.

Tarbali, K. and Bradley, B. A. (2015a). Bounds on causal parameters of prospective ground motions and their effect on characteristics of selected ground motions, department of civil and natural resources engineering, research report 2015-01, university of canterbury, new zealand, https://ir.canterbury.ac.nz/handle/10092/13314. Report.

Tarbali, K. and Bradley, B. A. (2015b). Ground-motion selection for scenario ruptures using the generalized conditional intensity measure (gcim) method. *Earthquake Engineering & Structural Dynamics*, 44(10):1601–1621.

Tarbali, K. and Bradley, B. A. (2016). The effect of causal parameter bounds in psha-based ground motion selection. *Earthquake Engineering & Structural Dynamics*, 45(9):1515–1535.

Tarbali, K., Bradley, B. A., and Baker, J. W. (2017). Consideration and propagation of ground motion selection epistemic uncertainties to seismic performance metrics. *Earthquake Spectra*, submitted.

Terzic, V., Schoettler, M., Restrepo, J., and Mahin, S. (2015). Concrete column blind prediction contest 2010: outcomes and observations. *PEER Rep. No*, 1.

Tothong, P., Cornell, A. C., and Baker, J. W. (2007). Explicit directivity-pulse inclusion in probabilistic seismic hazard analysis. *Earthquake Spectra*, 23(4):867–891.

Tothong, P. and Cornell, C. A. (2007). *Probabilistic seismic demand analysis using advanced ground motion intensity measures, attenuation relationships and near-fault effects. John A. Blume Earthquake Engineering Center, Department of Civil and Environmental Engineering, Stanford University, Stanford, CA.* Thesis.

Villaverde, R. (2007). Methods to assess the seismic collapse capacity of building structures: State of the art. *Journal of Structural Engineering*, 133(1):57–66.

Wang, G. (2011). A ground motion selection and modification method capturing response spectrum characteristics and variability of scenario earthquakes. *Soil Dynamics and Earthquake Engineering*, 31(4):611–625.

Wang, G. and Du, W. (2012). Empirical correlations between cumulative absolute velocity and spectral accelerations from nga ground motion database. *Soil Dynamics and Earthquake Engineering*, 43:229–236.

Wang, G., Youngs, R., Power, M., and Li, Z. (2015). Design ground motion library (dgml): An interactive tool for selecting earthquake ground motions. *Earthquake Spectra*, 31(2):617–635.

Watson-Lamprey, J. A. and Boore, D. M. (2007). Beyond sagmroti: Conversion to saarb, sasn, and samaxrot. *Bulletin of the Seismological Society of America*, 97(5):1511–1524.

WGCEP02 (2003). Working group on california earthquake probabilities: Earthquake probabilities in the san francisco bay region: 2002-2031, open-file report 03-214. Report.